Active Vibration Control of Long Suspension Bridges

Hansen, Henriette I.

Publication date:
1998

Document Version
Publisher's PDF, also known as Version of record

Aalborg **UNIVERSITY**

Active Vib

Active Vibration Control of Long Suspension Bridges

Henriette I. Hansen

Paper No 186

Structural Reliability Theory

Ph.D. Thesis defended publicly at Aalborg University on October 16, 1998

Active Vibration Control of Long Suspension Bridges

(Aktiv vibrationskontrol af lange hængebroer)

by

Henriette I. Hansen

Department of Building Technology and Structural Engineering

Aalborg University, Sohngaardsholmsvej 57, DK–9000 Aalborg, Denmark

Acknowledgements

The present thesis *Active Vibration Control of Long Suspension Bridges* has been prepared in connection with a Ph.D. study carried out in the period October 1993 to December 1997 at the *Department of Building Technology and Structural Engineering*, Aalborg University, Denmark. After the Ph.D. defence some misprints have been corrected.

Special thanks to my supervisor during the first year Reading Professor *Søren R.K. Nielsen*, Ph.D., and for the full period Professor *Palle Thoft-Christensen*, Ph.D., for the guidance offered. Furthermore, I would like to thank the following. *Allan Larsen*, Ph.D., *COWIconsult* for very valuable help both with the theory, preparation of the bridge section model for wind tunnel experiments, test set up and during the experiments. Professor *Fernando A. Branco* and *Pedro Mendes*, Ph.D., at *Instituto Superior Técnico* in Lisbon, Portugal, for lending the wind tunnel during the two weeks of experiments and help during the experiments. Reading Professor *Lars Pilegaard Hansen*, Ph.D., for valuable ideas to solve problems during the preparation of the bridge section model. Laboratory technicians *Henning Andersen* and *Morten Olsen* for careful building of the wind tunnel model and suspension system and for help during the first week of experiments in the wind tunnel. Associate Professor *Sven Hvid Nielsen* and *Jacob Buus-Andersen*, Ph.D., for recommendation of the servo system for regulation of the flaps on the bridge section model. *Lars Jakobsen*, M.Sc., and *Søren Rønnest*, M.Sc., for design and problematic implementation of the regulation of the servo motors in the bridge section model. Associate Professor *Ole Sørensen*, Ph.D., for solving noise problems and formulation of neural network model for simulation of dynamic systems. Senior Secretary *Kirsten Aakjær* for careful proofreading. Finally, I would like to thank collegues and friends at the department for support and inspiring discussions and *Peter Andersen*, *Asger Enggaard* and *Jens Ostenfeld* for valuable discussions during preparation of their M.Sc. report *Aktiv kontrol af hængebroer*.

The work has been sponsored by the Danish Technical Research Council within the programme *Structural Safety and Reliability*.

Aalborg, June 1998 Henriette I. Hansen

Summary in Danish

Hængebroer bygges med stadigt længere spænd og i fremtiden planlægges ultra-lange hængebroer, f.eks. over *Messinastrædet* og *Gibraltarstrædet*. Disse ultra-lange hængebroer vil blive følsomme over for dynamiske belastninger, og hovedproblemet forventes at være flutter. Spændvidden kan f.eks. forøges ved at optimere hængebroen mht. materialer, brodækkets tværsnitsform og kabler. Alternativt kan den *intelligente bro* introduceres, hvor aktive kontrolsystemer benyttes til at begrænse svingningerne.

I kapitel 1 beskrives to aktive kontrolsystemer med flapper. Det vælges at undersøge det aktive flapkontrolsystem, som består af flapper integreret i brodrageren. Når flapperne udsættes for vinden, opstår belastninger på brodrageren. Retningerne og størrelserne af disse belastninger afhænger af, hvordan flapperne reguleres. Følere inde i brodrageren måler positionen af drageren. Disse målinger benyttes i en kontrolalgoritme til beregning af optimale flappositioner. Flapperne bevæges herefter kontinuerligt svarende til de beregnede optimale positioner. Flapkontrolsystemet kan benyttes til opfyldelse af anvendelsestilstanden og komfortkrav, eller det kan benyttes til forøgelse af flutter vindhastigheden.

De bevægelses-inducerede vindbelastninger på en brosektion er defineret i kapitel 2 baseret på aerodynamiske koefficienter for brodrageren og yderligere aerodynamiske koefficienter for flapreguleringen. Ved at udtrykke flappernes vinkler ved torsionsvinklen af brosektionen kan man benytte eksisterende metoder beskrevet i litteraturen til estimering af flutter vindhastigheden for en brosektion med flapper. Dette gøres ved at erstatte nogle af de aerodynamiske koefficienter med udtryk, som indeholder parametre, der beskriver flapreguleringen. Estimering af flutter vindhastighed ved hjælp af Theodorsens metode og 'air material command' metoden til estimering af den nødvendige dæmpning af konstruktionen beskrives.

Et eksempel viser den teoretiske effekt af flapperne. Flutter vindhastigheden beregnes for forskellige flapkonfigurationer for en brosektionsmodel med flapper. I de efterfølgende eksempler approksimeres de aerodynamiske koefficienter med aerodynamiske koefficienter for en flad plade. Ved udledelse af yderligere aerodynamiske koefficienter for den ledende flap antages, at bevægelse af denne flap ikke har indflydelse på cirkulationen. Det konkluderes, at den følgende flap er mere effektiv end den ledende flap. Det er mere effektivt at bevæge begge flapper end kun at bevæge den følgende flap. Eksemplet viser, at det teoretisk set er muligt at eliminere flutterproblemet for den undersøgte brosektionsmodel ved benyttelse af flapkontrolsystemet.

Tre kontrolalgoritmer, som kan benyttes ved regulering af flapperne, er beskrevet i kapi-

tel 3, nemlig klassisk lineær optimal kontrol med lukket-løkke, øjeblikkelig optimal kontrol med lukket-løkke og kontrol med lukket-løkke med konstant fasevinkel mellem flapbevægelserne og torsionsbevægelsen for brosektionen. I klassisk lineær optimal kontrol minimeres et 'performance index' over hele kontrolintervallet. Ved øjeblikkelig optimal kontrol minimeres et tilsvarende 'performance index' til hvert tidspunkt i kontrolintervallet. Den øjeblikkelige optimale kontrollov er meget simplere end den klassiske lineære optimale kontrollov, da løsning af Riccatti-matricen undgås. Ved konstant fasevinkel kontrol udledes de optimale fasevinkler for flapperne baseret på energi input fra den bevægelsesinducerede vindbelastning.

Forskellen mellem klassisk lineær optimal kontrol og øjeblikkelig kontrol vises i et eksempel. Formerne af flapvinkelkurverne er temmelig ens, men flapperne er en smule forsinkede ved øjeblikkelig kontrol i forhold til klassisk lineær kontrol. Begge kontrolalgoritmer er meget effektive til at begrænse bevægelserne. Et eksempel med konstant fasevinkel kontrol viser, at der ikke vil opstå flutter for en flad plade med lange flapper for den undersøgte vindhastighed, hvis flapperne bevæges med optimale flapvinkler og amplituder som amplituden af torsionsvinklen for pladen.

I kapitel 4 beskrives, hvordan et 'multi-layer perceptron' neuralt netværk kan benyttes ved simulering af bevægelsen af en brosektion baseret på data fra eksempelvis et vindtunnel eksperiment. Under træningen af et aktivt kontrol neuralt netværk benyttes det trænede neurale netværk, som modellerer bevægelsen af brosektionen, som simulator. I den endelige aktive kontrolkonfiguration med lukket-løkke benyttes det trænede neurale netværk for brosektionen som 'one-step ahead predictor' til estimering af bevægelsen til det næste tidsstep. Kontrolkraften estimeres derefter af det trænede kontrol netværk baseret på de estimerede bevægelser. Desuden beskrives, hvordan aerodynamiske koefficienter for en brosektion kan udledes fra et trænet neuralt netværk for brosektionsmodellen.

Vindtunnelforsøg udføres for at undersøge princippet ved at benytte flapper til begrænsning af broens bevægelser. Forsøgsopstillingen ved vindtunnelforsøgene er beskrevet i kapitel 5. Vindtunnelen, brosektionsmodellen, ophængningssystemet, reguleringssystemet og specielle detaljer er beskrevet. Modellen er realistisk i forhold til en rigtig bro, men der undersøges ikke en bestemt bro. Reguleringssystemet har bevirket en hel del problemer og tidsforsinkelse. Endnu er reguleringssystemet langt fra perfekt, og det gav desværre problemer under vindtunnelforsøgene. Derfor kunne kun en lille del af de planlagte forsøg gennemføres.

Under vindtunnelforsøgene, der er beskrevet i kapitel 6, undersøges, hvorledes dæmpningen af modellen er afhængig af flapkonfigurationen for stigende vindhastigheder. Men igen var der uventede problemer, nemlig støjfyldte målinger af flytningerne, stående bølger i fjedrene, når flapperne reguleres, og statisk divergens af modellen ved en vindhastighed meget tæt ved flutter vindhastigheden. For at undgå at de støjfyldte målinger skulle give en ujævn regulering af flapperne, sættes servomotorerne til at reagere meget langsomt. Konstant fasevinkelkontrol benyttes ved vindtunnelforsøgene. Der udføres forsøg med modellen uden bevægelse af flapperne og med to gunstige og to ugunstige flapkonfigurationer.

Forsøgene viser, at både de cirkulære frekvenser for den lodrette bevægelse og torsionsbevægelsen og dæmpningsforholdet for torsionsbevægelsen er afhængige af vindhastigheden og flapkonfigurationen. Når der benyttes gunstige flapkonfigurationer, forøges dæmpningsforholdet drastisk, selv om flappernes fasevinkler måske ikke er optimale. Forsøgene viser også, at det er muligt, at bevæge flapperne så uheldigt, at modellen udfører flutter ved en relativ lav vindhastighed. Adskillige problemer under forsøgene nødvendiggjorde nye forsøg, bl.a. var det ikke muligt at vise effektiviteten af flapperne for vindhastigheder over fluttervindhastigheden. Men under disse nye forsøg opstod nye problemer, så disse forsøg kunne kun blive brugt til at finde gunstige fasevinkler for den følgende og ledende flap enkeltvis.

Data fra vindtunnelforsøgene benyttes ikke til at træne neurale netværk, da dataene er meget støjfyldte, specielt mht. de beregnede hastigheder. Desuden er mange af tidsserierne fra forsøgene meget korte og indeholder hovedsageligt data fra den langsomme start af flapperne. Endelig antages ved de neurale netværksmodeller, at flapperne kan bevæges hurtigt, dvs. at der ikke er forskel på de ønskede og aktuelle flappositioner.

I kapitel 7 sammenlignes de estimerede parametre fra vindtunnelforsøgene med de teoretiske parametre ved benyttelse af flad pladeapproximation. Ved både de gunstige og ugunstige flapkonfigurationer bevæges flapperne enten op eller ned på samme tid, og flapvinklerne er maksimale, når modellen er tilnærmelsesvis vandret. De vindhastighedsafhængige cirkulære frekvenser for lodret bevægelse og torsionsbevægelse sammenlignes med de teoretiske kurver for approximationen for flad plade for ren lodret bevægelse og ren torsionsbevægelse. For den lodrette bevægelse stemmer kurverne kun overens for temmelig lave vindhastigheder. Den cirkulære frekvens for den lodrette bevægelse er uafhængig af flapkonfigurationen. For torsionsbevægelsen følger de estimerede værdier generelt de teoretiske kurver; dette gælder især for relativt lave vindhastigheder. Den cirkulære frekvens for torsionsbevægelsen er afhængig af flapkonfigurationen. Det eksperimentielle dæmpningsforhold er mindre for flapkonfiguration 0 og 1 end det teoretiske dæmpningsforhold baseret på approximationen for flad plade, men kurveformen er næsten den samme. For flapkonfiguration 2 overstiger det eksperimentielle dæmpningsforhold det teoretiske. Ved flapkonfiguration 1 eller 2 forøges fluttervindhastigheden, eller flutter vil ikke opstå.

Baseret på yderligere forsøg, hvor flapperne bevæges enkeltvis, kan det konkluderes, at der blev benyttet gunstige fasevinkler under de første forsøg. Men baseret på de udførte forsøg er det ikke muligt at konkludere, hvilke fasevinkler der er optimale, og hvad den optimale effekt af flapkontrolsystemet er.

Summary in English

Still longer suspension bridges are built and in the future ultra-long span suspension bridges are planned, e.g. the *Messina Crossing* and the crossing of the *Gibraltar Straits*. These ultra-long span suspension bridges will be sensitive to dynamic loads and the main problem is expected to be flutter. The span length can e.g. be increased by optimizing the suspension bridge with regard to materials, deck shape and cables. Alternatively, the *intelligent bridge* may be introduced where active control systems are used to limit the vibrations.

In chapter 1 two active control systems with flaps are described. The active flap control system selected for investigation consists of flaps integrated in the bridge girder. When the flaps are exposed to the wind they exert forces on the bridge girder. The direction and sizes of the forces are dependent on the flap regulation. Sensors inside the bridge girder measure the position of the girder. These measurements are used in a control algorithm to calculate the optimal flap positions. The flaps are then regulated continuously according to the calculated optimal positions. The flap control system can be used to fulfil the serviceability state and comfort demands or it can be used to increase the flutter wind velocity.

The motion-induced wind loads on a bridge section are defined in chapter 2 based on aerodynamic derivatives for the bridge deck and additional aerodynamic derivatives for regulation of the flaps. By expressing the angles of the flaps in terms of the torsional angle of the bridge section the methods described in the literature can be used to estimate the flutter wind velocity for the bridge section with flaps. This is done by simply replacing some of the aerodynamic derivatives with expressions including the parameters describing the flap configuration. Estimation of flutter wind velocity by Theodorsen's method and the air material command method used to estimate the necessary structural damping are described.

The theoretical effect of the flaps is shown by an example. The flutter wind velocity is calculated for different flap configurations for a bridge section model with flaps. In the following examples the aerodynamic derivatives are approximated by the aerodynamic derivatives for a flat plate. In the derivation of the additional aerodynamic derivatives for the leading flap it is assumed that movement of this flap does not affect the circulation. It can be concluded that the trailing flap is more efficient than the leading flap. However, moving both flaps is again more efficient than moving only the trailing flap. The example shows that it is theoretically possible to eliminate the flutter problem for the investigated bridge section model by using the flap control system.

Three control algorithms that can be used to regulate the flaps are described in chapter 3, namely classical linear optimal closed-loop control, instantaneous optimal closed-loop control and closed-loop control with constant phase angle between the motion of the flaps and the torsional motion of the bridge. In classical linear optimal control a performance index is minimized during the entire control interval. In instantaneous optimal control the performance index is minimized at every time instant in the control interval. The instantaneous control law is much simpler than the classical linear optimal control law as solving the Riccatti matrix is omitted. In constant phase angle control the optimal phase angles of the flaps are derived based on the energy input from the motion-induced wind load.

The difference between classical linear optimal control and instantaneous control is shown in an example. The shapes of the flap angle curves are much alike, but the flaps are slightly delayed in instantaneous control compared to classical linear control. Both control algorithms are very efficient to limit the vibrations. An example with constant phase angle control shows that no flutter will occur for a flat plate with long flaps at the investigated wind velocity if the flaps are moved with optimal phase angles and amplitudes equal to the pitch angle of the plate.

In chapter 4 it is described how a multi-layer perceptron neural network can be used to simulate the motion of a bridge section based on data from e.g. a wind tunnel experiment. During training of an active controller neural network the trained neural network modelling the motion of the bridge section is used as a simulator. In the final active closed-loop control configuration the trained neural network of the bridge section is used as one-step ahead predictor to estimate the state vector to the next time step. The control force is then estimated by the trained controller network based on the estimated state variables. Further, it is described how aerodynamic derivatives for the bridge section can be extracted from a trained bridge section model network.

Wind tunnel experiments are performed to investigate the principle to use flaps to control the bridge excitation. The test setup for wind tunnel experiments is described in chapter 5. The wind tunnel, bridge section model, suspension system, regulation system and special details are described. The model is realistic compared to a real bridge, but no specific bridge is investigated. The regulation system has caused a lot of problems and time delay. Still the regulation system is far from perfect and unfortunately it caused problems during the wind tunnel experiments. Therefore, only a small part of the planned experiments could be performed.

During the wind tunnel experiments described in chapter 6 it is investigated how the damping of the model is dependent on the flap configuration for increasing wind velocities. Again, however, there were unanticipated problems, namely noisy measurements of the displacements, standing waves in the springs when the flaps are regulated and static divergency of the model at a wind velocity very close to the flutter wind velocity. To avoid the effects of the noisy measurements on the flap regulation the reaction of the servo motors is specified to be very slow. During the experiments constant phase angle

control is used. Experiments are performed with the model without moving the flaps, two favourable and two unfavourable flap configurations.

The experiments show that both the circular frequencies of the vertical and torsional motion and the damping ratio of the torsional motion are dependent on the wind speed and the flap configuration. When using favourable flap configurations the damping ratio is increased considerably even though the delay of the flaps compared to the torsional motion might not be optimal. The experiments also show that it is possible to make the flap configuration very unfavourable so the model makes flutter at a rather low wind speed. There were several problems during the experiments that recommended further experiments, e.g. that the effectiveness of the flaps could not be shown for wind speeds above the flutter wind speed. Therefore, new problems were introduced during these new experiments. However, they could only be used to find favourable phase angles for the trailing and leading flap, separately.

Data from the wind tunnel experiments are not used to train neural networks as the data are very noisy, especially with respect to the calculated velocities. Further, many of the time series from the wind tunnel experiments are very short and mainly contain data with slow start of the flaps. Finally, the neural network models assume that the flaps can be moved fast, i.e. that no distinction is made between the desired and actual flap positions.

In chapter 7 the estimated parameters from the wind tunnel experiments are compared with the theoretical parameters by using the flat plate approximation. In both the favourable and unfavourable flap configurations the flaps are moved either up or down at the same time and there are maximum angles of the flaps when the model is approximately horizontal. The wind speed dependent circular frequencies for vertical and torsional motion are compared to the theoretical curves for the flat plate approximation for pure vertical and pure torsional motions. For the vertical motion the curves only agree for rather low wind speeds. The circular frequency for the vertical motion is independent on the flap configuration. For the torsional motion the estimated values generally follow the theoretical curves especially for relatively low wind speeds. The circular frequency for the torsional motion is dependent on the flap configuration. The experimental damping ratio is smaller for flap configurations 0 and 1 than the theoretical damping ratio based on the flat plate approximation. However, the shape of the curve is almost the same. For flap configuration 2 the experimental damping ratio exceeds the theoretical ratio. By using flap configuration 1 or 2 the flutter wind velocity is increased or perhaps no binary flutter will occur.

Based on further experiments where flaps are moved separately it can be concluded that favourable phase angles are used during the first experiments. Based on the performed experiments, however, it is not possible to conclude which phase angles are optimal and the optimal effect of the flap control system.

Contents

Nomenclature

The list in this section contains the most frequently used symbols, typically applied in several sections of the thesis. Symbols used for several quantities are explained when used in the cases where the interpretation deviates from the list. Symbols not included in the list are explained when used.

Symbols:

a_l	flap amplification factor for leading flap
a_{la}	actual flap amplification factor for leading flap
a_t	flap amplification factor for trailing flap
a_{ta}	actual flap amplification factor for trailing flap
$A_i^\star$	aerodynamic derivatives
A_α	amplitude of the envelope curve for the torsional motion
b	half-chord length of plate or bridge section
B	width of plate or bridge section with flaps
B'	width of plate or bridge section without flaps
c	location of flap hinge relative to mid-chord
C	Theodorsen circulation function
E_{dis}	structural dissipated energy during a period
E_{input}	energy input from motion-induced wind load during a period
F	real part of Theodorsen circulation function
F_a	motion-induced force
g	damping coefficient used in AMC method
G	imaginary part of Theodorsen circulation function
G^{io}	instantaneous optimal closed-loop control gain matrix
G^{lo}	classical linear optimal closed-loop control gain matrix
$H_i^\star$	aerodynamic derivatives
I	mass moment of inertia of bridge section per unit length
J	performance index in structural control

k	reduced frequency based on half-width of plate or bridge section
k	time step in neural networks
K	reduced frequency based on width of plate or bridge section
k_f	reduced frequency for flutter based on half-width of plate or bridge section
m	mass of bridge section per unit length
$\boldsymbol{P}$	Riccatti matrix
$\boldsymbol{Q}$	weighting matrix in structural control
$\boldsymbol{R}$	weighting matrix in structural control
t	time
t_f	end of control interval
T_i	Theodorsen constants
$\boldsymbol{u}$	control vector
U	mean wind velocity measured in undisturbed stream
U_f	flutter wind velocity
U_r	reduced wind velocity
x	horizontal co-ordinate of plate or brige section, positive in the direction of the mean wind velocity
$\boldsymbol{y}$	vector af structural motion
z	vertical displacement of plate or bridge section, positive downwards
α	angle of plate or bridge section relative to horizontal, positive clockwise
α_l	angle of leading flap relative to undeflected position of plate or bridge section, positive clockwise
α_{la}	actual angle of leading flap relative to undeflected position of plate or bridge section, positive clockwise
α_t	angle of trailing flap relative to undeflected position of plate or bridge section, positive clockwise
α_{ta}	actual angle of trailing flap relative to undeflected position of plate or bridge section, positive clockwise
Δt_l	time delay of leading flap compared to the torsional motion
Δt_t	time delay of trailing flap compared to the torsional motion
ζ	damping ratio
ρ	mass density of air
φ_l	phase angle for leading flap relative to torsional motion of plate or bridge section

φ_{la}	actual phase angle for leading flap relative to torsional motion of plate or bridge section
φ_t	phase angle for trailing flap relative to torsional motion of plate or bridge section
φ_{ta}	actual phase angle for trailing flap relative to torsional motion of plate or bridge section
ω	circular frequency
$\boldsymbol{\omega}$	weights in neural networks
ω_f	circular flutter frequency

Indices:

f	filtered values
l	leading flap
m	model
p	prototype
t	trailing flap
z	vertical bending motion
α	torsional motion

Chapter 1

Introduction

1.1 Motivation

During the last decades the span length of suspension bridges has grown rapidly. In figure 1.1 major suspension bridges for the period 1973–1998 with the longest spans in Japan are shown. The *Akashi Kaikyo Bridge* with span length 1,991 m was opened for traffic in April 1998 and it is so far the longest suspension bridge of the world. Another long suspension bridge which was opened for traffic in June 1998 is the *Great Belt Bridge* with span length 1,624 m. Of future ultra-long span suspension bridges that may be constructed can be mentioned the *Messina Crossing* with the span length 3,300 m and the crossing of the *Gibraltar Straits* with the span length 3,550 m, see Brown [6].

As described by Ostenfeld [29] there are two major limitations for the growth of span length for suspension bridges:

1. The limits for known materials in carrying their own weight. The solution to this problem may be trial and error.

2. The inherent flexibility of long span bridges will cause such bridges to be very sensible to dynamic loads. Possible solutions to this problem are summarized below.

To increase the span length the suspension bridge can be optimized with regard to materials, deck shape and cables as described by Brown [6], Gimsing [12], Astiz [4], Ostenfeld [29] and Ostenfeld & Larsen [30]. Another possibility may be to introduce the *intelligent bridge*, where active control systems are used to limit the vibrations. A step in this direction is to introduce passive control systems, e.g. viscoelastic damping elements, tuned mass dampers and eccentric masses, as described by Ostenfeld & Larsen [30].

In advanced aircrafts actively controlled surfaces are moved relatively to the main surfaces (wings, flaps or ailerons) on which they exert control [30]. The control surfaces are moved by hydraulics based on measurements from sensors attached to the main surfaces. The same principle could be applied to bridges as patented by *COWIconsult* [1].

The main problem in designing ultra-long span suspension bridges is flutter, which is an aeroelastic phenomenon, see Astiz [4]. Flutter occurs when the bridge is exposed to a wind

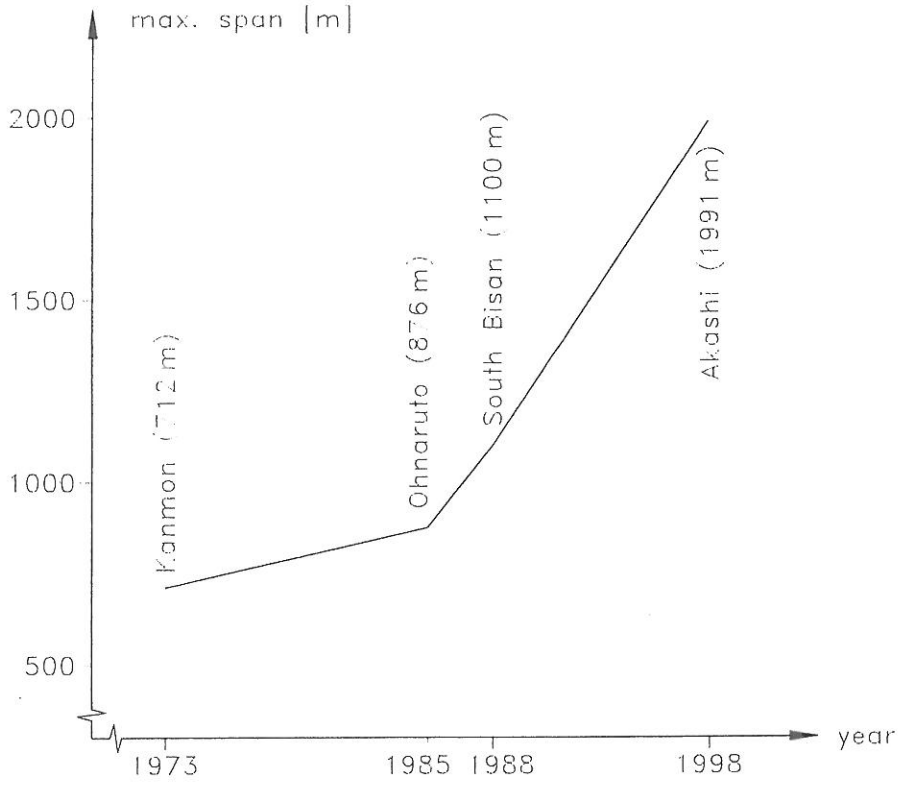

Figure 1.1: Longest span of suspension bridges in Japan during the last decades with data from Ito [21].

speed above a critical value called the flutter wind velocity. The oscillations in flutter are perpendicular to the wind direction and may be torsional, vertical or a combined torsional and vertical motion. The flutter wind velocity is decreased with decreasing structural stiffness and damping. The problem of flutter, therefore, becomes more important with increasing span lengths of bridges as flutter is closely related to the stiffness of the bridge, which in turn is dependent on the span length, see Madsen & Ostenfeld-Rosenthal [27].

Failure of bridges due to flutter has been experienced. The most famous example of bridge failure due to torsional oscillations is the *Tacoma Narrows Bridge*, which was destroyed by a relatively low 20 $^{m}/_{s}$ wind in 1940, see e.g. Ostenfeld & Larsen [30].

If the safety of a long suspension bridge has to rely on a control system it is preferred that such a system is passive. Active control systems for limitations of vibrations of civil engineering structures have primary been used to fulfil serviceability state and comfort demands. In this case failure of the control system is not critical for the users of the structure or the structure itself. Therefore, the reliability of such systems is of less importance. Active control systems may in the future be common elements in wind sensitive bridges to enhance the comfort of the users [30].

The safety of a suspension bridge is governed by its response to infrequent and extreme

loading, e.g. when it is exposed to the flutter wind velocity. As a result the active control system in an *intelligent bridge* may remain in stand-by mode for many years and perhaps decades without being activated. In this case it is very important that the control system is reliable at the very moment the dimensioning load is acting on the structure. The reliability of the control system can be improved by making several independent systems with separated power supplies and by performing regular tests, e.g. by frequent use of the active control system also to fulfill serviceability state and comfort demands.

1.2 Patented Control System with Flaps

In this section the active control system with flaps patented by *COWIconsult* [1] is described. Two types of actively controlled flaps are described in the patent:

- Flaps arranged on pylons below the leading and trailing edge of the streamlined bridge girder, see figure 1.2.
- Flaps integrated in the bridge girder so each flap is the streamlined part of the edge of the girder, see figure 1.3. This configuration obviates the additional flaps suspended below the bridge. This is important in terms of costs and gives the bridge an aesthetically nicer appearance [1].

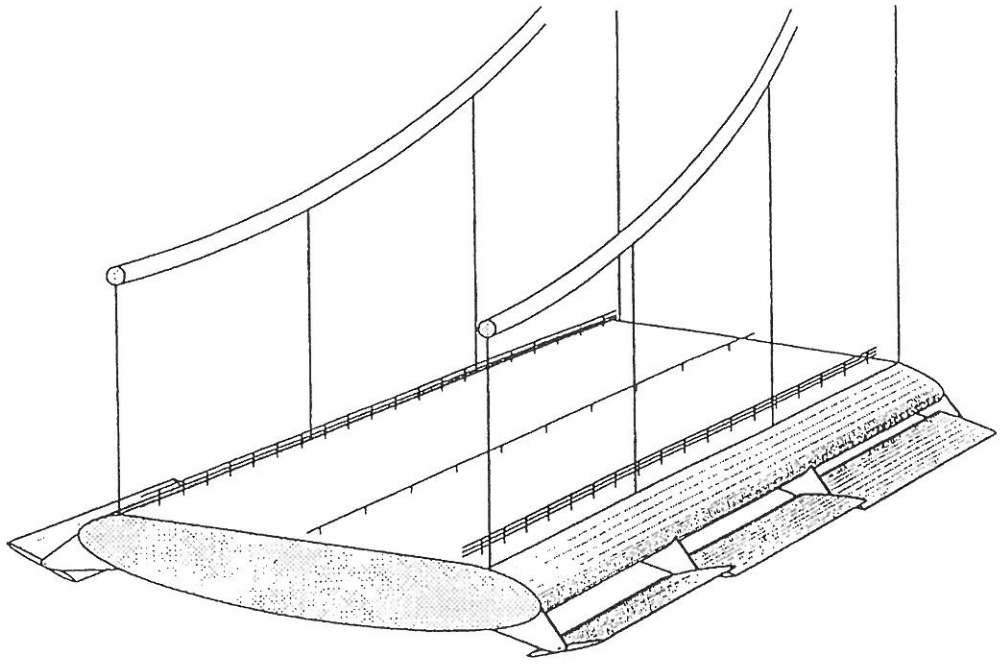

Figure 1.2: Flaps arranged on pylons under bridge girder [1].

When the flaps are exposed to the wind they exert forces on the bridge girder. The directions and sizes of the forces can be regulated by regulating the flaps. By providing forces which counteract the motion of the girder the oscillations are damped.

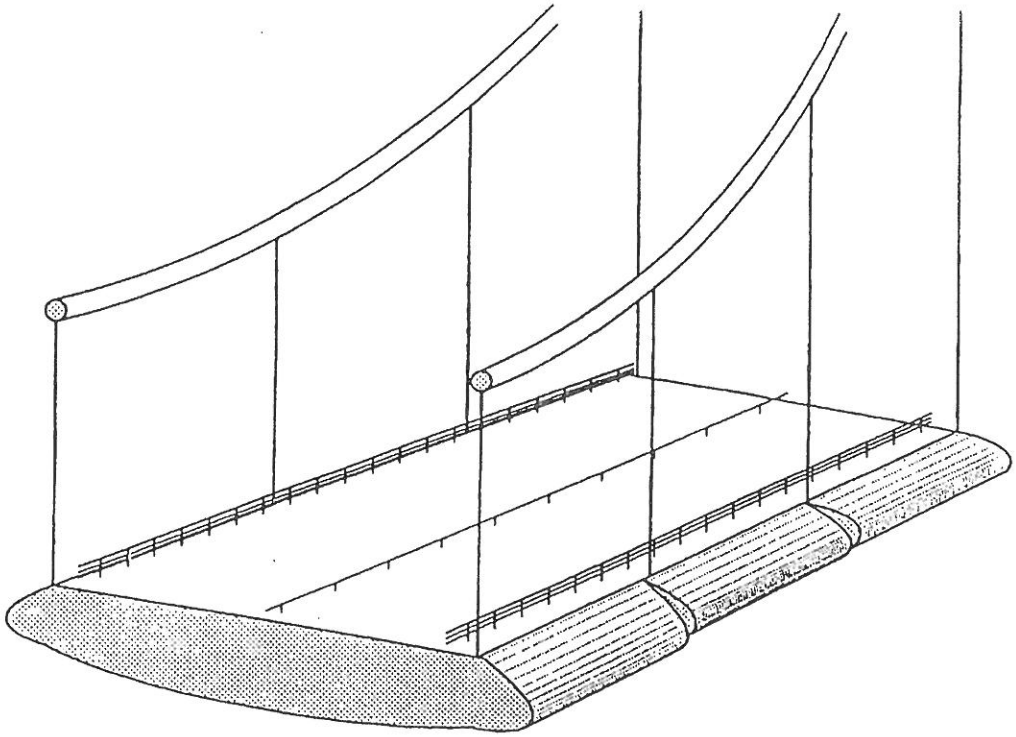

Figure 1.3: Flaps as integrated parts of the bridge girder [1].

A number of sensors are placed inside the bridge girder to measure the position or motion of the girder. The measurements are transmitted to the control unit, e.g. a computer. The flaps are regulated based on a control algorithm that uses the measurements. In this way the flaps can be regulated continuously to counteract the motion of the girder.

The flaps are divided into sections in the longitudinal direction of the bridge, and each of these sections can be regulated independently. The overall safety of the active control system is increased by the number of main control units and thus the number of independent sections.

It is not necessary to mount flaps to the bridge girder over the entire span of the bridge. They may be mounted where they have the greatest effect, i.e. where the girder has the largest deflections. For symmetric modes of oscillations the optimal place is about the central part of the span and for asymmetric modes the optimal places are near the quarter points of the span.

1.3 Scope of the Thesis

Much research is needed before the flap control system can be used in practice. Especially, if the safety of the bridge is dependent on the flap system it is very important that the flap control system is reliable. The following questions must be answered:

1. What is the optimal shape of the flaps and where should they be placed on the bridge?
2. How are the flap positions calculated?
3. Do the flaps have the expected effect?
4. How is the system made reliable?

The shape of the flaps and the placement are not optimized in this thesis. Instead, the flaps integrated in the bridge girder as described in the patent [1] are examined, see figure 1.3. Reliability of the flap control system can be increased by using several independent control systems and frequent tests. A reliability analysis of the flap control system involves formulation of all failure modes of the system, e.g. failure of energy supply. The reliability analysis is not performed in this thesis.

The main goal of this thesis is:

> *Comparing the theoretical and experimental effect of flap control based on wind tunnel experiments with a bridge section model.*

The specific goals of this thesis are:

- Extend the existing theory for dynamics of a long suspension bridge to include leading and trailing flaps.
- Formulate control algorithms.
- Neural networks modelling and system identification.
- Describe bridge section model, test set up and wind tunnel experiments.
- Compare the results from experiments with theory.

1.4 Thesis Outline

The structure of the thesis follows from the specific goals stated above.

All derivations and long descriptions are in the appendices. In the main report the conclusions are drawn and examples are shown. Whenever possible the parameters for the bridge section model used in the wind tunnel experiments idealized to a flat plate are used as example to illustrate the theory.

In *chapter 2* dynamics of long suspension bridges is summarized with special attention on the flutter phenomenom. The aerodynamic derivatives for a flat plate with flaps are derived based on the Theodorsen theory. Estimation of the flutter wind velocity is shown when both the Theodorsen method and the Air Material Command method are used.

Three control algorithms are described in *chapter 3*, namely Classical Linear Optimal closed-loop control, Instantaneous Optimal closed-loop control and control with constant phase angles between the motion of the bridge section and the flap motions.

In *chapter 4* it is described how data from wind tunnel experiments can be used to train an Innovation State-Space neural network model of a bridge section model and a closed-loop controller. Further, it is described how structural parameters and aerodynamic derivates can be extracted from the trained neural network model of the bridge section model.

The wind tunnel, bridge section model, suspension system and regulation system used in the wind tunnel experiments are described in *chapter 5*. The wind tunnel experiments are described in *chapter 6* and the experimental data are analysed. The results of the wind tunnel experiments are compared to the theory in *chapter 7*.

Finally, the conclusions of each chapter and the overall conclusion are given in *chapter 8*.

Chapter 2

Dynamics of Long Suspension Bridges

2.1 Introduction

Wind engineering of bridges is based on known or inferred meteorological data for the bridge site, see e.g. Scanlan [31]. By using extreme value statistics the design wind velocity for the bridge is estimated.

The motion-induced wind loads on a streamlined bridge deck with integrated flaps are described in section 2.2 by a number of coefficients called aerodynamic derivatives. For new bridge designs these coefficients must be estimated by wind tunnel tests or by numerical flow simulations. For flexible bridges the cross-sectional shape of the bridge deck is the most dominating factor on the wind loads, see Scanlan [32]. Therefore, bridge section models are used to estimate the aerodynamic derivatives. During preliminary design the aerodynamic derivatives may be approximated by the values for a flat plate which are summarized in section 2.2.

Estimation of the flutter wind velocity by Theodorsen's method is described in section 2.3. The Air Material Command (AMC) method for estimating the necessary structural damping of the bridge section as a function of the mean wind velocity is described in section 2.4. As an example, the flutter wind velocity and necessary structural damping are estimated for the model used in the wind tunnel experiments described in chapters 5 and 6. In the example the aerodynamic derivatives for a flat plate are used.

2.2 Wind Loads on Bridge Section with Flaps

A rather streamlined bridge section is investigated, see figure 2.1. As shown by Ostenfeld & Larsen [30], streamlining the bridge deck increases the flutter wind velocity. A coordinate system is defined in the centre of mass gravity CG of the bridge section. The x-axis is horizontal and defined to be positive in the direction of the trailing edge. The y-axis is horizontal and perpendicular to the x-axis. The z-axis is vertical and is defined to be positive downwards.

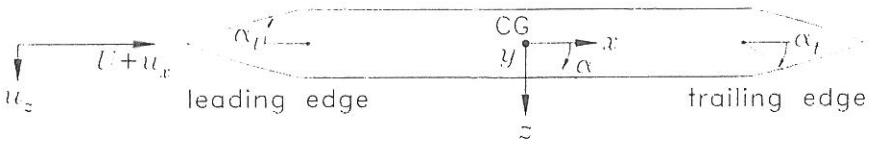

Figure 2.1: Definition of positive directions for bridge section.

The bridge section is considered to be stiff and the motion in the direction of the x-axis is ignored. Thereby, the bridge section has two degrees of freedom, selected as the vertical displacement in the z-direction and the rotation α of the centre of mass gravity of the bridge section (positive clockwise). The angle α_t of the trailing flap and the angle α_l of the leading flap are positive clockwise and refer to the undeflected position, i.e. relative to the bridge deck.

The modes that give coupled oscillations in vertical bending and torsion have their largest deflections in the same part of the bridge, i.e. the first symmetrical vertical bending mode may couple with the first symmetrical torsional mode, see Dyrbye & Hansen [9]. In the following it is assumed that the horizontal motion for the bridge deck is uncoupled with the bending/torsional motion. As described by Dyrbye & Hansen [9] the horizontal deflections may be significant for suspension bridges with very long spans. When the whole bridge span is analysed the following approach must therefore be extended by additional motion-induced load terms.

The wind is composed of a mean wind velocity U, measured in the undisturbed stream, and the turbulence components u_x and u_z, see figure 2.1. The turbulence component in the y-direction u_y is ignored. The stream around the model results in pressure differences on the upper and lower surface of the model. These pressure differences can be integrated into a load F^P (positive downwards) and a moment F^M (positive clockwise) both per unit length in the y-direction, see figure 2.2.

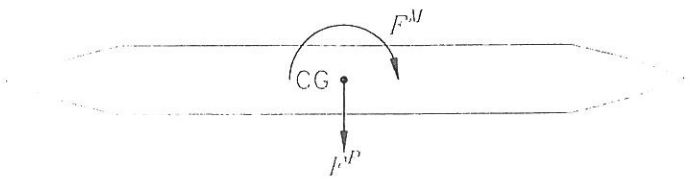

Figure 2.2: Definition of positive directions for load and moment.

The total wind load F_{tot} on a bridge section is composed of three components: the mean wind load F_U, wind load from turbulence F_u and the motion-induced (or aeroelastic) wind load F_a, see Dyrbye & Hansen [9].

$$F_{tot} = F_U + F_u + F_a \tag{2.1}$$

The suspension bridge must be designed to withstand the drag forces from the mean wind U and aeroelastic effects, such as torsional divergence, vortex-induced oscillation, flutter, galloping, and buffeting (caused by wind turbulence components u), see Simiu &

Scanlan [33].

For ultra-long span suspension bridges the main aeroelastic effect of concern is flutter, see Astiz [4] and Larsen & Walther [24]. In flutter the motion-induced wind load F_a is dominating in equation (2.1). Flutter occurs at a critical wind velocity at which the energy input from the motion-induced wind load is equal to the energy dissipated by structural damping, see Dyrbye & Hansen [9]. The critical wind velocity is called the flutter wind velocity U_f.

The flutter phenomenon was first investigated in aerospace engineering and the relevant terms were carried over to wind engineering. Flutter of bridge sections is described by Simiu & Scanlan [33] and Larsen & Walther [24]:

- Single-degree flutter in torsion, also called stall flutter, is a pure torsional motion of the bridge section. The amplitude of the torsional oscillation grows with increasing wind velocity.
- Binary flutter, also called classical flutter, is a coupled vertical and torsional motion of the bridge section. Once the wind velocity exceeds the flutter wind velocity the oscillations grow to catastrophic amplitudes.

As described by Simiu & Scanlan [33], flutter may involve nonlinear aerodynamics. However, the flutter problem has been successfully solved by linear analysis methods.

The motion-induced force F_a is divided into the motion-induced vertical load F_a^P and the motion-induced moment F_a^M. The equations of motion of a bridge section exposed to the motion-induced forces are

$$m(\ddot{z} + 2\zeta_z\omega_z\dot{z} + \omega_z^2 z) = F_a^P = F_{ad}^P + F_{at}^P + F_{al}^P \tag{2.2}$$

$$I(\ddot{\alpha} + 2\zeta_\alpha\omega_\alpha\dot{\alpha} + \omega_\alpha^2\alpha) = F_a^M = F_{ad}^M + F_{at}^M + F_{al}^M \tag{2.3}$$

where m and I are the mass and the mass moment of inertia, respectively, both per unit length, z denotes the vertical bending motion, α denotes the torsional motion, ζ is the damping ratio and ω is the undamped circular eigenfrequency.

The motion-induced wind loads F_a^P and F_a^M are described by three components:

- Loads F_{ad}^P and F_{ad}^M due to movement of the bridge deck, see section 2.2.1.
- Loads F_{at}^P and F_{at}^M due to movement of the trailing flap, see section 2.2.2.
- Loads F_{al}^P and F_{al}^M due to movement of the leading flap, see section 2.2.3.

2.2.1 Loads due to Movement of Bridge Deck

Based on principles of potential flow theory, Theodorsen [37] has shown that for thin airfoils (without flaps) in incompressible flow the expressions for F_{ad}^P and F_{ad}^M are linear in

z and α and their first and second derivatives. The results are shown in appendix A.2.1. Assuming harmonic vibrations at the frequency ω the motion-induced forces due to movement of the bridge deck can be written, see Scanlan [32],

$$F_{ad}^{P} = \frac{1}{2}\rho U^2 B\left[KH_1^\star(K)\frac{\dot{z}}{U} + KH_2^\star(K)\frac{B\dot{\alpha}}{U} + K^2H_3^\star(K)\alpha + K^2H_4^\star(K)\frac{z}{B}\right] \tag{2.4}$$

$$F_{ad}^{M} = \frac{1}{2}\rho U^2 B^2\left[KA_1^\star(K)\frac{\dot{z}}{U} + KA_2^\star(K)\frac{B\dot{\alpha}}{U} + K^2A_3^\star(K)\alpha + K^2A_4^\star(K)\frac{z}{B}\right] \tag{2.5}$$

where ρ is the mass density of air, B is the width of the bridge section, $K = B\omega/U$ is the reduced frequency and $H_1^\star,\ldots,H_4^\star$, $A_1^\star,\ldots,A_4^\star$ are non-dimensional aerodynamic derivatives.

The aerodynamic derivatives must be estimated by wind tunnel experiments or by numerical flow simulations, see Larsen & Walther [24]. During preliminary design of bridges the aerodynamic derivatives may be approximated by the corresponding values for a flat plate as derived by Theodorsen [37]. The results are summarized in appendix A.2. For a flat plate the aerodynamic derivatives are as follows, see appendix A.4.

$$H_1^\star(K) = -\frac{\pi F(k)}{k} \tag{2.6}$$

$$H_2^\star(K) = -\frac{\pi}{4k}\left[1 + F(k) + \frac{2G(k)}{k}\right] \tag{2.7}$$

$$H_3^\star(K) = -\frac{\pi}{2k^2}\left[F(k) - \frac{kG(k)}{2}\right] \tag{2.8}$$

$$H_4^\star(K) = \frac{\pi}{2}\left[1 + \frac{2G(k)}{k}\right] \tag{2.9}$$

$$A_1^\star(K) = \frac{\pi F(k)}{4k} \tag{2.10}$$

$$A_2^\star(K) = -\frac{\pi}{16k}\left[1 - F(k) - \frac{2G(k)}{k}\right] \tag{2.11}$$

$$A_3^\star(K) = \frac{\pi}{8k^2}\left[\frac{k^2}{8} + F(k) - \frac{kG(k)}{2}\right] \tag{2.12}$$

$$A_4^\star(K) = -\frac{\pi}{4}\frac{G(k)}{k} \tag{2.13}$$

where $F(k)$ and $G(k)$ are the real and imaginary parts of the Theodorsen circulatory function, see figure 2.3. The reduced frequency k is based on the half width of the bridge section, i.e. $k = K/2$. As seen in figure 2.3, the functions $F(k)$ and $G(k)$ are almost constant for $k > 1$.

The aerodynamic derivatives are shown in figure 2.4 and figure 2.5 for a flat plate as functions of the reduced velocity U_r defined by

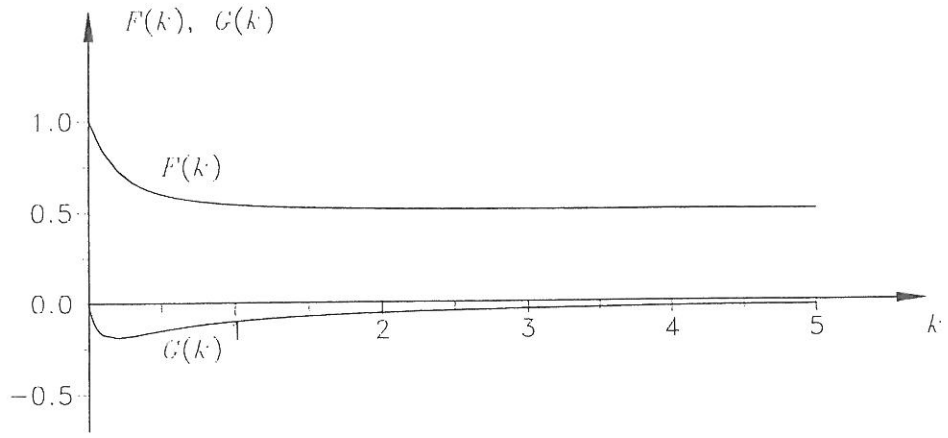

Figure 2.3: Real and imaginary parts of Theodorsen circulation function, see appendix A.2.3.

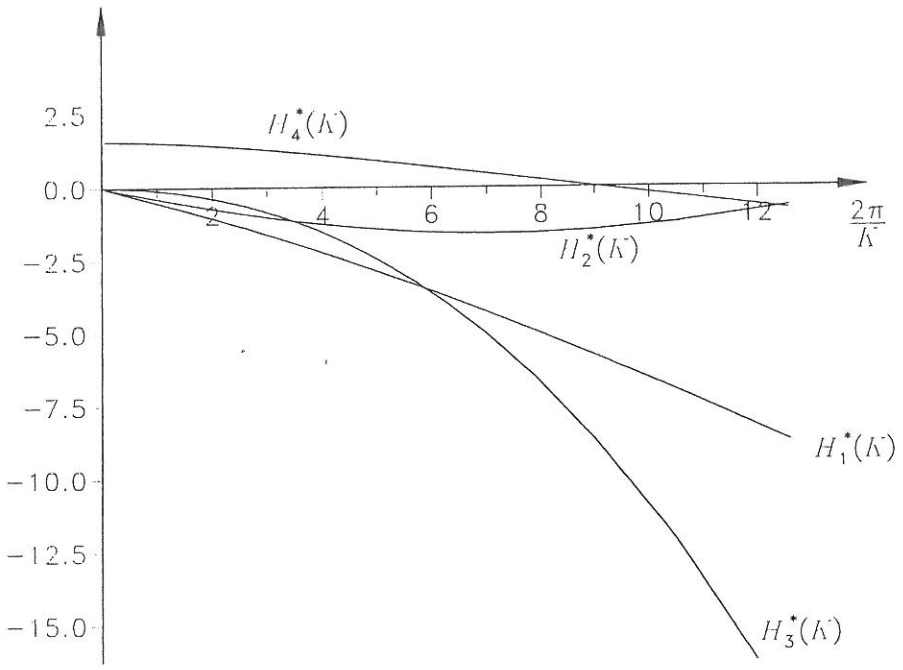

Figure 2.4: Aerodynamic derivatives for force on flat plate.

$$U_r = \frac{U}{fB} = \frac{2\pi U}{\omega B} = \frac{2\pi}{K} \tag{2.14}$$

where f is the frequency.

As seen in figures 2.4 and 2.5 the numerical values of the non-dimensional coefficients $H_i^\star$ and $A_i^\star$ are generally increasing with increasing reduced velocity.

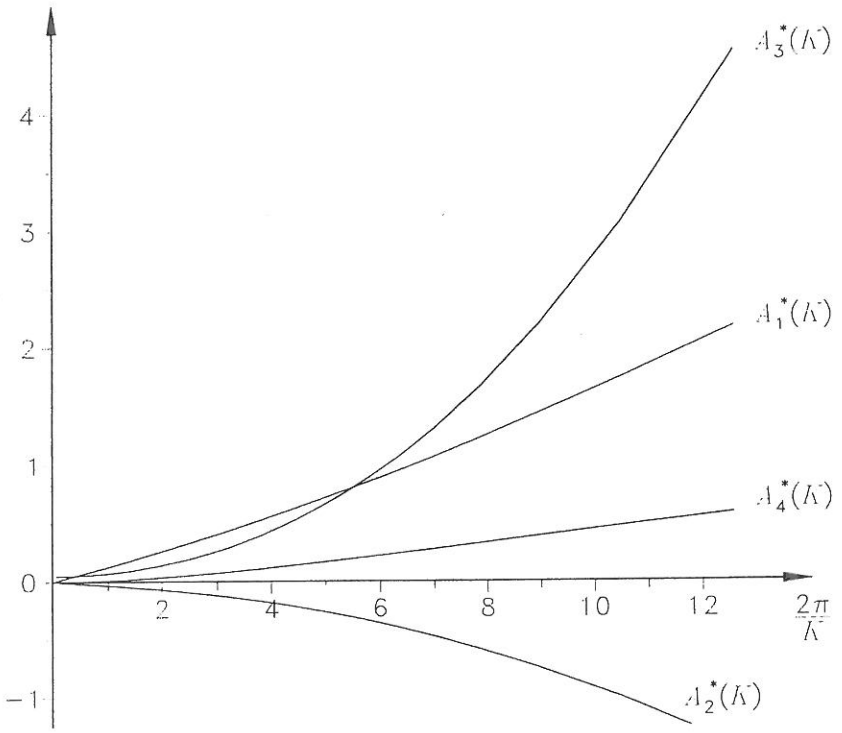

Figure 2.5: Aerodynamic derivatives for moment on flat plate.

2.2.2 Loads due to Movement of Trailing Flap

As for the bridge deck, Theodorsen [37] has shown that the loads due to movement of a trailing flap on a thin airfoil in incompressible flow are linear in the angle of the trailing flap α_t and the first and second derivatives. The results are shown in appendix A.2.2. Assuming that the trailing flap is moved at the same frequency ω as the bridge deck, the motion-induced forces due to movement of the trailing flap can be expressed by additional aerodynamic derivatives.

$$F_{at}^P = \frac{1}{2}\rho U^2 B \left[K H_5^\star(K) \frac{B\dot{\alpha}_t}{U} + K^2 H_6^\star(K) \alpha_t \right] \tag{2.15}$$

$$F_{at}^M = \frac{1}{2}\rho U^2 B^2 \left[K A_5^\star(K) \frac{B\dot{\alpha}_t}{U} + K^2 A_6^\star(K) \alpha_t \right] \tag{2.16}$$

where $H_5^\star(K)$, $H_6^\star(K)$, $A_5^\star(K)$ and $A_6^\star(K)$ are aerodynamic derivatives. For a flat plate with a trailing flap the derivatives are derived in appendix A.4.2.

$$H_5^\star(K) = \frac{1}{4k}\left[T_4 - F(k)T_{11} - \frac{2G(k)T_{10}}{k} \right] \tag{2.17}$$

$$H_6^\star(K) = \frac{1}{4k^2}\left[-k^2 T_1 - 2F(k)T_{10} + kG(k)T_{11} \right] \tag{2.18}$$

$$A_5^\star(K) = \frac{1}{8k}\left[-\left(T_1 - T_8 - cT_4 + \frac{T_{11}}{2} \right) + \frac{F(k)T_{11}}{2} + \frac{G(k)T_{10}}{k} \right] \tag{2.19}$$

$$A_6^*(K) = \frac{1}{8k^2}\left[-(T_4 + T_{10}) - k^2(T_7 + cT_1) + F(k)T_{10} - \frac{kG(k)T_{11}}{2}\right] \tag{2.20}$$

where T_i, $i = 1, 4, 7, 8, 10, 11$ are the Theodorsen constants [37]. The relevant constants are shown in appendix A.2.4. The constants depend on the location of the flap hinge relative to mid chord denoted by c, see figure 2.6. The width of the flat plate excluding flaps is denoted B'. In this section two lengths of flaps are investigated, namely with lengths $0.15B'$ (short flaps) and $0.25B'$ (long flaps). The lengths of the flaps and the corresponding c values are shown in figure 2.6.

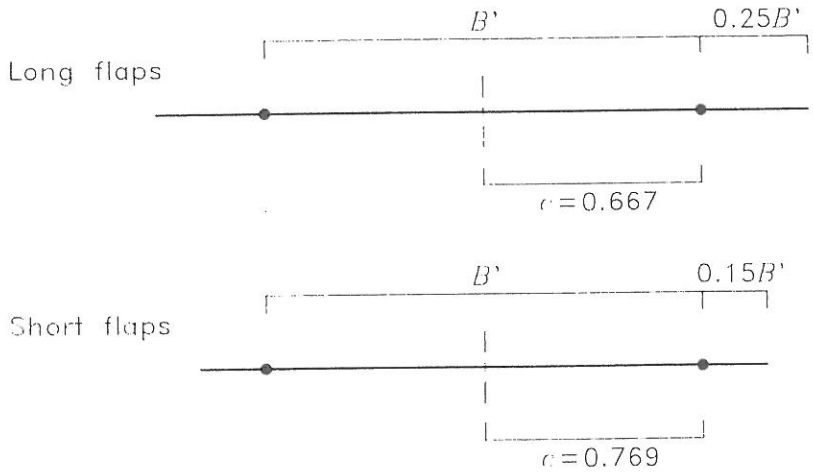

Figure 2.6: Different lengths of flaps investigated.

The Theodorsen constants are shown in table 2.1 for long and short flaps, see figure 2.6.

Constant	Long flaps	Short flaps
c	0.667	0.769
T_1	−0.0475	−0.019
T_4	−0.344	−0.202
T_7	0.011	0.006
T_8	0.091	0.068
T_{10}	1.586	1.333
T_{11}	0.712	0.414

Table 2.1: Theodorsen constants for long and short flaps.

The additional aerodynamic derivatives are shown in figure 2.7 and figure 2.8 for long and short flaps. The forces and moments introduced due to movement of the trailing flap are generally bigger for the long flaps than for the short flaps.

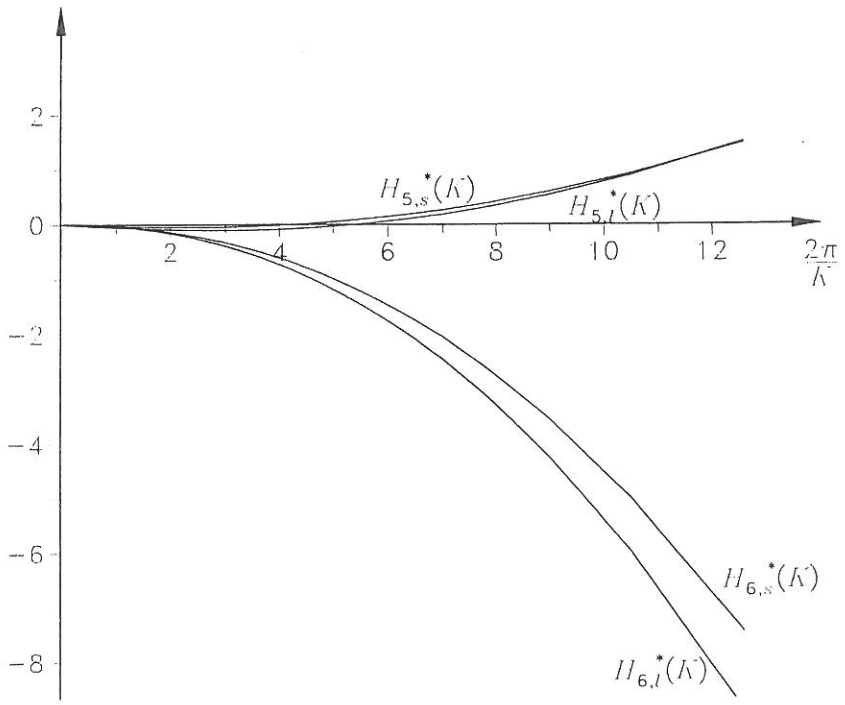

Figure 2.7: Aerodynamic derivatives for force on flat plate due to movement of trailing flap. Indices l and s denote long and short flap, respectively.

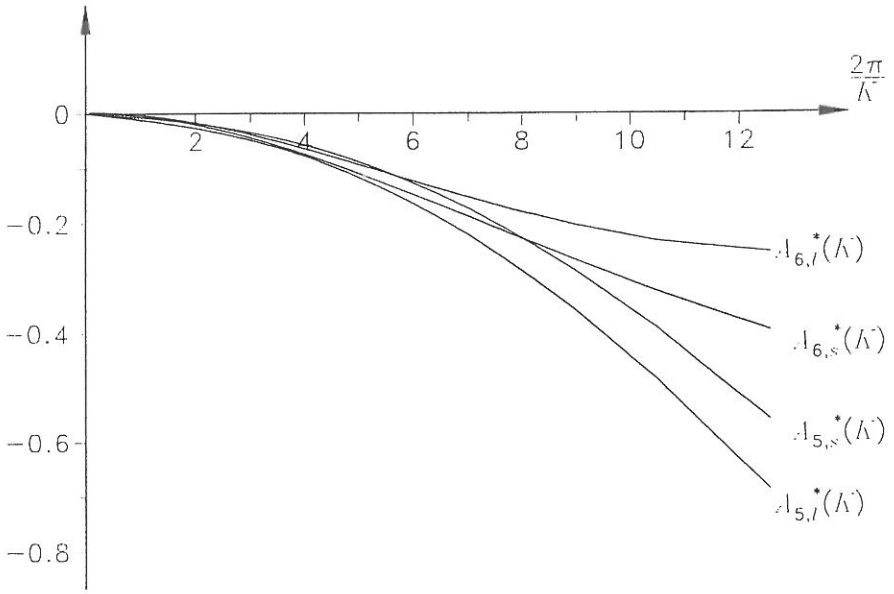

Figure 2.8: Aerodynamic derivatives for moment on flat plate due to movement of trailing flap. Indices l and s denote long and short flap, respectively.

2.2.3 Loads due to Movement of Leading Flap

In appendix A.3 Theodorsen's theory for a flat plate is extended to include a leading flap by assuming that the angle of the leading flap has no effect on the circulation. It is shown

that loads due to movement of a leading flap on a thin airfoil in incompressible flow are linear in the angle of the leading flap α_l and the first and second derivatives. The results are shown in appendix A.3.1. Assuming the leading flap is moved at the same frequency ω as the bridge deck and the trailing flap, the motion-induced forces due to movement of the leading flap can be expressed by additional aerodynamic derivatives.

$$F_{al}^P = \frac{1}{2}\rho U^2 B\left[KH_7^\star(K)\frac{B\dot{\alpha}_l}{U} + K^2 H_8^\star(K)\alpha_l\right] \tag{2.21}$$

$$F_{al}^M = \frac{1}{2}\rho U^2 B^2\left[KA_7^\star(K)\frac{B\dot{\alpha}_l}{U} + K^2 A_8^\star(K)\alpha_l\right] \tag{2.22}$$

where $H_7^\star(K)$, $H_8^\star(K)$, $A_7^\star(K)$ and $A_8^\star(K)$ are aerodynamic derivatives. For a flat plate with a leading flap the derivatives are derived in appendix A.4.3.

$$H_7^\star(K) = \frac{T_4}{4k} \tag{2.23}$$

$$H_8^\star(K) = -\frac{T_1}{4} \tag{2.24}$$

$$A_7^\star(K) = -\frac{1}{8k}\left[T_1 - T_8 - cT_4\right] \tag{2.25}$$

$$A_8^\star(K) = \frac{1}{8k^2}\left[-T_4 - k^2(T_7 + cT_1)\right] \tag{2.26}$$

The additional aerodynamic derivatives for short and long flaps are shown in figures 2.9 and 2.10. As for the trailing flap, the forces and moments due to movement of the leading flap are bigger for long flaps than for short flaps. By comparing figures 2.7 with 2.9 and 2.8 with 2.10 it is seen that turning the trailing flap is more efficient than turning the leading flap the angle $\alpha_l = -\alpha_t$. This is due to the effect of the trailing flap on the circulation.

2.3 Estimation of Flutter Wind Velocity

As described in section 2.2 two types of flutter are investigated, namely single-degree flutter in torsion and binary flutter. Estimation of flutter wind velocity for the two flutter types by using Theodorsen's method is described in appendix B. In this section the results are shown for a bridge section with leading and trailing flaps.

The angles of the leading flap α_l and the trailing flap α_t are expressed in terms of the torsional angle α of the bridge section, see appendix B.3.

$$\alpha_l(t) = a_l e^{-i\varphi_l}\alpha(t) \tag{2.27}$$

$$\alpha_t(t) = a_t e^{-i\varphi_t}\alpha(t) \tag{2.28}$$

where φ_l and φ_t are the phase angles between the flaps and the torsional angle and a_l and a_t are the flap amplification factors. A flap amplification factor is defined as the amplitude of the flap relative to the amplitude of the torsional motion. In the following, a flap configuration refers to fixed parameters a_l, a_t, φ_l and φ_t for the flaps. The results for a bridge section without flaps can be found by setting $a_l \equiv a_t \equiv 0$ in the expressions shown in this chapter.

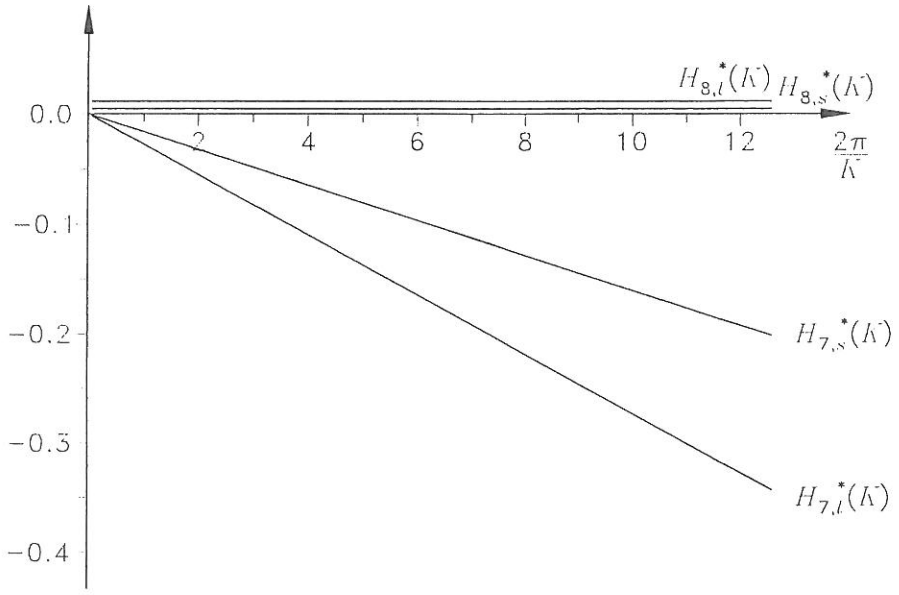

Figure 2.9: Aerodynamic derivatives for force on flat plate due to movement of leading flap. Indices l and s denote long and short flap, respectively.

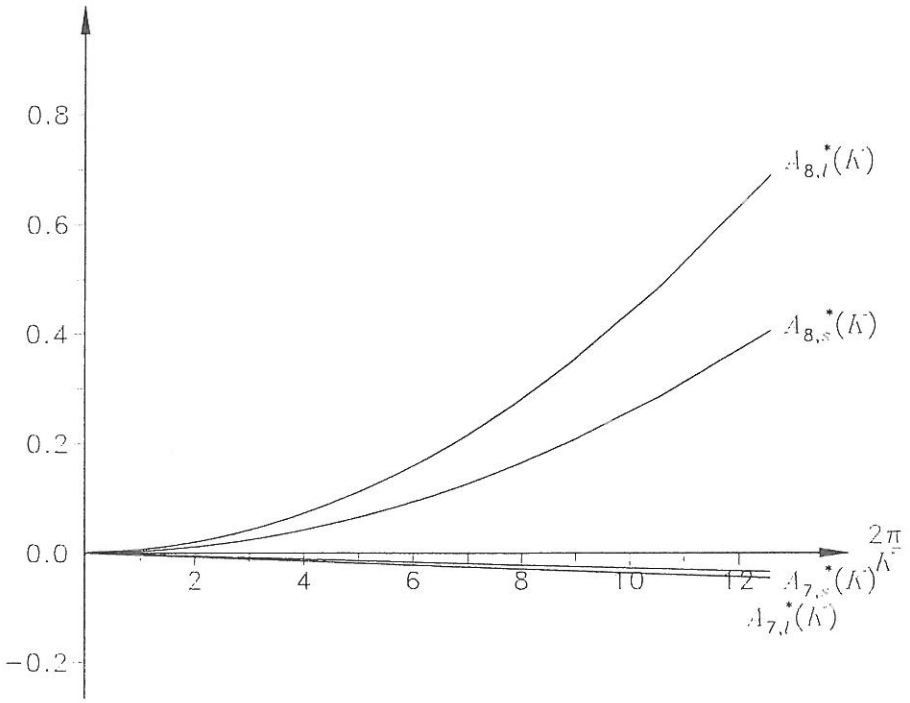

Figure 2.10: Aerodynamic derivatives for moment on flat plate due to movement of leading flap. Indices l and s denote long and short flap, respectively.

2.3.1 Single-Degree Flutter in Torsion

In single-degree flutter in torsion the flutter wind velocity U_f is defined as the velocity at which the total damping (structural and aerodynamic) in torsion is zero. The bridge

will oscillate at a circular eigenfrequency close to ω_α, see Dowell et al. [8]. Estimation of flutter wind velocity for single-degree flutter in torsion is derived in appendices B.2 and B.3.

The total damping is zero for

$$A_2^{\star'}(K) = \frac{4I\zeta_\alpha}{\rho B^4} \tag{2.29}$$

where

$$\begin{aligned} A_2^{\star'}(K) &= A_2^\star(K) + A_5^\star(K)a_t\cos(-\varphi_t) + A_6^\star(K)a_t\sin(-\varphi_t) + \\ &\quad A_7^\star(K)a_l\cos(-\varphi_l) + A_8^\star(K)a_l\sin(-\varphi_l) \end{aligned} \tag{2.30}$$

For a flap configuration the flutter wind velocity is

$$U_f \simeq \frac{B\omega_\alpha}{K_f} \tag{2.31}$$

where K_f is the largest value of K (corresponding to the smallest value of U) for which equation (2.29) is true.

For a flat plate without flaps the flutter condition yields

$$A_2^\star(K) = \frac{4I\zeta_\alpha}{\rho B^4} \tag{2.32}$$

where $A_2^\star(K)$ is negative, see figure 2.5. Thereby a flat plate will not perform single-degree flutter in torsion.

2.3.2 Binary Flutter

In binary flutter the oscillations of the bridge in both vertical and torsional directions will become harmonic at the circular eigenfrequency ω_f at a critical wind velocity U_f. Thereby the structural dissipated energy in the period $T_f = 2\pi/\omega_f$ will be equal to the energy input of the motion-induced wind load, see Dyrbye & Hansen [9]. The circular flutter eigenfrequency ω_f is between the circular eigenfrequencies for the bridge section in bending and torsion, i.e. $\omega_z \leq \omega_f \leq \omega_\alpha$.

Estimation of flutter wind velocity for binary flutter is derived in appendices B.2 and B.3. The binary flutter condition is

$$\boldsymbol{x}(t) = \boldsymbol{x}_0 e^{i\omega_f t} \tag{2.33}$$

where

$$\boldsymbol{x}(t) = \begin{bmatrix} z(t) \\ \alpha(t) \end{bmatrix} \tag{2.34}$$

$$\boldsymbol{x}_0 = \begin{bmatrix} z_0 \\ \alpha_0 e^{-i\varphi_\alpha} \end{bmatrix} \tag{2.35}$$

where z_0 and α_0 are the amplitudes of the vertical and torsional motion, respectively, and φ_α is the phase angle between the vertical and torsional motion.

By inserting the flutter condition in the matrix equation of motion the flutter point can be found graphically by the method described by Dowell et al. [8]. For a number of values of the reduced frequency K the values $X_r(K)$ and $X_i(K)$ are calculated as solutions to the following equations:

$$\begin{aligned}
&A_r(X_r(K),K)X_r^4(K) = \\
&\quad X_r^4(K)\left[mI+\frac{1}{2}\rho B^4 m A_3^{\star'}(K)+\frac{1}{2}\rho B^2 I H_4^\star(K)+\frac{1}{4}\rho^2 B^6\left(-H_1^\star(K)A_2^{\star'}(K)\right.\right. \\
&\quad \left.\left.+H_4^\star(K)A_3^{\star'}(K)+H_2^{\star'}(K)A_1^\star(K)-H_3^{\star'}(K)A_4^\star(K)\right)\right]+ \\
&\quad X_r^3(K)\left[\rho B^4 m\zeta_z A_2^{\star'}(K)+\rho B^2 I\zeta_\alpha\frac{\omega_\alpha}{\omega_z}H_1^\star(K)\right]+ \\
&\quad X_r^2(K)\left[-mI\frac{\omega_\alpha^2}{\omega_z^2}-mI4\zeta_z\zeta_\alpha\frac{\omega_\alpha}{\omega_z}-mI-\frac{1}{2}\rho B^4 m A_3^{\star'}(K)-\frac{1}{2}\rho B^2 I\frac{\omega_\alpha^2}{\omega_z^2}H_4^\star(K)\right]+ \\
&\quad mI\frac{\omega_\alpha^2}{\omega_z^2}=0
\end{aligned} \tag{2.36}$$

$$\begin{aligned}
&A_i(X_i(K),K)X_i^3(K) = \\
&\quad X_i^3(K)\left[\frac{1}{2}\rho B^4 m A_2^{\star'}(K)+\frac{1}{2}\rho B^2 I H_1^\star(K)+\frac{1}{4}\rho^2 B^6\left(H_1^\star(K)A_3^{\star'}(K)\right.\right. \\
&\quad \left.\left.+H_4^\star(K)A_2^{\star'}(K)-H_2^{\star'}(K)A_4^\star(K)-H_3^{\star'}(K)A_1^\star(K)\right)\right]+ \\
&\quad X_i^2(K)\left[-mI2\zeta_\alpha\frac{\omega_\alpha}{\omega_z}-mI2\zeta_z-\rho B^4 m\zeta_z A_3^{\star'}(K)+\rho B^2 I\zeta_\alpha\frac{\omega_\alpha}{\omega_z}H_4^\star(K)\right]+ \\
&\quad X_i(K)\left[-\frac{1}{2}\rho B^4 m A_2^{\star'}(K)-\frac{1}{2}\rho B^2 I\frac{\omega_\alpha^2}{\omega_z^2}H_1^\star(K)\right]+ \\
&\quad mI2\zeta_z\frac{\omega_\alpha^2}{\omega_z^2}+mI2\zeta_\alpha\frac{\omega_\alpha}{\omega_z}=0
\end{aligned} \tag{2.37}$$

where

$$\begin{aligned}
H_2^{\star'}(K) &= H_2^\star(K)+H_5^\star(K)a_t\cos(-\varphi_t)+H_6^\star(K)a_t\sin(-\varphi_t)+ \\
&\quad H_7^\star(K)a_l\cos(-\varphi_l)+H_8^\star(K)a_l\sin(-\varphi_l)
\end{aligned} \tag{2.38}$$

$$\begin{aligned}
H_3^{\star'}(K) &= H_3^\star(K)-H_5^\star(K)a_t\sin(-\varphi_t)+H_6^\star(K)a_t\cos(-\varphi_t)- \\
&\quad H_7^\star(K)a_l\sin(-\varphi_l)+H_8^\star(K)a_l\cos(-\varphi_l)
\end{aligned} \tag{2.39}$$

$$\begin{aligned}
A_2^{\star'}(K) &= A_2^\star(K)+A_5^\star(K)a_t\cos(-\varphi_t)+A_6^\star(K)a_t\sin(-\varphi_t)+ \\
&\quad A_7^\star(K)a_l\cos(-\varphi_l)+A_8^\star(K)a_l\sin(-\varphi_l)
\end{aligned} \tag{2.40}$$

$$\begin{aligned}
A_3^{\star'}(K) &= A_3^\star(K)-A_5^\star(K)a_t\sin(-\varphi_t)+A_6^\star(K)a_t\cos(-\varphi_t)- \\
&\quad A_7^\star(K)a_l\sin(-\varphi_l)+A_8^\star(K)a_l\cos(-\varphi_l)
\end{aligned} \tag{2.41}$$

The flutter point (X_f, K_f) is the point where the solution curves $X_r(K)$ and $X_i(K)$ cross. The circular flutter frequency ω_f and the flutter wind velocity U_f can determined by

$$\omega_f = X_f \omega_z \tag{2.42}$$

$$U_f = \frac{B\omega_f}{K_f} \tag{2.43}$$

When there is more than one intersection of the solution curves, the flutter point corresponds to the intersection point with the largest value of K (corresponding to the smallest value of U).

The factor $\frac{\alpha_0}{z_0} e^{-i\varphi_\alpha}$ defined by equations (2.33) and (2.35) can be calculated by inserting the values ω_f and K_f into the matrix equation of motion with the flutter condition, see equation (B.19). The phase angle φ_α between the vertical and torsional motion is

$$\varphi_\alpha = -\tan^{-1}\left(\frac{\mathrm{Im}\left(\frac{\alpha_0}{z_0} e^{-i\varphi_\alpha}\right)}{\mathrm{Re}\left(\frac{\alpha_0}{z_0} e^{-i\varphi_\alpha}\right)}\right) \tag{2.44}$$

As an example, the flutter wind velocity for binary flutter is estimated for the bridge section model used in the wind tunnel experiments described in chapters 5 and 6. The bridge section model is equipped with long flaps, see the corresponding flat plate in figure 2.6. The parameters of the model are shown in table 2.2. The scaling factors for the model are shown in table 5.1. The aerodynamic derivatives for the model are approximated by the values for a flat plate shown in section 2.2.

Parameter	Symbol	Value
Width of model incl. flaps	B	0.937 m
Mass per unit length	m	17.94 kg/m
Mass moment of inertia per unit length	I	0.589 kg m^2/m
Circular frequency for bending	ω_z	5.2 rad/s
Circular frequency for torsion	ω_α	10.1 rad/s
Structural damping in bending	ζ_z	0.012
Structural damping in torsion	ζ_α	0.008
Mass density of air	ρ	1.28 kg/m^3

Table 2.2: Parameters for bridge section model used in example.

The solution curves $X_r(K)$ and $X_i(K)$ are shown in figure 2.11. The flutter point is $(X_f, K_f) = (1.273, 0.758)$. The circular flutter frequency ω_f and flutter wind velocity U_f are

$$\omega_f = X_f \omega_z = 1.273 \cdot 5.2 = 6.62 \text{ rad/s} \tag{2.45}$$

$$U_f = \frac{B\omega_f}{K_f} = \frac{0.937 \cdot 6.62}{0.758} = 8.18 \text{ m/s} \tag{2.46}$$

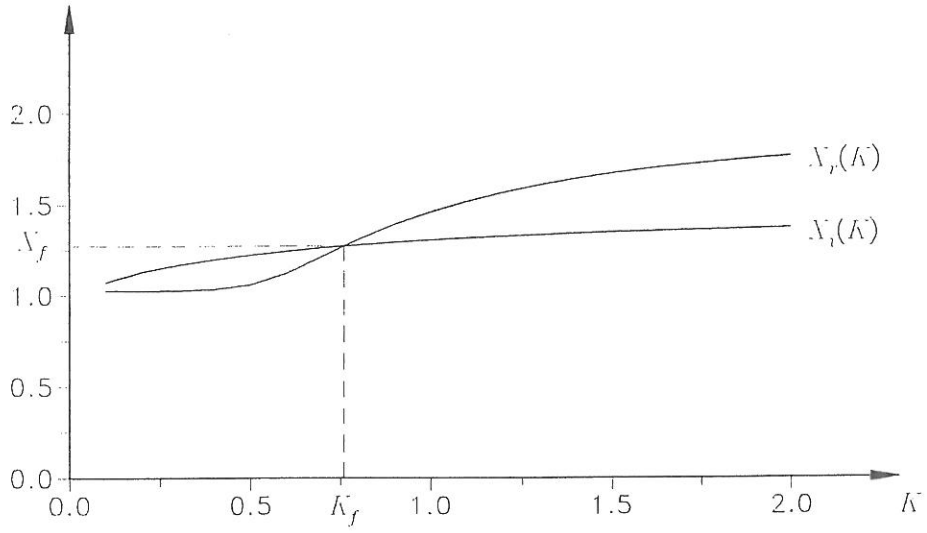

Figure 2.11: Solution curves for bridge section model.

As expected, the circular flutter frequency is between the circular frequencies for bending and torsion, see table 2.2.

By using equation (2.44) the phase angle between the vertical and torsional motion can be calculated

$$\varphi_\alpha = -\tan^{-1}\left(\frac{-1.192}{1.568}\right) = 0.650 \text{ rad} = 37° \tag{2.47}$$

The flutter wind velocity U_f for binary flutter is calculated for different flap amplification factors a_l and phase angles φ_l for the leading flap. The trailing flap is not moved, i.e. $a_t \equiv 0$. The results are shown in figure 2.12.

The flutter wind velocity is increased when the phase angle for the leading flap φ_l is in the interval $[0.6\pi/6; 6.6\pi/6]$, otherwise the flutter wind velocity is decreased. The phase angle for maximum increase of the flutter wind velocity is dependent on the value of the flap amplification factor a_l.

The flutter wind velocity U_f for binary flutter is calculated for different values of a_t and φ_t for the trailing flap. The leading flap is not moved, i.e. $a_l \equiv 0$. The results are shown in figure 2.13.

The interval where the flutter wind velocity is increased, when the trailing flap is moved, is dependent on the flap amplification factor a_t. The flutter wind velocity is generally decreased when the phase angle of the trailing flap φ_t is in the interval $[\pi/6; 6\pi/6]$. For phase angles outside this interval the flutter wind velocity is generally increased. Again the phase angle for maximum increase of the flutter wind velocity is dependent on the value of the flap amplification factor a_t.

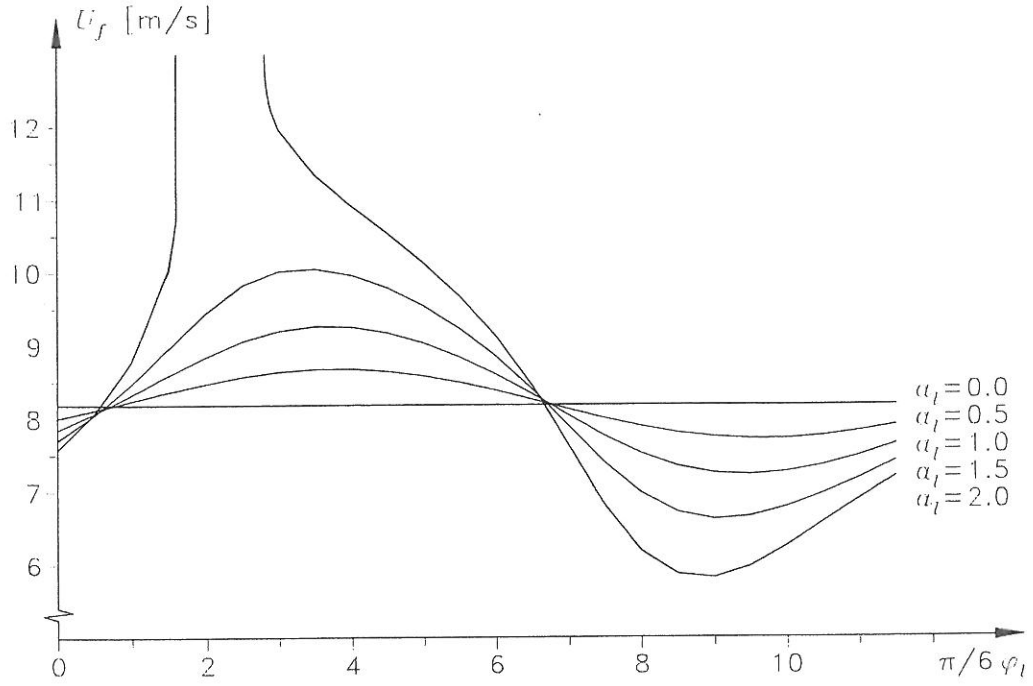

Figure 2.12: Flutter wind velocity when only the leading flap is used.

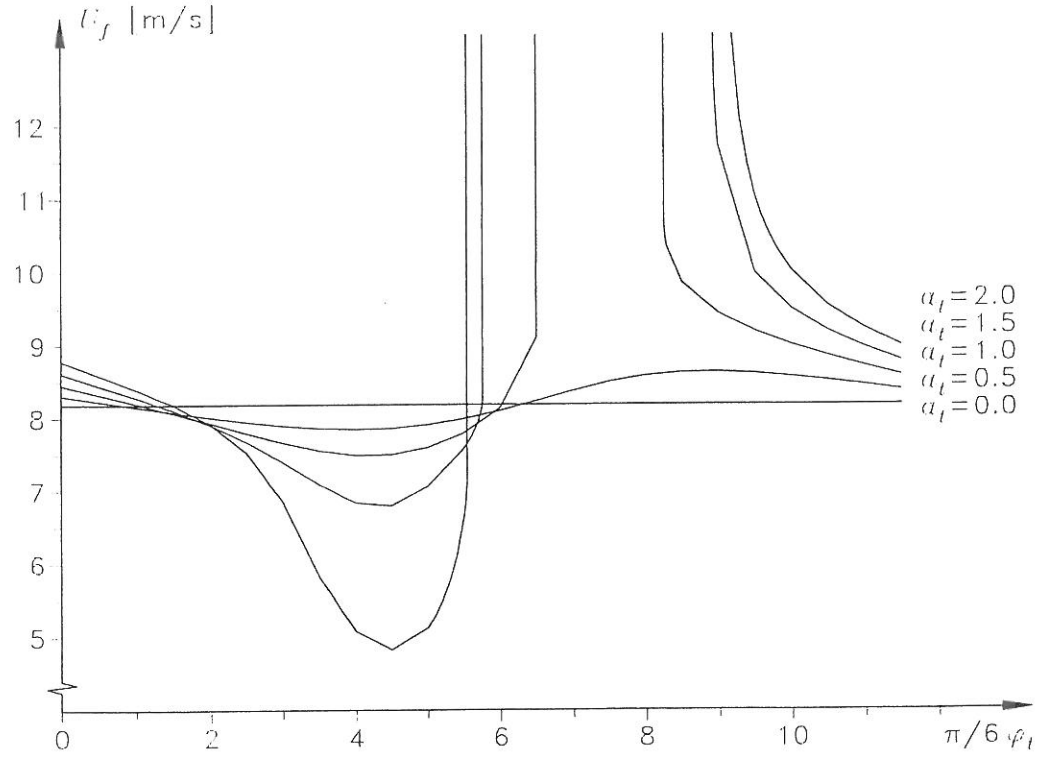

Figure 2.13: Flutter wind velocity when only the trailing flap is used.

By comparing figures 2.12 and 2.13 it is seen that the trailing flap is much more efficient than the leading flap. The potential theory used assumes that there is no separation of the flow around the flat plate. This assumption can hardly be met in practice, therefore it is expected that the effect of the trailing flap is overestimated by the Theodorsen theory for a flat plate.

For small values of the flap amplification factors the optimal phase angles are $\varphi_l \simeq 3\pi/6$ and $\varphi_t \simeq 8\pi/6$. These phase angles are used in figure 2.14 where movement of both flaps compared to movement of the leading and trailing flap separately is shown.

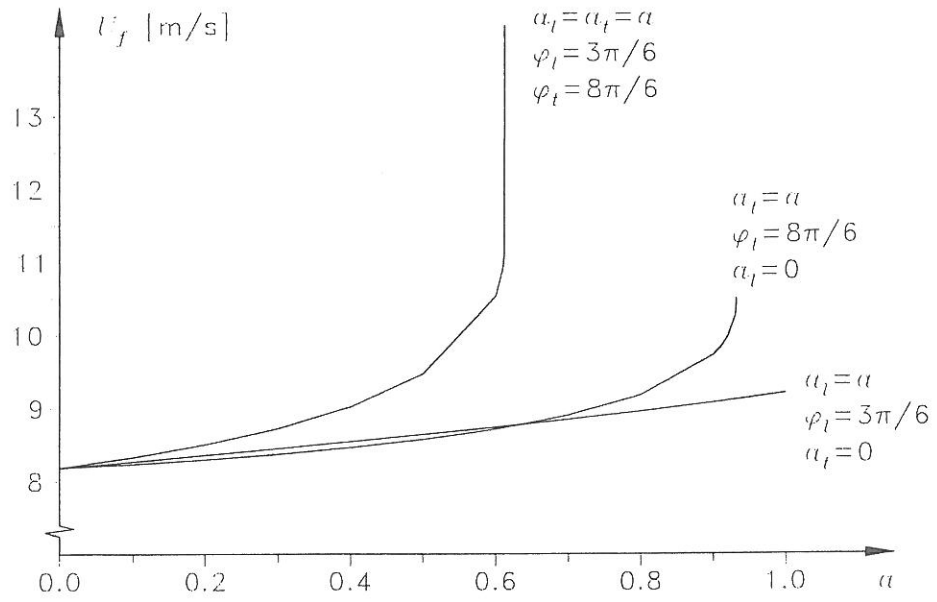

Figure 2.14: Movement of both flaps compared to movement of the flaps separately.

As seen in figure 2.14 the flutter wind velocity is only slightly increased for flap amplification factors below approximately 0.8 when only one flap is moved. When the trailing flap is moved with a flap amplification factor a_t above 0.8 the flutter wind velocity is increased considerably and for $a_t > 0.95$ binary flutter will not occur. By using both flaps, binary flutter will not occur when both flap amplification factors are above approximately 0.6.

2.4 Estimation of Damping by the AMC Method

In the Air Material Command (AMC) method the necessary structural damping of the bridge section for fulfilling the binary flutter condition in equation (2.33) is plotted against the mean wind velocity, see Fung [11]. Flutter occurs when the necessary structural damping exceeds the actual structural damping of the bridge section. The AMC method is described in appendix B.4.

By using the AMC method the following equation is solved with respect to the complex variable Z

$$Z^2\left[\left(\frac{\omega_z}{\omega_\alpha}\right)^2\right]+Z\left[-1-\left(\frac{\omega_z}{\omega_\alpha}\right)^2-\left(\frac{\omega_z}{\omega_\alpha}\right)^2\frac{\rho B^4}{2I}(A_2^{\star\prime}(K)i+A_3^{\star\prime}(K))-\frac{\rho B^2}{2m}(H_1^\star(K)i+H_4^\star(K))\right]+1+\frac{\rho B^4}{2I}(A_2^{\star\prime}(K)i+A_3^{\star\prime}(K))+\frac{\rho B^2}{2m}(H_1^\star(K)i+H_4^\star(K))+\frac{\rho^2 B^6}{4mI}\Big((H_1^\star(K)i+H_4^\star(K))(A_2^{\star\prime}(K)i+A_3^{\star\prime}(K))-(H_2^{\star\prime}(K)i+H_3^{\star\prime}(K))(A_1^\star(K)i+A_4^\star(K))\Big)=0 \tag{2.48}$$

For a number of reduced frequencies $K_1, K_2, \ldots$, equation (2.48) is solved and corresponding values of the mean wind velocity U and the damping factor g are calculated

$$U(K_i)=\frac{B\omega_\alpha}{K_i\sqrt{\mathrm{Re}(Z(K_i))}} \tag{2.49}$$

$$g(K_i)=\frac{\mathrm{Im}(Z(K_i))}{\mathrm{Re}(Z(K_i))} \tag{2.50}$$

The damping factor g is defined as twice the necessary structural damping ζ for binary flutter. It is assumed that the structural damping is the same for bending and torsion, i.e. $\zeta=\zeta_\alpha=\zeta_z$. The flutter wind velocity U_f is found by

$$g(U_f)=2\zeta \tag{2.51}$$

As in section 2.3, the bridge section model used in the wind tunnel experiments is used in the example. The parameters for the model are shown in table 2.2 and the aerodynamic derivatives for a flat plate are used. The following approximation is made: $\zeta=0.01$. The results are shown in figure 2.15 for no movement of the flaps, i.e. $a_l=a_t=0$, and for $a_l=a_t=0.6$, $\varphi_l=3\pi/6$ and $\varphi_t=8\pi/6$.

The flutter wind velocity for the bridge section model is found as the mean wind velocity for which $g=0.02$. For no movement of the flaps the flutter wind velocity is 8.22 m/s. This value is very close to the flutter wind velocity found by Theodorsen's method in section 2.3, i.e. 8.18 m/s. If it is assumed that the structural damping ζ is in the interval $[0.008; 0.012]$ corresponding to the structural damping for torsion and bending, respectively, then the flutter wind velocity is in the interval $[8.18; 8.27]$ m/s, which agrees very well with the flutter wind velocity found by Theodorsen's method.

When both flaps are moved using $a_l=a_t=0.6$ and the phase angles found in section 2.3, i.e. $\varphi_l=3\pi/6$ and $\varphi_t=8\pi/6$, then the flutter wind velocity is increased to 10.43 m/s in the interval $[10.08, 11.24]$ m/s. Again, this flutter wind velocity agrees very well with the flutter wind velocity of 10.53 m/s for this flap configuration found by the Theodorsen method.

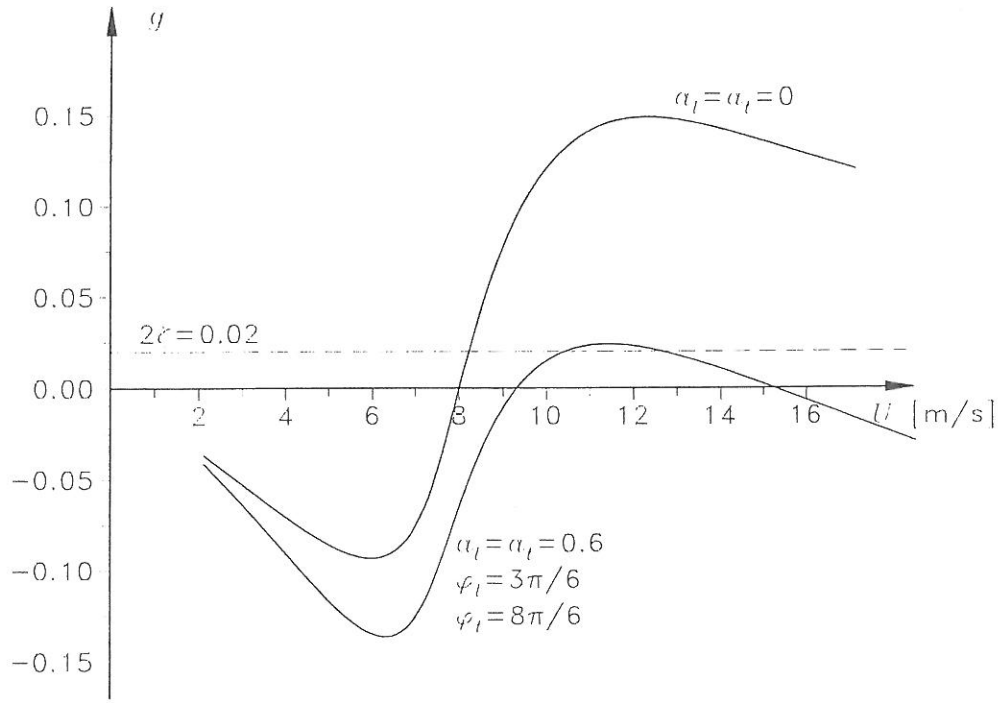

Figure 2.15: Damping factor as a function of the mean wind velocity.

2.5 Concluding Remarks

In this chapter, wind loads on a streamlined bridge section are described with emphasis on the motion-induced part. The aerodynamic derivatives for a flat plate with leading and trailing flaps are derived, and curves of the aerodynamic derivatives are shown for two lengths of flaps on a flat plate. Theoretically, the trailing flap is more efficient than the leading flap and, as expected, long flaps are more efficient than short flaps.

Two types of flutter are investigated, namely single-degree flutter in torsion and binary flutter. Estimation of flutter wind velocity for both types of flutter is given. In an example it is shown that single-degree flutter in torsion will not occur for a flat plate. Further, it is shown that binary flutter can be avoided for a flat plate if the trailing and/or leading flap is moved with specified phase angles compared to the torsional motion.

Chapter 3

Active Control Systems

3.1 Introduction

In active structural control the motion of the structure is controlled by means of the action of a control system through some external energy supply. The basic active control configuration consists of:

- Sensors located on or in the structure to measure excitation and/or structural response variables.
- Devices to process the measurements and to compute the control action based on a control algorithm.
- Actuators to make the control action.

A schematic diagram of closed–open-loop active control is shown in figure 3.1.

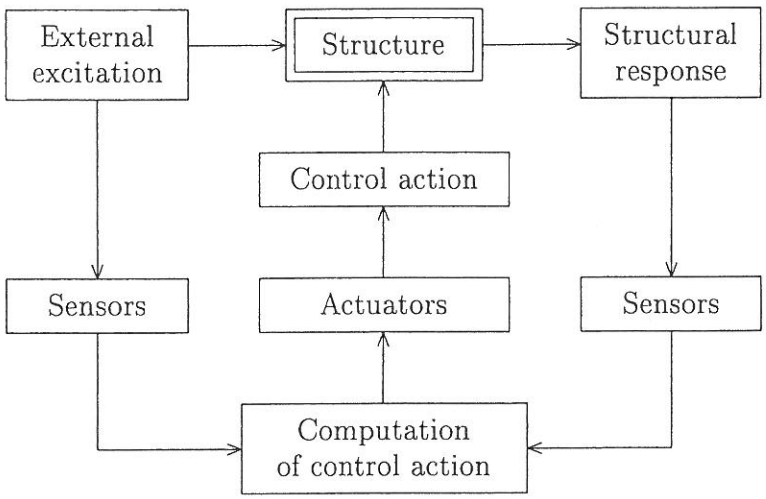

Figure 3.1: Schematic diagram of active control (from Soong [34]).

When the motion of the bridge is measured and used to calculate the flap positions (i.e. the control action), the control configuration is referred to as closed-loop control. The

effect of closed-loop control is to modify the structural parameters (stiffness and damping) so that the bridge responds more favourably to the excitation. When the wind velocity (i.e. the excitation) is measured and used to control the bridge the control configuration is referred to as open-loop control. The effect of the open-loop component is a modification of the excitation. In closed–open-loop control the flap positions are calculated based on both the measured motion of the bridge and the measured wind velocity.

Three methods of computing the flap positions are described:

- Classical linear optimal closed-loop control, see section 3.2.
- Instantaneous optimal closed-loop control, see section 3.3.
- Closed-loop control with constant phase angles between the motion of the flaps and the torsional motion of the bridge, see section 3.4.

Classical linear optimal closed–open-loop and open-loop control are generally not feasible in structural control applications since for this type of control the excitation must be known a priori during the control interval, see Soong [34]. For instantaneous optimal control it is possible to derive the open-loop and closed–open-loop control laws, see Soong [34]. But these control laws that contain information about the excitation term are much more complicated than the closed-loop control law.

3.2 Classical Linear Optimal Closed-Loop Control

In structural control applications of classical linear optimal control the usually studied performance index J to be minimized in the control interval $[0; t_f]$ can be written as follows, see Soong [34]

$$J = \int_0^{t_f} \left[\boldsymbol{y}^T(t) \boldsymbol{Q} \boldsymbol{y}(t) + \boldsymbol{u}^T(t) \boldsymbol{R} \boldsymbol{u}(t) \right] \, dt \tag{3.1}$$

where the vectors $\boldsymbol{y}$ and $\boldsymbol{u}$ are composed of the structural parameters and the control actions, respectively.

$$\boldsymbol{y}(t) = \begin{bmatrix} z(t) \\ \alpha(t) \\ \dot{z}(t) \\ \dot{\alpha}(t) \end{bmatrix} \tag{3.2}$$

$$\boldsymbol{u}(t) = \begin{bmatrix} \alpha_t(t) \\ \alpha_l(t) \end{bmatrix} \tag{3.3}$$

$\boldsymbol{Q}$ and $\boldsymbol{R}$ are weighting matrices, where the elements are selected to achieve the desired connection between the control effectiveness and the control energy consumption. I.e. large values of the elements in $\boldsymbol{Q}$ compared to the elements in $\boldsymbol{R}$ indicate that the reduction of the motion of the model is more important than the energy required to turn the flaps. The following weighting matrices are used by Wu et al. [39].

$$\boldsymbol{Q} = \begin{bmatrix} \boldsymbol{K}_s & \boldsymbol{0} \\ \boldsymbol{0} & \boldsymbol{M}_s \end{bmatrix} \tag{3.4}$$

$$\boldsymbol{R} = \beta \boldsymbol{I} \tag{3.5}$$

where $\boldsymbol{M}_s$ and $\boldsymbol{K}_s$ are the mass and stiffness matrices, respectively. $\boldsymbol{I}$ is the identity matrix. The factor β is the relative importance of the control effectiveness compared to the control energy consumption. For the uncontrolled case, $\beta = \infty$.

The linear optimal closed-loop control law is e.g. derived by Soong [34].

$$\boldsymbol{u}(t) = \boldsymbol{G}^{lo}(t)\boldsymbol{y}(t) \tag{3.6}$$

where the control gain matrix $\boldsymbol{G}^{lo}(t)$ is given by

$$\boldsymbol{G}^{lo}(t) = -\frac{1}{2}\boldsymbol{R}^{-1}\boldsymbol{B}^T\boldsymbol{P}(t) \tag{3.7}$$

The Riccatti matrix $\boldsymbol{P}(t)$ is found by solving the Riccatti equation

$$\dot{\boldsymbol{P}}(t) + \boldsymbol{P}(t)\boldsymbol{A} - \frac{1}{2}\boldsymbol{P}(t)\boldsymbol{B}\boldsymbol{R}^{-1}\boldsymbol{B}^T\boldsymbol{P}(t) + \boldsymbol{A}^T\boldsymbol{P}(t) + 2\boldsymbol{Q} = 0, \quad \boldsymbol{P}(t_f) = \boldsymbol{0} \tag{3.8}$$

The matrices $\boldsymbol{A}$ and $\boldsymbol{B}$ are defined in appendix C.1. The Riccatti equation can be solved as described in appendix C.2. The elements in the Riccatti matrix are constant during most of the control interval dropping to zero near the end of the control interval, i.e. near t_f. Therefore, the time-dependent Riccatti matrix is approximated by the constant matrix $\boldsymbol{P}$ corresponding to the values in the first part of the control interval.

Then the control gain matrix is

$$\boldsymbol{G}^{lo} = -\frac{1}{2}\boldsymbol{R}^{-1}\boldsymbol{B}^T\boldsymbol{P} \tag{3.9}$$

As an example, the gain matrix $\boldsymbol{G}^{lo}$ is calculated for the bridge section model used in the wind tunnel experiments described in chapters 5 and 6 for $\beta = 10$ and $\beta = 100$. The parameters of the model are shown in table 2.2. The aerodynamic derivatives for the model are approximated by the values for a flat plate shown in section 2.2. It is assumed that the model performs binary flutter with $\omega_f = 6.62$ rad/s and $U_f = 8.18$ m/s, see equations (2.45) and (2.46). The Riccatti matrices for $\beta = 10$ and $\beta = 100$ are shown in appendix C.2.

$$\beta = 10 \quad \Rightarrow \quad \boldsymbol{G}^{lo}_{10} = \begin{bmatrix} 2.89 & 0.91 & 1.76 & 0.09 \\ 0.73 & -0.28 & 0.22 & -0.30 \end{bmatrix} \tag{3.10}$$

$$\beta = 100 \quad \Rightarrow \quad \boldsymbol{G}^{lo}_{100} = \begin{bmatrix} 0.34 & 0.17 & 0.57 & 0.04 \\ 0.10 & -0.03 & 0.01 & -0.08 \end{bmatrix} \tag{3.11}$$

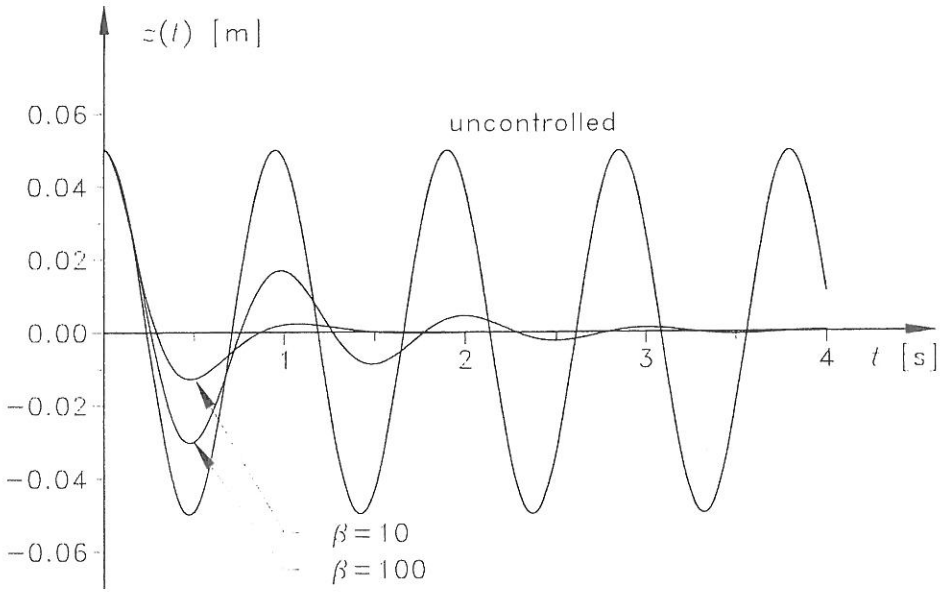

Figure 3.2: Uncontrolled and controlled vertical motion for $\beta = 10$ and $\beta = 100$ using classical linear optimal control.

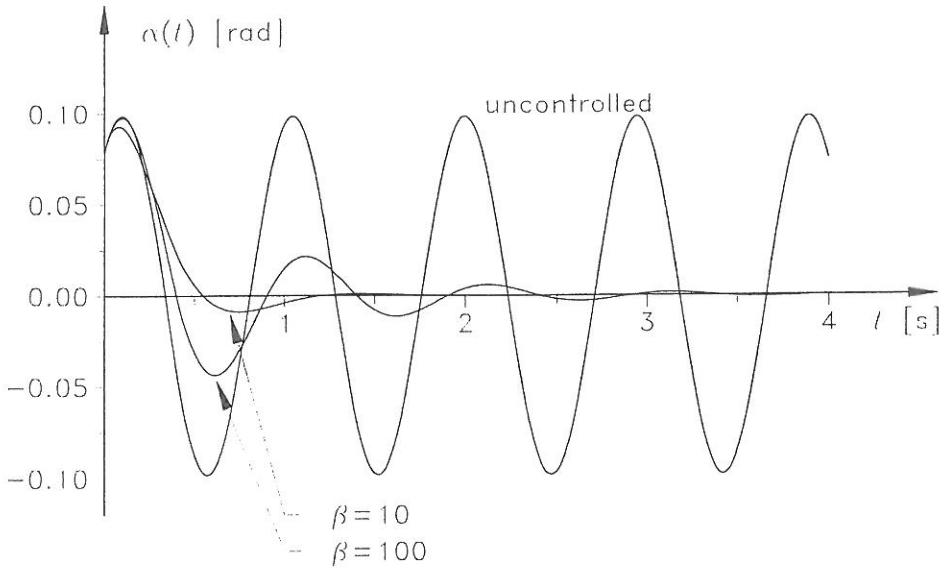

Figure 3.3: Uncontrolled and controlled torsional motion for $\beta = 10$ and $\beta = 100$ using classical linear optimal control.

As expected, the elements of the gain matrix are reduced when the β-value is increased.

Motion of the model with closed-loop control is described in appendix C.1. The vertical and torsional uncontrolled motion and controlled motion with $\beta = 10$ and $\beta = 100$ are shown in figures 3.2 and 3.3, respectively. Both the vertical and torsional oscillations are reduced very fast, especially for $\beta = 10$.

The movements of the trailing and leading flap are shown in figure 3.4 for $\beta = 10$ and in figure 3.5 for $\beta = 100$. The maximum flap angle for $\beta = 10$ is about 16° and for $\beta = 100$ the maximum angle is about 8°. For both β-values the trailing flap is turned more than the leading flap and there is a phase angle between the motion of the trailing flap and the leading flap.

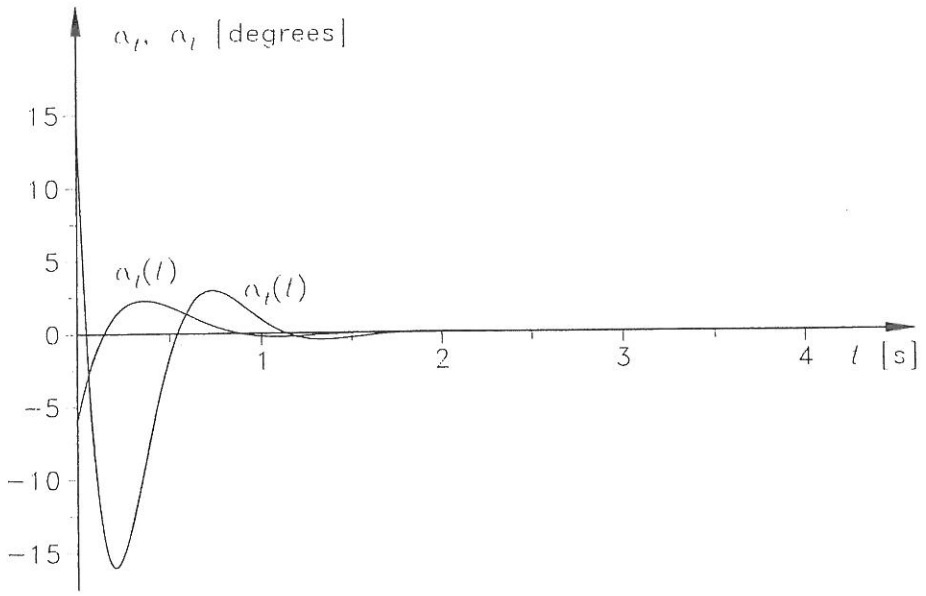

Figure 3.4: Flap angles for $\beta = 10$ using classical linear optimal control.

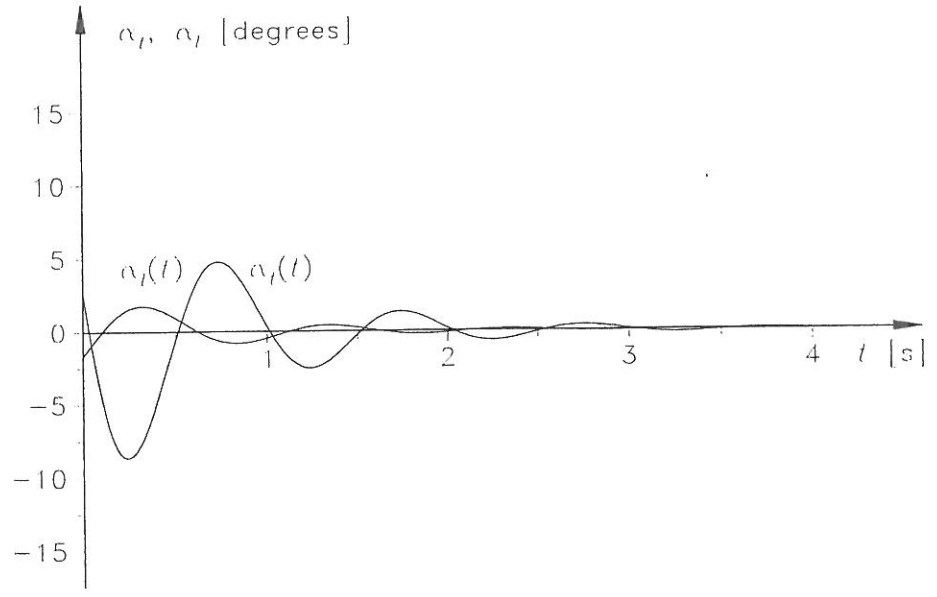

Figure 3.5: Flap angles for $\beta = 100$ using classical linear optimal control.

3.3 Instantaneous Optimal Closed-Loop Control

In instantaneous optimal control a time-dependent performance index $J(t)$ is defined by e.g.

$$J(t) = \boldsymbol{y}^T(t)\boldsymbol{Q}\boldsymbol{y}(t) + \boldsymbol{u}^T(t)\boldsymbol{R}\boldsymbol{u}(t) \tag{3.12}$$

This performance index is minimized at every time instant t during the control interval, i.e. for all $0 \leq t \leq t_f$, see Soong [34].

In instantaneous optimal closed-loop control the control law is

$$\boldsymbol{u}(t) = \boldsymbol{G}^{io}\boldsymbol{y}(t) \tag{3.13}$$

The control gain matrix is

$$\boldsymbol{G}^{io} = -\frac{\Delta t}{2}\boldsymbol{R}^{-1}\boldsymbol{B}^T\boldsymbol{Q} \tag{3.14}$$

where Δt is a small time interval, see Soong [34]. By comparing the gain matrices $\boldsymbol{G}^{lo}$ and $\boldsymbol{G}^{io}$ for linear optimal and instantaneous optimal closed-loop control it is seen that the Riccatti matrix $\boldsymbol{P}$ in equation (3.9) is replaced by $\Delta t\boldsymbol{Q}$ in equation (3.14). The instantaneous control law is thus much simpler than the linear optimal control law because solving the Riccatti matrix is omitted.

The control gain matrix is calculated for the example described in section 3.2 for $\beta = 2$ and $\beta = 10$. The weighting matrices in equations (3.4) and (3.5) for classical linear optimal control are used

$$\beta = 2 \quad \Rightarrow \quad \boldsymbol{G}_2^{io} = \begin{bmatrix} 0.000 & 0.000 & 1.230 & 0.060 \\ 0.000 & 0.000 & -0.004 & -0.098 \end{bmatrix} \tag{3.15}$$

$$\beta = 10 \quad \Rightarrow \quad \boldsymbol{G}_{10}^{io} = \begin{bmatrix} 0.000 & 0.000 & 0.246 & 0.012 \\ 0.000 & 0.000 & -0.001 & -0.020 \end{bmatrix} \tag{3.16}$$

When β is multiplied by a factor a, $\boldsymbol{G}$ is multiplied by $1/a$, as $\boldsymbol{R}^{-1} = 1/\beta\boldsymbol{I}$. The flap angles only depend on the vertical and torsional velocities for the current selection of weighting matrices $\boldsymbol{R}$ and $\boldsymbol{Q}$.

Motion of the model with closed-loop control is described in appendix C.1. The vertically and torsionally uncontrolled motion and controlled motion with $\beta = 2$ and $\beta = 10$ are shown in figures 3.6 and 3.7, respectively. Both the vertical and torsional oscillations are reduced very fast, especially for $\beta = 2$.

The movements of the trailing and leading flap are shown in figure 3.8 for $\beta = 2$. The flap angles shown in figure 3.8 can be compared with the flap angles shown in figure 3.4, where classical linear optimal control is used. The shapes of the flap angle curves are much alike, but the flaps are slightly delayed in instantaneous control compared to classical linear optimal control.

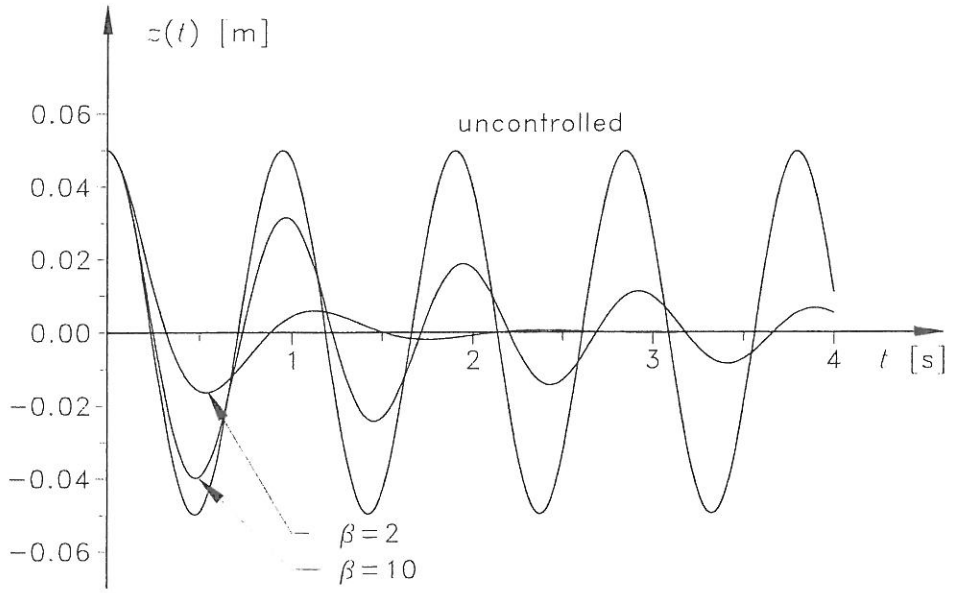

Figure 3.6: Uncontrolled and controlled vertical motion for $\beta = 2$ and $\beta = 10$ using instantaneous optimal control.

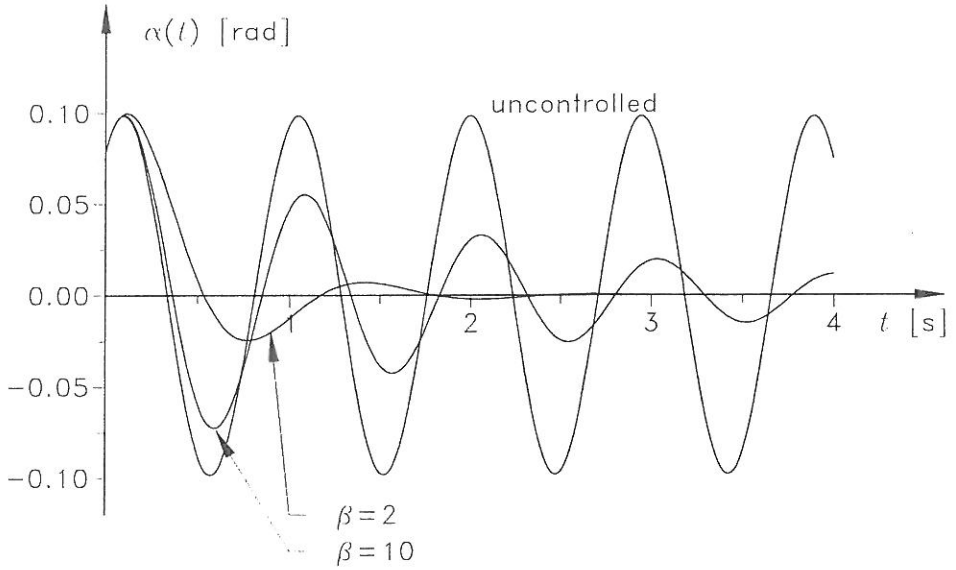

Figure 3.7: Uncontrolled and controlled torsional motion for $\beta = 2$ and $\beta = 10$ using instantaneous optimal control.

3.4 Constant Phase Angle

As described in section 2.3.2, binary flutter occurs when the structural dissipated energy E_{dis} is equal to the energy input E_{input} from the motion-induced wind load during a period. The binary flutter condition is

$$\begin{bmatrix} z(t) \\ \alpha(t) \end{bmatrix} = \begin{bmatrix} z_0 \cos(\omega_f t) \\ \alpha_0 \cos(\omega_f t - \varphi_\alpha) \end{bmatrix} \tag{3.17}$$

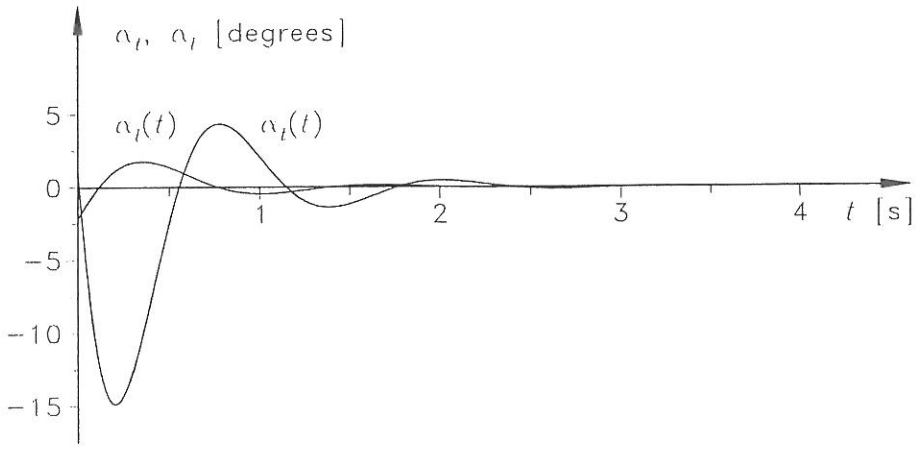

Figure 3.8: Flap angles for $\beta = 2$ using instantaneous optimal control.

where z_0 and α_0 are the amplitudes of the vertical and torsional oscillations and φ_α is the phase angle between the vertical and torsional oscillation.

The structural dissipated energy per metre during the period $T_f = 2\pi/\omega_f$ is

$$\begin{aligned} E_{dis} &= \int_0^{T_f} \left[m2\zeta_z\omega_z \frac{dz(t)}{dt} + I2\zeta_\alpha\omega_\alpha \frac{d\alpha(t)}{dt} \right] dt \\ &= \frac{K_f U_f}{B} 2\pi \left(m\zeta_z\omega_z z_0^2 + I\zeta_\alpha\omega_\alpha\alpha_0^2 \right) \end{aligned} \tag{3.18}$$

The energy input per metre during the period T_f for no regulation of the flaps is

$$\begin{aligned} E_{input} &= \int_0^{T_f} \left[F_{ad}^P(t) \frac{dz(t)}{dt} + F_{ad}^M(t) \frac{d\alpha(t)}{dt} \right] dt \\ &= \frac{1}{2}\rho U_f^2 B K_f^2 \pi z_0 \alpha_0 \left[\frac{z_0}{B\alpha_0} H_1^\star(K_f) + \frac{B\alpha_0}{z_0} A_2^\star(K_f) + \right. \\ &\quad \left. (H_2^\star(K_f) + A_1^\star(K_f)) \cos(-\varphi_\alpha) + (H_3^\star(K_f) - A_4^\star(K_f)) \sin(-\varphi_\alpha) \right] \end{aligned} \tag{3.19}$$

As both the oscillations and the motion-induced wind load have sine-shape, this shape is also selected for the control action and thereby the flap angles.

$$\begin{bmatrix} \alpha_t(t) \\ \alpha_l(t) \end{bmatrix} = \begin{bmatrix} \alpha_{t0} \cos(\omega_f t - \varphi_\alpha - \varphi_t) \\ \alpha_{l0} \cos(\omega_f t - \varphi_\alpha - \varphi_l) \end{bmatrix} \tag{3.20}$$

where α_{t0} and α_{l0} are the amplitudes of the flap angles and φ_t and φ_l are the phase angles between the torsional oscillation and the flap oscillations.

The additional energy input per metre $\Delta E_{input,t}$ and $\Delta E_{input,l}$ during the period T_f for regulation of the trailing and leading flap, respectively, is

$$\begin{aligned} \Delta E_{input,t} &= \int_0^{T_f} \left[F_{at}^P(t) \frac{dz(t)}{dt} + F_{at}^M(t) \frac{d\alpha(t)}{dt} \right] dt \\ &= \frac{1}{2}\rho U_f^2 B K_f^2 \pi z_0 \alpha_0 \left(\frac{\alpha_{t0}}{\alpha_0} \left[H_5^\star(K_f) \cos(-\varphi_\alpha - \varphi_t) + H_6^\star(K_f) \sin(-\varphi_\alpha - \varphi_t) \right] + \right. \\ &\quad \left. \frac{B\alpha_{t0}}{z_0} \left[A_5^\star(K_f) \cos(-\varphi_t) + A_6^\star(K_f) \sin(-\varphi_t) \right] \right) \end{aligned} \tag{3.21}$$

$$\begin{aligned}\Delta E_{input,l} &= \int_0^{T_f} \left[F_{al}^P(t)\frac{dz(t)}{dt} + F_{al}^M(t)\frac{d\alpha(t)}{dt} \right] dt \\ &= \frac{1}{2}\rho U_f^2 B K_f^2 \pi z_0 \alpha_0 \left(\frac{\alpha_{l0}}{\alpha_0} \left[H_7^\star(K_f)\cos(-\varphi_\alpha - \varphi_l) + H_8^\star(K_f)\sin(-\varphi_\alpha - \varphi_l) \right] + \right. \\ &\quad \left. \frac{B\alpha_{t0}}{z_0} \left[A_7^\star(K_f)\cos(-\varphi_l) + A_8^\star(K_f)\sin(-\varphi_l) \right] \right) \end{aligned} \tag{3.22}$$

The flap configuration parameters α_{t0}, α_{l0}, φ_t and φ_l can be selected so the energy input is reduced. The optimal phase angles are found for

$$\frac{d(\Delta E_{input,t})}{d\varphi_t} = 0 \quad \Rightarrow$$

$$\varphi_t = -\tan^{-1}\left(\frac{-z_0 H_5^\star(K_f)\sin(-\varphi_\alpha) + z_0 H_6^\star(K_f)\cos(-\varphi_\alpha) + B\alpha_0 A_6^\star(K_f)}{z_0 H_5^\star(K_f)\cos(-\varphi_\alpha) + z_0 H_6^\star(K_f)\sin(-\varphi_\alpha) + B\alpha_0 A_5^\star(K_f)} \right) \tag{3.23}$$

$$\frac{d(\Delta E_{input,l})}{d\varphi_l} = 0 \quad \Rightarrow$$

$$\varphi_l = -\tan^{-1}\left(\frac{-z_0 H_7^\star(K_f)\sin(-\varphi_\alpha) + z_0 H_8^\star(K_f)\cos(-\varphi_\alpha) + B\alpha_0 A_8^\star(K_f)}{z_0 H_7^\star(K_f)\cos(-\varphi_\alpha) + z_0 H_8^\star(K_f)\sin(-\varphi_\alpha) + B\alpha_0 A_7^\star(K_f)} \right) \tag{3.24}$$

For the example described in section 3.2 the force of the motion-induced wind load $F_{ad}^P(t)$ and the vertical velocity $\dot{z}(t)$ are shown in figure 3.9. The moment of the motion-induced wind load $F_{ad}^M(t)$ and the torsional velocity $\dot{\alpha}(t)$ are shown in figure 3.10.

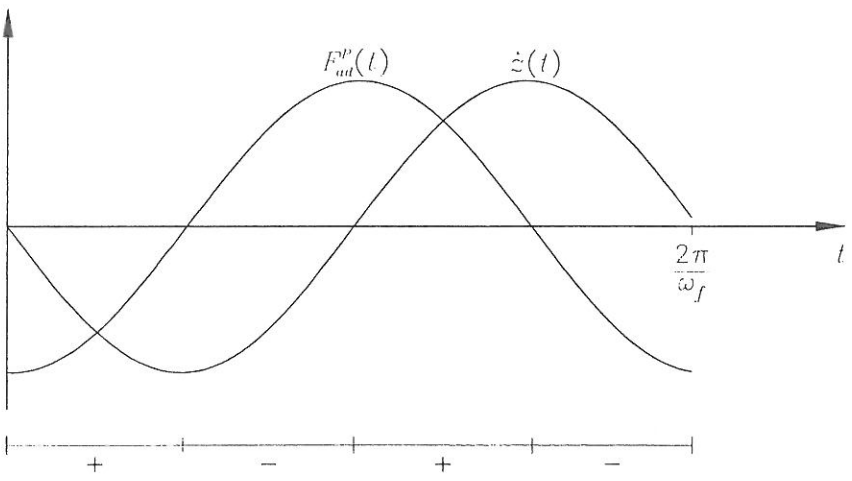

Figure 3.9: Sign of contribution to energy extracted from force of motion-induced wind load.

The time intervals with positive contribution to E_{input} are marked with '+' in figures 3.9 and 3.10. The time intervals with negative contribution to E_{input} are marked with '−'. The dissipated structural energy and the energy input are $E_{dis} = E_{input} = 0.136$ Nm/m.

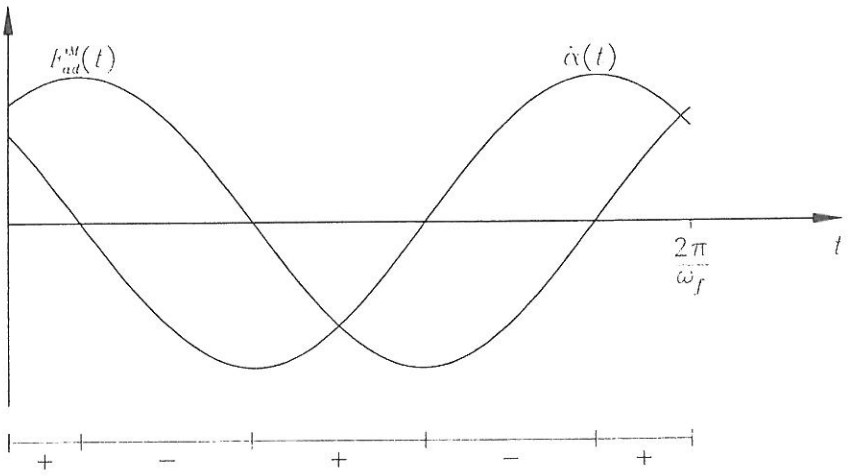

Figure 3.10: Sign of contribution to energy extracted from moment of motion-induced wind load.

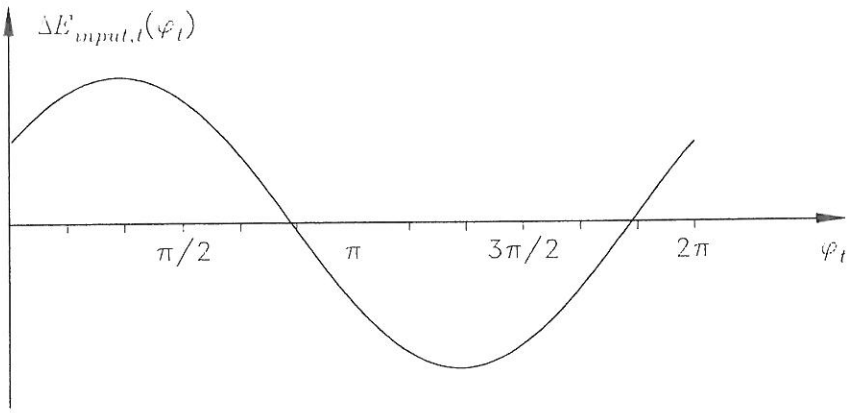

Figure 3.11: Energy input due to movement of trailing flap.

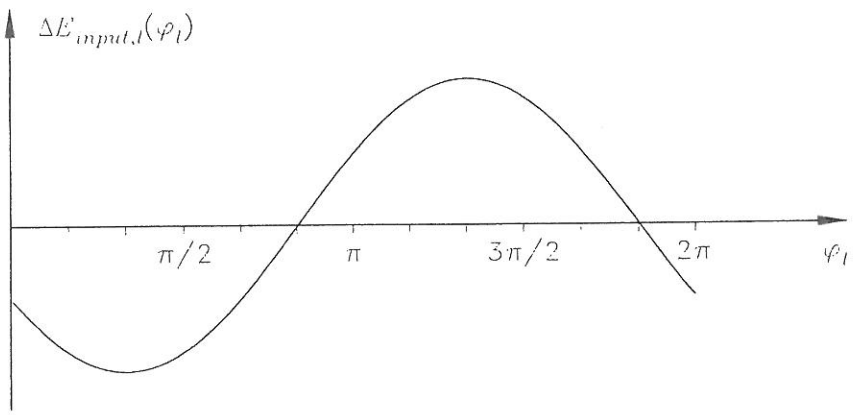

Figure 3.12: Energy input due to movement of leading flap.

The additional energy input per metre $\Delta E_{input,t}$ and $\Delta E_{input,l}$ during the period T_f is dependent on φ_t and φ_l, respectively, see figures 3.11 and 3.12.

The optimal flap angles and maximum contribution to energy input per metre are

$$\varphi_{t,opt} = 7.91 \cdot \frac{\pi}{6} = 237° \quad \Rightarrow \quad \min(\Delta E_{input,t}(\varphi_t)) = -12.68\alpha_{t0} \text{ Nm/m} \tag{3.25}$$

$$\varphi_{l,opt} = 2.02 \cdot \frac{\pi}{6} = 61° \quad \Rightarrow \quad \min(\Delta E_{input,l}(\varphi_l)) = -1.786\alpha_{t0} \text{ Nm/m} \tag{3.26}$$

For flap angle amplitudes equal to the amplitude of the torsional motion, i.e. $\alpha_{t0} = \alpha_{l0} = \alpha_0 = 0.098$ the total energy input is

$$\begin{aligned} &E_{input} + \Delta E_{input,t}(\varphi_{t,opt}) + \Delta E_{input,l}(\varphi_{l,opt}) \\ &\quad = 0.136 - 1.243 - 0.175 = -1.282 \text{ Nm/m} \end{aligned} \tag{3.27}$$

As seen the effect of the trailing flap is about seven times the effect of the leading flap. The flap configuration described decreases the energy extracted from the wind, so binary flutter will not occur for the investigated wind velocity.

3.5 Concluding Remarks

In this chapter three active closed-loop control algorithms are described, namely classical linear optimal closed-loop control, instantaneous optimal closed-loop control and closed-loop control with constant phase angles between the motion of the flaps and the torsional motion of the bridge.

In classical linear optimal closed-loop control a performance index is minimized during the entire control interval. In instantaneous optimal closed-loop control the performance index is minimized at every time instant. The importance of the control effectiveness compared to the control energy consumption can be regulated for both algorithms. In the examples with a flat plate with flaps it is shown that both algorithms are very efficient.

In constant phase angle closed-loop control the optimal phase angles of the flaps are derived based on the energy input from the motion-induced wind load. The example shows that no binary flutter will occur for a flat plate with long flaps for the investigated wind velocity if the flaps are moved with optimal phase angles and amplitudes equal to the pitch angle of the plate.

Chapter 4

Neural Network Modelling

4.1 Introduction

In this chapter it is described how neural networks trained with data from wind tunnel experiments can be used to

- simulate the motion of a bridge section model, see section 4.2,
- calculate flap positions, see section 4.3,
- extract the aerodynamic derivatives, see section 4.4.

The neural networks used are structured as Multi Layer Perceptron (MLP) neural networks as described in appendix D.1. A MLP neural network consists of three layers, namely an input layer with connections to a hidden layer, which again is connected to an output layer. During training of a neural network the connections, also called weights, are adjusted so the deviation between the actual output and the desired output is minimized.

Data from the wind tunnel experiments are not used to train neural networks as described in this chapter since the data are very noisy, especially with respect to the calculated velocities. Further, many of the time series from the wind tunnel experiments are very short and mainly contain data with the slow start of the flaps, see chapter 6. Finally, the neural network models described in this chapter assume that the flaps can be moved fast, i.e. no distinction is made between the desired and actual flap positions. In the performed wind tunnel experiments the flaps are moved very slowly.

4.2 Modelling of Bridge Section

The following Innovation State Space Model is used for a linear system where p state variables are observed, see Sørensen [36] and Hansen et al. [15]

$$\hat{\boldsymbol{y}}(k) = \boldsymbol{\Phi}\hat{\boldsymbol{y}}(k-1) + \boldsymbol{\Gamma}\boldsymbol{u}(k-1) + \boldsymbol{K}\boldsymbol{\varepsilon}(k-1) \tag{4.1}$$

$$\boldsymbol{z}(k) = \boldsymbol{L}\hat{\boldsymbol{y}}(k) - \boldsymbol{\varepsilon}(k) \tag{4.2}$$

where

$\hat{\boldsymbol{y}}^T(k) = (\hat{z}(k), \hat{\alpha}(k), \hat{\dot{z}}(k), \hat{\dot{\alpha}}(k))$ is the estimate of the state vector of the order n at the time step k.

$\boldsymbol{u}^T(k) = (\alpha_t(k), \alpha_l(k)) = (\alpha_{ta}(k), \alpha_{la}(k))$ is the control vector of the order m at the time step k.

$\boldsymbol{\varepsilon}(k)$ is the prediction error vector of the order p at the time step k.

$\boldsymbol{z}(k)$ is the measured observation vector of the order p at the time step k.

$\boldsymbol{L}$ is the observation matrix of the order $p \times n$.

In the linear case $\boldsymbol{\Phi}$, $\boldsymbol{\Gamma}$ and $\boldsymbol{K}$ are constant matrices of dimension $n \times n$, $n \times m$ and $n \times p$, respectively.

Incomplete State Information may occur, i.e. $\hat{\boldsymbol{y}}$ is not completely measurable. The matrix $\boldsymbol{L}$ can be chosen as $\boldsymbol{L} = [\mathbf{1}_{p,p}\mathbf{0}_{p,n-p}]$, where $\mathbf{1}_{p,p}$ is a $p \times p$ unity matrix and $\mathbf{0}_{p,n-p}$ is a $p \times (n-p)$ zero matrix. In this way the elements in $\boldsymbol{L}\hat{\boldsymbol{y}}(k)$ are equal to the first p elements of $\hat{\boldsymbol{y}}(k)$.

For a non-linear model the parameters $\boldsymbol{\Phi}$, $\boldsymbol{\Gamma}$ and $\boldsymbol{K}$ are not constant matrices, but depend on the actual values of the state, control and output vectors. The following multivariable Non-linear Innovation State Space Model is used, see Sørensen [36],

$$\hat{\boldsymbol{Y}}(k) = \boldsymbol{\mathcal{F}}\left(\hat{\boldsymbol{Y}}(k-1), \boldsymbol{U}(k-1), \boldsymbol{E}(k-1)\right) \tag{4.3}$$

$$\boldsymbol{Z}(k) = \boldsymbol{L}\hat{\boldsymbol{Y}}(k) + \boldsymbol{E}(k) \tag{4.4}$$

where $\boldsymbol{\mathcal{F}}$ is a non-linear function of the vector of weights $\boldsymbol{w}$ in the MLP neural network.

The input vector $\boldsymbol{I}$ of the order n to the neural network is

$$\boldsymbol{I}(k-1) = \begin{bmatrix} \hat{\boldsymbol{Y}}(k-1) \\ \boldsymbol{U}(k-1) \\ \boldsymbol{E}(k-1) \end{bmatrix} \tag{4.5}$$

The output vector $\hat{\boldsymbol{O}}$ of the order n is

$$\hat{\boldsymbol{O}}(k) = \hat{\boldsymbol{Y}}(k) \tag{4.6}$$

The desired output vector $\boldsymbol{O}$ of the order p is

$$\boldsymbol{O}(k) = \boldsymbol{Z}(k) \tag{4.7}$$

The prediction error $\boldsymbol{E}$ of the order p is

$$\boldsymbol{E}(k) = \boldsymbol{Z}(k) - \boldsymbol{L}\hat{\boldsymbol{Y}}(k) \tag{4.8}$$

On-line extraction of the parameters $\hat{\boldsymbol{\Phi}}$, $\hat{\boldsymbol{\Gamma}}$ and $\hat{\boldsymbol{K}}$ from the network gives an actual linearized Innovation State Space Model.

$$\hat{\boldsymbol{y}}(k) = \hat{\boldsymbol{\Phi}}\hat{\boldsymbol{y}}(k-1) + \hat{\boldsymbol{\Gamma}}\boldsymbol{u}(k-1) + \hat{\boldsymbol{K}}\boldsymbol{\varepsilon}(k-1) \tag{4.9}$$

$$\boldsymbol{z}(k) = \boldsymbol{L}\hat{\boldsymbol{y}}(k) - \boldsymbol{\varepsilon}(k) \tag{4.10}$$

The parameters are extracted from the network in the following way

$$\hat{\boldsymbol{\Phi}}(k) = \frac{\partial \hat{\boldsymbol{Y}}(k)}{\partial \hat{\boldsymbol{Y}}^T(k-1)} = \frac{\partial \hat{\boldsymbol{O}}(k)}{\partial \hat{\boldsymbol{Y}}^T(k-1)} \tag{4.11}$$

$$\hat{\boldsymbol{\Gamma}}(k) = \frac{\partial \hat{\boldsymbol{Y}}(k)}{\partial \boldsymbol{U}^T(k-1)} = \frac{\partial \hat{\boldsymbol{O}}(k)}{\partial \boldsymbol{U}^T(k-1)} \tag{4.12}$$

$$\hat{\boldsymbol{K}}(k) = \frac{\partial \hat{\boldsymbol{Y}}(k)}{\partial \boldsymbol{E}^T(k-1)} = \frac{\partial \hat{\boldsymbol{O}}(k)}{\partial \boldsymbol{E}^T(k-1)} \tag{4.13}$$

Output $\hat{\boldsymbol{O}}$ differentiated with regard to the input is shown in appendix D.1.2.

4.2.1 Training of Neural Network

The weights $\boldsymbol{w}$ in the neural network $\mathcal{F}$ in the model (4.3) are found by training. The training set consists of N input time series, each of the length K. The net is a partially recurrent network since output from the net is used as input in the next step.

Feedforward as described in appendix D.1.1 is used to estimate the output of the network. There are several methods for updating the weights $\boldsymbol{w}$, e.g. backpropagation and the second-order Recursive Prediction Error Method (RPEM). According to Billings et al. [5], RPEM often yields better predictions and faster convergence than backpropagation. In the following a second-order RPEM with a Gauss-Newton search direction is used as training algorithm.

Let $\boldsymbol{E}(n,k,\boldsymbol{w})$ be the error vector between the estimates and measurements of the nth training time series at the kth time step. In the second-order RPEM with a Gauss-Newton search direction the following performance index $J(\boldsymbol{w})$ is minimized, see Billings et al. [5]

$$J(\boldsymbol{w}) = \frac{1}{2}\sum_{n=1}^{N}\sum_{k=1}^{K}\boldsymbol{E}^T(n,k,\boldsymbol{w})\boldsymbol{E}(n,k,\boldsymbol{w}) \tag{4.14}$$

The gradient of $J(\boldsymbol{w})$ with respect to the weights $\boldsymbol{w}$ is needed as search direction in the iteration scheme. This is calculated from

$$\frac{dJ(\boldsymbol{w})}{d\boldsymbol{w}^T} = -\sum_{n=1}^{N}\sum_{k=1}^{K}\boldsymbol{E}^T(n,k,\boldsymbol{w})\boldsymbol{L}\frac{d\hat{\boldsymbol{Y}}(n,k,\boldsymbol{w})}{d\boldsymbol{w}^T} \tag{4.15}$$

The gradient of the estimated state variables $\hat{\boldsymbol{Y}}(n,k,\boldsymbol{w})$ with respect to the weights $\boldsymbol{w}$ can be updated from the recursive equation

$$\boldsymbol{\psi}(n,k) = \frac{d\hat{\boldsymbol{Y}}(n,k,\boldsymbol{w})}{d\boldsymbol{w}^T} = \boldsymbol{\varphi}(n,k) + \left[\hat{\boldsymbol{\Phi}}(n,k) - \hat{\boldsymbol{K}}(n,k)\boldsymbol{L}\right]\boldsymbol{\psi}(n,k-1) \tag{4.16}$$

where

$$\boldsymbol{\varphi}(n,k) = \frac{\partial \hat{\boldsymbol{Y}}(n,k,\boldsymbol{w})}{\partial \boldsymbol{w}^T} \tag{4.17}$$

$$\hat{\boldsymbol{\Phi}}(n,k) = \frac{\partial \hat{\boldsymbol{Y}}(n,k,\boldsymbol{w})}{\partial \hat{\boldsymbol{Y}}^T(n,k-1,\boldsymbol{w})} \tag{4.18}$$

$$\hat{\boldsymbol{K}}(n,k) = \frac{\partial \hat{\boldsymbol{Y}}(n,k,\boldsymbol{w})}{\partial \boldsymbol{E}^T(n,k-1,\boldsymbol{w})} \tag{4.19}$$

$\boldsymbol{\varphi}(k)$, $\hat{\boldsymbol{\Phi}}(k)$ and $\hat{\boldsymbol{K}}(k)$ can be found by differentiation of the output of the network with respect to the weights and input. $\hat{\boldsymbol{\Phi}}(k)$ can be interpreted as the dynamic transfer matrix of an equivalent linear system. $\hat{\boldsymbol{K}}(k)$ is the corresponding extended Kalman filter gain.

With increasing time the measurements obtained previously are discounted by assigning less weight to older measurements that are no longer representative of the system. A forgetting factor λ is introduced, see Söderström and Stoica [35]. The smaller the value of the forgetting factor, the quicker the information in previous data will be forgotten. The choice of the forgetting factor in the algorithm is often very important. Theoretically, one must have $\lambda = 1$ to get convergence. On the other hand, if $\lambda < 1$ the algorithm becomes more sensitive and the weight estimates can change quickly. For that reason the forgetting factor is updated at every time step by

$$\lambda(k) = \lambda_0 \lambda(k-1) + 1 - \lambda_0 \tag{4.20}$$

Further, the matrix $\boldsymbol{P}(n,k)$ is introduced. $\boldsymbol{P}(n,k)$ indicates the asymptotic accuracy of the estimate and corresponds to the stationary covariance matrix in the equivalent extended Kalman filter approach

$$\begin{aligned} \boldsymbol{P}(n,k) \;=\; & \frac{1}{\lambda(k)} \Big\{ \boldsymbol{P}(n,k-1) - \boldsymbol{P}(n,k-1)\boldsymbol{\psi}^T(n,k)\boldsymbol{L}^T \\ & \Big[\lambda(k)\mathbf{1}_{p,p} + \boldsymbol{L}\boldsymbol{\psi}(n,k)\boldsymbol{P}(n,k-1)\boldsymbol{\psi}^T(n,k)\boldsymbol{L}^T\Big]^{-1} \\ & \boldsymbol{L}\boldsymbol{\psi}(n,k)\boldsymbol{P}(n,k-1)\Big\} \end{aligned} \tag{4.21}$$

The RPEM algorithm can be summarized as follows, see Billings et al. [5] or Ljung [26].

1. Initialize the weights $\boldsymbol{w}$ of the neural network with small random values. Choose $\boldsymbol{P}(0,0)$ as a diagonal matrix with large diagonal values typically in the range 10^2 to 10^4, see Billings et al. [5]. Assign a value to the factor used to update the forgetting factor, typically $\lambda_0 = 0.99$, see Billings et al. [5].

2. At the start of each time series the following values are initialized: the forgetting factor $\lambda(0) = 0.95$, the initial errors $\boldsymbol{E}(n,0,\boldsymbol{w}) = \mathbf{0}$ and the gradient $\boldsymbol{\psi}(n,0) = \mathbf{0}$. The matrix $\boldsymbol{P}(n,k)$ is not initialized as it determines the asymptotical accuracy of the estimate, see Billings et al. [5].

3. Present input to the network and compute the network output $\hat{\boldsymbol{Y}}(n,k,\boldsymbol{w})$ by feed-forward, see appendix D.1.1.

4. Compare the network output with the desired output to give the prediction errors

$$\boldsymbol{E}(n,k,\boldsymbol{w}) = \boldsymbol{Z}(n,k) - \boldsymbol{L}\hat{\boldsymbol{Y}}(n,k,\boldsymbol{w}) \tag{4.22}$$

5. Compute elements of $\boldsymbol{\psi}(n,k)$ by using equation (4.16).

6. Compute the matrix $\boldsymbol{P}(n,k)$ by using equation (4.21).

7. Adjust the weights $\boldsymbol{w}$

$$\boldsymbol{w}(n,k) = \boldsymbol{w}(n,k-1) + \boldsymbol{P}(n,k)\boldsymbol{\psi}^T(n,k)\boldsymbol{L}^T\boldsymbol{E}(n,k,\boldsymbol{w}) \tag{4.23}$$

8. Update input vector $\boldsymbol{I}$ with network output $\hat{\boldsymbol{Y}}(n,k,\boldsymbol{w})$, new measurements of the flap positions $\boldsymbol{u}(n,k)$ and the errors $\boldsymbol{E}(n,k,\boldsymbol{w})$.

Steps 2 to 8 are repeated until convergence.

By using the last estimate of the weights the trained network $\mathcal{F}$ can estimate the response of the oscillator.

4.2.2 Simulation and State Prediction by Trained Neural Network

When the trained neural network $\mathcal{F}$ given by equation (4.3) is used as a simulator, only the initial values $\boldsymbol{Z}(n,0) = \boldsymbol{L}\boldsymbol{Y}(n,0)$ of the measurable state variables and the complete flap positions time series $\boldsymbol{U}(n,k)$ are measured without any error. The non-observed state variables are set to $\mathbf{0}$ to obtain the initial values $\boldsymbol{Y}(n,0) = \boldsymbol{Y}_0(n)$. As no further measurements of the state variables are made, the prediction error vector $\boldsymbol{E}(n,k,\boldsymbol{w})$ is fixed as $\mathbf{0}$. The state variables in the simulator neural network are predicted by

$$\hat{\boldsymbol{Y}}(n,k,\boldsymbol{w}) = \mathcal{F}\left(\hat{\boldsymbol{Y}}(n,k-1,\boldsymbol{w}), \boldsymbol{U}(n,k-1), \boldsymbol{E}(n,k-1,\boldsymbol{w}), \boldsymbol{w}\right) \tag{4.24}$$

$$\boldsymbol{Y}(n,0) = \boldsymbol{Y}_0(n) \tag{4.25}$$

$$\boldsymbol{E}(n,k-1,\boldsymbol{w}) = \mathbf{0} \tag{4.26}$$

When the trained neural network is used as a one-step ahead predictor the measurable state variables $\boldsymbol{Z}(n,k) = \boldsymbol{L}\boldsymbol{Y}(n,k)$ and the flap positions $\boldsymbol{U}(n,k)$ are measured at every time step. In this case the state variables are predicted by

$$\hat{\boldsymbol{Y}}(n,k,\boldsymbol{w}) = \mathcal{F}\left(\hat{\boldsymbol{Y}}(n,k-1,\boldsymbol{w}), \boldsymbol{U}(n,k-1), \boldsymbol{E}(n,k-1,\boldsymbol{w}), \boldsymbol{w}\right) \tag{4.27}$$

$$\boldsymbol{E}(n,k-1,\boldsymbol{w}) = \boldsymbol{Z}(n,k-1) - \boldsymbol{L}\hat{\boldsymbol{Y}}(n,k-1,\boldsymbol{w}) \tag{4.28}$$

4.3 Modelling of Active Controller

After the neural network model of the motion of the bridge section model has been settled, an active closed-loop controller is coupled to the system. The control force $\boldsymbol{U}(k)$, i.e. the vector of flap positions, is used to minimize the mean square of the observable part of the response $\boldsymbol{Y}(k)$ of the bridge section model. In the final active closed-loop control

configuration the neural network model of the bridge section is used as a one-step ahead predictor to estimate the state vector to the next time step. The control force can then be estimated by the controller network based on the estimated state variables.

Because no state variables can be measured during training of the controller neural network, the trained network $\mathcal{F}$ given by (4.3) is used as a simulator to estimate the response of the controlled bridge section model $\hat{\boldsymbol{Y}}(k)$. Hence,

$$\hat{\boldsymbol{Y}}(k) = \mathcal{F}\left(\hat{\boldsymbol{Y}}(k-1), \boldsymbol{U}(k-1), \boldsymbol{E}(k-1), \boldsymbol{w}\right), \quad \boldsymbol{E}(k-1) = \boldsymbol{0} \tag{4.29}$$

The control force $\boldsymbol{U}(k)$ is modelled by an MLP neural network by using closed-loop control

$$\boldsymbol{U}(k) = \mathcal{G}\left(\hat{\boldsymbol{Z}}(k), \boldsymbol{w}_c\right), \quad \hat{\boldsymbol{Z}}(k) = \boldsymbol{L}\hat{\boldsymbol{Y}}(k) \tag{4.30}$$

where $\boldsymbol{w}_c$ is a vector of weights in the network modelling the controller. Obviously, the feedback part of the control law can only depend on the state variables $\hat{\boldsymbol{Z}}(k) = \boldsymbol{L}\hat{\boldsymbol{Y}}(k)$ which are measured (observed), and no noise term is present in the model.

The weights $\boldsymbol{w}_c$ of equation (4.30) are estimated, so the response predicted by equation (4.29) becomes minimum.

4.3.1 Training of Neural Network

The following performance index J_c, which is widely used in structural control, see e.g. Soong [34], is minimized for the controller network in equation (4.30)

$$J_c(\boldsymbol{w}_c) = \frac{1}{2}\sum_{n=1}^{N}\sum_{k=1}^{K}\left(\hat{\boldsymbol{Z}}^T(n,k,\boldsymbol{w}_c)\hat{\boldsymbol{Z}}(n,k,\boldsymbol{w}_c) + a\boldsymbol{U}^T(n,k,\boldsymbol{w}_c)\boldsymbol{U}(n,k,\boldsymbol{w}_c)\right) \tag{4.31}$$

$$\hat{\boldsymbol{Z}}(n,k,\boldsymbol{w}_c) = \boldsymbol{L}\hat{\boldsymbol{Y}}(n,k,\boldsymbol{w}_c) \tag{4.32}$$

where a is a positive scaling factor and $\hat{\boldsymbol{Y}}(n,k,\boldsymbol{w}_c)$ specifies the output of (4.29) for the nth time series at time step k using the controller (4.30) with the weights $\boldsymbol{w}_c$.

The gradient of $J_c(\boldsymbol{w}_c)$ with regard to the weights $\boldsymbol{w}_c$ is

$$\frac{dJ_c(\boldsymbol{w}_c)}{d\boldsymbol{w}_c^T} = \sum_{n=1}^{N}\sum_{k=1}^{K}\left[\hat{\boldsymbol{Z}}^T(n,k,\boldsymbol{w}_c)\boldsymbol{L}\frac{d\hat{\boldsymbol{Y}}(n,k,\boldsymbol{w}_c)}{d\boldsymbol{w}_c^T} + a\boldsymbol{U}^T(n,k,\boldsymbol{w}_c)\frac{d\boldsymbol{U}(n,k,\boldsymbol{w}_c)}{d\boldsymbol{w}_c^T}\right] \tag{4.33}$$

The gradient of the estimated state variables $\hat{\boldsymbol{Y}}(n,k,\boldsymbol{w}_c)$ and the control force $\boldsymbol{U}(n,k,\boldsymbol{w}_c)$ with respect to the weights organized in the vector $\boldsymbol{w}_c$ can be updated from the recursive equations, cf. (4.16)

$$\boldsymbol{\psi}_c(n,k) = \frac{d\hat{\boldsymbol{Y}}(n,k,\boldsymbol{w}_c)}{d\boldsymbol{w}_c^T} = \hat{\boldsymbol{\Phi}}(n,k)\boldsymbol{\psi}_c(n,k-1) + \hat{\boldsymbol{\Gamma}}(n,k)\boldsymbol{\upsilon}_c(n,k-1) \tag{4.34}$$

$$\boldsymbol{\upsilon}_c(n,k) = \frac{d\boldsymbol{U}(n,k,\boldsymbol{w}_c)}{d\boldsymbol{w}_c^T} = \boldsymbol{\varphi}_c(n,k) + \hat{\boldsymbol{\Phi}}_c(n,k)\boldsymbol{H}\boldsymbol{\psi}_c(n,k) \tag{4.35}$$

where

$$\hat{\boldsymbol{\Gamma}}(n,k) = \frac{\partial \hat{\boldsymbol{Y}}(n,k,\boldsymbol{w}_c)}{\partial \boldsymbol{U}(n,k-1,\boldsymbol{w}_c)} \tag{4.36}$$

$$\boldsymbol{\varphi}_c(n,k) = \frac{\partial \boldsymbol{U}(n,k,\boldsymbol{w}_c)}{\partial \boldsymbol{w}_c^T} \tag{4.37}$$

$$\hat{\boldsymbol{\Phi}}_c(n,k) = \frac{\partial \boldsymbol{U}(n,k,\boldsymbol{w}_c)}{\partial \hat{\boldsymbol{Z}}^T(n,k,\boldsymbol{w}_c)} \tag{4.38}$$

As seen the gradient is no longer dependent on variations of the observation noise, because this has been fixed as $\boldsymbol{E} = \boldsymbol{0}$ during the training phase.

4.4 Aerodynamic Derivatives for Bridge Section

The matrix equation of motion in discrete state-space form for a bridge section with flap control is

$$\boldsymbol{y}(k) \approx (\boldsymbol{1} + \Delta t(\boldsymbol{A} + \boldsymbol{HF}))\boldsymbol{y}(k-1) + \Delta t \boldsymbol{B}'\boldsymbol{u}'(k-1) \tag{4.39}$$

see appendix D.2 for description of the parameters.

As described in section 4.2, the parameters of the Innovation State Space model can be extracted from a trained neural network by using equations (4.11)–(4.13). When the trained neural networks are used to extract aerodynamic derivatives the control force vector $\boldsymbol{U}^T(k) = (\alpha_t(k), \alpha_l(k))$ in the multivariable Non-linear Innovation State Space Model in equations (4.3) and (4.4) is replaced by $\boldsymbol{U}'^T(k) = (\alpha_t(k), \alpha_l(k), \dot{\alpha}_t(k), \dot{\alpha}_l(k))$. By comparing the Innovation State Space model in equation (4.9) and the matrix equation of motion in equation (4.39) the following relations are derived

$$\hat{\boldsymbol{\Phi}} = \boldsymbol{1} + \Delta t(\boldsymbol{A} + \boldsymbol{HF}) \quad \Rightarrow \quad \boldsymbol{F} = \boldsymbol{H}^{-1}\left[\frac{1}{\Delta t}(\hat{\boldsymbol{\Phi}} - \boldsymbol{1}) - \boldsymbol{A}\right] \tag{4.40}$$

$$\hat{\boldsymbol{\Gamma}} = \Delta t \boldsymbol{B}' \quad \Rightarrow \quad \boldsymbol{B}' = \frac{\hat{\boldsymbol{\Gamma}}}{\Delta t} \tag{4.41}$$

where the matrix $\boldsymbol{F}$ contains the aerodynamic derivatives $H_1^\star(K), \ldots, H_4^\star(K), A_1^\star(K), \ldots, A_4^\star(K)$ and $\boldsymbol{B}$ contains the aerodynamic derivatives $H_5^\star(K), \ldots, H_8^\star(K), A_5^\star(K), \ldots, A_8^\star(K)$. The reduced frequency K is equal to

$$K = \begin{cases} \dfrac{B\omega_{\alpha,U}}{U} & \text{for } H_2^\star,\ H_3^\star,\ H_5^\star, \ldots, H_8^\star,\ A_2^\star,\ A_3^\star,\ A_5^\star, \ldots, A_8^\star \\ \dfrac{B\omega_{z,U}}{U} & \text{for } H_1^\star,\ H_4^\star,\ A_1^\star \text{ and } A_4^\star \end{cases} \tag{4.42}$$

where $\omega_{\alpha,U}$ is the torsional frequency for the actual wind velocity and $\omega_{z,U}$ is the vertical frequency for the actual wind velocity.

4.5 Concluding Remarks

In this chapter it is described how a Multi Layer Perceptron neural network can be used to simulate the motion of a bridge section based on data from e.g. a wind tunnel experiment. During training of an active controller neural network, the trained neural network modelling the motion of the bridge section is used as a simulator. In the final active closed-loop control configuration the trained neural network of the bridge section is used as one-step ahead predictor to estimate the state vector to the next time step. The control force is then estimated by the trained controller network based on the estimated state variables.

Further, it is described how aerodynamic derivatives for the bridge section can be extracted from a trained bridge section model network. Data from the wind tunnel experiments described in chapter 6 are not used to train the described networks because of the short and noisy time series from the experiments. Further, the very slow reaction of the flaps in the experiments does not agree with the very fast movement assumed in the neural network models.

Chapter 5

Test Set Up

5.1 Introduction

This chapter describes test set up for the wind tunnel experiments. The purpose of the experiments is described in section 5.2. In section 5.3 the *Wind Tunnel for Building Aerodynamics* at the *Instituto Superior Técnico* in Lisbon used during the experiments is described. The bridge section model and the suspension system are constructed by the *Structural Research Laboratory* at the *Department of Building Technology and Structural Engineering* at *Aalborg University*. The bridge section model and the suspension system are described in sections 5.4 and 5.5, respectively. The main part of the regulation system is designed and implemented by two students at the *Institute of Electronic Systems* at *Aalborg University*. It is described in section 5.6. Finally, in section 5.7, special details during setup are mentioned.

5.2 Purpose of Experiments

The purpose of the experiments with the bridge section model in the wind tunnel is primarily to investigate the principle to use flaps to control the bridge excitation. The bridge section model is dimensioned to fit into the *Wind Tunnel for Building Aerodynamics* at the *Instituto Superior Técnico* in Lisbon, Portugal, whereby a practically usable model is dimensioned. Further, it is important that the model is realistic compared to a real bridge — but no specific bridge is investigated.

Both the trailing flap and the leading flap can be regulated in the model, since the effect of two flaps instead of one is essential. The purpose of the flap in the leading edge is primarily to introduce a load on the bridge opposite to the motion of the bridge. The purpose of the flap in the trailing edge is primarily to change the direction of the wake. The flaps are able to rotate approximately $\pm 20°$ from the horizontal positions. It is of interest to investigate flaps with different lengths. Therefore, flaps with lengths $0.15B'$ and $0.25B'$ are constructed, where B' is the width of the bridge section model excluding flaps. Unfortunately, there were many problems during the wind tunnel experiments, and therefore, only the long flaps have been used.

5.3 Wind Tunnel

The *Wind Tunnel for Building Aerodynamics* at the *Instituto Superior Técnico* in Lisbon, Portugal is described in the ROLLAB Report RR 079 [2]. The general layout of the wind tunnel is shown in figure 5.1.

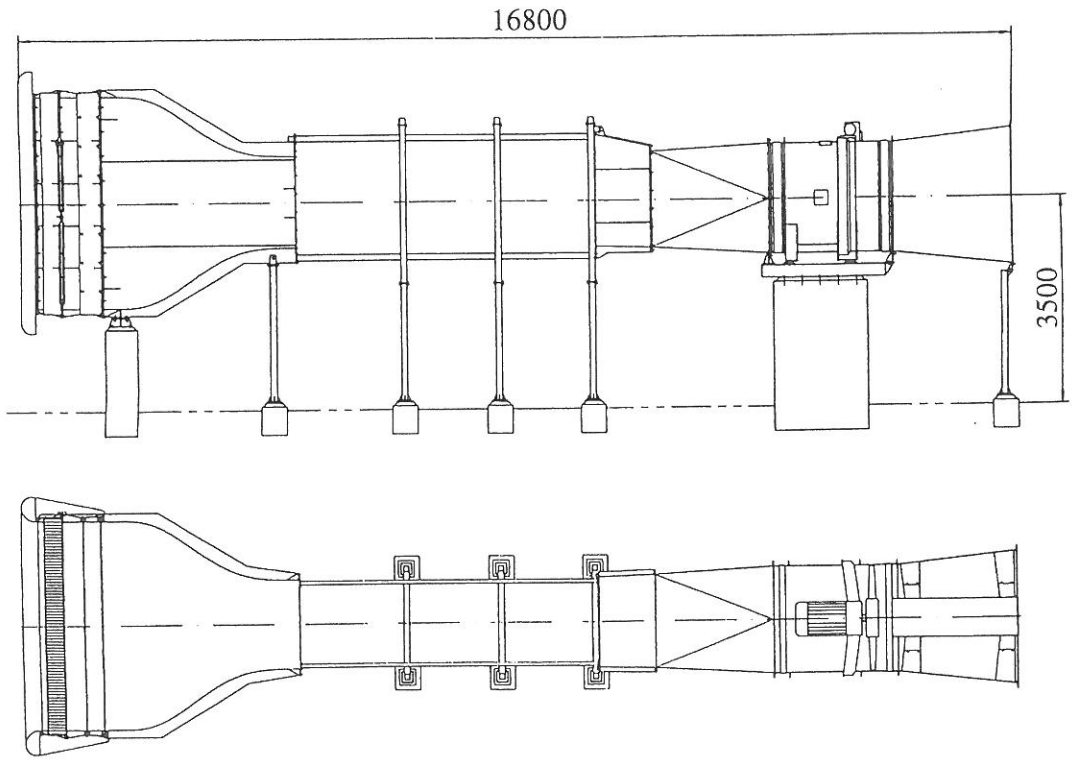

Figure 5.1: General layout of the wind tunnel [2]. Lengths in mm.

The tunnel is of the open return type and has a test section size of 1.5 m × 1.5 m × 5.0 m (nominal values). The maximum speed is 40 $^{m}/_{s}$. The fan can be controlled by means of a variable pitch device from 4 $^{m}/_{s}$ to 40 $^{m}/_{s}$. A collector (a funnel) will duct the air to a settling chamber, where a honeycomb and two gauzes are installed, whereupon a contraction unit (ratio 5.44:1) takes the air to the test section.

The test section steel 'cage' is mounted on separate steel frames bolted on concrete pads in the floor. Between the long top beams of the cage there are short cross beams to make the test section rigid. The nominal dimensions of the entrance to the test section are 1.5 m × 1.5 m. The general layout of the test section is shown in figure 5.2. In this basic version of the wind tunnel the side walls of the test section cannot be hoisted (opened).

In the test section the model can be elongated through two circular holes each with diameter 200 mm in the wind tunnel walls, see figure 5.3. The suspension system can be fixed to the metallic profiles shown in figure 5.3.

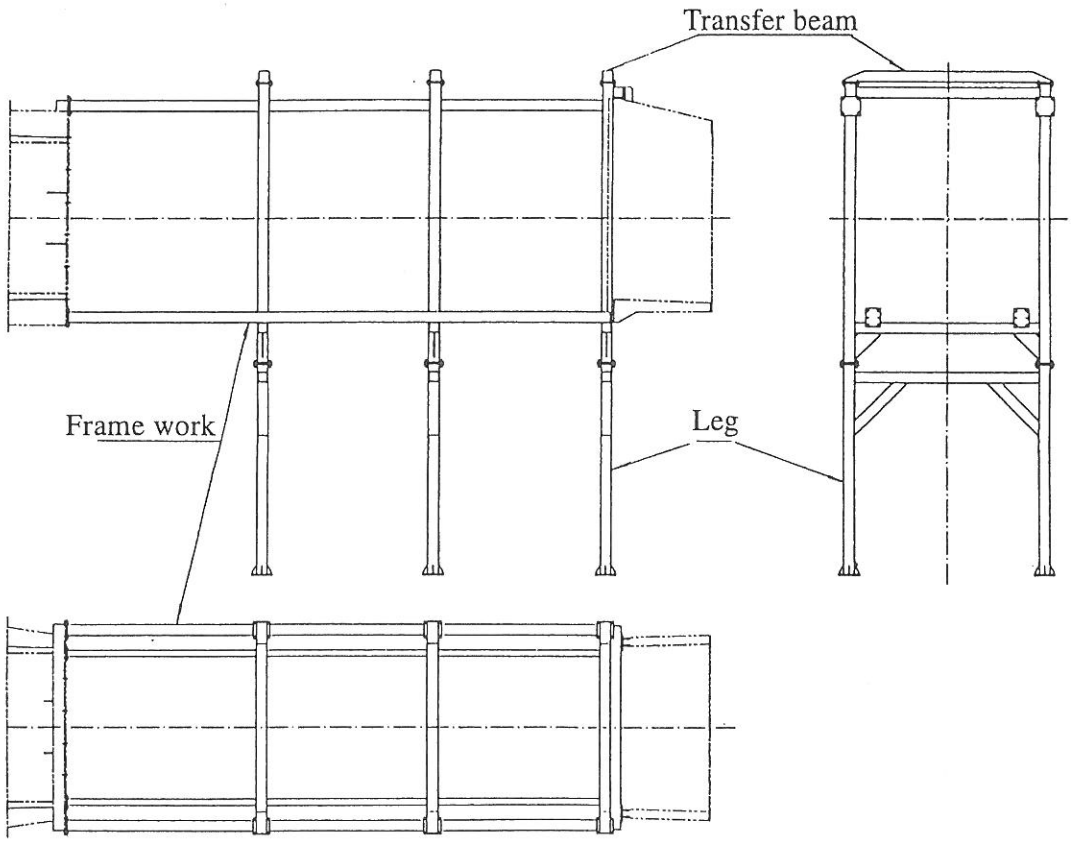

Figure 5.2: General layout of the test section [2].

After the test section there is a diffuser/transition unit. At the end of the transition unit (from square to circular) a safety gauze has been installed so that the fan will be protected from loose elements or tools which may be forgotten in the test section.

5.4 Bridge Section Model

Experiments have shown that the critical wind velocity for a streamlined girder is much higher than for a rectangular girder, see Ostenfeld & Larsen [30]. The bridge section model is therefore made streamlined with the flaps as the streamlined part.

A simplified model of the bridge section equipped with flaps is illustrated in figure 5.4. The width of the model excluding flaps is B' and the height of the model is $0.15B'$. In the experiments two short flaps with the length $0.15B'$ or two long flaps with the length $0.25B'$ are used. For illustration the model in figure 5.4 is shown with a long flap at the left hand side and a short flap at the right hand side.

The length of the model is 1,480 mm corresponding to the width of the test section of the wind tunnel minus 10 mm in each side. To avoid large end-effects where the model is elongated through the holes in the wind tunnel walls it is important to have a high aspect

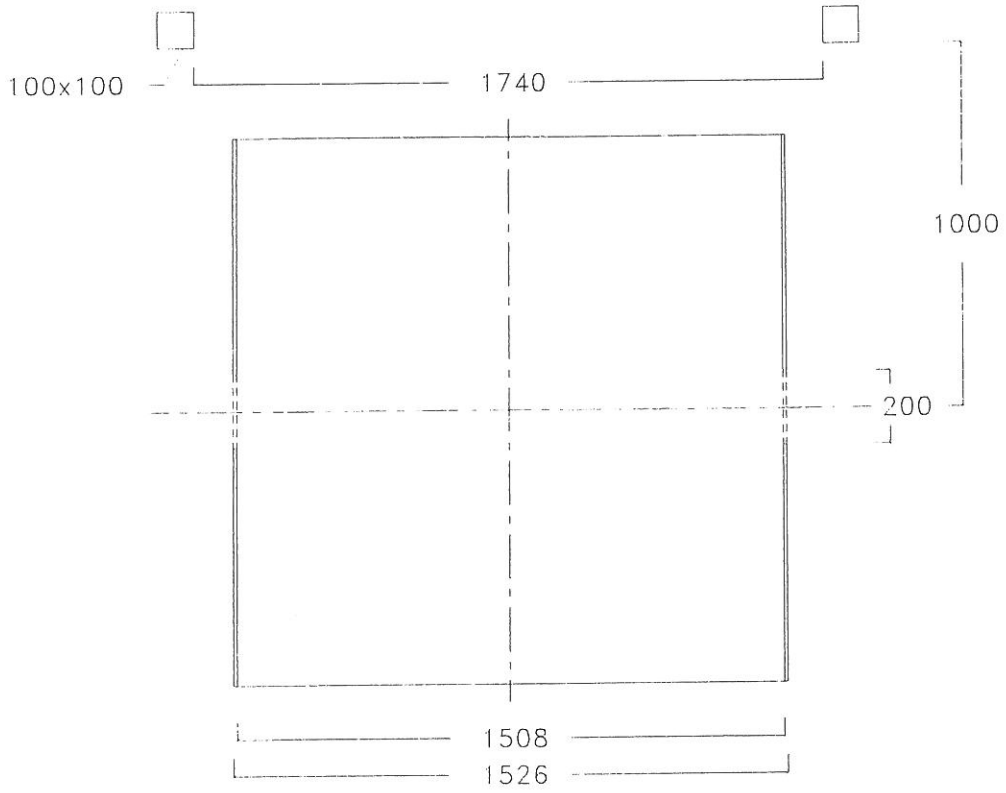

Figure 5.3: Holes in the wind tunnel walls and metallic profiles to fix the suspension system. Dimensions in mm.

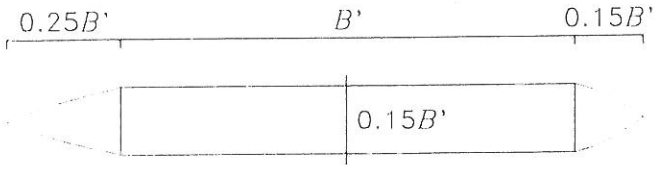

Figure 5.4: Simplified model of suspension bridge section with flaps.

ratio between the length and the width of the model as described by Hjorth-Hansen [20].

5.4.1 Model Laws

The model laws are described in appendix E.1. Three scaling factors are selected, namely the length scale, the wind velocity scale and the mass density scale for the surroundings. The selected and calculated scale factors are summarized in table 5.1.

The assumed ('typical') values of width, mass etc. for the prototype bridge equipped with long flaps are shown in table 5.2. Further, the corresponding calculated values for the model are shown.

Scale factor	Symbol	Value
Length	λ_L	1/40
Wind velocity	λ_V	1/4
Mass density of surroundings	λ_ρ	1
Frequency	λ_F	10
Time	λ_T	1/10
Mass density of model per unit length	λ_μ	1/1600
Mass moment of inertia per unit length	λ_I	$1/2.56 \cdot 10^6$

Table 5.1: Selected and calculated scale factors.

		Prototype	Model
Bridge	Width B' (excl. flaps) [m]	25	0.625
	Mass per unit length incl. cables μ_b [kg/m]	$25 \cdot 10^3$	15.6
	Mass moment of inertia per unit length incl. cables I_b [kg · m²/m]	$2.1 \cdot 10^6$	0.820
	First eigenfrequency (bending) f_1 [Hz]	0.08	0.8
	Second eigenfrequency (torsional) f_2 [Hz]	0.16	1.6
Long flaps	Mass per unit length μ_f [kg/m]	$1.16 \cdot 10^3$	0.725
	Mass moment of inertia per unit length around rotation point I_f [kg · m²/m]	$2.0 \cdot 10^3$	$7.8 \cdot 10^{-4}$

Table 5.2: Assumed values for the prototype and corresponding values for the model.

The dimensions of the simplified model are shown in figure 5.5.

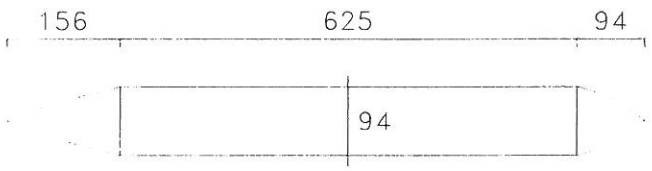

Figure 5.5: Dimensions of simplified model in mm.

5.4.2 Construction of Model

As the part of the regulation system to be fixed inside the model (two servo motors and two reduction gears) is relatively heavy the model is made as light as possible. Therefore, the model is made of foam with an aluminium frame to make it stiff. The aluminium profiles have a thickness of 1 mm and they are described/shown in [13]. Where it is possible there are holes in the aluminium frame to reduce the weight. Drawings for construction of the model are shown in [14]. The bridge section model has been constructed by the

Structural Research Laboratory at the *Department of Building Technology and Structural Engineering* at *Aalborg University.*

The bridge section model with main dimensions is shown in figure 5.6. The aluminium profiles and other aluminium elements of the model are hatched in figure 5.6. Hidden aluminium is shown with a light hatch. The aluminium plate over the servo motors and reduction gears is not shown. The foam parts of the model are coated after construction.

The actual (measured) and calculated (based on table 5.2) masses of the model are shown in table 5.3.

	Long flaps	Short flaps
Mass of model incl. flaps [kg]	14.653	13.820
Mass of regulation system inside model [kg]	11.400	
Assumed mass of wires etc. [kg]	0.500	
Measured total mass [kg]	26.553	25.720
Calculated total mass [kg]	25.234	—

Table 5.3: Actual and calculated masses of the model.

In figure 5.7 the model is shown suspended in a very simplified suspension system only used for testing of the behaviour of the model and regulation system.

To prevent the air flow from being interupted or separated in the joint between the flap and the model the hole inbetween is closed by a piece of fabric, see figure 5.8. Two types of fabric are used, namely a piece of airproof fabric covering the gap and a piece of elastic fabric around the edge of the flap.

5.5 Suspension System

The model is connected to a horizontal extension rod in each side which is going through the wind tunnel wall, see figure 5.6. Each of the extension rods can be separated into two parts, see the separation line in figure 5.6, so as the model can be placed inside the wind tunnel (the walls cannot be hoisted). The suspension system is the same in both sides. The extension rod is connected to an arm with dummy masses that can be moved on the arm so the model can represent the correct mass and mass inertia, see figure 5.9. Each side of the arm is suspended in a helical spring. The springs can be moved on the arm so the stiffness corresponding to the torsional motion of the model can be justified. Finally the extension rod is connected to a windward drag wire and a leeward drag wire.

The suspension system has been designed and constructed in the *Structural Research Laboratory* at the *Department of Building Technology and Structural Engineering* at *Aalborg University.* The resulting suspension system is very flexible as it can be regulated in both

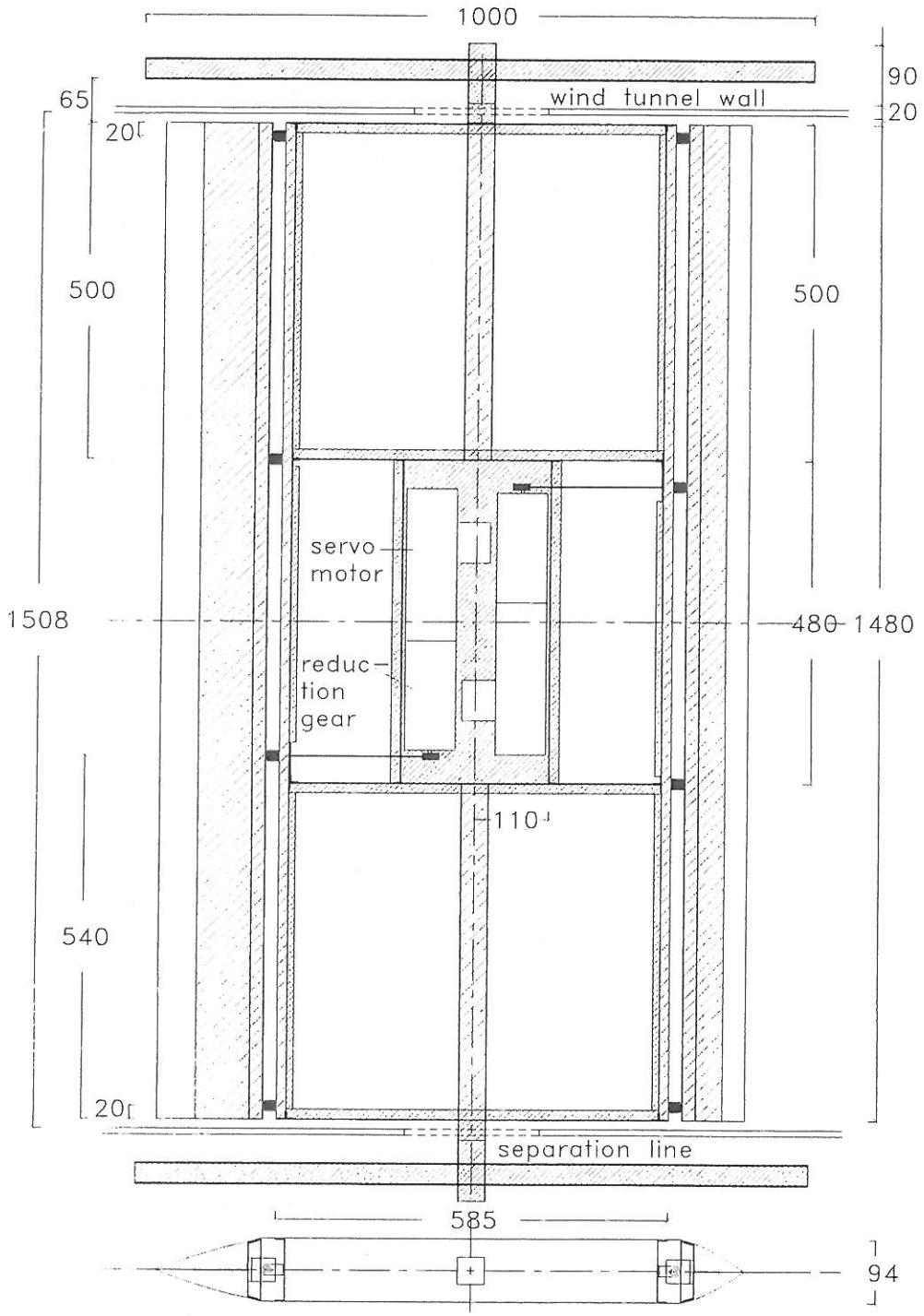

Figure 5.6: Bridge section model with main dimensions in mm. A long flap is shown in the left-hand side and a short flap is shown in the right-hand side. In the experiments two long flaps are used.

horizontal and vertical directions. As shown in figure 5.3, the suspension system is fixed to the metallic profiles by bolts. A simplified illustration of one side of the suspension system is shown in figure 5.9.

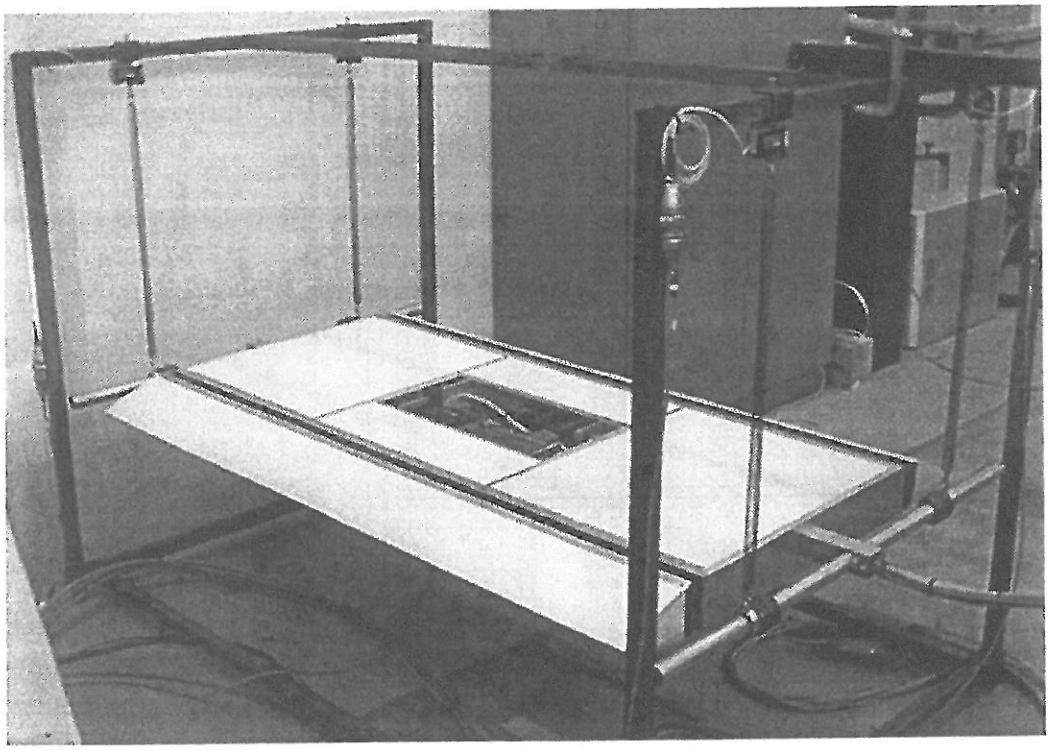

Figure 5.7: Bridge section model suspended in simplified suspension system.

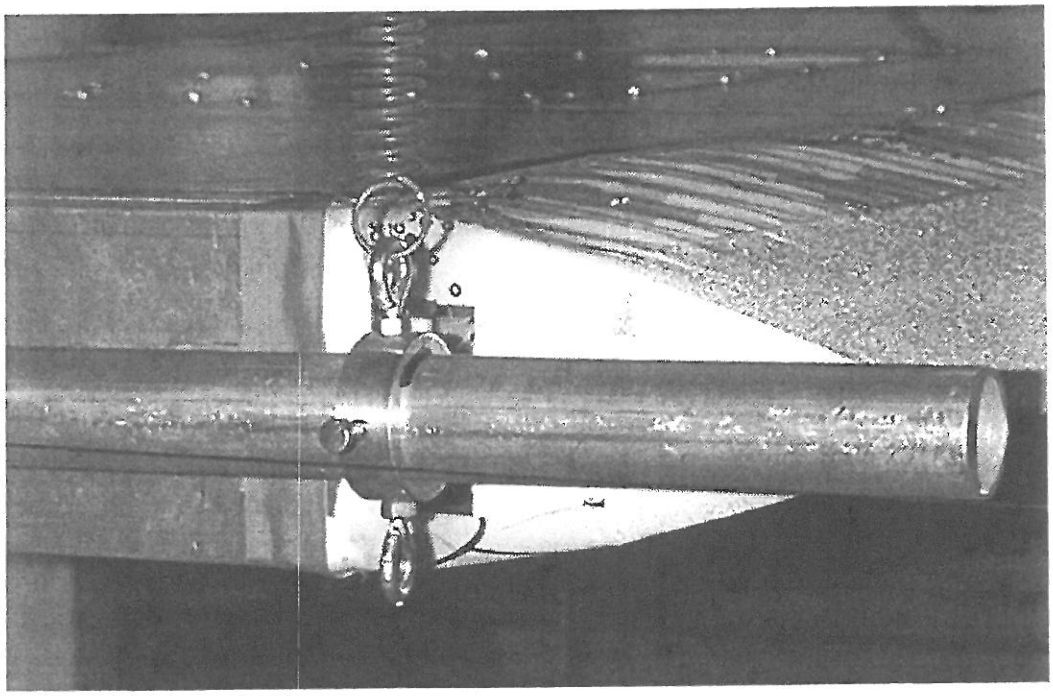

Figure 5.8: Hole between flap and model covered by two types of fabric.

During the experiments long wires are fixed to the wind tunnel to prevent movement in the wind direction. Four HBM load cells type Z8 with the nominal mass 10 kg are used

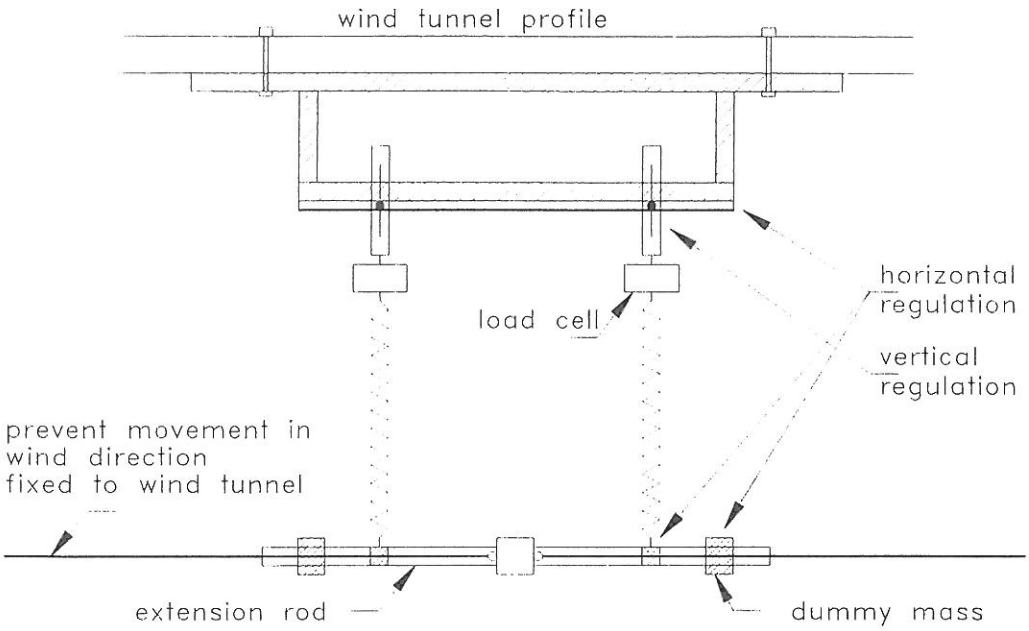

Figure 5.9: Simplified suspension system.

to measure the motion of the model.

The spring constant k for each suspension point is adjusted so the two-dimensional model has the same eigenfrequency as the lowest symmetric bending eigenmode of the real bridge, depending on the model laws. The torsional eigenfrequency can be adjusted by moving the springs horizontally. The ordered stiffness of each of the four helical springs is $k = 165\ ^{\mathrm{N}}/_{\mathrm{m}}$, see appendix E.3. The damping of the model is not justified in the experiments. Additional damping can be made by letting a vane at each support plane shear through silicone oil as described by Hjorth-Hansen [20].

5.6 Regulation System

The regulation system to move the flaps consists of three parts:

1. A servo system, see section 5.6.1.

2. Regulation software to position the flaps in the desired positions, see section 5.6.2.

3. Control software to calculate the desired positions of the flaps, the control algorithm used is described in the test programme in section 6.2.

The general layout of the regulation system for one flap is shown in figure 5.10. The control software is linked to the regulation software.

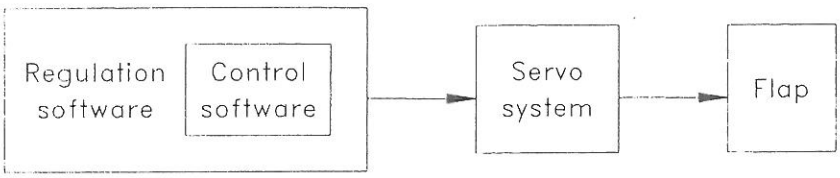

Figure 5.10: General layout of regulation system for one flap.

5.6.1 Servo System

The following servo system is recommended by Sven Hvid Nielsen, associate professor at the *Department of Production* at *Aalborg University*. A servo system consists of a servo amplifier, a servo motor and a reduction gear. Two servo systems are necessary as the flaps are regulated independently.

Specifications for the recommended servo amplifier, servo motor and reduction gear are shown in appendix E.4. The reduction gears and servo motors are fixed inside the bridge section model, see figure 5.11. Each reduction gear is connected to a flap via cables, see figure 5.12. Each servo motor is connected to a servo amplifier, which is placed outside the model.

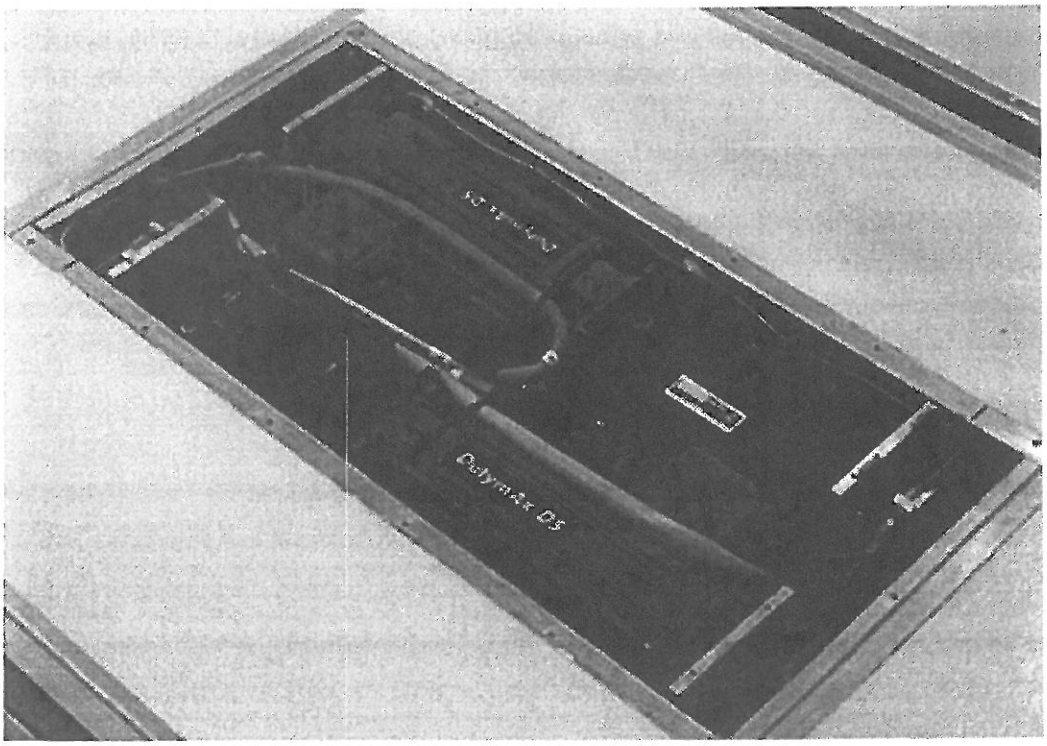

Figure 5.11: Servo system fixed inside model.

The servo amplifiers and a filter box are shown in figure 5.13.

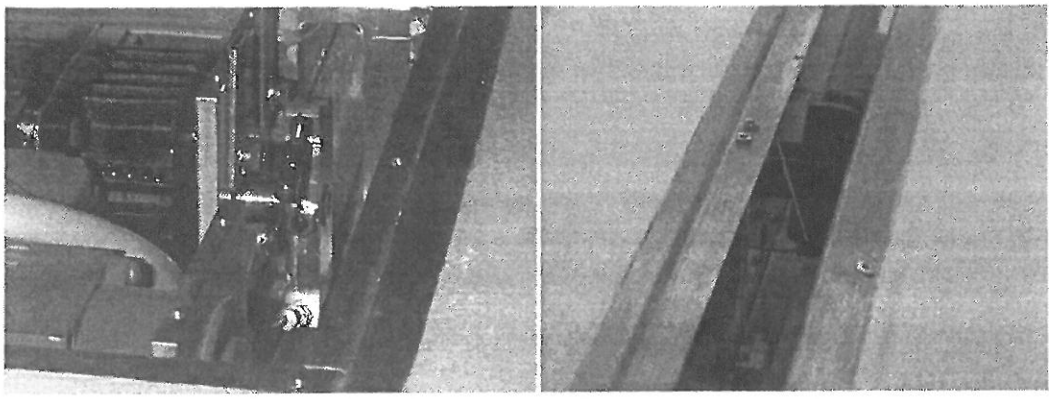

Figure 5.12: Cables to move to the flaps. At the left hand side the connection between the reduction gear and the cables is shown. At right hand side the connection between the cables and the flap is shown.

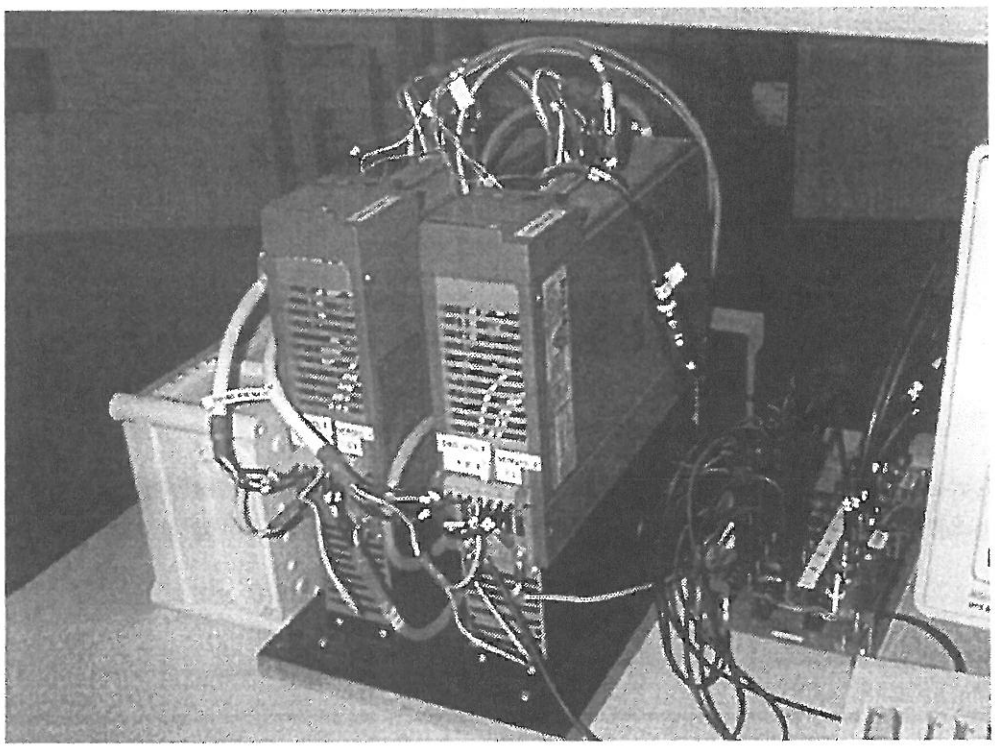

Figure 5.13: Servo amplifiers and filter box.

5.6.2 Regulation Software

The regulation software to position the flaps in the desired positions has been designed and implemented by Søren Rønnest and Lars Jakobsen (in 1995 students of the 9th semester

at the *Institute of Electronic Systems* at *Aalborg University* based on the servo system described in secion 5.6.1. The position regulator for one flap is illustrated in figure 5.14.

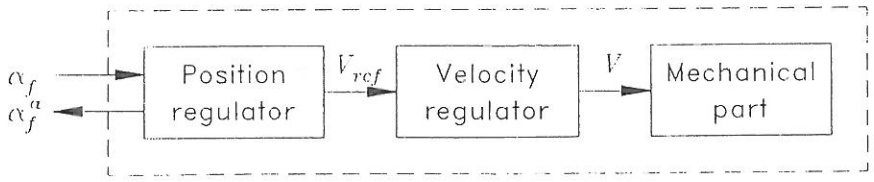

Figure 5.14: Illustration of position regulator for regulation of one flap.

In figure 5.14 the mechanical part consists of a servo motor, a reduction gear and a flap. The velocity regulator is a PID-regulator in the servo amplifier. The position regulator is basically also a PID-regulator implemented by Søren Rønnest and Lars Jakobsen in a program called SERVOREG. Further, in figure 5.14, the following notation is used

α_f is the desired position of the flap as calculated by the control software.

α_f^a is the actual position of the flap, this position is used to learn about the behaviour of the regulation system.

V_{ref} is the reference velocity calculated by the position regulator.

V is the velocity send to the servo motor.

The flaps can be positioned in the horizontal positions by using the keyboard on the computer or a manual box as shown in figure 5.15. During the experiments the flaps can only be regulated by the regulation and control software, i.e. the keyboard and manual box cannot be used.

If the flaps are turning too much with the risk of damaging the model then power to the motors is cut off by micro switches placed at the top and bottom of the model, see figure 5.16.

A lot of problems could have been avoided if the servo amplifiers had been position regulators instead of the recommended velocity regulators. Further, there were a lot of problems because of noise in the regulation system and an fundamental error on a counter card in the PC that caused random pauses of the software. All these problems caused about one year's delay of the regulation system and a lot of time was spent testing the different versions of the system.

The regulation software SERVOREG uses a kernel which switches between several processes (calculation of the desired positions of the flaps, position regulator, menu, storing results in a file and text on the screen). The flap positions are regulated by the software to fit the specified values at an interval of 6 ms.

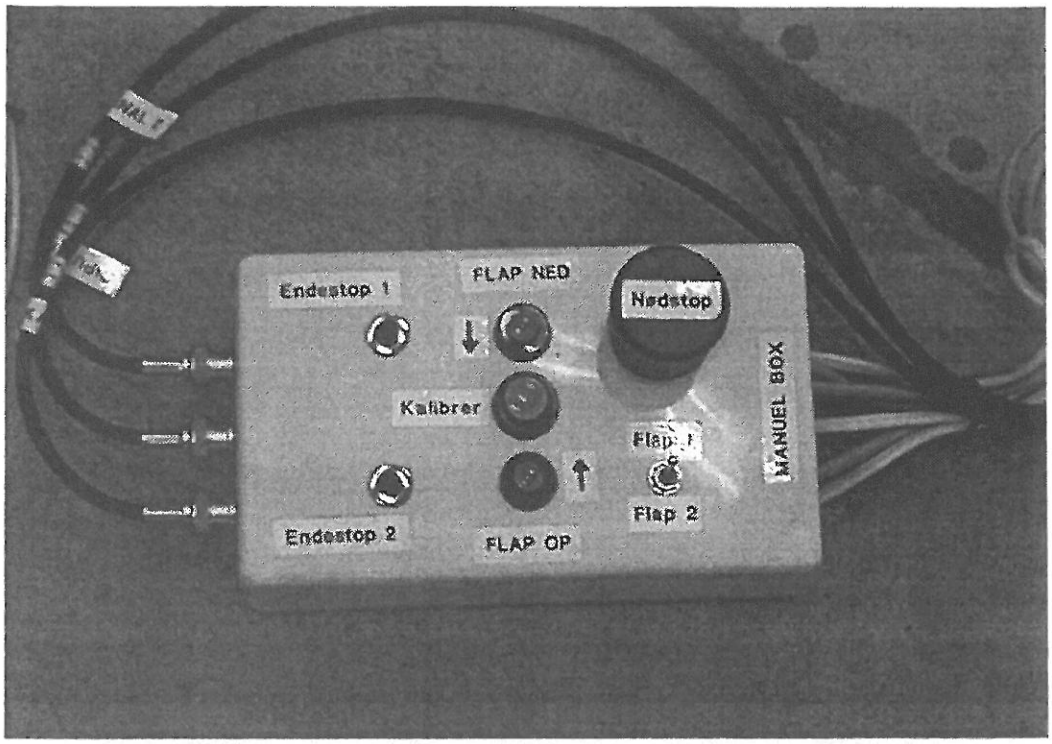

Figure 5.15: Manual box with buttons to regulate the flaps.

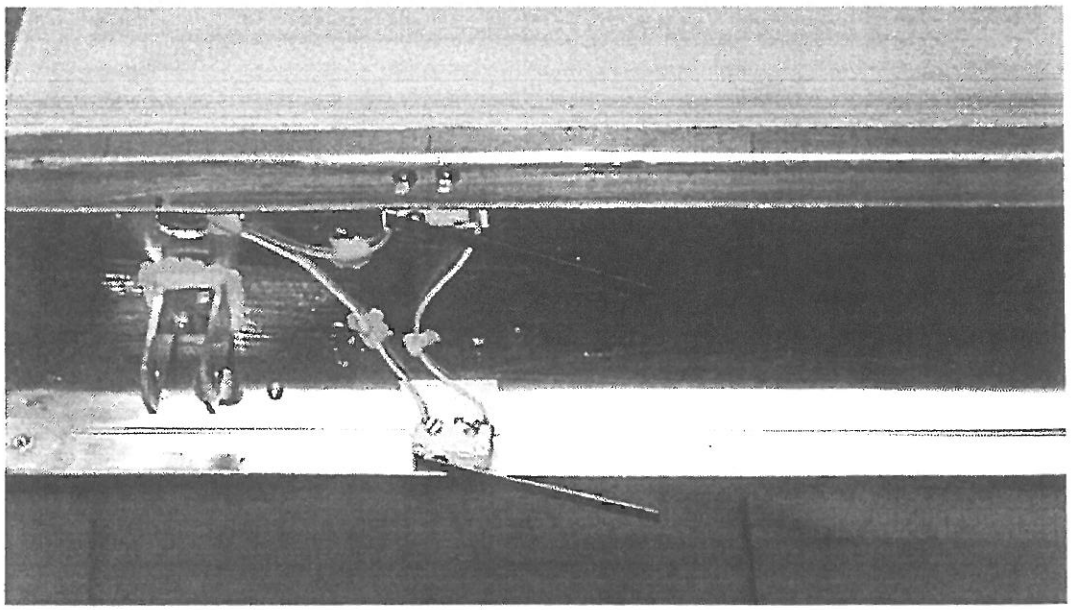

Figure 5.16: Micro switches to prevent damaging of the model.

5.7 Special Details during Set Up

The part of the regulation system placed inside the model requires power, and therefore there are wires inside the model too. Some of these wires are relatively stiff. Of practical

reasons the wires are guided through only one end of the model. To prevent these wires from dominating the motion of the model they are suspended by springs connected to the wind tunnel so they are almost horizontal when they leave the model, see figure 5.17.

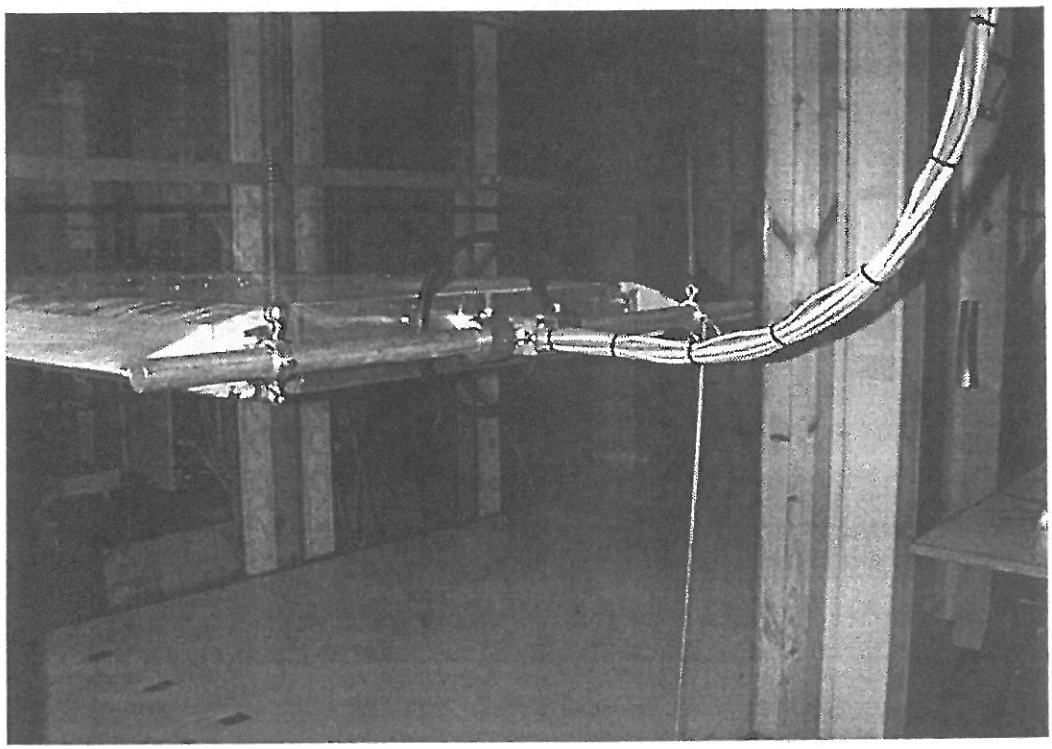

Figure 5.17: Wires from servo motors inside model.

As seen in figure 5.17, there is a string going downwards from one side of the extension rod. Another string is connected to the other extension rod. These strings are used to make a 'standard' initial motion of the model as described in chapter 6.

5.8 Concluding Remarks

In this chapter the wind tunnel, bridge section model, suspension system, regulation system and purpose of the experiments are described. A realistic (not specific) model is dimensioned to fit in the wind tunnel. The suspension system is made very flexible so it can be regulated both horizontally and vertically. There has been a lot of problems with the regulation system, but after approximately one year of delay (including a lot of tests) the regulation system was ready for the experiments. Still, the regulation system is far from being perfect and it caused a lot of problems during the experiments. The result was that only a small part of the planned experiments could be performed, as described in chapter 6.

Chapter 6

Wind Tunnel Experiments

6.1 Introduction

The purpose of the wind tunnel experiments with the bridge section model is to investigate how the damping of the model is dependent on the flap configuration for increasing wind velocities. These results are compared with the theoretical results for a flat plate by using the Air Material Command (AMC) method described in section 2.4.

During the preparations of the wind tunnel experiments in Lisbon there were some unanticipated problems:

- Noisy measurements of the displacements from the load cells. This noise comes from the servo motors and it was also present in Aalborg, but then it was possible to reduce it to an acceptable level by grounding of the components and by using an extension rod. Further, there is noise due to vibrations of the frame on the wind tunnel where the suspension system is connected. These vibrations are observed during experiments with wind.

- Standing waves in the springs when the flaps are regulated.

- Static divergence of the model.

The noisy measurements are in the experiments dealt with by decreasing the value of P in the PID-regulator in the regulation software, see section 5.6.2, whereby the servo motors react very slowly and are not so sensible to noise. By using a P-value of 7 it is possible to position the flaps with a phase angle of approximately $\pm\pi/2$ compared to the desired values.

The test programme used during the experiments is described in section 6.2. Examples of results of damping experiments are shown in section 6.3 and estimation of parameters is described in section 6.4. Because of the problems during the experiments as mentioned above, further experiments were planned as described in section 6.5. The results of the wind tunnel experiments are compared with the flat plate approximation in chapter 7.

6.2 Test Programme

In the experiments the following control algorithm is used to calculate the desired angles $\alpha_t(t)$ and $\alpha_l(t)$ of the trailing and leading flap:

$$\left.\begin{aligned} \alpha_t(t) &= a_t\alpha(t) \\ \alpha_l(t) &= -a_l\alpha(t) \end{aligned}\right\} \tag{6.1}$$

where $\alpha(t)$ is the torsional angle of the model at the time t, a_t and a_l are amplitude amplification factors for the trailing and leading flap, respectively.

The flaps are started slowly by multiplying the desired positions by a factor t/T_0 when $t < T_0$. The time for slow start is selected equal to $T_0 = 1$ s.

The following experiments are performed:

- The flaps are not regulated, flap configuration 0: $a_t \equiv a_l \equiv 0$.
  - Free vibration (vertical motion, torsional motion, both vertical and torsional motion).
  - Both vertical and torsional motion with the following wind speeds: 2.5 m/s, 4.0 m/s, 5.9 m/s, 7.1 m/s, 7.5 m/s and 8.2 m/s.
- Both flaps are regulated, flap configuration 1: $a_t = -6$ and $a_l = 6$.
  - Free vibration (torsional motion, both vertical and torsional motion).
  - Both vertical and torsional motion with the following wind speeds: 2.5 m/s, 4.0 m/s, 5.9 m/s, 7.1 m/s and 7.7 m/s.
- Both flaps are regulated, flap configuration 2: $a_t = -20$ and $a_l = 20$.
  - Free vibration (torsional motion, both vertical and torsional motion).
  - Both vertical and torsional motion with the following wind speeds: 2.8 m/s, 4.1 m/s and 6.1 m/s.
- Both flaps are regulated, flap configuration 3: $a_t = 6$ and $a_l = -6$.
  - Free vibration (torsional motion, both vertical and torsional motion).
  - Both vertical and torsional motion with the following wind speeds: 2.5 m/s, 4.0 m/s, 5.9 m/s and 7.1 m/s.
- Both flaps are regulated, flap configuration 4: $a_t = 20$ and $a_l = -20$.
  - Both vertical and torsional motion with the following wind speeds: 2.8 m/s, 4.2 m/s and 6.1 m/s.

For the above-mentioned experiments the distance between the springs is 704 mm and the distance between the loads on the horizontal arms is 150 mm.

All experiments are repeated 3–5 times. A damping experiment follows the following procedure:

1. Justification of wind velocity.
2. The model is given a 'standardized' initial displacement by pulling a rope that is connected to the horizontal arms of the model.
3. Start of the program that measures the position of the model every 12 milliseconds.
4. The flaps are started slowly at the first upcrossing of the torsional motion with the desired flap configuration. The actual positions of the flaps are measured and new values are specified every 12 milliseconds.
5. The results are stored and used to estimate the damping of the model from the free vibration following the initial displacement.

During a damping experiment the following parameters are stored every 12 milliseconds:

- t: time in milliseconds.
- z: the vertical displacement in metres.
- α: the angle of torsion in degrees.
- α_t: the specified angle of trailing flap in degrees.
- α_l: the specified angle of leading flap in degrees.
- α_{ta}: the actual angle of trailing flap in degrees.
- α_{la}: the actual angle of leading flap in degrees.

A list of all damping experiments is shown in appendix F.1. For each type of experiment the vertical motion, the torsional motion and the flap positions are shown in appendix F.2.

6.3 Examples of Damping Experiments

In this section the torsional motion is shown as a function of time for wind speed 6.1 $^{m}/_{s}$ and flap configurations 0, 2 and 4.

Figure 6.1 shows the torsional motion when the flaps are not regulated. The measurements are very noisy. During the first period the amplitude of the torsional motion is reduced from 2.6° to 2.4°, i.e. 8%. Figure 6.2 shows that flap configuration 2 is very efficient to control the torsional motion of the model. Even though the flaps are started slowly during the first second the amplitude of the torsional motion is reduced from 2.7° to 1.1°, i.e. 62%. Figure 6.3 shows the actual positions for the trailing flap for the example in figure 6.2. The flap movement is smooth because of the very slow regulation. Figure 6.4

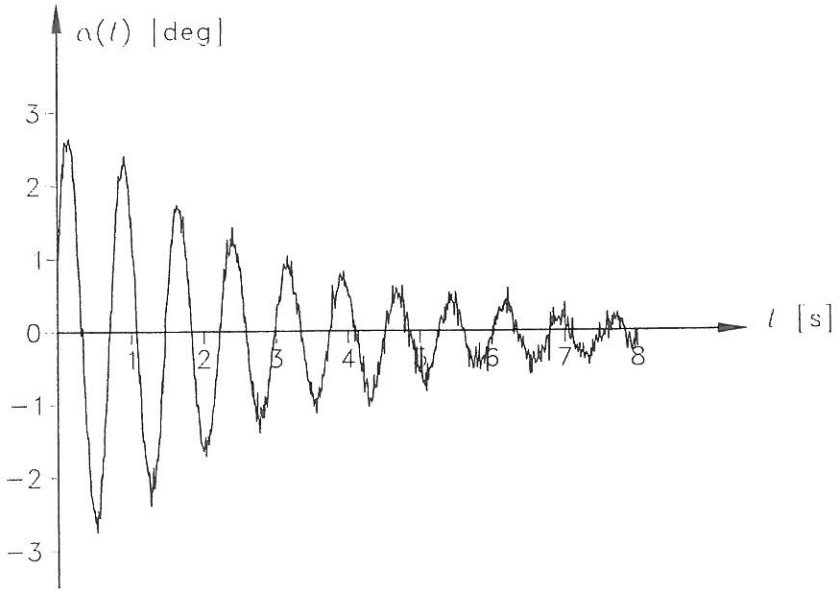

Figure 6.1: Example of torsional motion for flap configuration 0 and with wind speed 6.1 m/s.

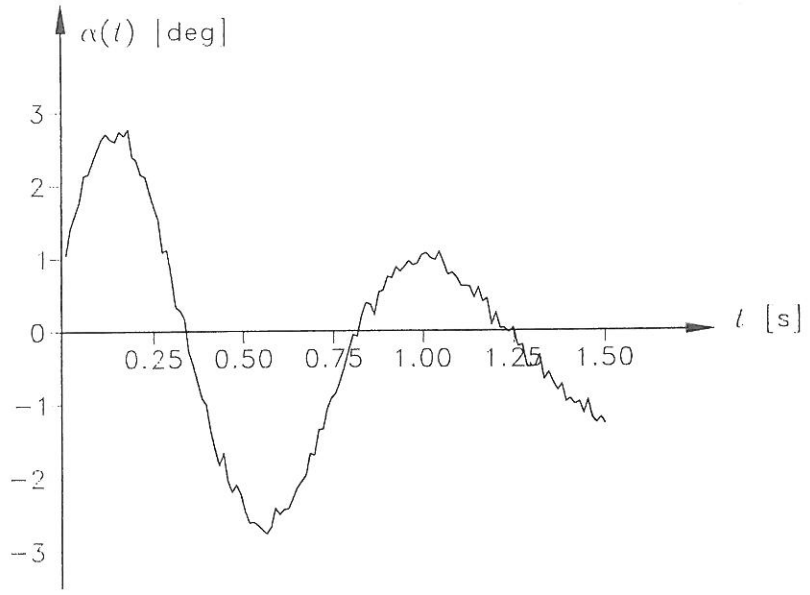

Figure 6.2: Example of torsional motion for flap configuration 2 and with wind speed 6.1 m/s.

shows that the angular motion is growing, i.e. there is flutter, when flap configuration 4 is used.

This example shows that moving the flaps in the right way can reduce the oscillations considerably. Flap configuration 2 shows very good results even though it might not be the optimal configuration. Further, this example shows that it is possible to make the flap configuration very unfavourable so that the model makes flutter at a rather low wind

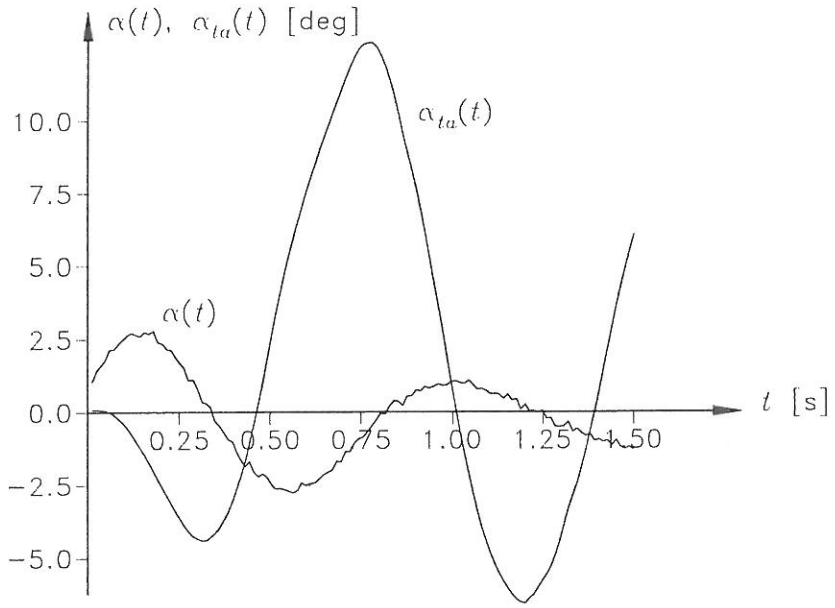

Figure 6.3: Example of torsional motion and actual flap positions for the trailing flap for flap configuration 2 and with wind speed 6.1 m/s.

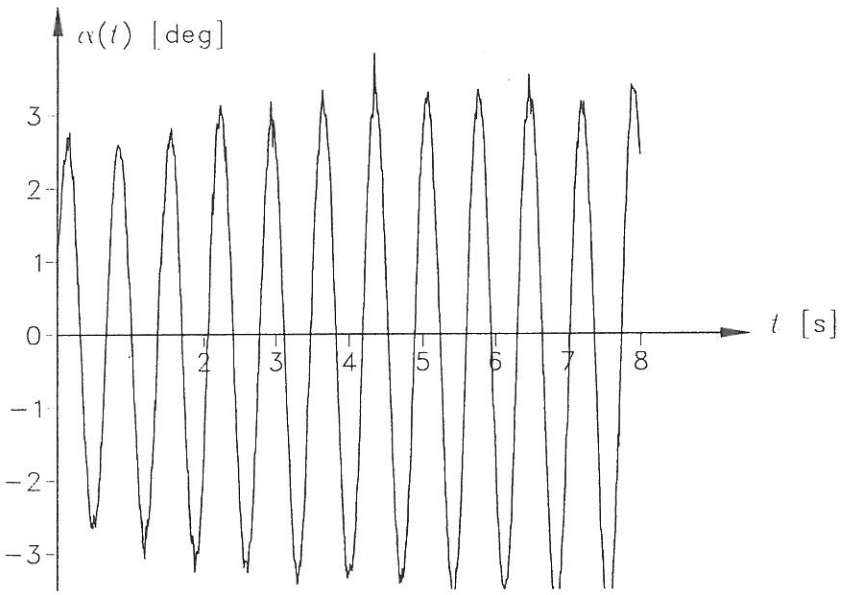

Figure 6.4: Example of torsional motion for flap configuration 4 and with wind speed 6.1 m/s.

speed.

6.4 Estimation of Parameters

The following parameters are estimated based on the experiments:

- ω_z and ω_α: the circular frequencies for the vertical and torsional motion, respectively. The circular frequencies are estimated by counting a number of cycles for the time series $z(t)$ and $\alpha(t)$.
- ζ_α: the damping ratio for the torsional motion. The damping is estimated by using Hilbert transformation.
- a_{ta} and a_{la}: the actual amplitude amplification factors between the angular motion of the model and the actual positions of the flaps. These factors are estimated by optimization.
- φ_{ta} and φ_{la}: the phase angles between the angular motion of the model and the actual positions of the flaps. These factors are estimated by optimization.

As described, the measured postions $z(t)$, $\alpha(t)$, $\alpha_{ta}(t)$ and $\alpha_{la}(t)$ are noisy, and therefore they are filtered. The filtered positions $z_f(t)$, $\alpha_f(t)$, $\alpha_{ta,f}(t)$ and $\alpha_{la,f}(t)$ are then used to estimate the above-mentioned parameters. The methods used to filter the positions and estimate the parameters are described in appendix G.

6.4.1 Estimated Frequencies

In figure 6.5 the circular frequencies for the vertical motion without wind are shown based on the estimated values in appendix G.3. The estimated frequencies are rather constant independently of the flap configuration and the main motion. The mean value of the circular frequency for the vertical motion is 5.2 $^{\text{rad}}/_{\text{S}}$.

The circular frequency for the vertical motion can be estimated without wind. When the wind is blowing the vertical motion becomes rather irregular until it is possible to estimate it again. The frequencies based on the estimated values in appendix G.3 are shown in figure 6.6. With increasing wind velocity the circular frequency for the vertical motion is reduced. It is not possible to estimate the circular frequency for the vertical motion when flap configuration 2 is used.

In figure 6.7 the circular frequencies for the torsional motion without wind are shown based on the estimated values in appendix G.3. As for the vertical motion, the estimated frequencies are rather constant independently of the flap configuration and the main motion. But there is a small tendency towards larger deviation of the results the more the flaps are moved. Note that flap configurations 1 and 3 specify small movement of the flaps. The mean value of the circular frequency for the torsional motion is 10.1 $^{\text{rad}}/_{\text{S}}$.

The circular frequencies for the torsional motion used to estimate the damping of the motion are shown in figure 6.8. Again, with increasing wind velocity the circular frequency for the torsional motion is reduced dependent on the flap configuration used.

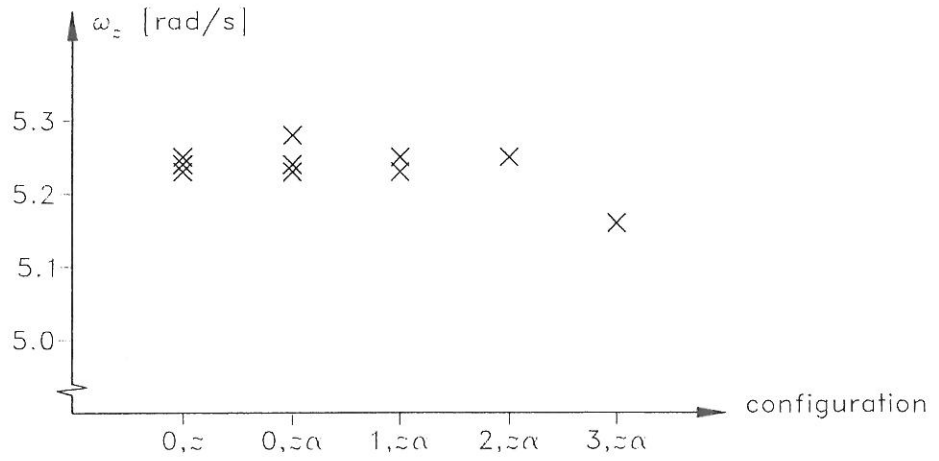

Figure 6.5: Estimated circular frequency for vertical motion without wind. The configuration is described by the flap configuration and the main motion, i.e. zα denotes a combined motion.

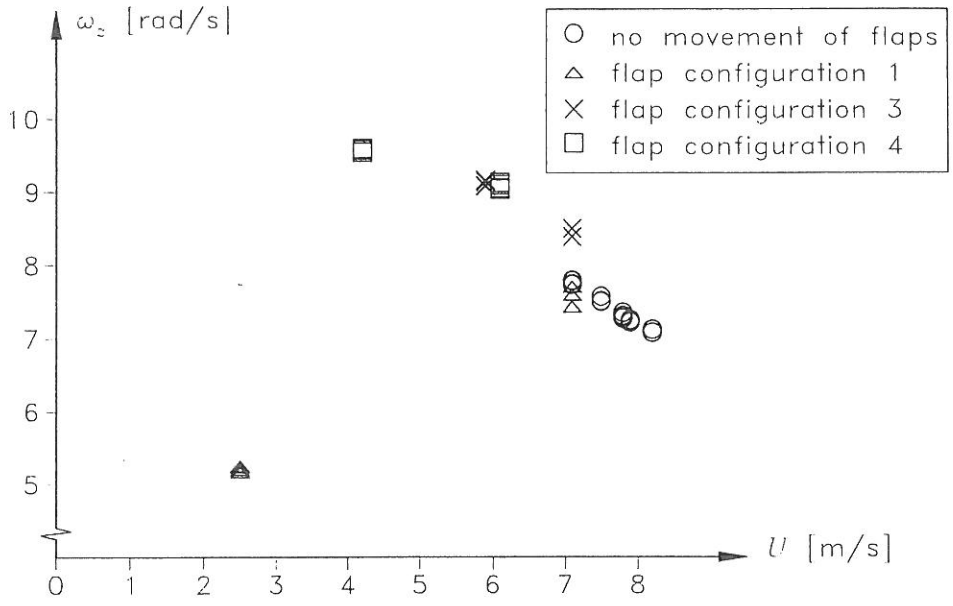

Figure 6.6: Estimated circular frequency for vertical motion with wind.

6.4.2 Estimated Damping Ratios

In figure 6.9 the damping ratios for the torsional motion without wind are shown based on the estimated values in appendix G.3. The estimated damping ratios are rather constant independently of the flap configuration and the main motion. But when the flaps are moved the damping ratio is larger for the main torsional motion than for the combined motion. Further, the more the flaps are turned the larger the damping ratio. The mean value of the damping ratio for the torsional motion is 0.008.

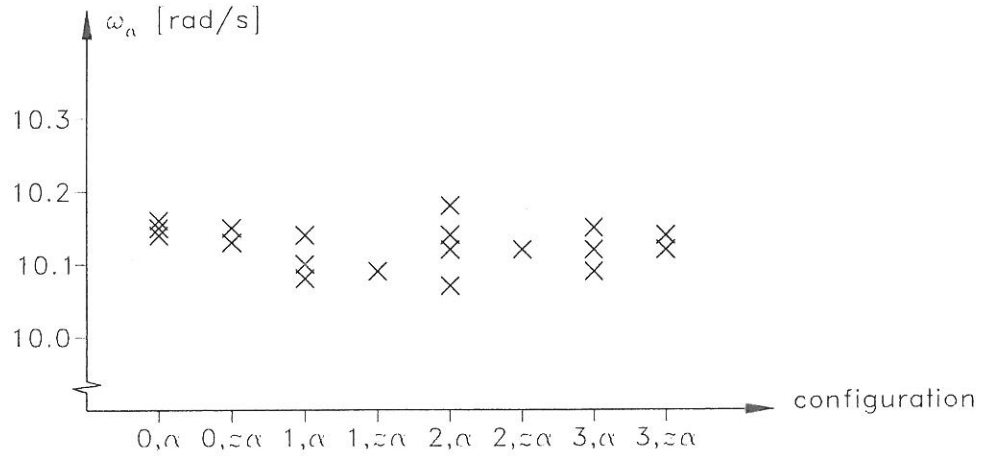

Figure 6.7: Estimated circular frequency for torsional motion without wind. The configuration is described by the flap configuration and the main motion, i.e. zα denotes a combined motion.

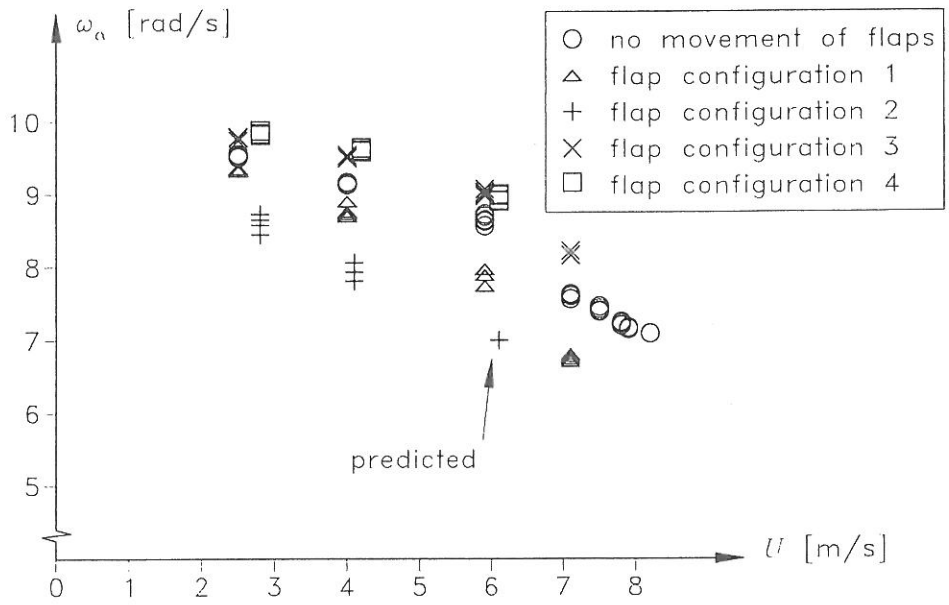

Figure 6.8: Estimated circular frequency for torsional motion with wind. For the wind speed 6.1 m/s the motion is damped very fast when flap configuration 2 is used. The frequency for this wind speed and flap configuration is therefore predicted based on the estimated values for other wind speeds and flap configurations.

The damping ratio for the torsional motion for different flap configurations is shown as a function of the wind speed in figure 6.10. When flap configurations 1 and especially 2 are used the damping ratio is increased considerably, and when flap configurations 3 and 4 are used the damping ratio is decreased.

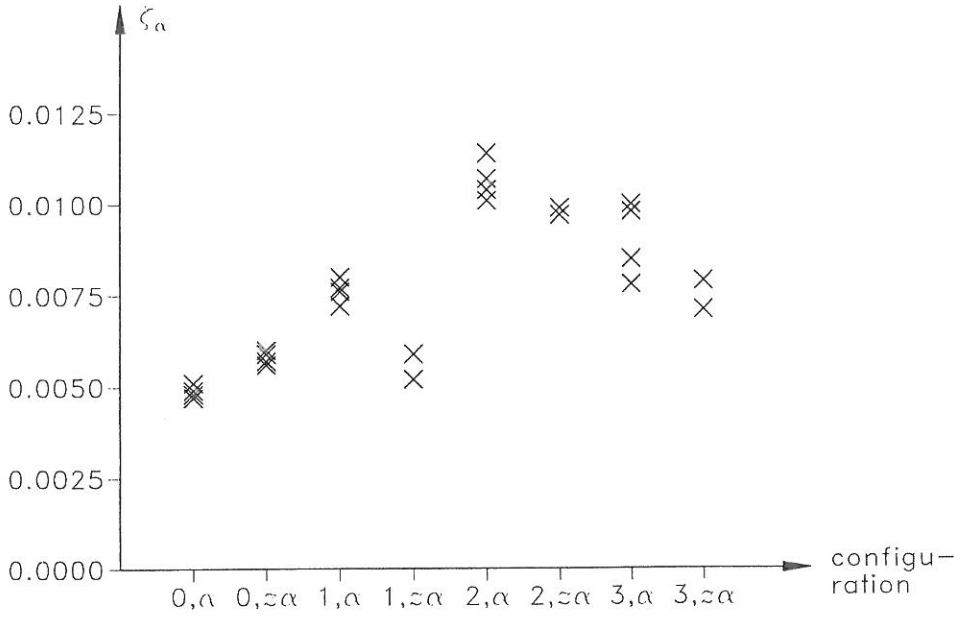

Figure 6.9: Estimated damping ratio for torsional motion without wind. The configuration is described by the flap configuration and the main motion, i.e. zα denotes a combined motion.

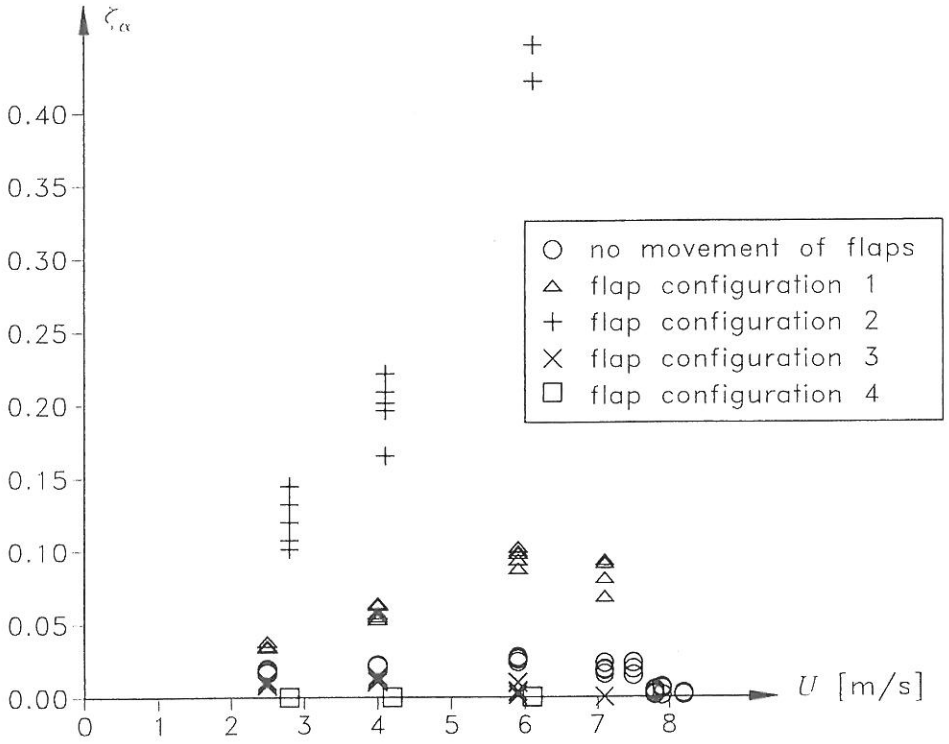

Figure 6.10: Estimated damping ratio for torsional motion with wind.

6.4.3 Estimated Amplifications and Phases

The torsional motion can be described by

$$\alpha(t) = A_\alpha(t)\cos(\omega'_\alpha t) \tag{6.2}$$

where $A_\alpha(t)$ is the amplitude of the envelope curve for the torsional motion and ω'_α is the circular eigenfrequency for the damped torsional motion.

The actual flap position for e.g. the trailing flap can be described by

$$\alpha_{ta}(t) = a_{ta}A_\alpha(t)\cos(\omega'_\alpha t - \varphi_{ta}) \tag{6.3}$$

where a_{ta} is the amplification factor and φ_{ta} is the phase angle for the trailing flap. The phase angle is equal to the damped circular frequency multiplied by the delay of the flap compared to the torsional motion, i.e. $\varphi_{ta} = \omega'_\alpha \Delta t_t$. In the same way the actual flap position for the leading flap can be described by the amplification factor a_{la} and the phase angle φ_{la}.

$$\alpha_{la}(t) = a_{la}A_\alpha(t)\cos(\omega'_\alpha t - \varphi_{la}) \tag{6.4}$$

where $\varphi_{la} = \omega'_\alpha \Delta t_l$. The amplifications a_{ta} and a_{la} and the phase angles φ_{ta} and φ_{la} are estimated for each flap configuration as described in appendix G.4. The mean values are shown in table 6.1.

Flap configuration	Amplification		Phase angles	
	a_{ta}	a_{la}	φ_{ta} [rad]	φ_{la} [rad]
0	0	0	—	—
1	1.9	2.0	4.5	4.5
2	3.4	3.6	4.6	4.6
3	2.0	2.0	1.5	1.5
4	*3.4* *	*3.6* *	*1.5* *	*1.5* *

*Table 6.1: Estimated amplification factors and phase angles. * For flap configuration 4 the parameters are predicted based on the results for other flap configurations.*

As seen in table 6.1 the trailing and leading flaps are moving with the same delay compared to the torsional motion. Note that the phase angles are equal because the angles of both flaps are positive downwards. Further, the amplitudes of the leading flap are slightly bigger than the amplitudes of the trailing flap. As expected the flap amplication factors are almost the same for flap configurations 1 and 3 and the phase angles are almost the same for flap configurations 1 and 2. Finally, as aspected the difference between the phase angles for flap configurations 1 and 3 is approximately equal to π.

6.5 Further Experiments

As described in section 6.1 there were some unanticipated problems during the experiments, therefore new experiments were planned.

A major problem is the noise of the position measurements from the load cells from the servo motors and vibrations of the wind tunnel frame. The noise problems can be eliminated by using a second-order filter with pole 0.5 as described in appendix G.2. Thereby a minor amplitude reduction and phase angle is introduced, as shown in figure G.1. This is not any problem, however, as these factors can be taken into account in the control algorithm. By using the filter when the desired flap positions are calculated the flaps can be moved faster, i.e. the P-value in the PID-regulator is increased.

Another problem is that the divergence wind velocity is too small for the model. All focus was on the flutter problem as flutter is usually a greater problem for suspension bridges than divergence. It was therefore an error not to check the divergence wind velocity for the model before the experiments. The divergence and flutter velocities are calculated in appendix G.5 based on the estimated parameters from the experiments. The divergence velocity is 8.5 $^{m}/_{s}$ and the flutter velocity is 8.7 $^{m}/_{s}$. Thereby it is not possible to perform experiments with wind speeds above the flutter wind velocity. This problem is eliminated by regulating the positions of the springs and loads of the suspension system and to use stiffer springs so the divergence and flutter wind velocities are separated. By using the regulated parameters and stiffer springs the divergence wind velocity is 12.1 $^{m}/_{s}$ and the flutter wind velocity is 10.0 $^{m}/_{s}$.

Stiffer springs will also have another eigenfrequency with regard to the standing waves, so this problem is also solved. The divergence and flutter wind velocities are estimated in appendix G.5 for both existing and new springs.

As described in chapter 7, it is not optimal to move the flaps using the same phase angle as in the described wind tunnel experiments. In the next experiments it is therefore the intention to move first one flap and then the other flap with different amplification factors and phase angles. Finally, the optimal flap configuration can be found by experiments with combinations of the optimal amplifications and phase angles.

The following control algorithm is used

$$\left.\begin{aligned} \alpha_t(t) &= a_t\alpha(t)\left\{\cos(-\varphi_\Delta-\varphi_t)-\tan(\omega'_\alpha t-{}^{\pi}/_{2})\sin(-\varphi_\Delta-\varphi_t)\right\} \\ \alpha_l(t) &= -a_l\alpha(t)\left\{\cos(-\varphi_\Delta-\varphi_l)-\tan(\omega'_\alpha t-{}^{\pi}/_{2})\sin(-\varphi_\Delta-\varphi_l)\right\} \end{aligned}\right\} \tag{6.5}$$

where a_t and a_l are the flap amplication factors. φ_Δ is the delay of the flap, i.e. the time to move the flaps in the desired positions. Note that this delay is independent of the angle the flap is turned. φ_t and φ_l are the desired phase angles between the torsional motion and the flaps. The algorithm is derived in appendix G.6.

The control algorithm in equation (6.5) gives numerical problems because the desired angles of the flaps can have maximum when the torsional angle of the bridge section

model is zero. Theoretically, this should not give any problems as shown in appendix G.7, but anyway there are numerical problems.

Another problem when using the control algorithm in equation (6.5) is that the damped circular torsional frequency must be known. This is really a problem as the frequency is both dependent on the wind speed and the flap configuration, as shown in figure 6.8. Different solutions were applied but none of them was working well. Anyway, it was possible from the experiments to see if the phase angle used was favourable or unfavourable to control the motion. In the following the factors f_l and f_t are used to describe the flap configurations.

$$\varphi_l = f_l \frac{\pi}{6} \tag{6.6}$$

$$\varphi_t = f_t \frac{\pi}{6} \tag{6.7}$$

As seen in table 6.2, the favourable phase angles of the leading flap are for $f_l \in [9, 10, 11, 0]$. For the trailing flap the favourable phase angles are for $f_t \in [8, 9, 10]$, see table 6.3. These phase angles cannot directly be compared with the results in chapter 2 because of the changed bridge section model parameters. Further, it should be noted that the defined positive direction in this chapter for the leading flap is opposite to the defined positive direction in chapter 2.

U	f_l											
[m/s]	0	1	2	3	4	5	6	7	8	9	10	11
4.0	+	−	−	−	−	−	−	+	+	+	+	+
6.0	+	+	−	−	−	−	−	−	−	+	+	+
8.0	+	−	−	−	−	−	−	−	+	+	+	+
9.0	+	+	+	−	−	−	−	−	−	+	+	+

Table 6.2: Favourable (+) and unfavourable (−) phase angles when only the leading flap is used.

U	f_t											
[m/s]	0	1	2	3	4	5	6	7	8	9	10	11
4.0	−	−	−	−	−	−	+	+	+	+	+	+
6.0	−	−	−	−	−	−	+	+	+	+	+	+
8.0	−	−	−	−	−	−	−	+	+	+	+	−
9.0	−	−	−	−	−	−	−	−	+	+	+	−

Table 6.3: Favourable (+) and unfavourable (−) phase angles when only the trailing flap is used.

Unfortunately, the problems with the control algorithm made it impossible to train a neural network with data from the experiments to model the motion of the section model

for different flap positions.

6.6 Concluding Remarks

In this section the wind tunnel experiments are described. Experiments are performed with the model without moving the flaps, and two favourable and two unfavourable flap configurations are examined. The experiments show that both the circular frequencies of the vertical and torsional motion and the damping ratio of the torsional motion are dependent on the wind speed and the flap configuration. When using favourable flap configurations the damping ratio is increased considerably even though the delay of the flaps in the experiments compared to the torsional motion might not be optimal. The experiments also show that it is possible to make the flap configuration very unfavourable so the model makes flutter at a rather low wind speed.

There were several problems during the experiments that recommended further experiments, e.g. that the effectiveness of the flaps could not be shown for wind speeds above the flutter wind speed. During these further experiments, new problems were introduced. Based on the experiments, however, it was possible to find favourable phase angles for the trailing flap and leading flap, separately.

Chapter 7

Experimental Results Compared with Theory

7.1 Introduction

In this chapter the estimated parameters from the wind tunnel experiments described in chapter 6 are compared with the theoretical parameters by using the flat plate approximation described in chapter 2.

The flap configurations used in the wind tunnel experiments are shown in section 7.2. The wind dependent change of frequency and damping are compared with the theoretical values in sections 7.3 and 7.4. The optimal phase angles found in chapter 2 are in section 7.5 compared to the phase angles used during the experiments.

7.2 Flap Configurations

The positive directions of the vertical and torsional motions of the bridge section model and of flap positions are shown in figure 7.1. The positive directions are equal to the positive directions defined in chapter 2. In chapter 6 the angle of the leading flap is defined as positive downwards, e.g. opposite to the definition used in this chapter.

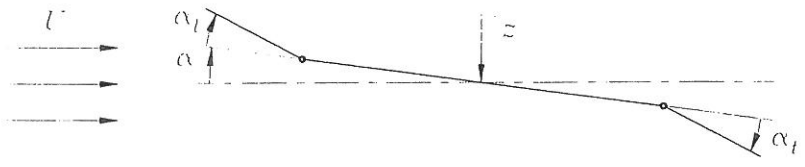

Figure 7.1: Definition of positive directions.

The positions of the flaps (with positive directions as shown in figure 7.1) at selected time instants for flap configurations 1–4 described in chapter 6 are shown in figures 7.2–7.5. When flap configuration 0 is used the flaps are not moved. Based on the torsional motion

$\alpha(t)$, the actual flap positions α_t and α_l are calculated by using equations (6.3) and (6.4) with the estimated parameters shown in table 6.1 for each of the flap configurations. At eight time steps during a period the angle of the model and flaps are shown in the upper part of figures 7.2–7.5.

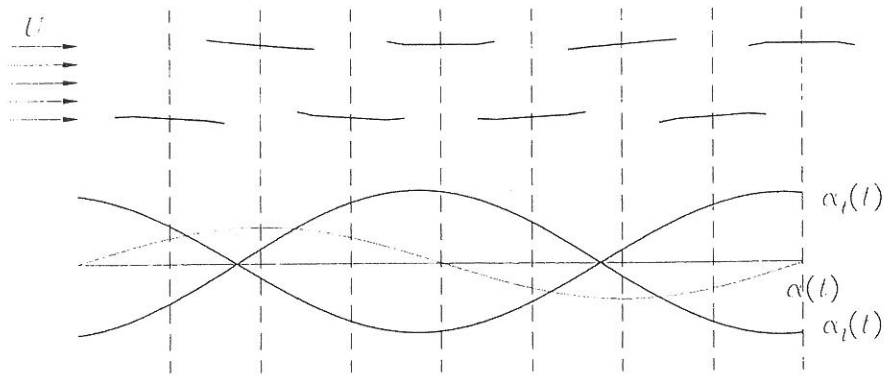

Figure 7.2: Movement of flaps for flap configuration 1.

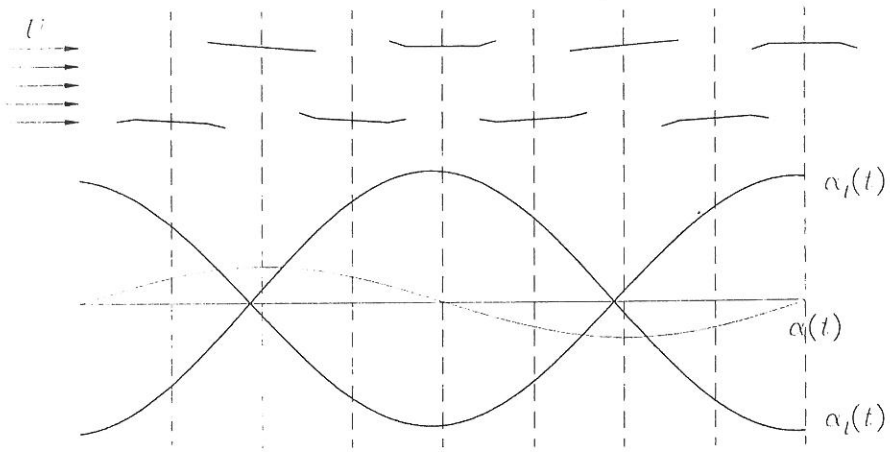

Figure 7.3: Movement of flaps for flap configuration 2.

For all flap configurations the flaps are near their horizontal positions when the angle of the torsional motion is maximum. Further, for all flap configurations the flaps are moved either up or down at the same time and the maximum angles of the flaps are when the model is approximately horizontal.

7.3 Wind Dependent Change of Frequency

In figure 6.6 the circular frequency for the vertical motion as a function of the wind velocity is shown based on the wind tunnel experiments. The stiffness of the bridge section model with flaps for a pure vertical motion is

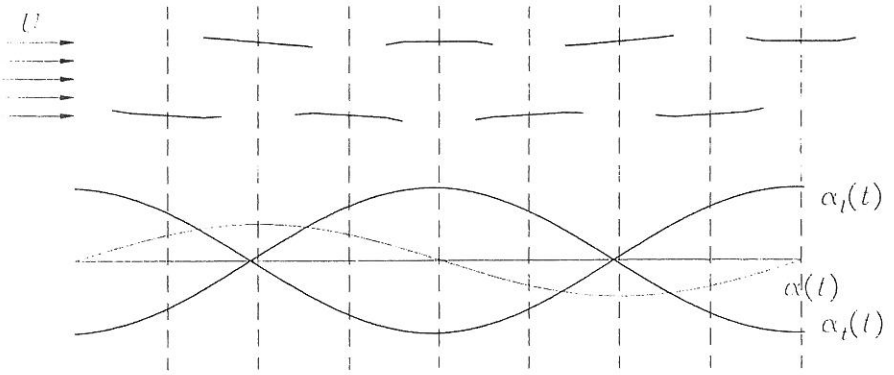

Figure 7.4: Movement of flaps for flap configuration 3.

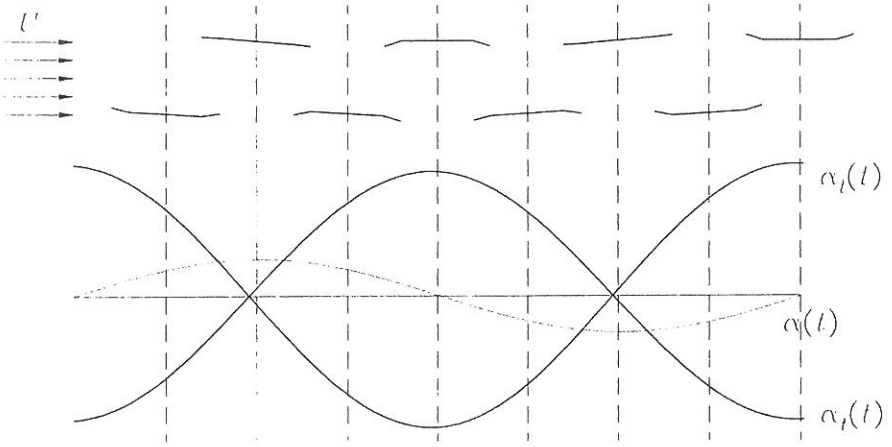

Figure 7.5: Movement of flaps for flap configuration 4.

$$k_{z,U} = m\omega_z^2 - \frac{1}{2}\rho U^2 K_{z,U}^2 H_4^\star(K_{z,U}) \tag{7.1}$$

with the notation used in appendix B.2 and

$$K_{z,U} = \frac{B\omega_{z,U}}{U} \tag{7.2}$$

where $\omega_{z,U}$ is the circular frequency of the vertical motion dependent on the wind velocity U. The wind dependent circular frequency of the vertical motion is

$$\omega_{z,U} = \omega_z \sqrt{1 - \frac{\rho B^2}{2m}\left(\frac{\omega_{z,U}}{\omega_z}\right)^2 H_4^\star\left(\frac{B\omega_{z,U}}{U}\right)} \tag{7.3}$$

According to Dyrbye & Hansen [9] the following approximation is quite accurate

$$\left(\frac{\omega_{z,U}}{\omega_z}\right)^2 H_4^\star\left(\frac{B\omega_{z,U}}{U}\right) \simeq H_4^\star\left(\frac{B\omega_z}{U}\right) \tag{7.4}$$

where ω_z is the circular eigenfrequency for the vertical motion, i.e. without wind. Equation (7.3) can thereby be written

$$\omega_{z,U} \simeq \omega_z \sqrt{1 - \frac{\rho B^2}{2m} H_4^\star\left(\frac{B\omega_z}{U}\right)} \tag{7.5}$$

Note, that the vertical frequency is independent of the flap configuration. The frequencies estimated based on the experimental data are compared to the theoretical frequencies by using Theodorsen's theory for a flat plate, see figure 7.6.

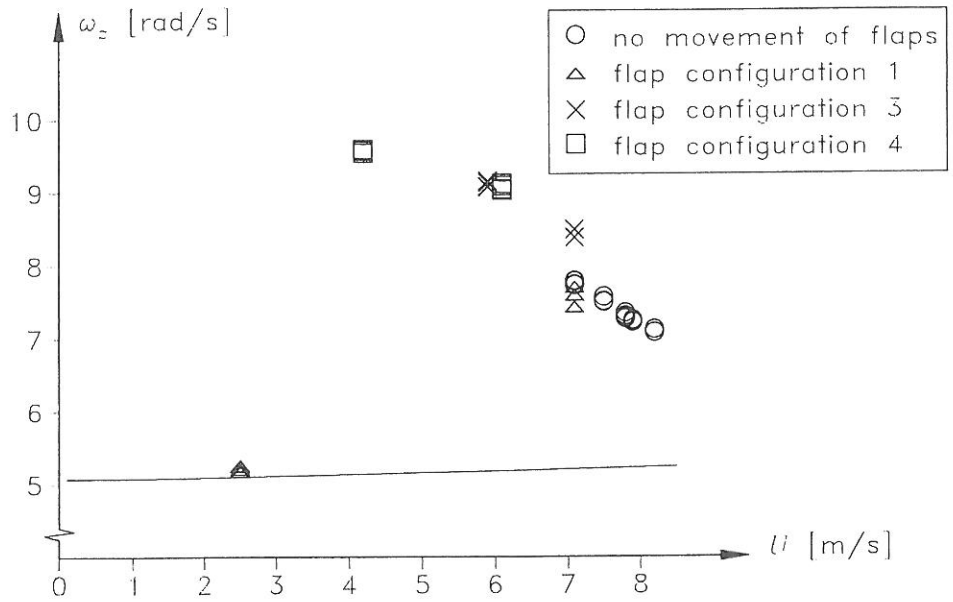

Figure 7.6: Theoretical and experimental circular frequency for vertical motion with wind.

As seen in figure 7.6, only the first values of the circular frequency for the vertical motion for flap configuration 1 are on the theoretical curve. However, the theoretical curve for pure vertical motion does not agree with the binary flutter theory either, since the flutter wind velocity for the bridge section model is $\omega_f = 6.62$ rad/s and the flutter wind velocity is $U_f = 8.18$ m/s, see section 2.3. This may be explained by the pure vertical motion assumption for equation (7.5) contrary to the combined vertical and torsional motion for binary flutter. Perhaps the results would fit better if a Fourier Analysis had been made. Also, for the experimental data the vertical frequency is independent of the flap configuration.

In figure 6.8 the circular frequency for the torsional motion as a function of the wind velocity is shown based on the wind tunnel experiments. The stiffness of the bridge section model with flaps for a pure torsional motion is

$$k_{\alpha,U} = I\omega_\alpha^2 - \frac{1}{2}\rho U^2 K_{\alpha,U}^2 B^2 A_3^{\star\prime}(K_{\alpha,U}) \tag{7.6}$$

with the notation used in appendix B.2 and

$$K_{\alpha,U} = \frac{B\omega_{\alpha,U}}{U} \tag{7.7}$$

where $\omega_{\alpha,U}$ is the circular frequency of the torsional motion dependent on the wind velocity U and

$$A_3^{\star\prime}(K) = A_3^{\star}(K) - A_5^{\star}(K)a_t \sin(-\varphi_t) + A_6^{\star}(K)a_t \cos(-\varphi_t) - A_7^{\star}(K)a_l \sin(-\varphi_l) + A_8^{\star}(K)a_l \cos(-\varphi_l) \tag{7.8}$$

The wind dependent circular frequency of the torsional motion is

$$\omega_{\alpha,U} = \omega_\alpha \sqrt{1 - \frac{\rho B^4}{2I}\left(\frac{\omega_{\alpha,U}}{\omega_\alpha}\right)^2 A_3^{\star\prime}\left(\frac{B\omega_{\alpha,U}}{U}\right)} \simeq \omega_\alpha \sqrt{1 - \frac{\rho B^4}{2I} A_3^{\star\prime}\left(\frac{B\omega_\alpha}{U}\right)} \tag{7.9}$$

where ω_α is the circular eigenfrequency for the torsional motion, i.e. without wind. Note that the torsional frequency is dependent on the flap configuration specified by the flap amplification factors a_t and a_l and the phase angles φ_t and φ_l. The frequencies estimated based on the experimental data are compared to the theoretical frequencies by using the aerodynamic derivatives for a flat plate for flap configurations 0–4, see figure 7.7.

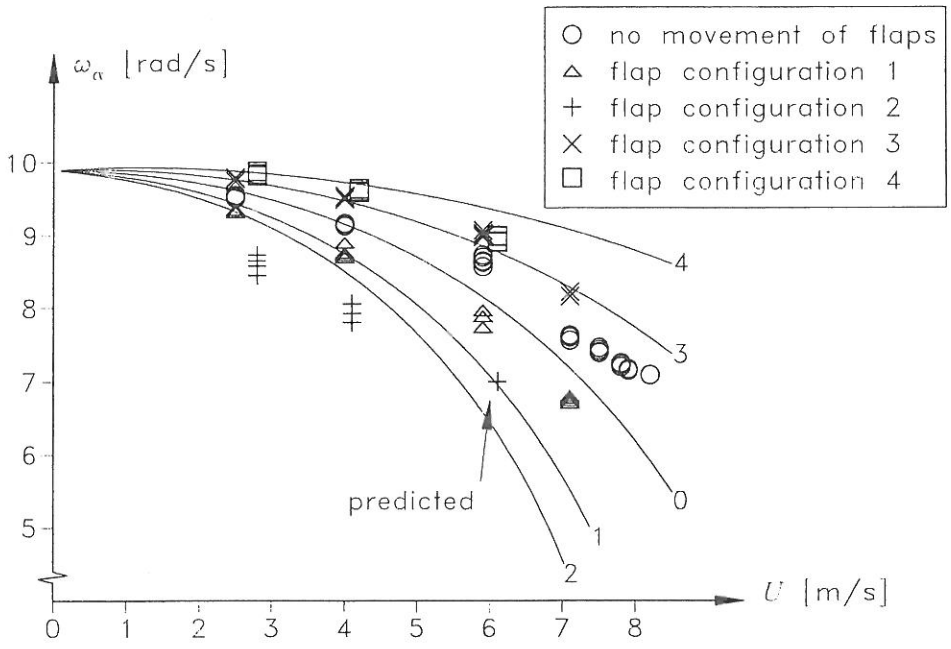

Figure 7.7: Theoretical and experimental circular frequency for torsional motion with wind for flap configuration 0–4. The number at the end of a solid line denotes the actual flap configuration.

As seen in figure 7.7 the estimated values generally follow the theoretical curves for wind velocities below approximately 5 m/s. The only exception is flap configuration 2, but the deviations for this flap configuration can be caused by the relatively short time series because of the effective damping. The pure torsional motion does not completely agree with the binary flutter theory but the fit is much better than for the pure vertical motion described above.

7.4 Wind Dependent Change of Damping

In figure 6.10 the damping ratio for the torsional motion is shown as a function of the wind velocity based on the wind tunnel experiments. The damping ratio can also be estimated by the AMC method described in section 2.4. The damping ratio $g(U)$ defined in section 2.4 as twice the necessary structural damping is replaced by $-0.5g(U) + \zeta_{\alpha,0}$ to be compared with the experimental damping ratios. The mean value of the damping ratio without wind is $\zeta_{\alpha,0} = 0.008$, see section 6.4.2.

The damping ratios estimated based on the experimental data are compared to the theoretical damping ratios by using the AMC method and the aerodynamic derivatives for a flat plate for flap configurations 0–4, see figure 7.8.

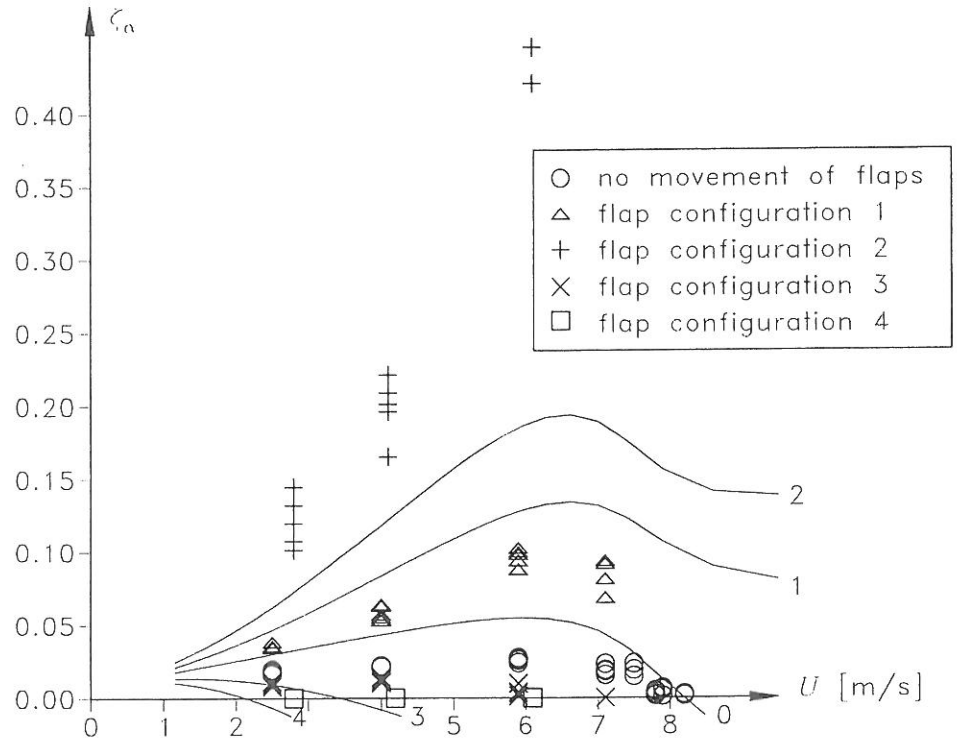

Figure 7.8: Theoretical and experimental damping for torsional motion with wind for flap configuration 0–4. The number at the end of a solid line denotes the actual flap configuration.

As seen in figure 7.8, the experimental damping ratio is smaller for flap configuration 0 and 1 than the theoretical damping ratio but the shape of the curve is almost the same. For flap configuration 2 the experimental damping ratio exceeds the theoretical ratio. For flap configurations 1 and 2 the theoretical curves show that no binary flutter will occur. For the flap configurations 3 and 4 the flutter wind velocity is decreased compared to flap configuration 0, where the flaps are not moved. Unfortunately, it was not possible during the wind tunnel experiments to perform experiments with wind velocities above

the relatively low divergence wind velocity (8.5 m/s) without the risk to damage the model.

7.5 Optimal Flap Positions

There is no guarantee that the phase angles used in the wind tunnel experiments $\varphi_l \simeq 1.5$ rad and $\varphi_t \simeq 4.5$ rad are optimal. When the flat plate approximation is used then the optimal phase angles are about $\varphi_l \simeq 3\pi/6 = 1.57$ rad and $\varphi_t \simeq 8\pi/6 = 4.19$ rad for small values of flap amplification factors a_l and a_t, see section 2.3.

With changed bridge section model parameters described in section 6.5 the favourable phase angles are $\varphi_l \in [3\pi/6; 6\pi/6]$ and $\varphi_t \in [8\pi/6; 10\pi/6]$. These favourable phase angles fit the results in section 2.3 mentioned above very well. Therefore, it can be concluded that favourable phase angles are used during the first experiments. Based on the performed experiments, however, it is not possible to conclude which phase angles are optimal for the model, and therefore, it is also not possible to predict the optimal effect of the flap control system.

7.6 Concluding Remarks

In this chapter the estimated parameters from the wind tunnel experiments are compared with the theoretical parameters by using the flat plate approximation. The time-dependent torsional angle and the flap positions are shown for flap configurations 1–4. The flaps are moved either up or down at the same time and there are maximum angles of the flaps when the model is approximately horizontal.

The wind speed dependent circular frequencies for vertical and torsional motion are compared to the theoretical curves for the flat plate approximation for pure vertical and pure torsional motions. For the vertical motion the curves only agree for rather low wind speeds. The circular frequency for the vertical motion is independent of the flap configuration. For the torsional motion the estimated values generally follow the theoretical curves especially for relatively low wind speeds. The circular frequency for the torsional motion is dependent on the flap configuration.

The experimental damping ratio is smaller for flap configurations 0 and 1 than the theoretical damping ratio based on the flat plate approximation. However, the shape of the curve is almost the same. For flap configuration 2 the experimental damping ratio exceeds the theoretical ratio. By using flap configurations 1 or 2 the flutter wind velocity is increased or perhaps no binary flutter will occur. Unfortunately, it was not possible to perform experiments with wind speeds above the flutter wind velocity for flap configuration 0.

Based on further experiments, where flaps are moved separately, it can be concluded that favourable phase angles are used during the first experiments. However based on the

experiments performed it is not possible to conclude which phase angles are optimal and the optimal effect of the flap control system.

Chapter 8

Conclusion

This chapter is divided into two parts. In section 8.1 there is a summary of the thesis and some conclusions. Main conclusions, a list of new contributions in the thesis and some suggestions for future research are shown in section 8.2.

8.1 Summary of the Thesis

Still longer suspension bridges are built and in the future ultra-long span suspension bridges are planned, e.g. the *Messina Crossing* and the crossing of the *Gibraltar Straits*. These ultra-long span suspension bridges will be sensitive to dynamic loads and the main problem is expected to be flutter. The span length can e.g. be increased by optimizing the suspension bridge with regard to materials, deck shape and cables. Alternatively, the *intelligent bridge* may be introduced where active control systems are used to limit the vibrations.

In **chapter 1** two active control systems with flaps are described. The active flap control system selected for investigation consists of flaps integrated in the bridge girder. When the flaps are exposed to the wind they exert forces on the bridge girder. The direction and sizes of the forces are dependent on the flap regulation. Sensors inside the bridge girder measure the position of the girder. These measurements are used in a control algorithm to calculate the optimal flap positions. The flaps are then regulated continuously according to the calculated optimal positions. The flap control system can be used to fulfil the serviceability state and comfort demands or it can be used to increase the flutter wind velocity.

The motion-induced wind loads on a bridge section are defined in **chapter 2** based on aerodynamic derivatives for the bridge deck and additional aerodynamic derivatives for regulation of the flaps. By expressing the angles of the flaps in terms of the torsional angle of the bridge section the methods described in the literature can be used to estimate the flutter wind velocity for the bridge section with flaps. This is done by simply replacing some of the aerodynamic derivatives with expressions including the parameters describing the flap configuration. Estimation of flutter wind velocity by Theodorsen's method and the air material command method used to estimate the necessary structural damping are

described.

The theoretical effect of the flaps is shown by an example. The flutter wind velocity is calculated for different flap configurations for a bridge section model with flaps. In the following examples the aerodynamic derivatives are approximated by the aerodynamic derivatives for a flat plate. In the derivation of the additional aerodynamic derivatives for the leading flap it is assumed that movement of this flap does not affect the circulation. It can be concluded that the trailing flap is more efficient than the leading flap. However, moving both flaps is again more efficient than moving only the trailing flap. The example shows that it is theoretically possible to eliminate the flutter problem for the investigated bridge section model by using the flap control system.

Three control algorithms that can be used to regulate the flaps are described in **chapter 3**, namely classical linear optimal closed-loop control, instantaneous optimal closed-loop control and closed-loop control with constant phase angle between the motion of the flaps and the torsional motion of the bridge. In classical linear optimal control a performance index is minimized during the entire control interval. In instantaneous optimal control the performance index is minimized at every time instant in the control interval. The instantaneous control law is much simpler than the classical linear optimal control law as solving the Riccatti matrix is omitted. In constant phase angle control the optimal phase angles of the flaps are derived based on the energy input from the motion-induced wind load.

The difference between classical linear optimal control and instantaneous control is shown in an example. The shapes of the flap angle curves are much alike, but the flaps are slightly delayed in instantaneous control compared to classical linear control. Both control algorithms are very efficient to limit the vibrations. An example with constant phase angle control shows that no flutter will occur for a flat plate with long flaps at the investigated wind velocity if the flaps are moved with optimal phase angles and amplitudes equal to the pitch angle of the plate.

In **chapter 4** it is described how a multi-layer perceptron neural network can be used to simulate the motion of a bridge section based on data from e.g. a wind tunnel experiment. During training of an active controller neural network the trained neural network modelling the motion of the bridge section is used as a simulator. In the final active closed-loop control configuration the trained neural network of the bridge section is used as one-step ahead predictor to estimate the state vector to the next time step. The control force is then estimated by the trained controller network based on the estimated state variables. Further, it is described how aerodynamic derivatives for the bridge section can be extracted from a trained bridge section model network.

Wind tunnel experiments are performed to investigate the principle to use flaps to control the bridge excitation. The test setup for wind tunnel experiments is described in **chapter 5**. The wind tunnel, bridge section model, suspension system, regulation system and special details are described. The model is realistic compared to a real bridge, but no specific bridge is investigated. The regulation system has caused a lot of problems

and time delay. Still the regulation system is far from perfect and unfortunately it caused problems during the wind tunnel experiments. Therefore, only a small part of the planned experiments could be performed.

During the wind tunnel experiments described in **chapter 6** it is investigated how the damping of the model is dependent on the flap configuration for increasing wind velocities. Again, however, there were unanticipated problems, namely noisy measurements of the displacements, standing waves in the springs when the flaps are regulated and static divergency of the model at a wind velocity very close to the flutter wind velocity. To avoid the effects of the noisy measurements on the flap regulation the reaction of the servo motors is specified to be very slow. During the experiments constant phase angle control is used. Experiments are performed with the model without moving the flaps, two favourable and two unfavourable flap configurations.

The experiments show that both the circular frequencies of the vertical and torsional motion and the damping ratio of the torsional motion are dependent on the wind speed and the flap configuration. When using favourable flap configurations the damping ratio is increased considerably even though the delay of the flaps compared to the torsional motion might not be optimal. The experiments also show that it is possible to make the flap configuration very unfavourable so the model makes flutter at a rather low wind speed. There were several problems during the experiments that recommended further experiments, e.g. that the effectiveness of the flaps could not be shown for wind speeds above the flutter wind speed. However, new problems were introduced during these new experiments. Therefore, they could only be used to find favourable phase angles for the trailing and leading flap, separately.

Data from the wind tunnel experiments are not used to train neural networks as the data are very noisy, especially with respect to the calculated velocities. Further, many of the time series from the wind tunnel experiments are very short and mainly contain data with slow start of the flaps. Finally, the neural network models assume that the flaps can be moved fast, i.e. that no distinction is made between the desired and actual flap positions.

In **chapter 7** the estimated parameters from the wind tunnel experiments are compared with the theoretical parameters by using the flat plate approximation. In both the favourable and unfavourable flap configurations the flaps are moved either up or down at the same time and there are maximum angles of the flaps when the model is approximately horizontal. The wind speed dependent circular frequencies for vertical and torsional motion are compared to the theoretical curves for the flat plate approximation for pure vertical and pure torsional motions. For the vertical motion the curves only agree for rather low wind speeds. The circular frequency for the vertical motion is independent on the flap configuration. For the torsional motion the estimated values generally follow the theoretical curves especially for relatively low wind speeds. The circular frequency for the torsional motion is dependent on the flap configuration. The experimental damping ratio is smaller for flap configurations 0 and 1 than the theoretical damping ratio based on the flat plate approximation. However, the shape of the curve is almost the same. For flap configuration 2 the experimental damping ratio exceeds the theoretical ratio. By

using flap configuration 1 or 2 the flutter wind velocity is increased or perhaps no binary flutter will occur.

Based on further experiments where flaps are moved separately it can be concluded that favourable phase angles are used during the first experiments. Based on the performed experiments, however, it is not possible to conclude which phase angles are optimal and the optimal effect of the flap control system.

8.2 Overall Conclusion

The main conclusions are summarized as:

- Both theoretically and experimentally the flap control system was very efficient to limit the vibrations of the bridge section model.
- Theoretically, long flaps are more efficient than short flaps.
- Theoretically, the trailing flap is more efficient than the leading flap. It is optimal to use both flaps.
- It is very important that the flaps are regulated as specified by the selected control algorithm as the flutter wind velocity can be decreased if the flap configuration is unfavourable.

To the author's knowledge, new contributions in the thesis are the following:

- The existing theory for dynamics of long suspension bridges is extended to include leading and trailing flaps.
- Formulation of constant phase angle control with derivation of optimal phase angles.
- Derivation of aerodynamic derivatives for bridge section based on trained neural networks.
- Wind tunnel experiments with bridge section model with flaps.

List of topics suggested for further research:

- Further wind tunnel experiments.
- Investigation of the optimal shape of the flaps and where they should be placed on the bridge.
- Reliability analysis of the flap control system with formulation of all failure modes of the system.

Bibliography

[1] *European Patent Specification. A System and a Method of Counteracting Wind induced Oscillations in a Bridge Girder.* EP 0 627 031 B1. Bulletin 1996/24.

[2] *Description of IST Wind Tunnel.* ROLLAB Report RR 079.

[3] *Proceedings of the 15th Congress of IABSE.* Copenhagen, Denmark, June 16–20, 1996.

[4] M.A. Astiz. *Wind Related Behaviour of Alternative Suspension Systems.* In [3], pages 1079–1090.

[5] S.A. Billings, H.B. Jamaluddin, and S. Chen. *A Comparison of the Backpropagation and Recursive Prediction Error Algorithms for Training Neural Networks.* Mechanical Systems and Signal Processing **5**(3), pages 233–255, 1991.

[6] W.C. Brown. *Development of the Deck for the 3300 m Span Messina Crossing.* In [3], pages 1019–1030.

[7] N.J. Cook, editor. *Wind Engineering. 1st IAWE European and African Regional Conference*, London, 1993. Thomas Telford. Proceedings of the conference *Wind Engineering* organized by the International Association of Wind Engineering and held in Guernsey on 20–24 September 1993.

[8] E.H. Dowell, H.C. Curtiss, R.H. Scanlan, and F. Sisto. *A Modern Course in Aeroelasticity.* Sijthoff & Noordhoff, 1978.

[9] C. Dyrbye and S.O. Hansen. *Wind Load on Structures.* John Wiley & Sons, 1996.

[10] A.G. Frandsen. *Wind Stability of Suspension Bridges*, pages 55–78. Bygningsstatiske meddelelser. Teknisk Forlag, Årgang XLI. Nr. 2. August 1970.

[11] Y.C. Fung. *An Introduction to the Theory of Aeroelasticity.* John Wiley & Sons, 1955.

[12] N.J. Gimsing. *Large Bridges of the Future.* In [22], pages 295–304.

[13] H.I. Hansen. *Brosektionsmodel. Bukkeliste.* 1996. Aalborg University.

[14] H.I. Hansen. *Brosektionsmodel. Tegninger.* 1996. Aalborg University.

[15] H.I. Hansen, S.R.K. Nielsen, and P. Thoft-Christensen. *Active Vibration Control of Hysteretic Oscillators using Neural Networks.* Eleventh World Conference on Earthquake Engineering, Acapulco, Mexico, June 1996, Paper No. 1266.

[16] H.I. Hansen and P. Thoft-Christensen. *Active Control of Long Bridges Using Flaps.* Presented at Second World Conference on Structural Control, June 28–July 1, 1998, Kyoto, Japan.

[17] H.I. Hansen and P. Thoft-Christensen. *Wind Tunnel Experiments with Active Control of Bridge Section Model.* Presented at IABSE Symposium on Long-Span and High-Rise Structures, September 2–4, 1998, Kobe, Japan.

[18] H.I. Hansen and P. Thoft-Christensen. *Wind Tunnel Testing of Active Control Systems for Bridges.* In [3], pages 775–780.

[19] J. Hertz, A. Krogh, and R.G. Palmer. *Introduction to the Theory of Neural Computation.* Addison-Wesley, Redwood City, CA., 1991.

[20] E. Hjorth-Hansen. *Section Model Tests.* In [22], pages 95–112.

[21] M. Ito. *Super Long Span Cable-Suspended Bridges in Japan.* In [3], pages 1009–1018.

[22] A. Larsen, editor. *Aerodynamics of Large Bridges*, Proceedings of the First International Symposium on Aerodynamics of Large Bridges, Copenhagen, Denmark, 1992.

[23] A. Larsen and N.J. Gimsing. *Wind Engineering Aspects of the East Bridge Tender Project. Journal of Wind Engineering and Industrial Aerodynamics.* 41–44 (1992), pages 1405–1416.

[24] A. Larsen and J.H. Walther. *A New Computational Method for Assessment of the Aeroelastic Stability of Long Span Bridges.* In [3], pages 93–98.

[25] J.D. Littler. *An Assessment of some of the Different Methods for Estimating Damping from Full-Scale Testing.* In [7] pages 209–219.

[26] L. Ljung. *System Identification. Theory for the User.* Prentice-Hall, 1987.

[27] H.O. Madsen and P. Ostenfeld-Rosenthal. *Wind Criteria for Long Span Bridges.* In [22], pages 33–43.

[28] L. Meirovitch. *Dynamics and Control of Structures.* John Wiley & Sons, 1990.

[29] K.H. Ostenfeld. *Comparison between Different Structural Solutions. The Great Belt Project.* In [3], pages 1063–1078.

[30] K.H. Ostenfeld and A. Larsen. *Bridge Engineering and Aerodynamics.* In [22], pages 3–22.

[31] R.H. Scanlan. *Wind Engineering of Bridges: An Examination of the State of the Art.* In *Wind Loads on Structures.* Oxford & IBH Publishing Co. Pvt. Ltd. Proceedings of International Symposium Experimental Determination of Wind Loads on Civil Engineering Structures, New Delhi, 5–7 December 1990, pages 113–121.

[32] R.H. Scanlan. *Wind Dynamics of Long-Span Bridges.* In [22], pages 47–57.

[33] E. Simiu and R.H. Scanlan. *Wind Effects of Structures.* John Wiley & Sons, second edition, 1986.

[34] T.T. Soong. *Active Structural Control. Theory and Practice.* Longman Scientific and Technical, 1990.

[35] T. Söderström and P. Stoica. *System Identification.* Prentice-Hall, 1989.

[36] O. Sørensen. *Neural Networks for Non-Linear Control.* Proceedings of the 3th IEEE Conference on Control Applications, Glasgow, pages 161–166.

[37] T. Theodorsen. *General Theory of Aerodynamic Instability and the Mechanism of Flutter*, pages 22–31. AIAA Selected Reprint Series, Vol. V, Aerodynamic Flutter. American Institute of Aeronautics and Astronautics, 1976. NACA Rep. No. 496 (1935).

[38] Thomas and Finney. *Calculus and Analytic Geometry.* Addison-Wesley, sixth edition, 1984.

[39] Z. Wu, T.T. Soong, V. Gattulli, and R.C. Lin. *Nonlinear Control Algorithms for Peak Response Reduction.* State University of New York at Buffalo, Department of Civil Engineering, Buffalo, New York. Technical Report NCEER-95-0004, 1995.

Appendix A

Loads on Flat Plate with Flaps

A.1 Introduction

In this appendix the Theodorsen theory for a flat plate with a trailing flap is reviewed and the theory is extended to include a leading flap. Section A.2 reviews Theodorsen's results for loads on a flat plate with a movable trailing flap. The context is extended in section A.3 to include a movable leading flap. It is assumed that rotation of the leading flap has no effect on the circulation. In section A.4 the corresponding flutter derivatives for a flat plate with flaps are derived.

A.2 Theodorsen Theory for Flat Plate with Trailing Flap

This section reviews Theodorsen's results described in: NACA Report 496 *General Theory of Aerodynamic Instability and Mechanism of Flutter* [37], and all equations in this section are from the report. The lift force and pitching moment on an oscillating flat plate equipped with a movable trailing edge flap are considered, see figure A.1. Secondary effects such as: the effects of a finite span, of section shape, of deviations from potential flow, twisting and bending of the plate are not considered.

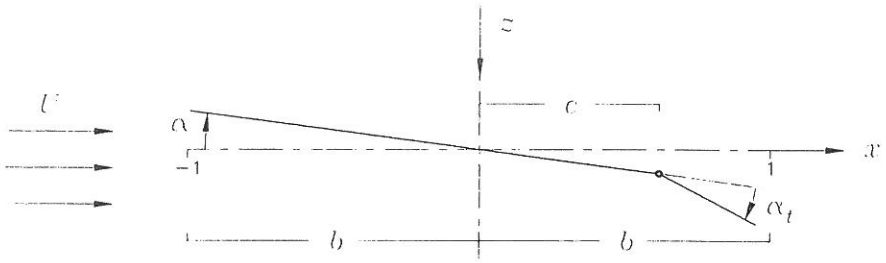

Figure A.1: Parameters of the flat plate with a movable trailing edge flap.

The half-chord length of the plate is denoted b and the location of the flap hinge relative to mid-chord is denoted c. The centre of rotation of the plate is located at mid-chord (i.e.

$a = 0$ compared to the report of Theodorsen). The mean wind velocity U is to the right and horizontal. The angles α and α_t are positive clockwise. The angle of attack α refers to the horizontal. The angle of the flap α_t refers to the undeflected position, i.e. relative to the flat plate. The leading edge is located at $x = -1$ and the trailing edge is located at $x = 1$. The vertical displacement z of the plate is positive downwards.

The lift force (positive downwards) and pitching moment (positive clockwise) are found for a flat plate in section A.2.1. The effect of the trailing edge is shown in section A.2.2.

A.2.1 Flat Plate

The surface potential of a straight line is described by the function φ_ε

$$\varphi_\varepsilon = \frac{\varepsilon}{2\pi} \log \frac{(x-x_1)^2 + (y-y_1)^2}{(x-x_1)^2 + (y+y_1)^2} \tag{A.1}$$

where the x-axis is shown in figure A.1, (x, y) and (x_1, y_1) are points on a circle with radius 1 and centre at mid-chord, i.e. $y = \sqrt{1-x^2}$ and $y_1 = \sqrt{1-x_1^2}$.

The following integrals are used to determine φ_α, $\varphi_{\dot{z}}$ and $\varphi_{\dot{\alpha}}$.

$$\int_{-1}^{1} \log \frac{(x-x_1)^2 + (y-y_1)^2}{(x-x_1)^2 + (y+y_1)^2} dx_1 = -2\pi\sqrt{1-x^2} \tag{A.2}$$

$$\int_{-1}^{1} \log \frac{(x-x_1)^2 + (y-y_1)^2}{(x-x_1)^2 + (y+y_1)^2} (x_1+1) dx_1 = -(x+2)\pi\sqrt{1-x^2} \tag{A.3}$$

To obtain the effect of the angle α of the plate, $-U\alpha b$ is substituted for ε and the contribution is integrated over the entire plate.

$$\begin{aligned} \varphi_\alpha &= \int_{-1}^{1} \left(-\frac{U\alpha b}{2\pi} \log \frac{(x-x_1)^2 + (y-y_1)^2}{(x-x_1)^2 + (y+y_1)^2} \right) dx_1 \\ &= U\alpha b\sqrt{1-x^2} \end{aligned} \tag{A.4}$$

The effect of a downward motion $\dot{z}$ of the plate is found by setting $\alpha = \dot{z}/U$ in equation (A.4).

$$\varphi_{\dot{z}} = \dot{z} b\sqrt{1-x^2} \tag{A.5}$$

A rotation around the mid-chord at an angular velocity $\dot{\alpha}$ consists of a rotation around the leading edge $x = -1$ at an angular velocity $\dot{\alpha}$ plus a vertical motion at the velocity $-\dot{\alpha}b$, i.e. $\varepsilon = -(x_1+1)\dot{\alpha}b^2 + \dot{\alpha}b^2$ and the contribution is integrated over the entire plate.

$$\begin{aligned} \varphi_{\dot{\alpha}} &= \int_{-1}^{1} -\frac{\dot{\alpha}b^2}{2\pi} \log \frac{(x-x_1)^2 + (y-y_1)^2}{(x-x_1)^2 + (y+y_1)^2} (x_1+1) dx_1 \\ &\quad + \int_{-1}^{1} \frac{\dot{\alpha}b^2}{2\pi} \log \frac{(x-x_1)^2 + (y-y_1)^2}{(x-x_1)^2 + (y+y_1)^2} dx_1 \\ &= \frac{\dot{\alpha}b^2 x}{2}\sqrt{1-x^2} \end{aligned} \tag{A.6}$$

Lift Force and Pitching Moment on Flat Plate

The pressure difference p_p between the upper and lower surfaces of the flat plate is given by

$$p_p(x) = -2\rho\left(U\frac{\partial\varphi_p}{\partial x} + \frac{\partial\varphi_p}{\partial t}\right) \tag{A.7}$$

where

$$\varphi_p = \varphi_\alpha + \varphi_{\dot{z}} + \varphi_{\dot{\alpha}} = b\sqrt{1-x^2}\left(U\alpha + \dot{z} + \frac{\dot{\alpha}bx}{2}\right) \tag{A.8}$$

The total force P_p on the plate (positive downwards) is

$$\begin{aligned} P_p &= b\int_{-1}^{1} p_p(x)dx = -2\rho b\int_{-1}^{1}\left(U\frac{\partial\varphi_p}{\partial x} + \frac{\partial\varphi_p}{\partial t}\right)dx = -2\rho b\int_{-1}^{1}\dot{\varphi}_p dx \\ &= -\rho b^2(U\pi\dot{\alpha} + \pi\ddot{z}) \end{aligned} \tag{A.9}$$

In the same way the moment M_p on the plate (positive clockwise) can be found, see Theodorsen [37, eq. (III)].

$$M_p = -\rho b^2\left(-\pi U^2\alpha + \frac{\pi}{8}b^2\ddot{\alpha} - \pi U\dot{z}\right) \tag{A.10}$$

Lift Force and Pitching Moment on Flat Plate due to Circulatory Flow

The force P_{pc} and the moment M_{pc} on the plate corresponding to the circulatory flow are given by Theodorsen [37, eq. (VIII) and (X)].

$$P_{pc} = -2\rho U b\pi C\left(U\alpha + \dot{z} + \frac{b}{2}\dot{\alpha}\right) \tag{A.11}$$

$$M_{pc} = \pi\rho U b^2(C-1)\left(U\alpha + \dot{z} + \frac{b}{2}\dot{\alpha}\right) \tag{A.12}$$

where C is the Theodorsen circulation function, see appendix A.2.3.

Total Lift Force and Pitching Moment on Flat Plate

The total lift force P_{pt} and the total pitching moment M_{pt} on the flat plate are given by

$$P_{pt} = P_p + P_{pc} = -\rho b^2(U\pi\dot{\alpha} + \pi\ddot{z}) - 2\rho U b\pi C\left(U\alpha + \dot{z} + \frac{b}{2}\dot{\alpha}\right) \tag{A.13}$$

$$M_{pt} = M_p + M_{pc} = -\rho b^2\left(\frac{\pi}{2}Ub\dot{\alpha} + \frac{\pi}{8}b^2\ddot{\alpha}\right) + \pi\rho U b^2 C\left(U\alpha + \dot{z} + \frac{b}{2}\dot{\alpha}\right) \tag{A.14}$$

A.2.2 Trailing Flap

The following integrals are used to determine φ_{α_t} and $\varphi_{\dot{\alpha}_t}$.

$$\int_c^1 \log \frac{(x-x_1)^2+(y-y_1)^2}{(x-x_1)^2+(y+y_1)^2} dx_1 = 2(x-c)\log N(c,x) - 2\sqrt{1-x^2}\cos^{-1}(c) \quad \text{(A.15)}$$

$$\int_c^1 \log \frac{(x-x_1)^2+(y-y_1)^2}{(x-x_1)^2+(y+y_1)^2}(x_1-c)dx_1 = -\sqrt{1-c^2}\sqrt{1-x^2} - \cos^{-1}(c)(x-2c)\sqrt{1-x^2} + (x-c)^2\log N(c,x) \quad \text{(A.16)}$$

where

$$N(c,x) = \frac{1-cx-\sqrt{1-x^2}\sqrt{1-c^2}}{x-c} \quad \text{(A.17)}$$

The effect of the trailing flap bent down at an angle α_t is found by setting $\varepsilon = -U\alpha_t b$, and the contribution is integrated over the trailing flap.

$$\begin{aligned}\varphi_{\alpha_t} &= \int_c^1 \left(-\frac{U\alpha_t b}{2\pi}\log\frac{(x-x_1)^2+(y-y_1)^2}{(x-x_1)^2+(y+y_1)^2}\right)dx_1 \\ &= \frac{U\alpha_t b}{\pi}\left(\sqrt{1-x^2}\cos^{-1}(c) - (x-c)\log N(c,x)\right)\end{aligned} \quad \text{(A.18)}$$

The effect of the trailing flap going down at an angular velocity $\dot{\alpha}_t$ is found by setting $\varepsilon = -(x_1-c)\dot{\alpha}_t b^2$, and the contribution is integrated over the trailing flap.

$$\begin{aligned}\varphi_{\dot{\alpha}_t} &= \int_c^1 \left(-\frac{\dot{\alpha}_t b^2}{2\pi}\log\frac{(x-x_1)^2+(y-y_1)^2}{(x-x_1)^2+(y+y_1)^2}(x_1-c)\right)dx_1 \\ &= \frac{\dot{\alpha}_t b^2}{2\pi}\left(\sqrt{1-c^2}\sqrt{1-x^2} + \cos^{-1}(c)(x-2c)\sqrt{1-x^2}\right. \\ &\quad \left. - (x-c)^2\log N(c,x)\right)\end{aligned} \quad \text{(A.19)}$$

Lift Force and Pitching Moment due to Movement of Trailing Flap

The additional force P_t on the plate due to movement of the trailing flap is given by Theodorsen [37, eq. (I)].

$$P_t = -\rho b^2(-UT_4\dot{\alpha}_t - bT_1\ddot{\alpha}_t) \quad \text{(A.20)}$$

where T_i, $i = 1, 2, \ldots, 14$ are constants defined by Theodorsen. The definitions of the constants used in this appendix, namely T_1, T_4, T_7, T_8, T_{10} and T_{11} are shown in appendix A.2.4.

The additional moment M_t on the plate due to movement of the trailing flap is given by Theodorsen [37, eq. (III)].

$$M_t = -\rho b^2\left(U^2T_4\alpha_t + (T_1 - T_8 - cT_4)b\dot{\alpha}_t U - (T_7 + cT_1)b^2\ddot{\alpha}_t\right) \quad \text{(A.21)}$$

Lift Force and Pitching Moment due to Movement of Trailing Flap and Circulatory Flow

The force P_{tc} and the moment M_{tc} on the plate due to movement of the trailing flap and corresponding to the circulatory flow is given by Theodorsen [37, eq. (VIII) and (X)].

$$P_{tc} = -2\rho U b \pi C \left(\frac{T_{10}}{\pi} U \alpha_t + b \frac{T_{11}}{2\pi} \dot{\alpha}_t \right) \tag{A.22}$$

$$M_{tc} = \pi \rho U b^2 (C - 1) \left(\frac{T_{10}}{\pi} U \alpha_t + b \frac{T_{11}}{2\pi} \dot{\alpha}_t \right) \tag{A.23}$$

Total Lift Force and Pitching Moment on Flat Plate due to Movement of Trailing Flap

The additional lift force P_{tt} and additional pitching moment M_{tt} on the flat plate due to movement of the trailing flap are given by

$$P_{tt} = P_t + P_{tc} = -\rho b^2 (-U T_4 \dot{\alpha}_t - b T_1 \ddot{\alpha}_t) - 2\rho U b \pi C \left(\frac{T_{10}}{\pi} U \alpha_t + b \frac{T_{11}}{2\pi} \dot{\alpha}_t \right) \tag{A.24}$$

$$\begin{aligned} M_{tt} &= M_t + M_{tc} \\ &= -\rho b^2 \left((T_4 + T_{10}) U^2 \alpha_t + \left(T_1 - T_8 - c T_4 + \frac{T_{11}}{2} \right) b \dot{\alpha}_t U - (T_7 + c T_1) b^2 \ddot{\alpha}_t \right) \\ &\quad + \pi \rho U b^2 C \left(\frac{T_{10}}{\pi} U \alpha_t + b \frac{T_{11}}{2\pi} \dot{\alpha}_t \right) \end{aligned} \tag{A.25}$$

A.2.3 Theodorsen Circulation Function

The Theodorsen circulation function is defined by

$$C(k) = \frac{\int_1^\infty \frac{x_0}{\sqrt{x_0^2 - 1}} e^{-ikx_0} dx_0}{\int_1^\infty \frac{x_0 + 1}{\sqrt{x_0^2 - 1}} e^{-ikx_0} dx_0} \tag{A.26}$$

k is the reduced frequency $k = b\omega/U$ where ω is the circular frequency, b is the half-chord length of the plate and U is the mean wind velocity. Eq. (A.26) can be rewritten

$$C(k) = F(k) + iG(k) \tag{A.27}$$

where

$$F = \frac{J_1 (J_1 + Y_0) + Y_1 (Y_1 - J_0)}{(J_1 + Y_0)^2 + (Y_1 - J_0)^2} \tag{A.28}$$

$$G = -\frac{Y_1 Y_0 + J_1 J_0}{(J_1 + Y_0)^2 + (Y_1 - J_0)^2} \tag{A.29}$$

where J_j and Y_j are Bessel functions of the order j.

A.2.4 Theodorsen Constants

Theodorsen defines the following constants

$$T_1 = -\frac{1}{3}\sqrt{1-c^2}(2+c^2) + c\cos^{-1}c \tag{A.30}$$

$$T_4 = -\cos^{-1}c + c\sqrt{1-c^2} \tag{A.31}$$

$$T_7 = -\left(\frac{1}{8}+c^2\right)\cos^{-1}c + \frac{1}{8}c\sqrt{1-c^2}(7+2c^2) \tag{A.32}$$

$$T_8 = -\frac{1}{3}\sqrt{1-c^2}(2c^2+1) + c\cos^{-1}c \tag{A.33}$$

$$T_{10} = \sqrt{1-c^2} + \cos^{-1}c \tag{A.34}$$

$$T_{11} = \cos^{-1}c(1-2c) + \sqrt{1-c^2}(2-c) \tag{A.35}$$

A.3 Extension of Theodorsen Theory to include Leading Flap

It is assumed that the leading flap is of the same size as the trailing flap, see figure A.2. The angle of the leading flap α_l refers to the undeflected position and it is positive clockwise. Further, it is assumed that rotation of the leading flap has no effect on the circulation.

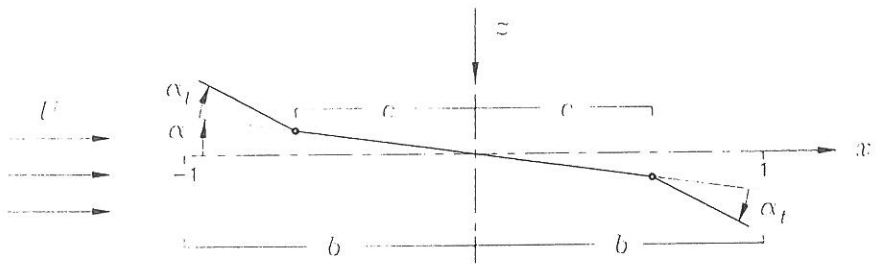

Figure A.2: Parameters of the flat plate with movable leading and trailing edge flap.

A.3.1 Leading Flap

The following integrals are used to determine φ_{α_l} and $\varphi_{\dot{\alpha}_l}$.

$$\int_{-1}^{-c} \log\frac{(x-x_1)^2+(y-y_1)^2}{(x-x_1)^2+(y+y_1)^2}dx_1 =$$
$$2(-x-c)\log N(c,-x) - 2\sqrt{1-x^2}\cos^{-1}(c) \tag{A.36}$$

$$\int_{-1}^{-c} \log \frac{(x-x_1)^2+(y-y_1)^2}{(x-x_1)^2+(y+y_1)^2}(-x_1-c)dx_1 = \\ -\sqrt{1-c^2}\sqrt{1-x^2} - \cos^{-1}(c)(-x-2c)\sqrt{1-x^2} + \\ (-x-c)^2 \log N(c,-x) \tag{A.37}$$

The results of these integrals are seen to be the same as the results for the trailing flap with x replaced by $-x$.

The effect of the leading flap bent up at an angle α_l is found by setting $\varepsilon = -U\alpha_l b$, and the contribution is integrated over the leading flap.

$$\begin{aligned} \varphi_{\alpha_l} &= \int_{-1}^{-c} \left(-\frac{U\alpha_l b}{2\pi} \log \frac{(x-x_1)^2+(y-y_1)^2}{(x-x_1)^2+(y+y_1)^2} \right) dx_1 \\ &= \frac{U\alpha_l b}{\pi} \left(\sqrt{1-x^2}\cos^{-1}(c) - (-x-c)\log N(c,-x) \right) \end{aligned} \tag{A.38}$$

The effect of the trailing flap going down at an angular velocity $\dot{\alpha}_t$ is found by setting $\varepsilon = -(-x_1-c)\dot{\alpha}_l b^2$, and the contribution is integrated over the leading flap.

$$\begin{aligned} \varphi_{\dot{\alpha}_l} &= \int_{c}^{1} \left(-\frac{\dot{\alpha}_l b^2}{2\pi} \log \frac{(x-x_1)^2+(y-y_1)^2}{(x-x_1)^2+(y+y_1)^2}(-x_1-c) \right) dx_1 \\ &= \frac{\dot{\alpha}_l b^2}{2\pi} \left(\sqrt{1-c^2}\sqrt{1-x^2} + \cos^{-1}(c)(-x-2c)\sqrt{1-x^2} \right. \\ &\quad \left. - (-x-c)^2 \log N(c,-x) \right) \end{aligned} \tag{A.39}$$

Lift Force and Pitching Moment due to Movement of Leading Flap

The potentials φ_{α_l} and $\varphi_{\dot{\alpha}_l}$ are the same as the results for the trailing flap with x replaced by $-x$. When the potentials are integrated over the entire plate they will give the same additional force P_l and moment M_l on the plate as the trailing flap (for the same movement).

$$P_l = -\rho b^2(-UT_4\dot{\alpha}_l - bT_1\ddot{\alpha}_l) \tag{A.40}$$

$$M_l = -\rho b^2 \left(U^2 T_4 \alpha_l + (T_1 - T_8 - cT_4)b\dot{\alpha}_l U - (T_7 + cT_1)b^2\ddot{\alpha}_l \right) \tag{A.41}$$

A.4 Aerodynamic Derivatives for Flat Plate with Flaps

By assuming that both the vertical and torsional motion of the plate are harmonic at the circular frequency ω and that the leading and trailing flap are moved at the same circular frequency, then the derived forces and moments can be expressed by aerodynamic derivatives $H_i^\star$ and $A_i^\star$. The derivatives corresponding to the flat plate without flaps are derived in appendix A.4.1. Additional derivatives are derived for movement of the trailing and leading flaps in appendix A.4.2 and A.4.3, respectively.

A.4.1 Flat Plate

It is assumed that the vibration is harmonic at the frequency ω. The following relations are then valid.

$$z(t) = z_0 e^{i\omega t} \quad \Rightarrow \quad \dot{z}(t) = i\omega z(t) \quad \Rightarrow \quad \ddot{z}(t) = -\omega^2 z(t) \tag{A.42}$$

$$\alpha(t) = \alpha_0 e^{i(\omega t - \varphi_\alpha)} \quad \Rightarrow \quad \dot{\alpha}(t) = i\omega\alpha(t) \quad \Rightarrow \quad \ddot{\alpha}(t) = -\omega^2\alpha(t) \tag{A.43}$$

The Theodorsen circulation function $C(k)$ is divided into the real part $F(k)$ and the imaginary part $G(k)$.

$$C(k) = F(k) + iG(k) \tag{A.44}$$

The reduced frequencies k and K are defined by

$$k = \frac{b\omega}{U} \tag{A.45}$$

$$K = \frac{B\omega}{U} \tag{A.46}$$

where $B = 2b$ and thereby $K = 2k$.

To derive the aerodynamic derivatives for a flat plate the total force and moment found in equations (A.13) and (A.14) are rewritten to contain only real parts.

$$\begin{aligned} P_{pt} &= -\rho b^2(U\pi\dot{\alpha} + \pi\ddot{z}) - 2\rho Ub\pi(F(k) + iG(k))\left(U\alpha + \dot{z} + \frac{b}{2}\dot{\alpha}\right) \\ &= (-2\rho Ub\pi F(k))\,\dot{z} + \left(-\rho Ub^2\pi - \rho Ub^2\pi F(k) - \frac{2\rho Ub^2\pi G(k)}{k}\right)\dot{\alpha} + \\ &\quad \left(-2\rho U^2 b\pi F(k) + \rho U^2 b\pi k G(k)\right)\alpha + \left(\rho U^2\pi k^2 + 2\rho U^2\pi k G(k)\right) z \end{aligned} \tag{A.47}$$

$$\begin{aligned} M_{pt} &= -\rho b^2\left(\frac{\pi}{2}Ub\dot{\alpha} + \frac{\pi}{8}b^2\ddot{\alpha}\right) + \pi\rho Ub^2(F(k) + iG(k))\left(U\alpha + \dot{z} + \frac{b}{2}\dot{\alpha}\right) \\ &= \left(\pi\rho Ub^2F(k)\right)\dot{z} + \left(-\frac{\rho Ub^3\pi}{2} + \frac{\rho Ub^3\pi F(k)}{2} + \frac{\rho Ub^3\pi G(k)}{k}\right)\dot{\alpha} + \\ &\quad \left(\frac{\rho U^2b^2\pi k^2}{8} + \rho U^2b^2\pi F(k) - \frac{\rho U^2b^2\pi k G(k)}{2}\right)\alpha + \\ &\quad \left(-\rho U^2 b\pi k G(k)\right) z \end{aligned} \tag{A.48}$$

The total force and moment on the flat plate can be expressed by aerodynamic derivatives as shown in equations (2.4) and (2.5).

$$P_{pt} = \frac{1}{2}\rho U^2 B\left[KH_1^\star(K)\frac{\dot{z}}{U} + KH_2^\star(K)\frac{B\dot{\alpha}}{U} + K^2H_3^\star(K)\alpha + K^2H_4^\star(K)\frac{z}{B}\right] \tag{A.49}$$

$$M_{pt} = \frac{1}{2}\rho U^2 B^2\left[KA_1^\star(K)\frac{\dot{z}}{U} + KA_2^\star(K)\frac{B\dot{\alpha}}{U} + K^2A_3^\star(K)\alpha + K^2A_4^\star(K)\frac{z}{B}\right] \tag{A.50}$$

The aerodynamic derivatives $H_1^\star(K),\ldots,H_4^\star(K)$ are found by setting equation (A.47) equal to equation (A.49).

$$\frac{1}{2}\rho UBKH_1^\star(K)\dot{z} = -2\rho Ub\pi F(k)\dot{z} \quad \Rightarrow \quad H_1^\star(K) = -\frac{\pi F(k)}{k} \tag{A.51}$$

$$\frac{1}{2}\rho UB^2KH_2^\star(K)\dot{\alpha} = -\rho Ub^2\pi\left(1+F(k)+\frac{2G(k)}{k}\right)\dot{\alpha} \quad \Rightarrow$$

$$H_2^\star(K) = -\frac{\pi}{4k}\left[1+F(k)+\frac{2G(k)}{k}\right] \tag{A.52}$$

$$\frac{1}{2}\rho U^2BK^2H_3^\star(K)\alpha = -\rho U^2b\pi\left(2F(k)-kG(k)\right)\alpha \quad \Rightarrow$$

$$H_3^\star(K) = -\frac{\pi}{2k^2}\left[F(k)-\frac{kG(k)}{2}\right] \tag{A.53}$$

$$\frac{1}{2}\rho U^2K^2H_4^\star(K)z = \rho U^2\pi\left(k^2+2kG(k)\right)z \quad \Rightarrow \quad H_4^\star(K) = \frac{\pi}{2}\left[1+\frac{2G(k)}{k}\right] \tag{A.54}$$

The aerodynamic derivatives $A_1^\star(K),\ldots,A_4^\star(K)$ are found by setting equation (A.48) equal to equation (A.50).

$$\frac{1}{2}\rho UB^2KA_1^\star(K)\dot{z} = \left(\pi\rho Ub^2F(k)\right)\dot{z} \quad \Rightarrow \quad A_1^\star(K) = \frac{\pi F(k)}{4k} \tag{A.55}$$

$$\frac{1}{2}\rho UB^3KA_2^\star(K)\dot{\alpha} = -\frac{\rho Ub^3\pi}{2}\left(1-F(k)-\frac{2G(k)}{k}\right)\dot{\alpha} \quad \Rightarrow$$

$$A_2^\star(K) = -\frac{\pi}{16k}\left[1-F(k)-\frac{2G(k)}{k}\right] \tag{A.56}$$

$$\frac{1}{2}\rho U^2B^2K^2A_3^\star(K)\alpha = \rho U^2b^2\pi\left(\frac{k^2}{8}+F(k)-\frac{kG(k)}{2}\right)\alpha \quad \Rightarrow$$

$$A_3^\star(K) = \frac{\pi}{8k^2}\left[\frac{k^2}{8}+F(k)-\frac{kG(k)}{2}\right] \tag{A.57}$$

$$\frac{1}{2}\rho U^2BK^2A_4^\star(K)z = \left(-\rho U^2b\pi G(k)k\right)z \quad \Rightarrow \quad A_4^\star(K) = -\frac{\pi}{4}\frac{G(k)}{k} \tag{A.58}$$

A.4.2 Trailing Flap

It is assumed that the trailing flap is moved harmonically at the same frequency ω as the flat plate. The following relations are then valid

$$\alpha_t(t) = \alpha_{t0}e^{i(\omega t-\varphi_\alpha-\varphi_t)} \quad \Rightarrow \quad \dot{\alpha}_t(t) = i\omega\alpha_t(t) \quad \Rightarrow \quad \ddot{\alpha}_t(t) = -\omega^2\alpha_t(t) \tag{A.59}$$

To derive the additional aerodynamic derivatives for movement of a trailing flap on the flat plate the total force and moment found in equations (A.24) and (A.25) are rewritten to contain only real parts.

$$\begin{aligned} P_{tt} &= -\rho b^2(-UT_4\dot{\alpha}_t - bT_1\ddot{\alpha}_t) - 2\rho Ub\pi(F(k)+iG(k))\left(\frac{T_{10}}{\pi}U\alpha_t + b\frac{T_{11}}{2\pi}\dot{\alpha}_t\right) \\ &= \left(\rho Ub^2T_4 - \rho Ub^2F(k)T_{11} - \frac{2\rho Ub^2G(k)T_{10}}{k}\right)\dot{\alpha}_t + \\ &\quad \left(-\rho U^2bk^2T_1 - 2\rho U^2bF(k)T_{10} + \rho U^2bkG(k)T_{11}\right)\alpha_t \end{aligned} \tag{A.60}$$

$$\begin{aligned} M_{tt} &= -\rho b^2\left((T_4+T_{10})U^2\alpha_t + \left(T_1 - T_8 - cT_4 + \frac{T_{11}}{2}\right)b\dot{\alpha}_tU - (T_7+cT_1)b^2\ddot{\alpha}_t\right) \\ &\quad + \pi\rho Ub^2(F(k)+iG(k))\left(\frac{T_{10}}{\pi}U\alpha_t + b\frac{T_{11}}{2\pi}\dot{\alpha}_t\right) \\ &= \left(-\rho Ub^3\left(T_1 - T_8 - cT_4 + \frac{T_{11}}{2}\right) + \frac{\rho Ub^3F(k)T_{11}}{2} + \frac{\rho Ub^3G(k)T_{10}}{k}\right)\dot{\alpha}_t + \\ &\quad \left(-\rho U^2b^2(T_4+T_{10}) - \rho U^2b^2k^2(T_7+cT_1) + \rho U^2b^2F(k)T_{10} - \right. \\ &\quad \left.\frac{\rho U^2b^2kG(k)T_{11}}{2}\right)\alpha_t \end{aligned} \tag{A.61}$$

The total force and moment on the flat plate from movement of the trailing flap can be expressed by additional aerodynamic derivatives as shown in equations (2.15) and (2.16).

$$P_{tt} = \frac{1}{2}\rho U^2B\left[KH_5^\star(K)\frac{B\dot{\alpha}_t}{U} + K^2H_6^\star(K)\alpha_t\right] \tag{A.62}$$

$$M_{tt} = \frac{1}{2}\rho U^2B^2\left[KA_5^\star(K)\frac{B\dot{\alpha}_t}{U} + K^2A_6^\star(K)\alpha_t\right] \tag{A.63}$$

The aerodynamic derivatives $H_5^\star(K)$ and $H_6^\star(K)$ are found by setting equation (A.60) equal to equation (A.62).

$$\frac{1}{2}\rho UB^2KH_5^\star(K)\dot{\alpha}_t = \rho Ub^2\left(T_4 - F(k)T_{11} - \frac{2G(k)T_{10}}{k}\right)\dot{\alpha}_t \quad \Rightarrow$$

$$H_5^\star(K) = \frac{1}{4k}\left[T_4 - F(k)T_{11} - \frac{2G(k)T_{10}}{k}\right] \tag{A.64}$$

$$\frac{1}{2}\rho U^2BK^2H_6^\star(K)\alpha_t = \rho U^2b\left(-k^2T_1 - 2F(k)T_{10} + kG(k)T_{11}\right)\alpha_t \quad \Rightarrow$$

$$H_6^\star(K) = \frac{1}{4k^2}\left[-k^2T_1 - 2F(k)T_{10} + kG(k)T_{11}\right] \tag{A.65}$$

The aerodynamic derivatives $A_5^\star(K)$ and $A_6^\star(K)$ are found by setting equation (A.61) equal to equation (A.63).

$$\frac{1}{2}\rho UB^3KA_5^\star(K)\dot{\alpha}_t = \rho Ub^3\left(-\left(T_1 - T_8 - cT_4 + \frac{T_{11}}{2}\right) + \frac{F(k)T_{11}}{2} + \frac{G(k)T_{10}}{k}\right)\dot{\alpha}_t \quad \Rightarrow$$

$$A_5^\star(K) = \frac{1}{8k}\left[-\left(T_1 - T_8 - cT_4 + \frac{T_{11}}{2}\right) + \frac{F(k)T_{11}}{2} + \frac{G(k)T_{10}}{k}\right] \tag{A.66}$$

$$\frac{1}{2}\rho U^2 B^2 K^2 A_6^\star(K)\alpha_t = \rho U^2 b^2\left[-(T_4 + T_{10}) - k^2(T_7 + cT_1) + F(k)T_{10} - \frac{kG(k)T_{11}}{2}\right]\alpha_t \Rightarrow$$

$$A_6^\star(K) = \frac{1}{8k^2}\left[-(T_4 + T_{10}) - k^2(T_7 + cT_1) + F(k)T_{10} - \frac{kG(k)T_{11}}{2}\right] \tag{A.67}$$

A.4.3 Leading Flap

Derivation of aerodynamic derivatives for the leading flap follows the procedure described for the trailing flap. It is assumed that the leading flap also is moved harmonically at the same frequency ω as the flat plate. The following relations are then valid

$$\alpha_l(t) = \alpha_{l0}e^{i(\omega t - \varphi_\alpha - \varphi_l)} \quad \Rightarrow \quad \dot{\alpha}_l(t) = i\omega\alpha_l(t) \quad \Rightarrow \quad \ddot{\alpha}_l(t) = -\omega^2\alpha_l(t) \tag{A.68}$$

To derive the additional aerodynamic derivatives for movement of a leading flap on the flat plate the total force and moment found in equations (A.40) and (A.41) are rewritten to contain only real parts

$$\begin{aligned} P_l &= -\rho b^2(-UT_4\dot{\alpha}_l - bT_1\ddot{\alpha}_l) \\ &= \left(\rho U b^2 T_4\right)\dot{\alpha}_l + \left(-\rho U^2 b k^2 T_1\right)\alpha_l \end{aligned} \tag{A.69}$$

$$\begin{aligned} M_l &= -\rho b^2\left(U^2 T_4\alpha_l + (T_1 - T_8 - cT_4)b\dot{\alpha}_l U - (T_7 + cT_1)b^2\ddot{\alpha}_l\right) \\ &= \left(-\rho U b^3(T_1 - T_8 - cT_4)\right)\dot{\alpha}_l + \left(-\rho U^2 b^2 T_4 - \rho U^2 b^2 k^2(T_7 + cT_1)\right)\alpha_l \end{aligned} \tag{A.70}$$

The total force and moment on the flat plate from movement of the leading flap can be expressed by additional aerodynamic derivatives as shown in equations (2.21) and (2.22)

$$P_l = \frac{1}{2}\rho U^2 B\left[KH_7^\star(K)\frac{B\dot{\alpha}_l}{U} + K^2 H_8^\star(K)\alpha_l\right] \tag{A.71}$$

$$M_l = \frac{1}{2}\rho U^2 B^2\left[KA_7^\star(K)\frac{B\dot{\alpha}_l}{U} + K^2 A_8^\star(K)\alpha_l\right] \tag{A.72}$$

The aerodynamic derivatives $H_7^\star(K)$ and $H_8^\star(K)$ are found by setting equation (A.69) equal to equation (A.71)

$$\frac{1}{2}\rho U B^2 K H_7^\star(K)\dot{\alpha}_l = \rho U b^2 T_4\dot{\alpha}_l \quad \Rightarrow \quad H_7^\star(K) = \frac{T_4}{4k} \tag{A.73}$$

$$\frac{1}{2}\rho U^2 B K^2 H_8^\star(K)\alpha_l = -\rho U^2 b k^2 T_1\alpha_l \quad \Rightarrow \quad H_8^\star(K) = -\frac{T_1}{4} \tag{A.74}$$

The aerodynamic derivatives $A_7^\star(K)$ and $A_8^\star(K)$ are found by setting equation (A.70) equal to equation (A.72)

$$\frac{1}{2}\rho U B^3 K A_7^\star(K)\dot{\alpha}_l = -\rho U b^3(T_1 - T_8 - cT_4)\dot{\alpha}_l \quad \Rightarrow$$

$$A_7^*(K) = -\frac{1}{8k}\left[T_1 - T_8 - cT_4\right] \tag{A.75}$$

$$\frac{1}{2}\rho U^2 B^2 K^2 A_8^*(K)\alpha_l = \rho U^2 b^2 \left[-T_4 - k^2(T_7 + cT_1)\right]\alpha_l \quad \Rightarrow$$

$$A_8^*(K) = \frac{1}{8k^2}\left[-T_4 - k^2(T_7 + cT_1)\right] \tag{A.76}$$

Appendix B

Estimation of Flutter Wind Velocity

B.1 Introduction

Two kinds of flutter are investigated

- Single-degree flutter in torsion. Pure torsional oscillation of the bridge.
- Binary flutter. Coupling between vertical and torsional oscillations.

In appendix B.2 estimation of the flutter wind velocity by Theodorsen's method for single-degree flutter in torsion and binary flutter is described for a bridge section without flaps. The context is extended in appendix B.3 to include leading and trailing flaps.

The Air Material Command (AMC) method for estimating the necessary structural damping as a function of the mean wind velocity is described in appendix B.4.

B.2 Bridge Section without Flaps

The matrix equation of motion for a bridge section without flaps can be written

$$\boldsymbol{M}_s\ddot{\boldsymbol{x}}(t) + \boldsymbol{C}_s\dot{\boldsymbol{x}}(t) + \boldsymbol{K}_s\boldsymbol{x}(t) = \boldsymbol{F}_{ad}(t) \tag{B.1}$$

where (2.2) and (2.3) are used with

$$\boldsymbol{x}(t) = \begin{bmatrix} z(t) \\ \alpha(t) \end{bmatrix} \tag{B.2}$$

$$\boldsymbol{M}_s = \begin{bmatrix} m & 0 \\ 0 & I \end{bmatrix} \tag{B.3}$$

m is the mass per unit length and I is the mass moment of inertia per unit length.

$$\boldsymbol{C}_s = \begin{bmatrix} m2\zeta_z\omega_z & 0 \\ 0 & I2\zeta_\alpha\omega_\alpha \end{bmatrix} \tag{B.4}$$

ζ_z and ζ_α are the damping ratios in bending and torsion, respectively.

$$\boldsymbol{K}_s = \begin{bmatrix} m\omega_z^2 & 0 \\ 0 & I\omega_\alpha^2 \end{bmatrix} \tag{B.5}$$

ω_z and ω_α are the circular eigenfrequencies in bending and torsion, respectively.

$$\boldsymbol{F}_{ad}(t) = \begin{bmatrix} F_{ad}^P(t) \\ F_{ad}^M(t) \end{bmatrix} \tag{B.6}$$

By using equations (2.4) and (2.5) the motion-induced wind load on the bridge section is written

$$\boldsymbol{F}_{ad}(t) = \boldsymbol{C}_d\dot{\boldsymbol{x}}(t) + \boldsymbol{K}_d\boldsymbol{x}(t) \tag{B.7}$$

where

$$\boldsymbol{C}_d = \frac{1}{2}\rho UBK \begin{bmatrix} H_1^\star(K) & BH_2^\star(K) \\ BA_1^\star(K) & B^2A_2^\star(K) \end{bmatrix} \tag{B.8}$$

$$\boldsymbol{K}_d = \frac{1}{2}\rho U^2K^2 \begin{bmatrix} H_4^\star(K) & BH_3^\star(K) \\ BA_4^\star(K) & B^2A_3^\star(K) \end{bmatrix} \tag{B.9}$$

In these equations ρ is the mass density of air, U is the mean wind velocity, B is the width of the bridge deck, K is the reduced frequency based on the width of the bridge deck and $H_1^\star(K), \ldots, H_4^\star(K), A_1^\star(K), \ldots, A_4^\star(K)$ are the non-dimensional aerodynamic derivatives.

By inserting equation (B.7) into (B.1) the matrix equation of motion can be written

$$\boldsymbol{M}_s\ddot{\boldsymbol{x}}(t) + (\boldsymbol{C}_s - \boldsymbol{C}_d)\dot{\boldsymbol{x}}(t) + (\boldsymbol{K}_s - \boldsymbol{K}_d)\boldsymbol{x}(t) = \boldsymbol{0} \tag{B.10}$$

B.2.1 Single-Degree Flutter in Torsion

For single-degree flutter in torsion there is no vertical oscillation, i.e.

$$z(t) \equiv \dot{z}(t) \equiv \ddot{z}(t) \equiv 0 \tag{B.11}$$

The equation of motion becomes

$$\ddot{\alpha}(t) + 2\zeta_\alpha\omega_\alpha\dot{\alpha}(t) + \omega_\alpha^2\alpha(t) = \frac{\rho U^2B^2}{2I}\left[KA_2^\star(K)\frac{B\dot{\alpha}(t)}{U} + K^2A_3^\star(K)\alpha(t)\right] \quad \Rightarrow$$

$$\ddot{\alpha}(t) + 2(\zeta_\alpha + \zeta_{\alpha a})\omega_\alpha\dot{\alpha}(t) + \omega_\alpha^2\alpha(t) = \frac{\rho U^2B^2K^2A_3^\star(K)}{2I}\alpha(t) \tag{B.12}$$

where

$$\zeta_{\alpha a} = -\frac{\rho B^4A_2^\star(K)}{4I} \tag{B.13}$$

Flutter in torsion will occur at the circular flutter frequency $\omega_f \simeq \omega_\alpha$ when the total damping (structural damping ζ_α and aerodynamic damping $\zeta_{\alpha a}$) is zero, i.e. when

$$\zeta_\alpha + \zeta_{\alpha a} = 0 \quad \Rightarrow \quad A_2^\star(K) = \frac{4I\zeta_\alpha}{\rho B^4} \tag{B.14}$$

The flutter wind velocity U_f for single-degree flutter in torsion is found by

$$U_f = \frac{B\omega_f}{K_f} \simeq \frac{B\omega_\alpha}{K_f} \tag{B.15}$$

where K_f is the reduced frequency for which equation (B.14) is true.

B.2.2 Binary Flutter

The binary flutter condition is

$$\boldsymbol{x}(t) = \boldsymbol{x}_0 e^{i\omega_f t} \tag{B.16}$$

where

$$\boldsymbol{x}_0 = \begin{bmatrix} z_0 \\ \alpha_0 e^{-i\varphi_\alpha} \end{bmatrix} \tag{B.17}$$

$$\boldsymbol{x}(t) = \boldsymbol{x}_0 e^{i\omega_f t} \quad \Rightarrow \quad \dot{\boldsymbol{x}}(t) = i\omega_f \boldsymbol{x}(t) \quad \Rightarrow \quad \ddot{\boldsymbol{x}}(t) = -\omega_f^2 \boldsymbol{x}(t) \tag{B.18}$$

The flutter condition is inserted into the matrix equation of motion (B.10)

$$\left(\boldsymbol{M}_s\left(-\omega_f^2\right) + (\boldsymbol{C}_s - \boldsymbol{C}_d)i\omega_f + (\boldsymbol{K}_s - \boldsymbol{K}_d)\right)\boldsymbol{x}_0 e^{i\omega_f t} = \boldsymbol{0} \tag{B.19}$$

Equation (B.19) contains two unknowns, namely the flutter wind velocity U_f and the circular flutter frequency ω_f. It is more convenient to use the following variables as unknown

$$X_f = \frac{\omega_f}{\omega_z} \tag{B.20}$$

$$K_f = \frac{B\omega_f}{U_f} \tag{B.21}$$

Equation (B.19) is divided by ω_f^2 and the variables X_f and K_f are inserted

$$\left(-\boldsymbol{M}_s + (\boldsymbol{C}'_s - \boldsymbol{C}'_d)i + (\boldsymbol{K}'_s - \boldsymbol{K}'_d)\right)\boldsymbol{x}_0 e^{i\omega_f t} = \boldsymbol{0} \tag{B.22}$$

where

$$\boldsymbol{C}'_s = \frac{1}{\omega_f}\boldsymbol{C}_s = \begin{bmatrix} m2\zeta_z\frac{1}{X_f} & 0 \\ 0 & I2\zeta_\alpha\frac{\omega_\alpha}{\omega_z}\frac{1}{X_f} \end{bmatrix} \tag{B.23}$$

$$\boldsymbol{K}'_s = \frac{1}{\omega_f^2}\boldsymbol{K}_s = \begin{bmatrix} m\frac{1}{X_f^2} & 0 \\ 0 & I\frac{\omega_\alpha^2}{\omega_z^2}\frac{1}{X_f^2} \end{bmatrix} \tag{B.24}$$

$$\boldsymbol{C}'_d = \frac{1}{\omega_f}\boldsymbol{C}_d = \frac{1}{2}\rho B^2 \begin{bmatrix} H_1^\star(K_f) & BH_2^\star(K_f) \\ BA_1^\star(K_f) & B^2A_2^\star(K_f) \end{bmatrix} \tag{B.25}$$

$$\boldsymbol{K}'_d = \frac{1}{\omega_f^2}\boldsymbol{K}_d = \frac{1}{2}\rho B^2 \begin{bmatrix} H_4^\star(K_f) & BH_3^\star(K_f) \\ BA_4^\star(K_f) & B^2A_3^\star(K_f) \end{bmatrix} \tag{B.26}$$

For $\boldsymbol{x}_0 \neq \boldsymbol{0}$ the solution is found by

$$\left|-\boldsymbol{M}_s + (\boldsymbol{C}'_s - \boldsymbol{C}'_d)i + (\boldsymbol{K}'_s - \boldsymbol{K}'_d)\right| = A_r(X_f, K_f) + i \cdot A_i(X_f, K_f) = 0 \tag{B.27}$$

where the above determinant consists of a real part $A_r(X_f, K_f)$ and an imaginary part $i \cdot A_i(X_f, K_f)$ both of which must be zero for flutter. By rearranging equation (B.27) the real and imaginary parts are found

$$\begin{aligned}
&A_r(X_f, K_f)X_f^4 = \\
&\quad X_f^4\left[mI + \frac{1}{2}\rho B^4 m A_3^\star(K_f) + \frac{1}{2}\rho B^2 I H_4^\star(K_f) + \frac{1}{4}\rho^2 B^6\left(-H_1^\star(K_f)A_2^\star(K_f)\right.\right. \\
&\quad \left.\left. + H_4^\star(K_f)A_3^\star(K_f) + H_2^\star(K_f)A_1^\star(K_f) - H_3^\star(K_f)A_4^\star(K_f)\right)\right] + \\
&\quad X_f^3\left[\rho B^4 m\zeta_z A_2^\star(K_f) + \rho B^2 I\zeta_\alpha\frac{\omega_\alpha}{\omega_z}H_1^\star(K_f)\right] + \\
&\quad X_f^2\left[-mI\frac{\omega_\alpha^2}{\omega_z^2} - mI4\zeta_z\zeta_\alpha\frac{\omega_\alpha}{\omega_z} - mI - \frac{1}{2}\rho B^4 m A_3^\star(K_f) - \frac{1}{2}\rho B^2 I\frac{\omega_\alpha^2}{\omega_z^2}H_4^\star(K_f)\right] + \\
&\quad mI\frac{\omega_\alpha^2}{\omega_z^2}
\end{aligned} \tag{B.28}$$

$$\begin{aligned}
&A_i(X_f, K_f)X_f^3 = \\
&\quad X_f^3\left[\frac{1}{2}\rho B^4 m A_2^\star(K_f) + \frac{1}{2}\rho B^2 I H_1^\star(K_f) + \frac{1}{4}\rho^2 B^6\left(H_1^\star(K_f)A_3^\star(K_f)\right.\right. \\
&\quad \left.\left. + H_4^\star(K_f)A_2^\star(K_f) - H_2^\star(K_f)A_4^\star(K_f) - H_3^\star(K_f)A_1^\star(K_f)\right)\right] + \\
&\quad X_f^2\left[-mI2\zeta_\alpha\frac{\omega_\alpha}{\omega_z} - mI2\zeta_z - \rho B^4 m\zeta_z A_3^\star(K_f) - \rho B^2 I\zeta_\alpha\frac{\omega_\alpha}{\omega_z}H_4^\star(K_f)\right] + \\
&\quad X_f\left[-\frac{1}{2}\rho B^4 m A_2^\star(K_f) - \frac{1}{2}\rho B^2 I\frac{\omega_\alpha^2}{\omega_z^2}H_1^\star(K_f)\right] + \\
&\quad mI2\zeta_z\frac{\omega_\alpha^2}{\omega_z^2} + mI2\zeta_\alpha\frac{\omega_\alpha}{\omega_z}
\end{aligned} \tag{B.29}$$

The flutter point can also be determined graphically by the method described by Dowell et al. [8]. By using this method the real part A_r and the imaginary part A_i of the determinant (B.27) are treated independently, see equations (B.28) and (B.29). For a number of values of K over a chosen range the values $X_r(K)$ and $X_i(K)$ are calculated as solutions to the following equations

$$A_r(X_r(K), K) = 0 \tag{B.30}$$

$$A_i(X_i(K), K) = 0 \tag{B.31}$$

The flutter point is the point where the solution curves $X_r(K)$ and $X_i(K)$ cross. The flutter point is denoted (X_f, K_f). The circular flutter frequency ω_f and the flutter wind velocity U_f can determined by

$$\omega_f = X_f\omega_z \tag{B.32}$$

$$U_f = \frac{B\omega_f}{K_f} \tag{B.33}$$

When there is more than one intersection of the solution curves the flutter point corresponds to the intersection point with the largest value of K (corresponding to the smallest value of U).

B.3 Bridge Section with Flaps

The angles of the flaps are expressed in terms of the pitch angle α of the bridge section

$$\alpha(t) = \alpha_0 e^{i(\omega t - \varphi_\alpha)} \quad \Rightarrow \quad \dot{\alpha}(t) = i\omega\alpha(t) \tag{B.34}$$

$$\alpha_l(t) = \alpha_{l0} e^{i(\omega t - \varphi_\alpha - \varphi_l)} = a_l e^{-i\varphi_l}\alpha(t) \;\Rightarrow\; \dot{\alpha}_l(t) = a_l e^{-i\varphi_l} i\omega\alpha(t) = a_l e^{-i\varphi_l}\dot{\alpha}(t) \tag{B.35}$$

$$\alpha_t(t) = \alpha_{t0} e^{i(\omega t - \varphi_\alpha - \varphi_t)} = a_t e^{-i\varphi_t}\alpha(t) \;\Rightarrow\; \dot{\alpha}_t(t) = a_t e^{-i\varphi_t} i\omega\alpha(t) = a_t e^{-i\varphi_t}\dot{\alpha}(t) \tag{B.36}$$

where a_l and a_t are the flap amplification factors for the leading and trailing flap, respectively. A flap amplification factor is defined as the amplitude of the flap relative to the amplitude of the torsional motion, i.e.

$$a_l = \frac{\alpha_{l0}}{\alpha_0} \tag{B.37}$$

$$a_t = \frac{\alpha_{t0}}{\alpha_0} \tag{B.38}$$

The phase angles φ_l and φ_t for the leading and trailing flap, respectively, are relative to the torsional motion.

Hereby the total motion-induced wind load defined by equations (2.2)–(2.5), (2.15), (2.16), (2.21) and (2.22) can be written

$$\begin{aligned} F_a^P &= \frac{1}{2}\rho U^2 B \left[K H_1^\star(K)\frac{\dot{z}}{U} + K\left(H_2^\star(K) + H_5^\star(K) a_t \cos(-\varphi_t) + \right.\right. \\ &\quad H_7^\star(K) a_l \cos(-\varphi_l) + H_6^\star(K) a_t \sin(-\varphi_t) + H_8^\star(K) a_l \sin(-\varphi_l)\Big)\frac{B\dot{\alpha}}{U} + \\ &\quad K^2\left(H_3^\star(K) + H_6^\star(K) a_t \cos(-\varphi_t) + H_8^\star(K) a_l \cos(-\varphi_l) - \right. \\ &\quad \left.\left. H_5^\star(K) a_t \sin(-\varphi_t) - H_7^\star(K) a_l \sin(-\varphi_l)\right)\alpha + K^2 H_4^\star(K)\frac{z}{B}\right] \end{aligned} \tag{B.39}$$

$$\begin{aligned} F_a^M &= \frac{1}{2}\rho U^2 B^2 \left[K A_1^\star(K)\frac{\dot{z}}{U} + K\left(A_2^\star(K) + A_5^\star(K) a_t \cos(-\varphi_t) + \right.\right. \\ &\quad A_7^\star(K) a_l \cos(-\varphi_l) + A_6^\star(K) a_t \sin(-\varphi_t) + A_8^\star(K) a_l \sin(-\varphi_l)\Big)\frac{B\dot{\alpha}}{U} + \\ &\quad K^2\left(A_3^\star(K) + A_6^\star(K) a_t \cos(-\varphi_t) + A_8^\star(K) a_l \cos(-\varphi_l) - \right. \\ &\quad \left.\left. A_5^\star(K) a_t \sin(-\varphi_t) - A_7^\star(K) a_l \sin(-\varphi_l)\right)\alpha + K^2 A_4^\star(K)\frac{z}{B}\right] \end{aligned} \tag{B.40}$$

The expressions shown in section B.2 can thereby be used to estimate the flutter wind velocity for single-degree flutter in torsion and binary flutter when $H_2^\star(K)$, $H_3^\star(K)$, $A_2^\star(K)$ and $A_3^\star(K)$ are replaced by $H_2^{\star'}(K)$, $H_3^{\star'}(K)$, $A_2^{\star'}(K)$ and $A_3^{\star'}(K)$ defined as follows.

$$\begin{aligned} H_2^{\star'}(K) &= H_2^\star(K) + H_5^\star(K) a_t \cos(-\varphi_t) + H_6^\star(K) a_t \sin(-\varphi_t) + \\ &\quad H_7^\star(K) a_l \cos(-\varphi_l) + H_8^\star(K) a_l \sin(-\varphi_l) \end{aligned} \tag{B.41}$$

$$H_3^{\star'}(K) = H_3^\star(K) - H_5^\star(K)a_t\sin(-\varphi_t) + H_6^\star(K)a_t\cos(-\varphi_t) - H_7^\star(K)a_l\sin(-\varphi_l) + H_8^\star(K)a_l\cos(-\varphi_l) \quad \text{(B.42)}$$

$$A_2^{\star'}(K) = A_2^\star(K) + A_5^\star(K)a_t\cos(-\varphi_t) + A_6^\star(K)a_t\sin(-\varphi_t) + A_7^\star(K)a_l\cos(-\varphi_l) + A_8^\star(K)a_l\sin(-\varphi_l) \quad \text{(B.43)}$$

$$A_3^{\star'}(K) = A_3^\star(K) - A_5^\star(K)a_t\sin(-\varphi_t) + A_6^\star(K)a_t\cos(-\varphi_t) - A_7^\star(K)a_l\sin(-\varphi_l) + A_8^\star(K)a_l\cos(-\varphi_l) \quad \text{(B.44)}$$

B.4 Estimation of Damping by AMC Method

The Air Material Command (AMC) method described by Fung [11] can also be used to estimate the flutter wind velocity for binary flutter. By using this method the necessary structural damping of the bridge section for fulfilling the flutter condition is plotted against the mean wind velocity. Flutter occurs when the actual structural damping is exceeded.

The equations of motion (2.2) and (2.3) with insertion of the flutter condition (B.16)–(B.18) yields

$$m\left[-1+\left(\frac{\omega_z}{\omega_\alpha}\right)^2\left(\frac{\omega_\alpha}{\omega}\right)^2\left(1+2\zeta_z\frac{\omega}{\omega_z}i\right)\right]z = \frac{F_a^P}{\omega^2} \quad \text{(B.45)}$$

$$I\left[-1+\left(\frac{\omega_\alpha}{\omega}\right)^2\left(1+2\zeta_\alpha\frac{\omega}{\omega_\alpha}i\right)\right]\alpha = \frac{F_a^M}{\omega^2} \quad \text{(B.46)}$$

The following complex variable is used as unknown

$$Z = \left(\frac{\omega_\alpha}{\omega}\right)^2(1+gi) \quad \text{(B.47)}$$

where the following damping coefficients are defined

$$g_z = 2\zeta_z\frac{\omega}{\omega_z} \quad \text{(B.48)}$$

$$g_\alpha = 2\zeta_\alpha\frac{\omega}{\omega_\alpha} \quad \text{(B.49)}$$

$$g = g_z \simeq g_\alpha \quad \text{(B.50)}$$

as

$$1+ig_\alpha = 1+ig_z+i(g_\alpha-g_z) \simeq (1+ig_z)(1+i(g_\alpha-g_z)) \quad \text{(B.51)}$$

The equation of motion can thereby be written

$$m\left[-1+\left(\frac{\omega_z}{\omega_\alpha}\right)^2 Z\right]z = \frac{F_a^P}{\omega^2} \quad \text{(B.52)}$$

$$I\left[-1+Z\right]\alpha = \frac{F_a^M}{\omega^2} \tag{B.53}$$

For $\boldsymbol{x}_0 \neq \mathbf{0}$ the solution is found by

$$\det\begin{bmatrix} m\left[-1+\left(\frac{\omega_z}{\omega_\alpha}\right)^2 Z\right] - \frac{F_a^P(z)}{\omega^2} & -\frac{F_a^P(\alpha)}{\omega^2} \\ -\frac{F_a^M(z)}{\omega^2} & I\left[-1+Z\right] - \frac{F_a^M(\alpha)}{\omega^2} \end{bmatrix} = 0 \tag{B.54}$$

where $F_a^P(z)$ and $F_a^M(z)$ denote the parts of the motion-induced wind load depending on the vertical motion z, and $F_a^P(\alpha)$ and $F_a^M(\alpha)$ denote the parts of the motion-induced wind load depending on the torsional motion α.

The solution can be written

$$a_Z Z^2 + b_Z Z + c_Z = 0 \tag{B.55}$$

where

$$a_Z = \left(\frac{\omega_z}{\omega_\alpha}\right)^2 \tag{B.56}$$

$$b_Z = -1 - \left(\frac{\omega_z}{\omega_\alpha}\right)^2 - \left(\frac{\omega_z}{\omega_\alpha}\right)^2 \frac{\rho B^4}{2I}(A_2^{\star\prime}(K)i + A_3^{\star\prime}(K)) - \frac{\rho B^2}{2m}(H_1^\star(K)i + H_4^\star(K)) \tag{B.57}$$

$$\begin{aligned} c_Z \;=\; & 1 + \frac{\rho B^4}{2I}(A_2^{\star\prime}(K)i + A_3^{\star\prime}(K)) + \frac{\rho B^2}{2m}(H_1^\star(K)i + H_4^\star(K)) + \\ & \frac{\rho^2 B^6}{4mI}\Big((H_1^\star(K)i + H_4^\star(K))(A_2^{\star\prime}(K)i + A_3^{\star\prime}(K)) - \\ & (H_2^{\star\prime}(K)i + H_3^{\star\prime}(K))(A_1^\star(K)i + A_4^\star(K))\Big) \end{aligned} \tag{B.58}$$

The flutter equation (B.55) is solved for a number of reduced frequencies $K_1, K_2, \ldots$ The interesting solution to the flutter equation is

$$Z_{(-)}(K_i) = \frac{-b_Z - \sqrt{b_Z^2 - 4a_Z c_Z}}{2a_Z} \tag{B.59}$$

The circular frequency corresponding to K_i is found by

$$\omega(K_i) = \frac{\omega_\alpha}{\sqrt{\mathrm{Re}(Z_{(-)}(K_i))}} \tag{B.60}$$

The corresponding wind velocity is

$$U(K_i) = \frac{B\omega(K_i)}{K_i} \tag{B.61}$$

and the damping coefficient is

$$g(K_i) = \frac{\mathrm{Im}(Z_{(-)}(K_i))}{\mathrm{Re}(Z_{(-)}(K_i))} \tag{B.62}$$

The damping coefficient is equal to twice the necessary structural damping of the bridge section.

Appendix C

Closed-Loop Control

C.1 Motion of Model with Closed-Loop Control

The matrix equation of motion for a bridge section without flaps is written

$$\boldsymbol{M}_s\ddot{\boldsymbol{x}}(t) + \boldsymbol{C}_s\dot{\boldsymbol{x}}(t) + \boldsymbol{K}_s\boldsymbol{x}(t) = \boldsymbol{F}_{ad}(t) \tag{C.1}$$

Where $\boldsymbol{M}_s$, $\boldsymbol{C}_s$ and $\boldsymbol{K}_s$ are the mass, damping and stiffness matrices, $\boldsymbol{F}_{ad}(t)$ is the load on the bridge section without moving the flaps and $\boldsymbol{x}$ is the displacement vector, i.e.

$$\boldsymbol{x}(t) = \begin{bmatrix} z(t) \\ \alpha(t) \end{bmatrix} \tag{C.2}$$

The control action is described by $\boldsymbol{D}\boldsymbol{u}(t)$, where

$$\boldsymbol{D} = \frac{1}{2}\rho U^2 BK^2 \begin{bmatrix} H_6^\star(K) & H_8^\star(K) \\ BA_6^\star(K) & BA_8^\star(K) \end{bmatrix} \tag{C.3}$$

$$\boldsymbol{u}(t) = \begin{bmatrix} \alpha_t(t) \\ \alpha_l(t) \end{bmatrix} \tag{C.4}$$

In this formulation of the control law the control action corresponding to the first and second derivatives of the flap angles is ignored. The matrix equation of motion for a bridge section with control action is

$$\boldsymbol{M}_s\ddot{\boldsymbol{x}}(t) + \boldsymbol{C}_s\dot{\boldsymbol{x}}(t) + \boldsymbol{K}_s\boldsymbol{x}(t) = \boldsymbol{F}_{ad}(t) + \boldsymbol{D}\boldsymbol{u}(t) \tag{C.5}$$

The matrix equation of motion can be written in state-space form, see e.g. Soong [34]

$$\dot{\boldsymbol{y}}(t) = \boldsymbol{A}\boldsymbol{y}(t) + \boldsymbol{B}\boldsymbol{u}(t) + \boldsymbol{H}\boldsymbol{F}_{ad}(t) \tag{C.6}$$

where

$$\boldsymbol{y}(t) = \begin{bmatrix} \boldsymbol{x}(t) \\ \dot{\boldsymbol{x}}(t) \end{bmatrix} \tag{C.7}$$

$$\boldsymbol{A} = \begin{bmatrix} \boldsymbol{0} & \boldsymbol{I} \\ -\boldsymbol{M}_s^{-1}\boldsymbol{K}_s & -\boldsymbol{M}_s^{-1}\boldsymbol{C}_s \end{bmatrix} \tag{C.8}$$

$$\boldsymbol{B} = \begin{bmatrix} \mathbf{0} \\ \boldsymbol{M}_s^{-1}\boldsymbol{D} \end{bmatrix} \tag{C.9}$$

$$\boldsymbol{H} = \begin{bmatrix} \mathbf{0} \\ \boldsymbol{M}_s^{-1} \end{bmatrix} \tag{C.10}$$

Equations (2.4), (2.5) and (3.6) are inserted in (C.6)

$$\dot{\boldsymbol{y}}(t) = (\boldsymbol{A} + \boldsymbol{BG} + \boldsymbol{HF})\,\boldsymbol{y}(t) = \boldsymbol{A}_c\boldsymbol{y}(t) \tag{C.11}$$

where

$$\boldsymbol{F} = \frac{1}{2}\rho UK \begin{bmatrix} UKH_4^\star(K) & UBKH_3^\star(K) & BH_1^\star(K) & B^2H_2^\star(K) \\ UBKA_4^\star(K) & UB^2KA_3^\star(K) & B^2A_1^\star(K) & B^3A_2^\star(K) \end{bmatrix} \tag{C.12}$$

Equation (C.11) can e.g. be solved by using the transition matrix approach, see Meirovitch [28]. The solution is

$$\boldsymbol{y}(k\Delta t) = \boldsymbol{\Phi}_c^k(\Delta t)\boldsymbol{y}(0) \tag{C.13}$$

where the transition matrix $\boldsymbol{\Phi}_c$ has the form of a series

$$\boldsymbol{\Phi}_c(\Delta t) = \boldsymbol{I} + \Delta t\boldsymbol{A}_c + \frac{\Delta t^2}{2!}\boldsymbol{A}_c^2 + \frac{\Delta t^3}{3!}\boldsymbol{A}_c^3 + \frac{\Delta t^4}{4!}\boldsymbol{A}_c^4 + \cdots \tag{C.14}$$

The initial conditions $\boldsymbol{y}(0)$ for a structural system performing binary flutter at the circular eigenfrequency ω_f and the phase angle φ_α are found by

$$\left.\begin{array}{lll} z(t) = z_0\cos(\omega_f t) & \Rightarrow & z(0) = z_0 \\ \alpha(t) = \alpha_0\cos(\omega_f t - \varphi_\alpha) & \Rightarrow & \alpha(0) = \alpha_0\cos(-\varphi_\alpha) \\ \dot{z}(t) = -\omega_f z_0\sin(\omega_f t) & \Rightarrow & \dot{z}(0) = 0 \\ \dot{\alpha}(t) = -\omega_f\alpha_0\sin(\omega_f t - \varphi_\alpha) & \Rightarrow & \dot{\alpha}(0) = -\omega_f\alpha_0\sin(-\varphi_\alpha) \end{array}\right\} \tag{C.15}$$

where

$$\alpha_0 = \frac{\mathrm{Re}\left(\frac{\alpha_0}{z_0}e^{-\varphi_\alpha}\right)}{\cos(-\varphi_\alpha)}z_0 \tag{C.16}$$

By using the values for the bridge section model derived in section 2.3.2 the initial conditions are calculated based on the initial vertical displacement $z_0 = 0.05$ m

$$\alpha_0 = \frac{1.568}{\cos(-0.650)}0.05 = 0.098 \text{ rad} = 5.64° \tag{C.17}$$

$$\alpha(0) = 0.098 \cdot \cos(-0.650) = 0.078 \text{ rad} = 4.47° \tag{C.18}$$

$$\dot{\alpha}(0) = -6.62 \cdot 0.098 \cdot \sin(-0.650) = 0.394 \text{ rad/s} = 22.6 \text{ °/s} \tag{C.19}$$

C.2 Solution of Riccatti Equation

In order to use the classical linear optimal closed-loop control algorithm described in section 3.2 the Riccatti equation must be solved. The matrix Riccatti equation can be written

$$\dot{\boldsymbol{P}}(t) + \boldsymbol{P}(t)\boldsymbol{A} - \frac{1}{2}\boldsymbol{P}(t)\boldsymbol{B}\boldsymbol{R}^{-1}\boldsymbol{B}^T\boldsymbol{P}(t) + \boldsymbol{A}^T\boldsymbol{P}(t) + 2\boldsymbol{Q} = 0, \quad \boldsymbol{P}(t_f) = \boldsymbol{0} \tag{C.20}$$

where the matrices $\boldsymbol{A}$, $\boldsymbol{B}$, $\boldsymbol{Q}$ and $\boldsymbol{R}$ are described in section 3.2 and appendix C.1.

Solution of the Riccatti equation follows the procedure described by Meirovitch [28]. The following transformation is introduced

$$\boldsymbol{P}(t) = \boldsymbol{E}(t)\boldsymbol{F}^{-1}(t) \tag{C.21}$$

By using this transformation the Riccatti equation can be written

$$\begin{bmatrix} \dot{\boldsymbol{E}}(t) \\ \dot{\boldsymbol{F}}(t) \end{bmatrix} = \begin{bmatrix} -\boldsymbol{A}^T & -2\boldsymbol{Q} \\ -\frac{1}{2}\boldsymbol{B}\boldsymbol{R}^{-1}\boldsymbol{B}^T & \boldsymbol{A} \end{bmatrix} \begin{bmatrix} \boldsymbol{E}(t) \\ \boldsymbol{F}(t) \end{bmatrix}, \quad \boldsymbol{E}(t_f) = \boldsymbol{0}, \quad \boldsymbol{F}(t_f) = \boldsymbol{I} \tag{C.22}$$

This equation can be integrated backward in time by using the transition matrix approach for a discrete-time system, see Meirovitch [28]. The solution is

$$\begin{bmatrix} \boldsymbol{E}(k\Delta t) \\ \boldsymbol{F}(k\Delta t) \end{bmatrix} = \left(\boldsymbol{\Phi}_P^{-1}(\Delta t)\right)^k \begin{bmatrix} \boldsymbol{E}(t_f) \\ \boldsymbol{F}(t_f) \end{bmatrix} \tag{C.23}$$

where the time instants are described by $k\Delta t = 0, \Delta t, 2\Delta t, \ldots, t_f$. The transition matrix has the form of a series

$$\boldsymbol{\Phi}_P(\Delta t) = \boldsymbol{I} + \Delta t\boldsymbol{A}_P + \frac{\Delta t^2}{2!}\boldsymbol{A}_P^2 + \frac{\Delta t^3}{3!}\boldsymbol{A}_P^3 + \frac{\Delta t^4}{4!}\boldsymbol{A}_P^4 + \cdots \tag{C.24}$$

where

$$\boldsymbol{A}_P = \begin{bmatrix} -\boldsymbol{A}^T & -2\boldsymbol{Q} \\ -\frac{1}{2}\boldsymbol{B}\boldsymbol{R}^{-1}\boldsymbol{B}^T & \boldsymbol{A} \end{bmatrix} \tag{C.25}$$

As an example, the Riccatti matrix is calculated for the bridge section model used in the wind tunnel experiments described in chapters 5 and 6. The parameters of the model are shown in table 2.2. The aerodynamic derivatives for the model are approximated by the values for a flat plate shown in section 2.2. The weighting matrices are selected as shown in equations (3.4) and (3.5) with $\beta = 10$ and $\beta = 100$. It is assumed that the model performs binary flutter with $\omega_f = 6.62$ rad/s and $U_f = 8.18$ m/s, see equations (2.45) and (2.46).

The elements of the Riccatti matrix remain constant over the control period dropping rapidly to zero near the end of the control interval. Therefore, the time-dependent Riccatti matrix $\boldsymbol{P}(t)$ can be replaced by the constant matrix $\boldsymbol{P}$ corresponding to the first part of the control period. The constant Riccatti matrix is shown below for $\beta = 10$ and $\beta = 100$.

$$\beta = 10 \quad \Rightarrow \quad \boldsymbol{P}_{10} = \begin{bmatrix} 331.99 & -10.09 & 14.65 & -1.33 \\ -10.09 & 59.24 & 3.23 & 0.50 \\ 14.65 & 3.23 & 8.32 & -0.41 \\ -1.33 & 0.50 & -0.41 & 0.55 \end{bmatrix} \tag{C.26}$$

$$\beta = 100 \quad \Rightarrow \quad \boldsymbol{P}_{100} = \begin{bmatrix} 722.67 & -5.99 & 17.46 & -1.86 \\ -5.99 & 151.92 & 6.61 & 0.53 \\ 17.46 & 6.61 & 25.23 & -0.26 \\ -1.86 & 0.53 & -0.26 & 1.47 \end{bmatrix} \tag{C.27}$$

Appendix D

Neural Networks

D.1 Multi Layer Perceptron Neural Networks

The neural networks used are structured as Multi Layer Perceptron (MLP) neural networks, see e.g. Hertz et al. [19]. The MLP neural networks contain:

- An input layer with n_I input neurons with linear neuron functions without offsets.
- A fictitious input layer with one neuron with constant value '1'.
- A hidden layer with a sufficient number of neurons n_H with non-linear neuron functions including offsets. The non-linear neuron function used is the tanh-function.

$$\tanh(x) = \frac{e^x - e^{-x}}{e^x + e^{-x}} = \frac{e^{2x} - 1}{e^{2x} + 1} \tag{D.1}$$

  The output of the tanh-function is between -1 and 1. Offsets in the hidden layer are organized by adding the fictitious input neuron. The necessary number of neurons is found by trial and error.

- An output layer with n_O neurons with linear neuron functions.

There are connections between all input neurons (including the fictitious one) and all hidden neurons. The weight $w_{hi,H}$ is to the hidden neuron h from the input neuron i. In the same way there are connections between all hidden neurons and all output neurons. The weight $w_{oh,O}$ is to the output neuron o from the hidden neuron h. The neural network is illustrated in figure D.1.

D.1.1 Feedforward

The output $O_1, \ldots, O_{n_O}$ of the network can be calculated based on the weights and the input $I_1, \ldots, I_{n_I+1}$.

The activation A_h of the hth neuron in the hidden layer is

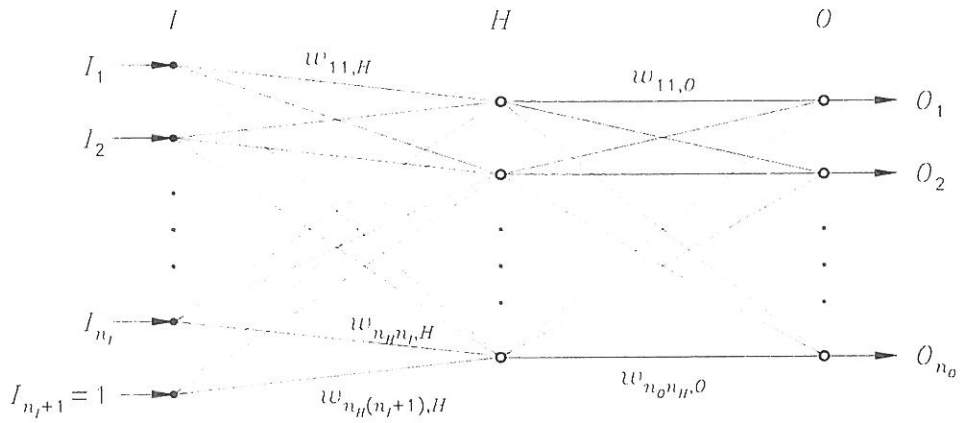

Figure D.1: Structure of MLP neural network with three layers: input (I), hidden (H) and output (O).

$$A_h = \sum_{i=1}^{n_I+1} w_{hi,H} I_i \tag{D.2}$$

The output H_h of the hth hidden neuron is

$$H_h = \tanh(A_h) = \tanh\left(\sum_{i=1}^{n_I+1} w_{hi,H} I_i\right) \tag{D.3}$$

The activation A_o and the output O_o of the oth neuron in the output layer are

$$A_o = \sum_{h=1}^{n_H} w_{oh,O} H_h \tag{D.4}$$

$$O_o = A_o = \sum_{h=1}^{n_H} w_{oh,O} \tanh\left(\sum_{i=1}^{n_I+1} w_{hi,H} I_i\right) \tag{D.5}$$

D.1.2 Deviations of Network Output

During training of a neural network an error or a performance index is minimized by changing the weights of the network. In the minimization algorithm the gradients of the error or performance index with regard to the input and weights are needed. In the following the deviations of the output of the neural network with regard to the input values and the weights are shown. An underlined index denotes a weight or input value being differentiated with regard to.

Deviations of the output with regard to the input values

$$\begin{aligned}\frac{\partial O_{\underline{o}}}{\partial I_{\underline{i}}} &= \frac{\partial}{\partial I_{\underline{i}}}\left(\sum_{h=1}^{n_H} w_{\underline{o}h,O} \tanh\left(\sum_{i=1}^{n_I+1} w_{hi,H} I_i\right)\right) \\ &= \sum_{h=1}^{n_H} w_{\underline{o}h,O} \frac{\partial}{\partial I_{\underline{i}}}\left(\tanh\left(\sum_{i=1}^{n_I+1} w_{hi,H} I_i\right)\right)\end{aligned}$$

$$= \sum_{h=1}^{n_H} w_{\underline{o}h,O} w_{h\underline{i},H} \tanh'\left(\sum_{i=1}^{n_I+1} w_{hi,H} I_i\right) \tag{D.6}$$

where

$$\tanh'(x) = \frac{4e^{2x}}{(e^{2x}+1)^2} \tag{D.7}$$

Deviations of the output with regard to the weights between the input and hidden layers

$$\begin{aligned}\frac{\partial O_{\underline{o}}}{\partial w_{\underline{h}i,H}} &= \frac{\partial}{\partial w_{\underline{h}i,H}}\left(\sum_{h=1}^{n_H} w_{\underline{o}h,O} \tanh\left(\sum_{i=1}^{n_I+1} w_{hi,H} I_i\right)\right) \\ &= w_{\underline{o}\underline{h},O} \frac{\partial}{\partial w_{\underline{h}i,H}}\left(\tanh\left(\sum_{i=1}^{n_I+1} w_{\underline{h}i,H} I_i\right)\right) \\ &= w_{\underline{o}\underline{h},O} I_{\underline{i}} \tanh'\left(\sum_{i=1}^{n_I+1} w_{\underline{h}i,H} I_i\right)\end{aligned} \tag{D.8}$$

Deviations of the output with regard to the weights between the hidden and output layers

$$\begin{aligned}\frac{\partial O_{\underline{o}}}{\partial w_{\underline{o}\underline{h},O}} &= \frac{\partial}{\partial w_{\underline{o}\underline{h},O}}\left(\sum_{h=1}^{n_H} w_{\underline{o}h,O} \tanh\left(\sum_{i=1}^{n_I+1} w_{hi,H} I_i\right)\right) \\ &= \begin{cases} \tanh\left(\sum_{i=1}^{n_I+1} w_{\underline{h}i,H} I_i\right) & \text{for } \underline{o} = o \\ 0 & \text{for } \underline{o} \neq o \end{cases}\end{aligned} \tag{D.9}$$

D.2 Discrete State-Space Equation of Motion

The matrix equation of motion in discrete state-space form for the bridge section model with flap control is

$$\dot{\boldsymbol{y}}(k) = (\boldsymbol{A} + \boldsymbol{H}\boldsymbol{F})\boldsymbol{y}(k) + \boldsymbol{B}'\boldsymbol{u}'(k) \tag{D.10}$$

where k is the time instant and

$$\boldsymbol{y}(k) = \begin{bmatrix} z(k) \\ \alpha(k) \\ \dot{z}(k) \\ \dot{\alpha}(k) \end{bmatrix} \tag{D.11}$$

$$\boldsymbol{u}'(k) = \begin{bmatrix} \alpha_t(k) \\ \alpha_l(k) \\ \dot{\alpha}_t(k) \\ \dot{\alpha}_l(k) \end{bmatrix} \tag{D.12}$$

$$\boldsymbol{A} = \begin{bmatrix} \boldsymbol{0} & \boldsymbol{I} \\ -\boldsymbol{M}_s^{-1}\boldsymbol{K}_s & -\boldsymbol{M}_s^{-1}\boldsymbol{C}_s \end{bmatrix} \tag{D.13}$$

$$\boldsymbol{H} = \begin{bmatrix} \mathbf{0} \\ \boldsymbol{M}_s^{-1} \end{bmatrix} \tag{D.14}$$

$$\boldsymbol{F} = \frac{1}{2}\rho UK \begin{bmatrix} UKH_4^\star(K) & UBKH_3^\star(K) & BH_1^\star(K) & B^2H_2^\star(K) \\ UBKA_4^\star(K) & UB^2KA_3^\star(K) & B^2A_1^\star(K) & B^3A_2^\star(K) \end{bmatrix} \tag{D.15}$$

$$\boldsymbol{B}' = \begin{bmatrix} \mathbf{0} \\ \boldsymbol{M}_s^{-1}\boldsymbol{D}' \end{bmatrix} \tag{D.16}$$

$$\boldsymbol{D}' = \frac{1}{2}\rho UBK \begin{bmatrix} UKH_6^\star(K) & UKH_8^\star(K) & BH_5^\star(K) & BH_7^\star(K) \\ UBKA_6^\star(K) & UBKA_8^\star(K) & B^2A_5^\star(K) & B^2A_7^\star(K) \end{bmatrix} \tag{D.17}$$

$\boldsymbol{M}_s$, $\boldsymbol{C}_s$ and $\boldsymbol{K}_s$ are the structural mass, damping and stiffness matrices.

By using the approximation

$$\dot{\boldsymbol{y}}(k) \approx \frac{1}{\Delta t}(\boldsymbol{y}(k+1) - \boldsymbol{y}(k)) \tag{D.18}$$

where Δt is the time step, the matrix equation of motion can be written

$$\boldsymbol{y}(k+1) \approx (\mathbf{1} + \Delta t(\boldsymbol{A} + \boldsymbol{HF}))\boldsymbol{y}(k) + \Delta t\boldsymbol{Bu}(k) \tag{D.19}$$

where $\mathbf{1}$ is a 4×4 unity matrix.

Appendix E

Parameters for Bridge Section Model

E.1 Model Laws

Ratios between such quantities as e.g. length, frequency, density and velocity must be maintained constant from prototype to model, see Simiu & Scanlan [33]. Since this holds true for geometric ratios as well as geometric shapes in general it implies that all model shapes must be geometrically similar to prototype shapes and that vibrational modal shapes of the prototype must be maintained in the model. Likewise, frequencies from all sources must bear the same ratios to each other in model as in prototype. Further, since oscillatory deflections must maintain proper proportionality from prototype to model, non-dimensional damping ratios that affect such deflections must remain the same in prototype and model.

The assumed ('typical') values of width, mass, etc. for the prototype bridge and long flaps are shown in table 5.2.

In the following index p denotes the prototype, and index m denotes the model. Three scaling factors can be arbitrarily chosen. The first factor is an arbitrary length scale

$$\lambda_L = \frac{B_m}{B_p} = \frac{1}{40} \tag{E.1}$$

set by comparison of model width B'_m to prototype width B'_p. By this choice of λ_L there is enough room for a part of the regulation system to be fixed inside the model. The length of the model is 1.48 m, see section 5.4. The aspect ratio is then 2.37 for the bridge section model without flaps.

A second choice of factor is a convenient wind velocity scale

$$\lambda_V = \frac{U_{cr,m}}{U_{cr,p}} = \frac{1}{4} \tag{E.2}$$

set by comparison of the model flutter velocity $U_{cr,m} \approx 10$ m/s to the prototype flutter velocity $U_{cr,p}$, see Appendix E.2.

A third choice of factor is a mass density scale

$$\lambda_\rho = \frac{\rho_m}{\rho_p} = 1 \tag{E.3}$$

as the experiments are performed in air of the same mass density ρ as that surrounding the prototype.

Given the fundamental exigencies of mass, length and time, the three fixed scale choices condition all others in consequence of the requirement that the non-dimensional groups maintain their constancy from prototype to model and vice versa.

The frequency scale λ_F is set by the requirement that the reduced velocity in the prototype and the model must be the same, i.e.

$$\frac{U_p}{f_p B'_p} = \frac{U_m}{f_m B'_m} \quad \Rightarrow \quad \lambda_F = \frac{f_m}{f_p} = \frac{\lambda_V}{\lambda_L} = 10 \tag{E.4}$$

where U is the wind velocity and f is the frequency. The reciprocal of λ_F is the time scale $\lambda_T = 1/10$.

The scale λ_μ between the mass per unit length μ in the prototype and in the model is

$$\frac{\mu_p}{\rho_p B'^2_p} = \frac{\mu_m}{\rho_m B'^2_m} \quad \Rightarrow \quad \lambda_\mu = \lambda_L^2 = \frac{1}{1600} \tag{E.5}$$

where ρ is the mass density of surroundings.

The scale λ_I between the mass moment of inertia per unit length I in the prototype and in the model is

$$\frac{I_p}{\rho_p B_p^4} = \frac{I_m}{\rho_m B_m^4} \quad \Rightarrow \quad \lambda_I = \lambda_L^4 = \frac{1}{2.56 \cdot 10^6} \tag{E.6}$$

E.2 Flutter Velocities for Prototype and Model

The critical flutter velocity U_{cr} can be found by the Selberg formula [23]

$$\frac{U_{cr}}{f_2 B} = 3.72 \sqrt{\frac{\sqrt{I\mu}}{\rho B^3}\left[1 - \left(\frac{f_1}{f_2}\right)^2\right]} \tag{E.7}$$

where I is the mass moment of inertia per unit length, μ is the mass per unit length, ρ is the air density (1.2 $^{\mathrm{kg}}/_{\mathrm{m}^3}$), $B = 1.5B'$ is the width of the bridge with the longest flaps, f_1 is the bending eigenfrequency and f_2 is the torsional eigenfrequency.

The constants used for the prototype are listed in table 5.2. The flutter velocity for the prototype is

$$\begin{aligned} U_{cr,p} &= 3.72 \sqrt{\frac{\sqrt{2.1 \cdot 10^6 \cdot 25 \cdot 10^3}}{1.2 \cdot (1.5 \cdot 25)^3}\left[1 - \left(\frac{0.08}{0.16}\right)^2\right]} \cdot 0.16 \cdot 1.5 \cdot 25 \\ &= 36.78 \ {}^{\mathrm{m}}/_{\mathrm{s}} \end{aligned} \tag{E.8}$$

Above, $I \approx I_b$ and $\mu \approx \mu_b$ are used.

The desired flutter velocity for the prototype is approximately 10 $^{\mathrm{m}}/_{\mathrm{s}}$. The following wind velocity scale is then selected

$$\lambda_V = \frac{U_{cr,m}}{U_{cr,p}} = \frac{1}{4} \tag{E.9}$$

whereby the flutter velocity in the model is $U_{cr,m} = 9.2$ $^{\mathrm{m}}/_{\mathrm{s}}$. This implies the following frequency scale $\lambda_F = 10$, see equation (E.4). The mass moment of inertia per unit length I_m times the mass per unit length μ_m can then be determined for the model.

$$U_{cr,m} = 3.72\sqrt{\frac{\sqrt{I_m\mu_m}}{1.2\cdot(1.5\cdot 0.625)^3}\left[1-\left(\frac{10\cdot 0.08}{10\cdot 0.16}\right)^2\right]}\cdot 10\cdot 0.16\cdot 1.5\cdot 0.625 \quad \Rightarrow$$

$$I_m\mu_m = 12.82 \text{ kg}^2 \tag{E.10}$$

which is in accordance with the calculated values in table 5.2, where $I_m = 15.6$ kg m^2/m and $\mu_m = 0.820$ kg/m, i.e. $I_m\mu_m = 12.79$ kg^2.

E.3 Spring Stiffness for Suspension System

The spring constant k for each suspension point is adjusted so that the two-dimensional model has the same eigenfrequency as the lowest symmetric bending eigenmode of the real bridge, depending on the model laws.

The first eigenfrequency (bending) $f_{1,m}$ for the model is

$$f_{1,m} = 0.8 \text{ Hz} \quad \Rightarrow \quad \omega_{1,m} = 2\pi f_{1,m} = 5.03 \text{ rad/s} \tag{E.11}$$

where $\omega_{1,m}$ is the first circular eigenfrequency (bending) for the model. Total stiffness $(4k)$ of springs

$$\sqrt{\frac{4k}{m}} = \omega_{1,m} \quad \Rightarrow \quad 4k = \omega_{1,m}^2 m = 5.03^2 m \tag{E.12}$$

The mass of the model including flaps m is shown in table 5.3.

Stiffness k_l for model with long flaps

$$4k_l = 5.03^2 \cdot 26.553 = 671.0 \text{ } ^{\mathrm{N}}/_{\mathrm{m}} \quad \Rightarrow \quad k_l = 167.7 \text{ } ^{\mathrm{N}}/_{\mathrm{m}} \tag{E.13}$$

Stiffness k_s for model with short flaps

$$4k_s = 5.03^2 \cdot 25.720 = 649.8 \text{ } ^{\mathrm{N}}/_{\mathrm{m}} \quad \Rightarrow \quad k_s = 162.5 \text{ } ^{\mathrm{N}}/_{\mathrm{m}} \tag{E.14}$$

The stiffness of a spring is selected as

$$k = 165 \text{ } ^{\mathrm{N}}/_{\mathrm{m}} \tag{E.15}$$

Thereby, the first eigenfrequency (bending) for the model with long and short flaps is

$$f_{1,ml} = \frac{1}{2\pi}\sqrt{\frac{660}{26.553}} = 0.79 \text{ Hz} \tag{E.16}$$

$$f_{1,ms} = \frac{1}{2\pi}\sqrt{\frac{660}{25.720}} = 0.81 \text{ Hz} \tag{E.17}$$

which is in accordance with the assumed value $f_{1,m} = 0.8$ Hz, see table 5.2.

E.4 Specifications for Servo System

Specifications for servo amplifier, servo motor and reduction gear:

Servo amplifier	DigitAx type DB140, 3·380 V, 50 Hz, maximum motor effect/current: 1.4 kW/2.8 A.
Servo-motor	DutymAx DS type 75DSA013301 with brake, standard connector, rated torque: 1.2 Nm, rated power: 0.4 kW, power dissipated: 140–180 W, efficiency range: 77–82 %. Dimensions: 75 × 75.5 × 225 mm (125.4×75.5×48.4 mm). Weight: 3.0 kg. Brake specifications: holding torque: 2 Nm, weight: 0.3 kg.
Reduction gear	Harmonic type HDGP33, $i = 1 : 12$, load limit: 12 Nm, efficiency range: 96–98 %. Dimensions: 75 × 75 × 162.5 mm. Weight: 2.45 kg.

Appendix F

Damping Experiments

F.1 List of Experiments

The following tables show lists of the damping experiments performed. There is a table for each flap configuration defined in section 6.2. A damping experiment is stored in a file with the name: *Filename.Extension*, where *Filename* and *Extension* are shown in the tables. Thus, results of damping experiments without wind ($U = 0$ m/s), vertical motion and flap configuration 0 are stored in the following files: 00000000.000, 00000000.001, 00000000.002, 00000000.003 and 00000000.004.

U [m/s]	Main motion	File name	Extensions
0.0	vertical	00000000	000, 001, 002, 003, 004
0.0	torsional	00000000	007, 008, 009, 010
0.0	vertical/torsional	00000000	017, 018, 019, 020
2.5	vertical/torsional	00000000	022, 023, 024, 025, 026
4.0	vertical/torsional	00000000	027, 028, 029, 030, 031, 032
5.9	vertical/torsional	00000000	033, 034, 035, 036, 037
7.1	vertical/torsional	00000000	038, 039, 040, 041, 042
7.5	vertical/torsional	00000000	048, 049, 051, 052
7.8	vertical/torsional	00000000	053, 055, 056, 057, 058, 059
7.9	vertical/torsional	00000000	060, 061, 062
8.2	vertical/torsional	00000000	069, 070

Table F.1: List of damping experiments for flap configuration 0.

U [m/s]	Main motion	File name	Extensions
0.0	torsional	-0606000	000, 001, 002, 004
0.0	vertical/torsional	-0606000	005, 006
2.5	vertical/torsional	-0606000	007, 008, 009, 010, 011
4.0	vertical/torsional	-0606000	013, 014, 015, 016, 017
5.9	vertical/torsional	-0606000	018, 019, 020, 021, 022
7.1	vertical/torsional	-0606000	023, 024, 025, 026

Table F.2: List of damping experiments for flap configuration 1.

U [m/s]	Main motion	File name	Extensions
0.0	torsional	-2020000	000, 001, 002, 003, 004
0.0	vertical/torsional	-2020000	005, 006
2.8	vertical/torsional	-2020000	008, 009, 010, 011, 012
4.1	vertical/torsional	-2020000	013, 014, 015, 016, 017
6.1	vertical/torsional	-2020000	018, 019

Table F.3: List of damping experiments for flap configuration 2.

U [m/s]	Main motion	File name	Extensions
0.0	torsional	06-06000	001, 002, 003, 004, 005
0.0	vertical/torsional	06-06000	006, 007
2.5	vertical/torsional	06-06000	008, 009, 010, 011, 012
4.0	vertical/torsional	06-06000	013, 014, 015, 016
5.9	vertical/torsional	06-06000	017, 018, 019, 020, 021
7.1	vertical/torsional	06-06000	022, 023

Table F.4: List of damping experiments for flap configuration 3.

U [m/s]	Main motion	File name	Extensions
2.8	vertical/torsional	20-20000	000, 001, 002, 003, 004
4.2	vertical/torsional	20-20000	005, 006, 007, 008, 009
6.1	vertical/torsional	20-20000	010, 011, 012, 013, 014

Table F.5: List of damping experiments for flap configuration 4.

F.2 Graphs of Selected Experiments

For each type of damping experiment the first experiment is selected. For the selected experiments graphs show the vertical motion, torsional motion and flap positions.

In most of the experiments the mean value of the vertical displacement z is not zero. During the experiments the flaps are regulated based on the torsional motion α, i.e. the regulation is independent of the value of z. When the time series are analysed they are justified so the mean value is zero.

Because of the very slow regulation the actual positions of the flaps α_{ta} and α_{la} are smooth although they are regulated based on the noisy torsional angle of the bridge section.

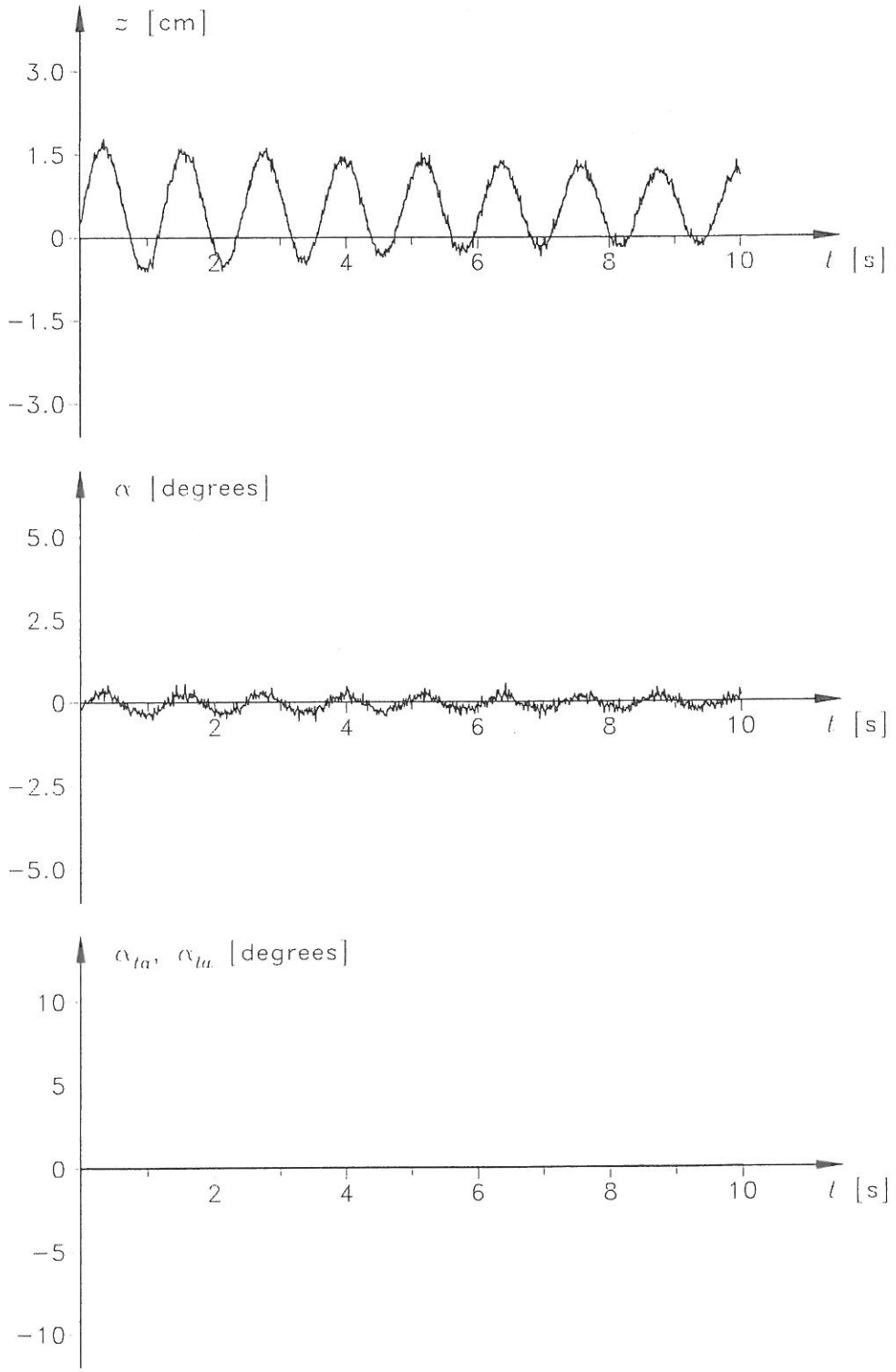

Figure F.1: Vertical motion, torsional motion and flap positions for experiment 00000000.000.

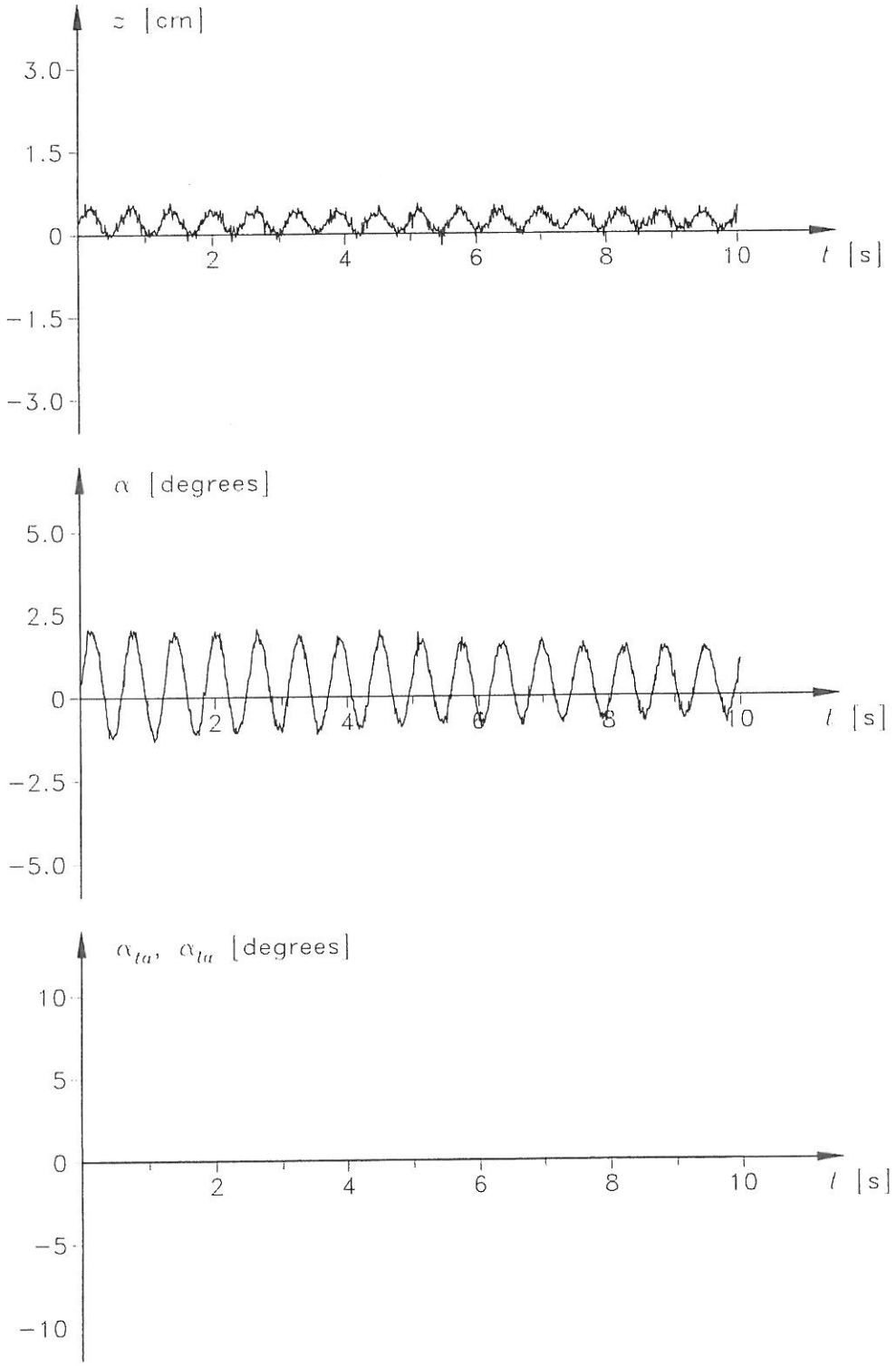

Figure F.2: Vertical motion, torsional motion and flap positions for experiment 00000000.007.

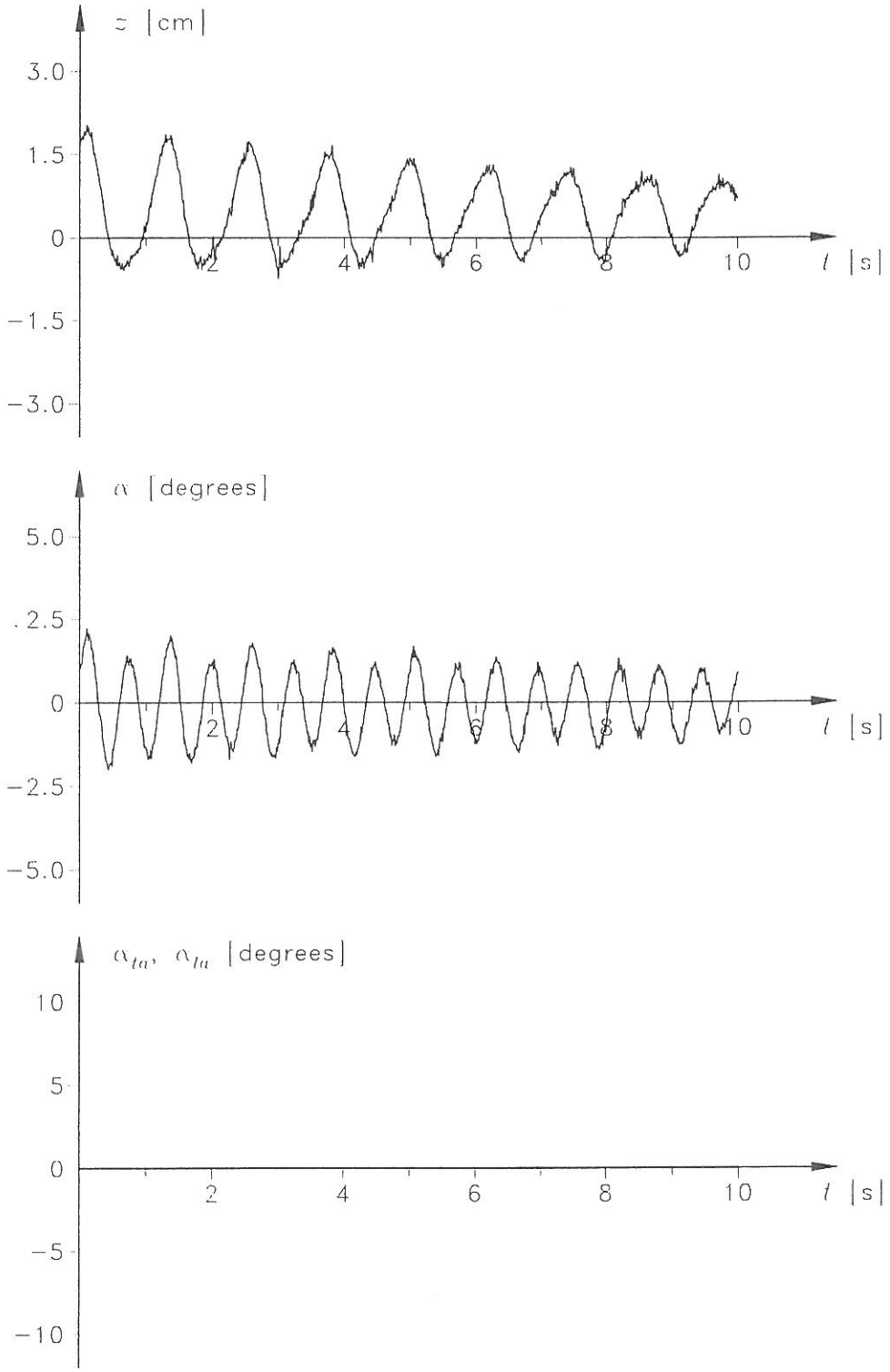

Figure F.3: Vertical motion, torsional motion and flap positions for experiment 00000000.017.

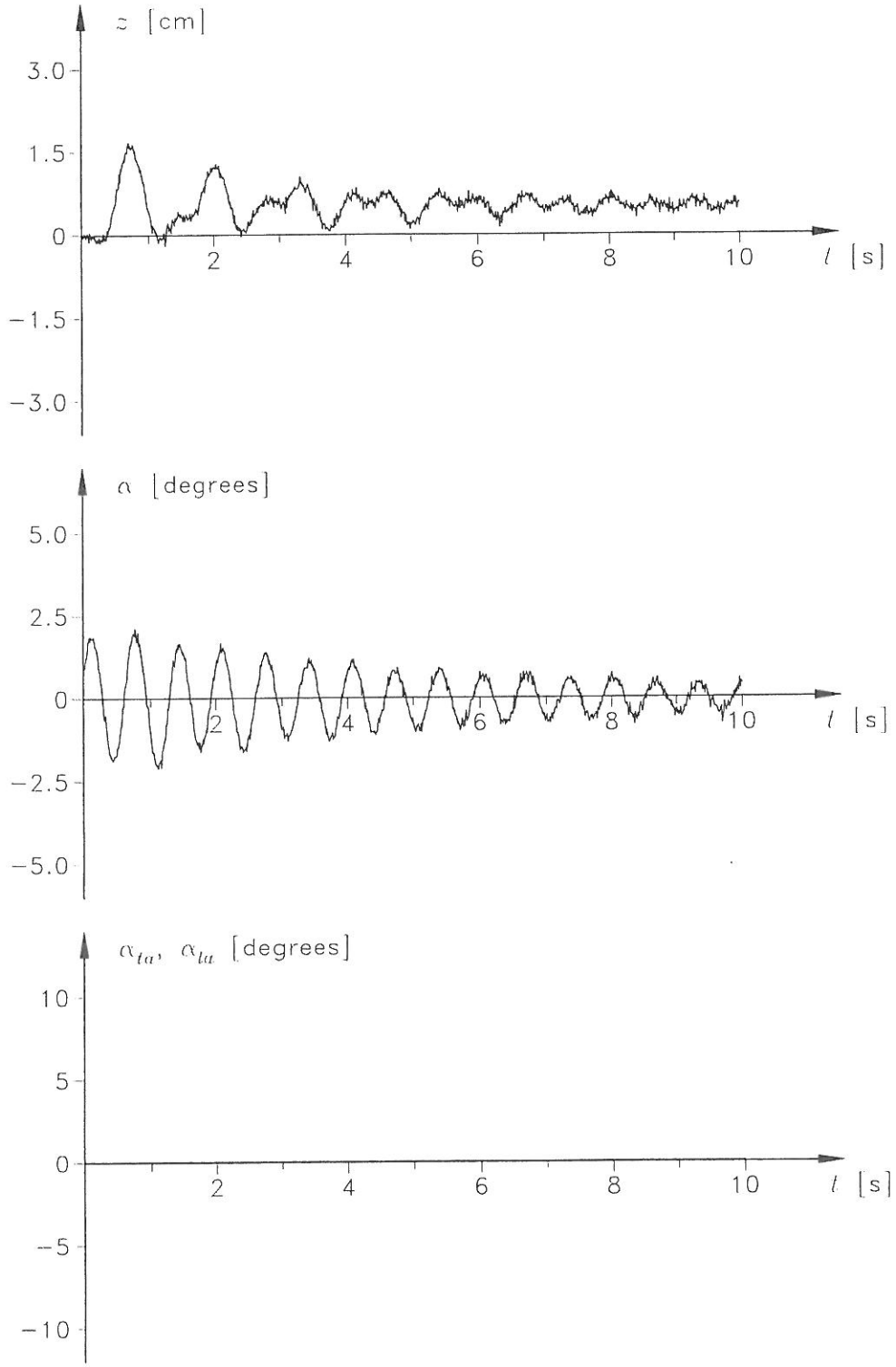

Figure F.4: Vertical motion, torsional motion and flap positions for experiment 00000000.022.

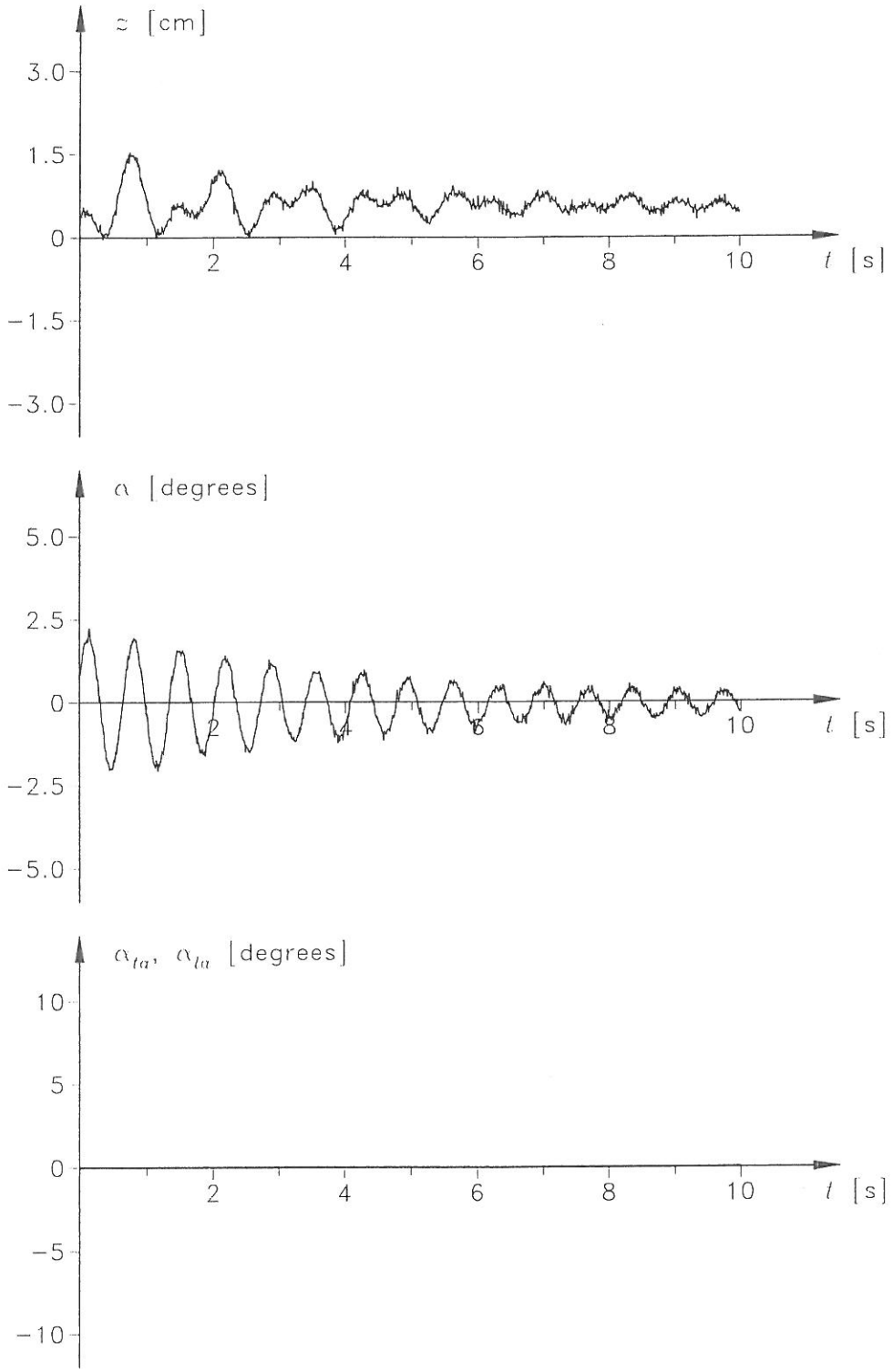

Figure F.5: Vertical motion, torsional motion and flap positions for experiment 00000000.027.

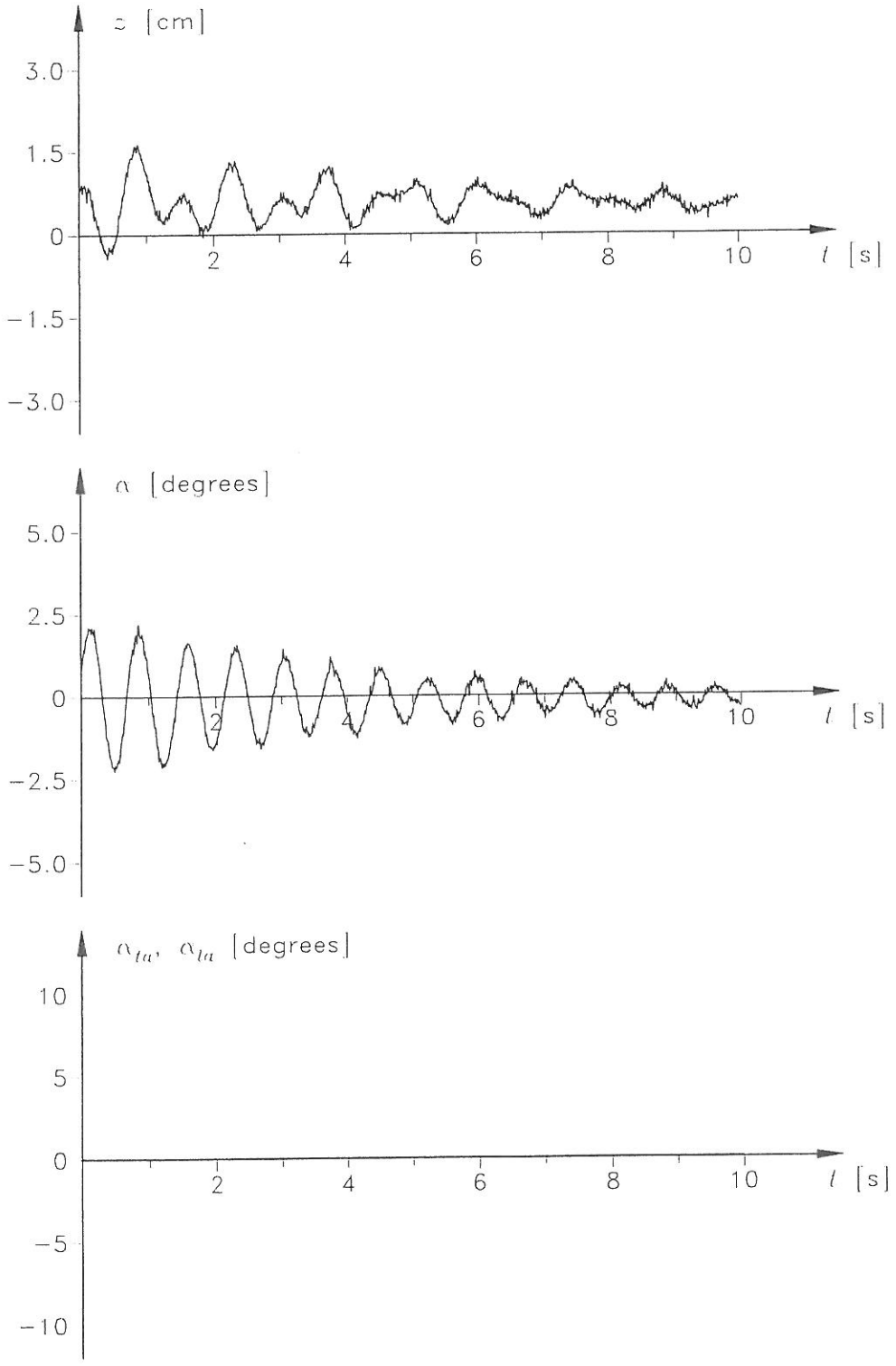

Figure F.6: Vertical motion, torsional motion and flap positions for experiment 00000000.033.

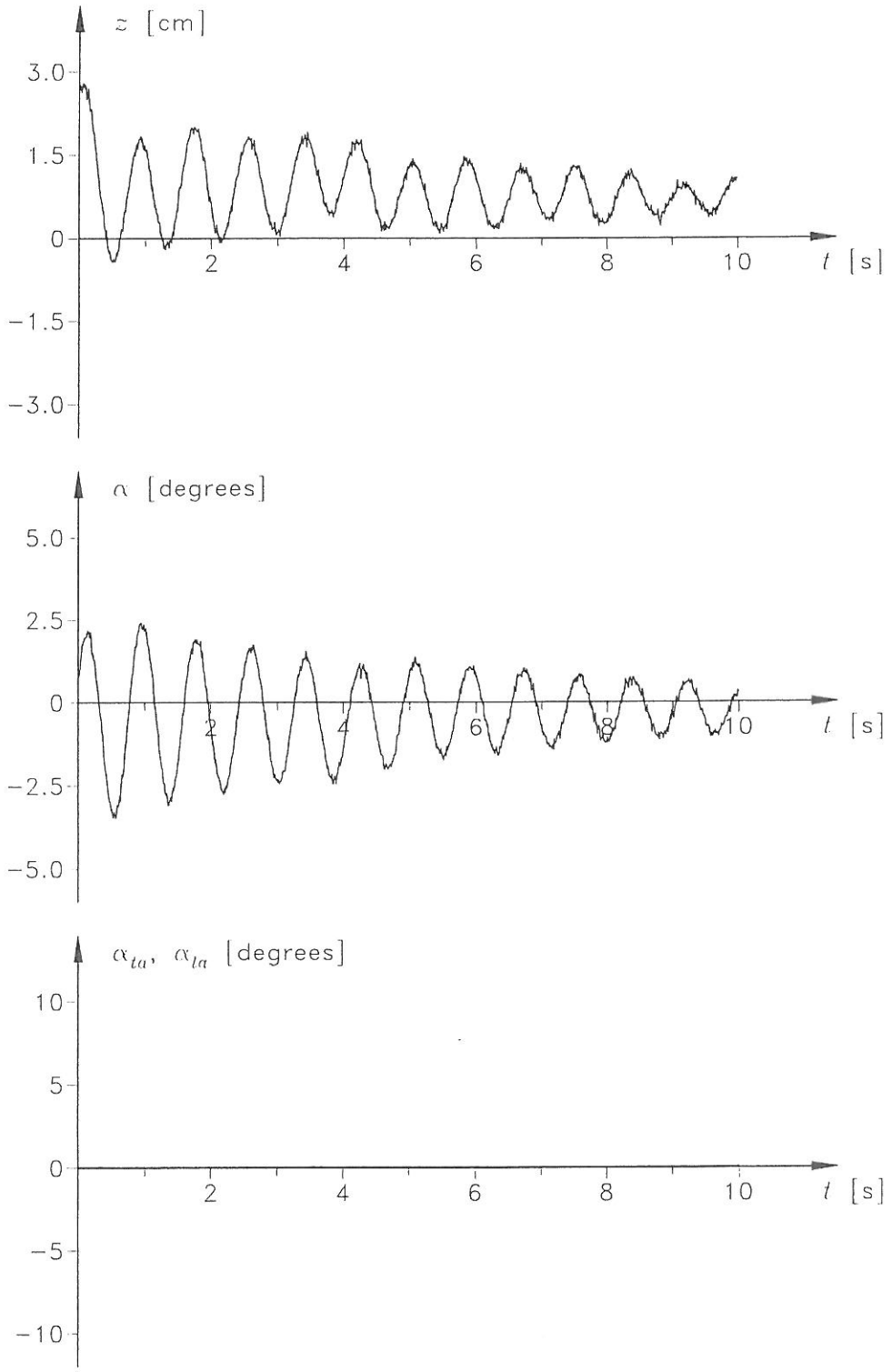

Figure F.7: Vertical motion, torsional motion and flap positions for experiment 00000000.038.

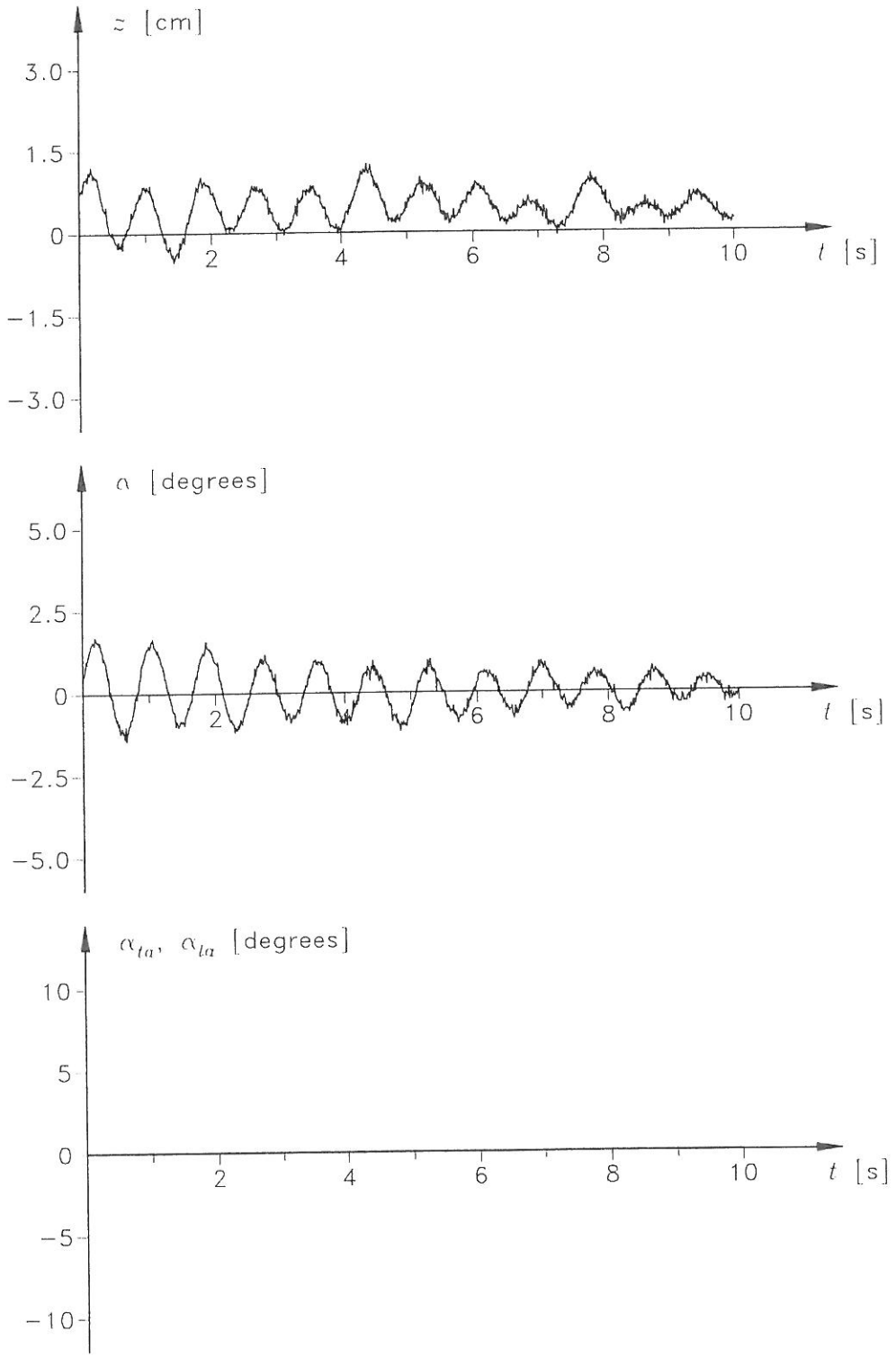

Figure F.8: Vertical motion, torsional motion and flap positions for experiment 00000000.048.

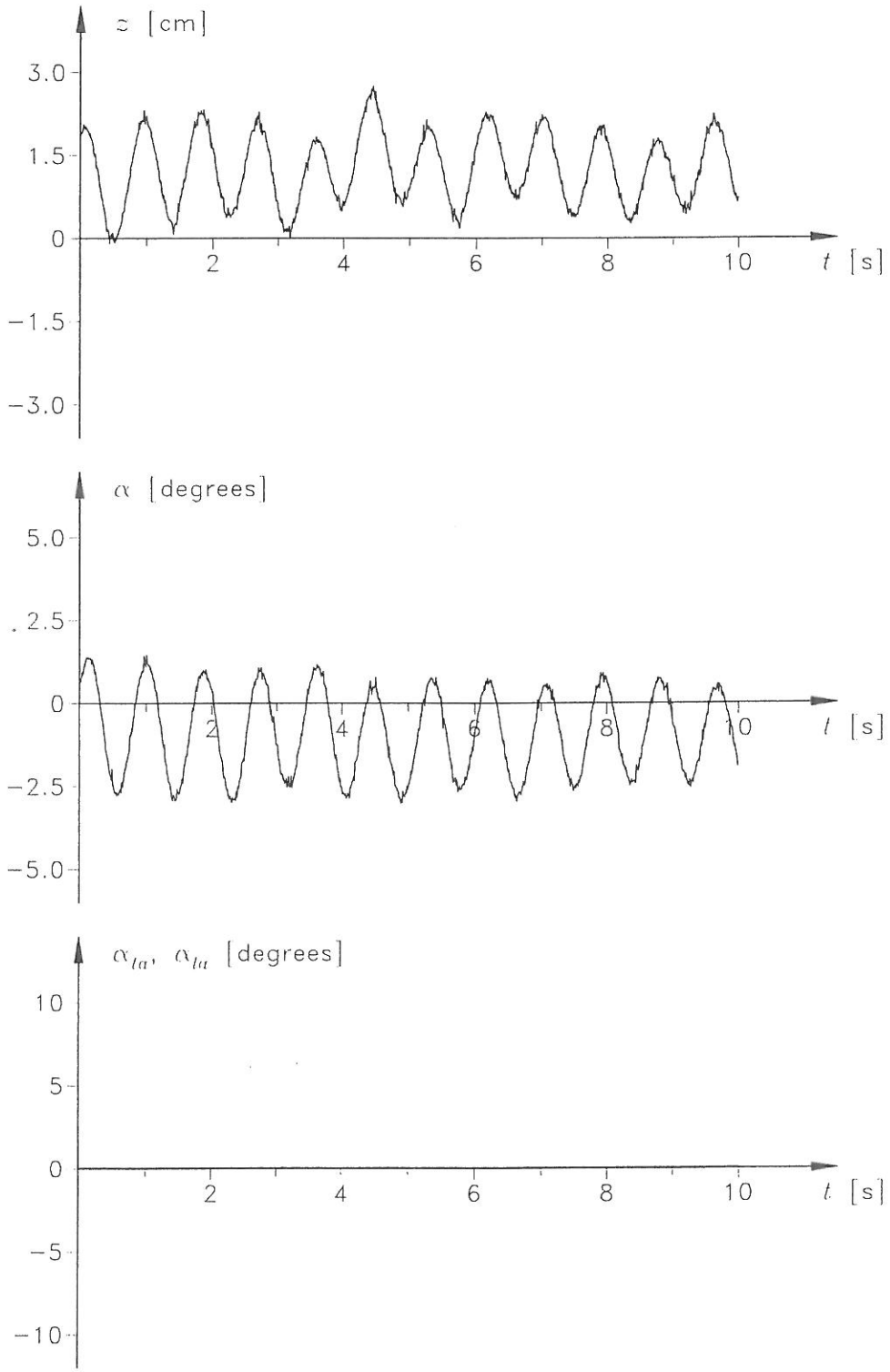

Figure F.9: Vertical motion, torsional motion and flap positions for experiment 00000000.053.

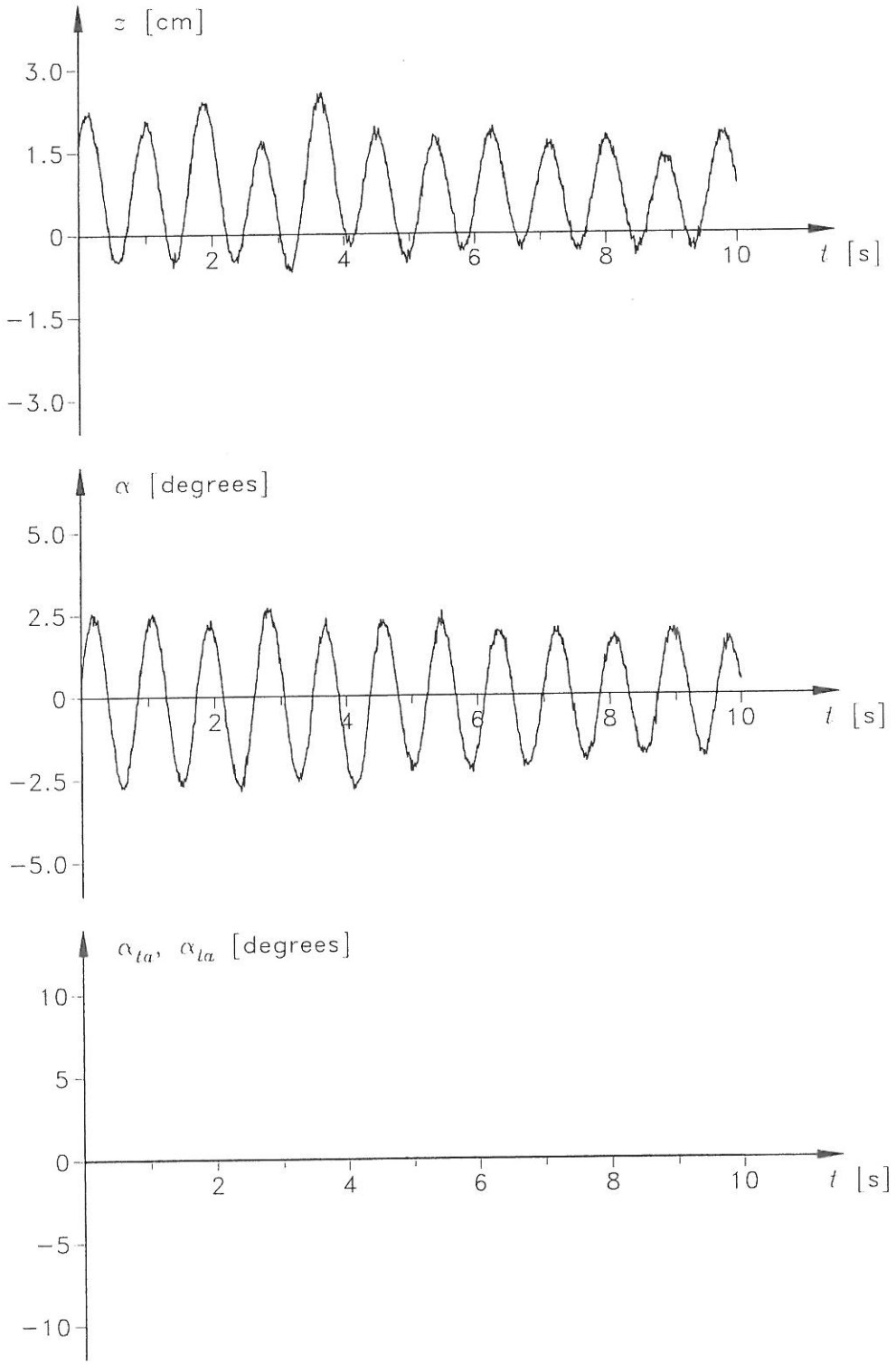

Figure F.10: Vertical motion, torsional motion and flap positions for experiment 00000000.060.

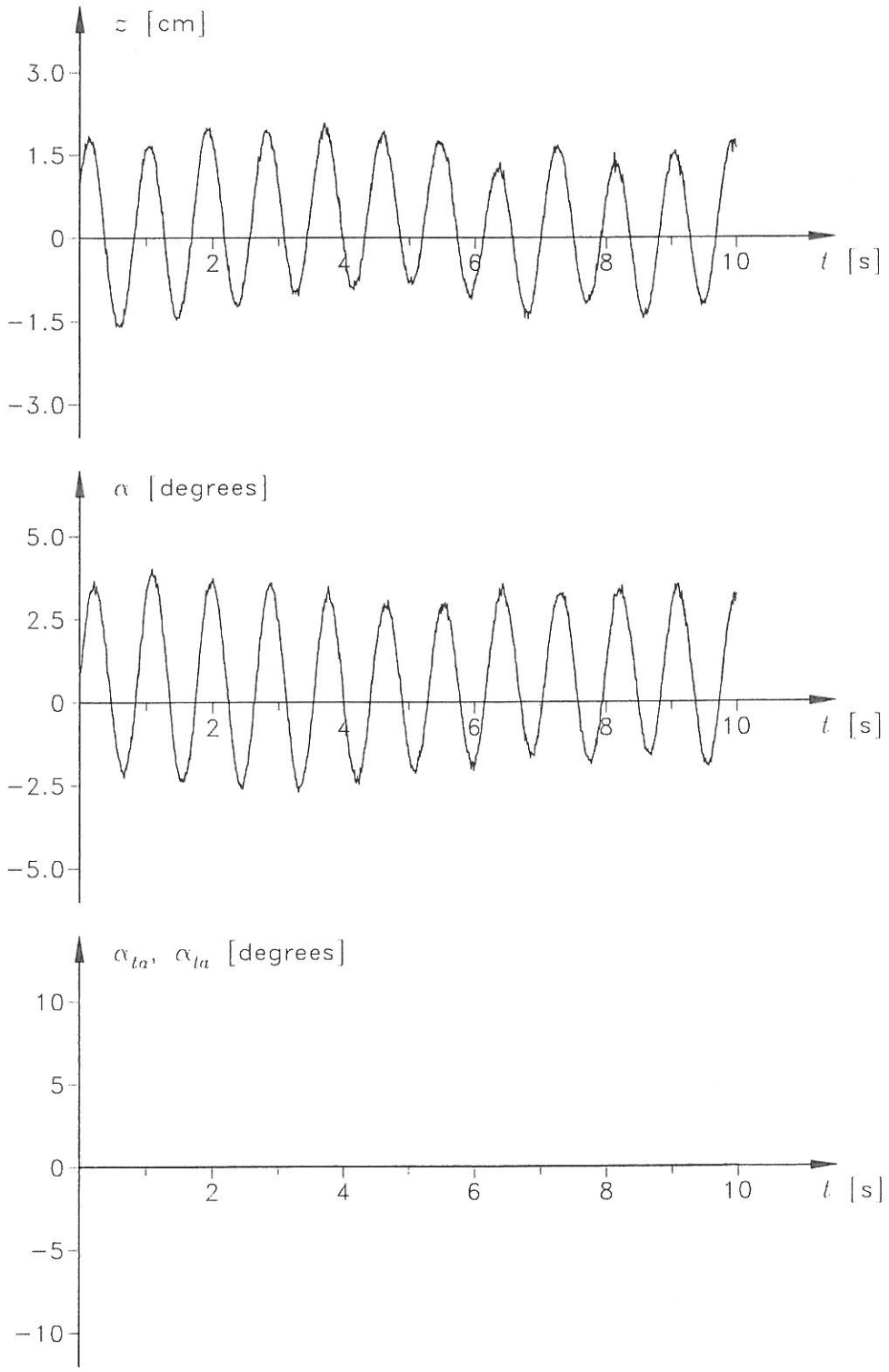

Figure F.11: Vertical motion, torsional motion and flap positions for experiment 00000000.069.

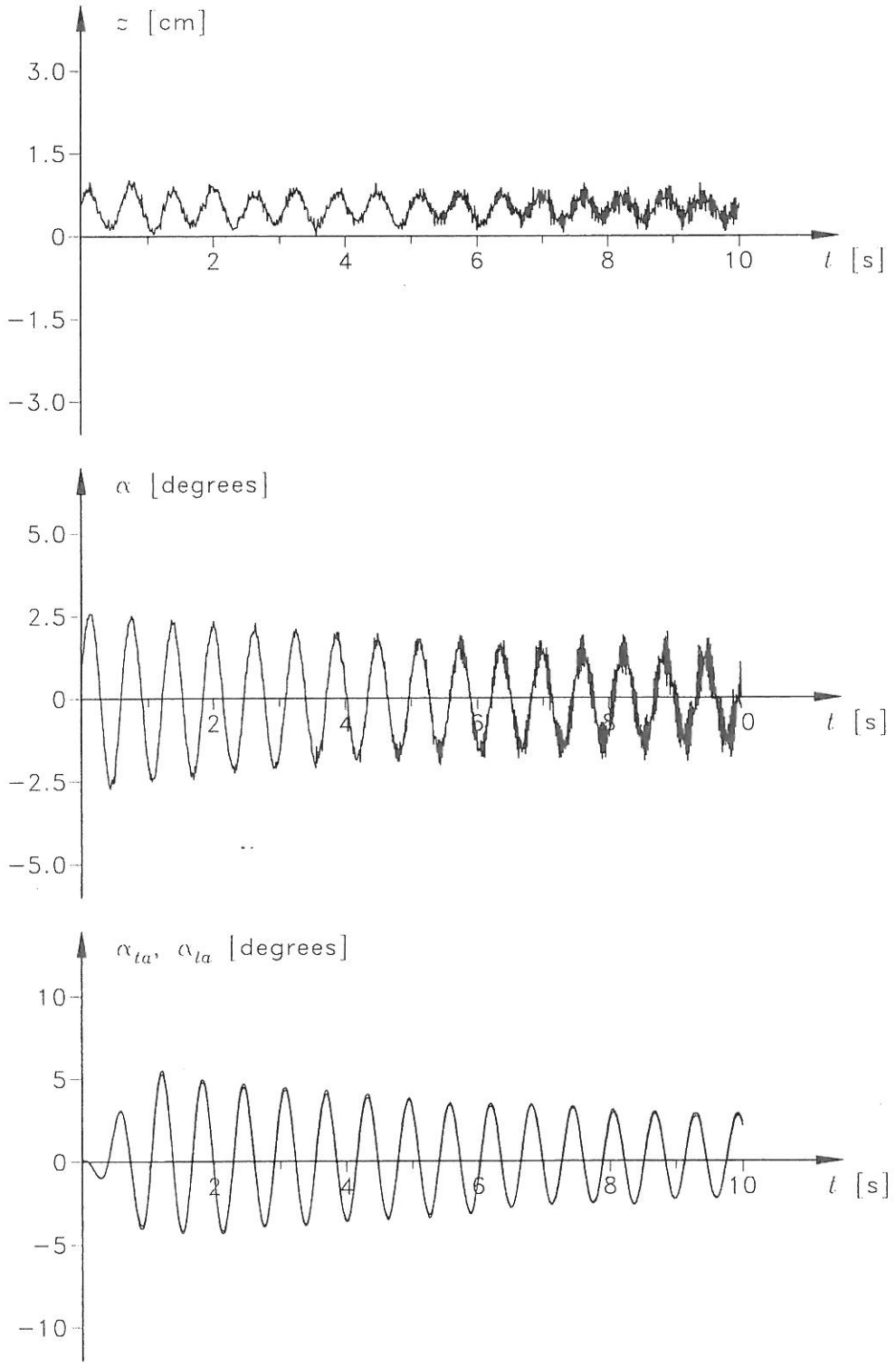

Figure F.12: Vertical motion, torsional motion and flap positions for experiment -0606000.000.

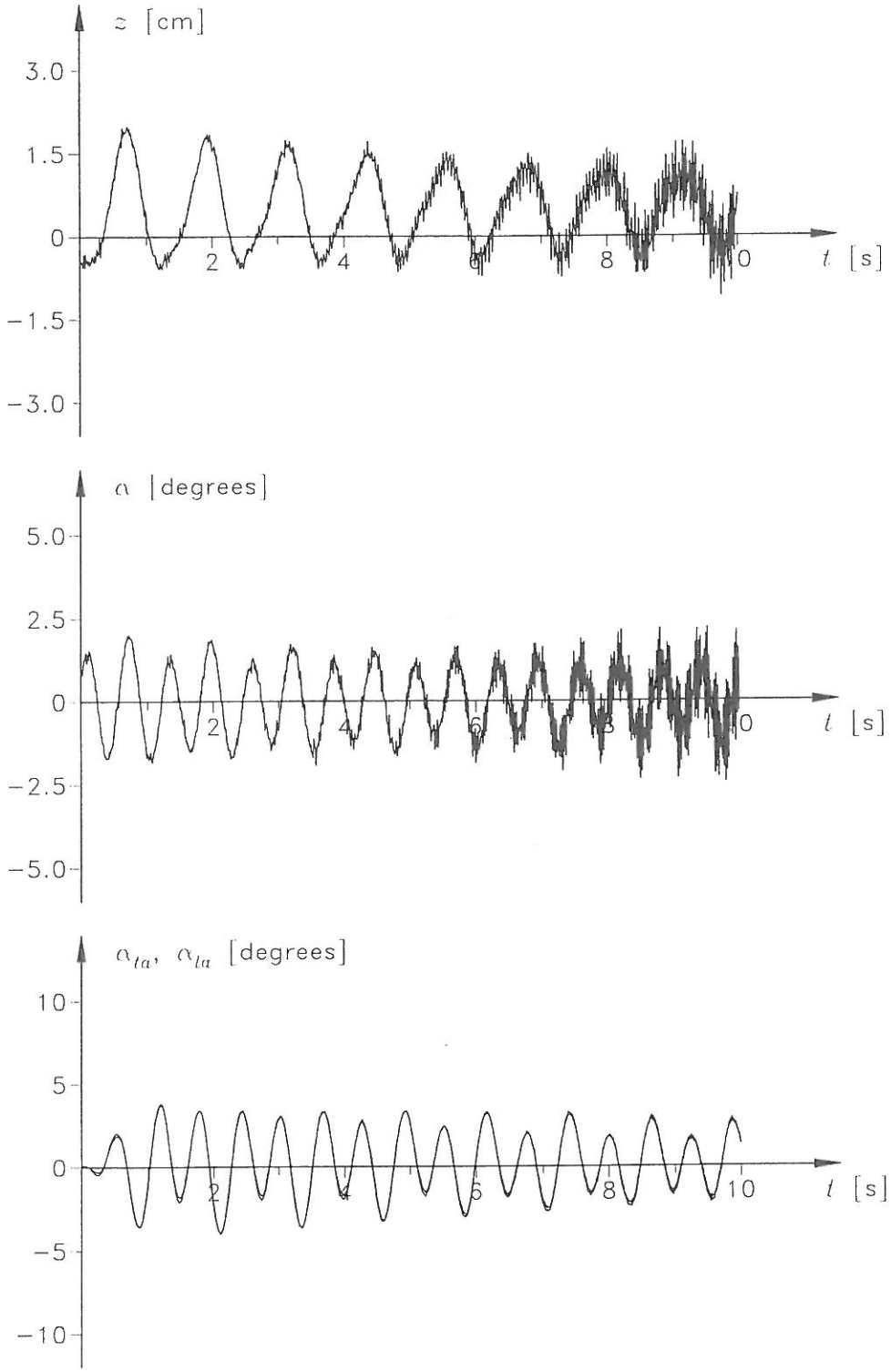

Figure F.13: Vertical motion, torsional motion and flap positions for experiment -0606000.005.

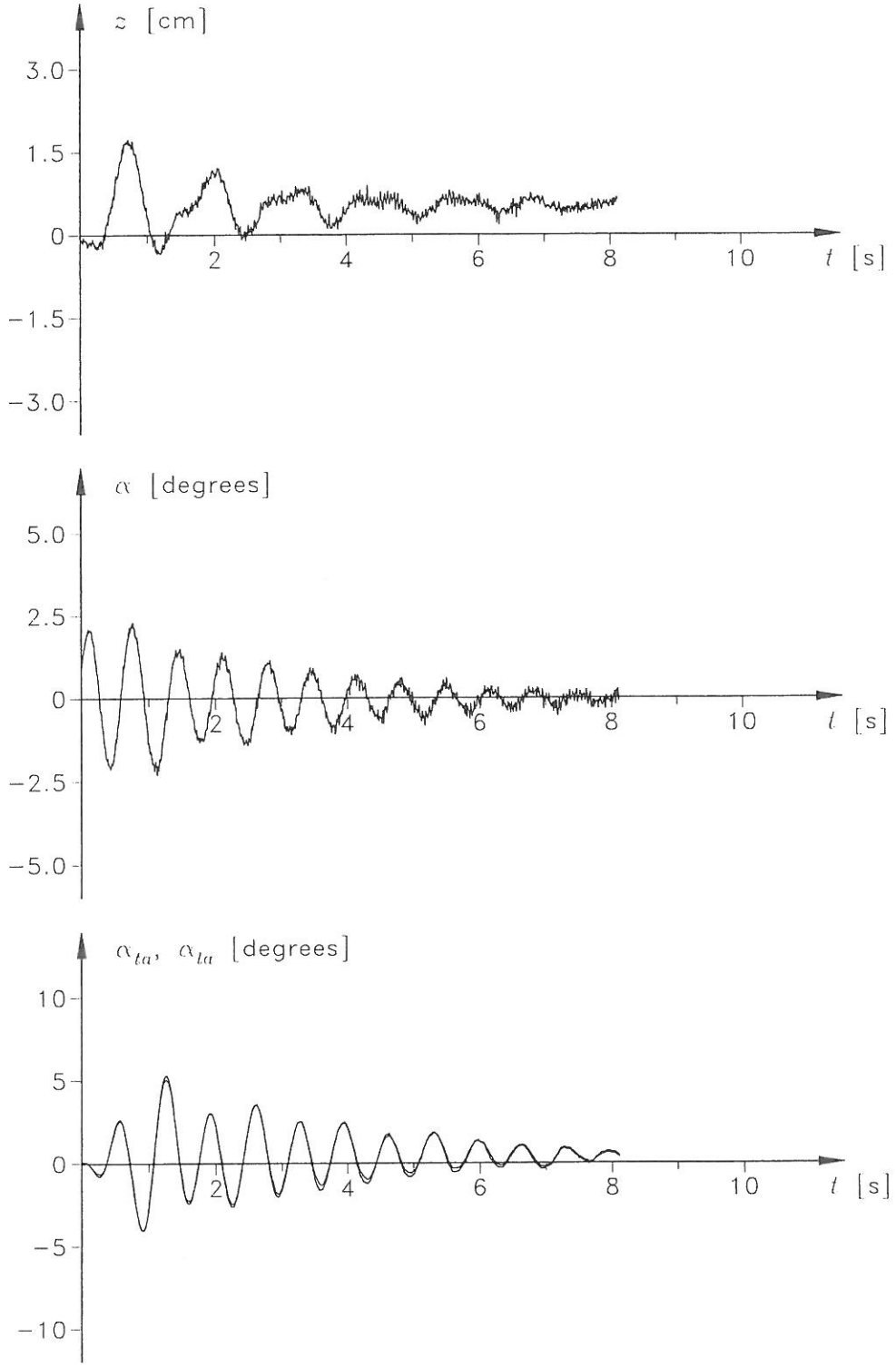

Figure F.14: Vertical motion, torsional motion and flap positions for experiment -0606000.007.

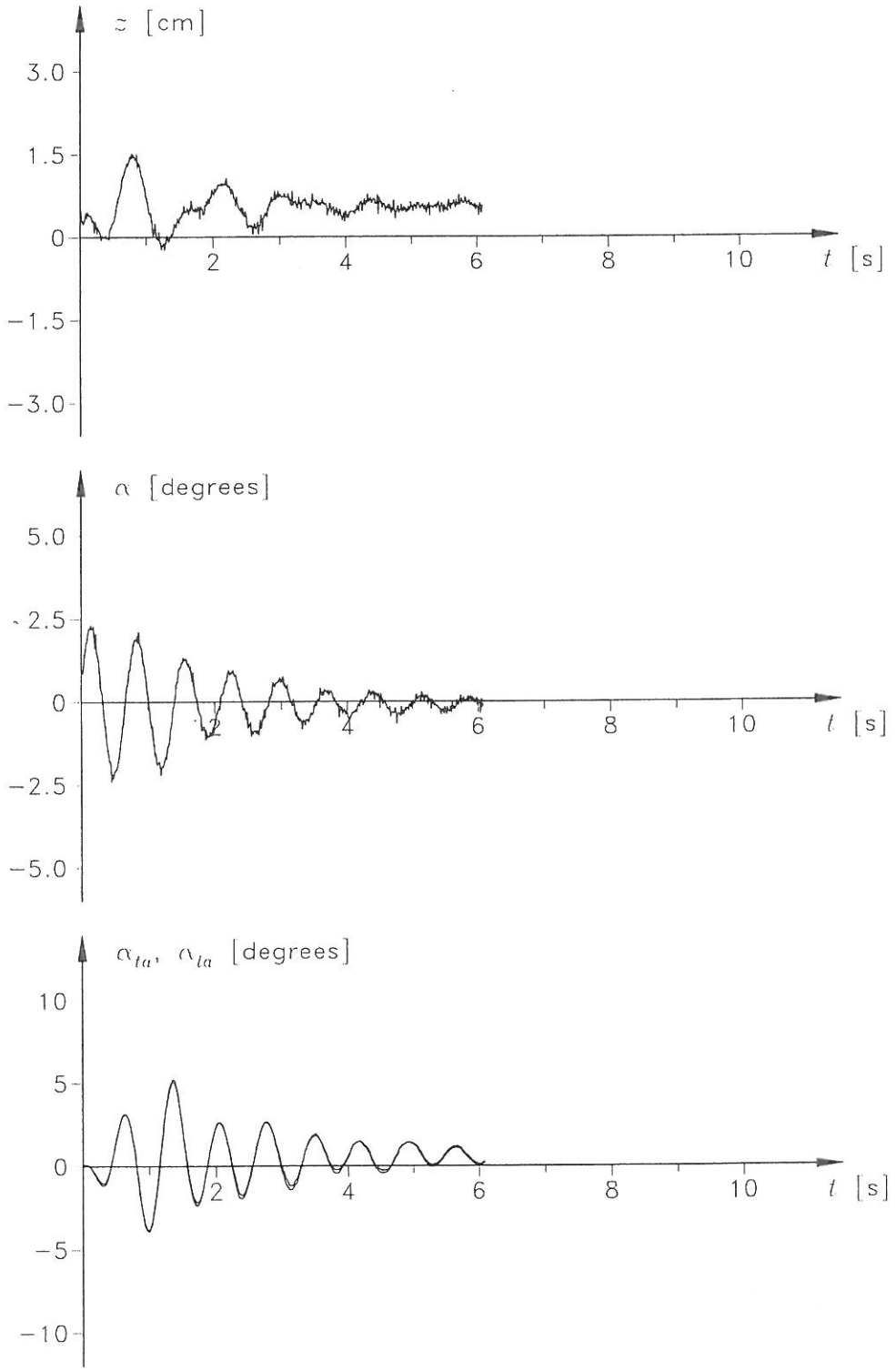

Figure F.15: Vertical motion, torsional motion and flap positions for experiment -0606000.013.

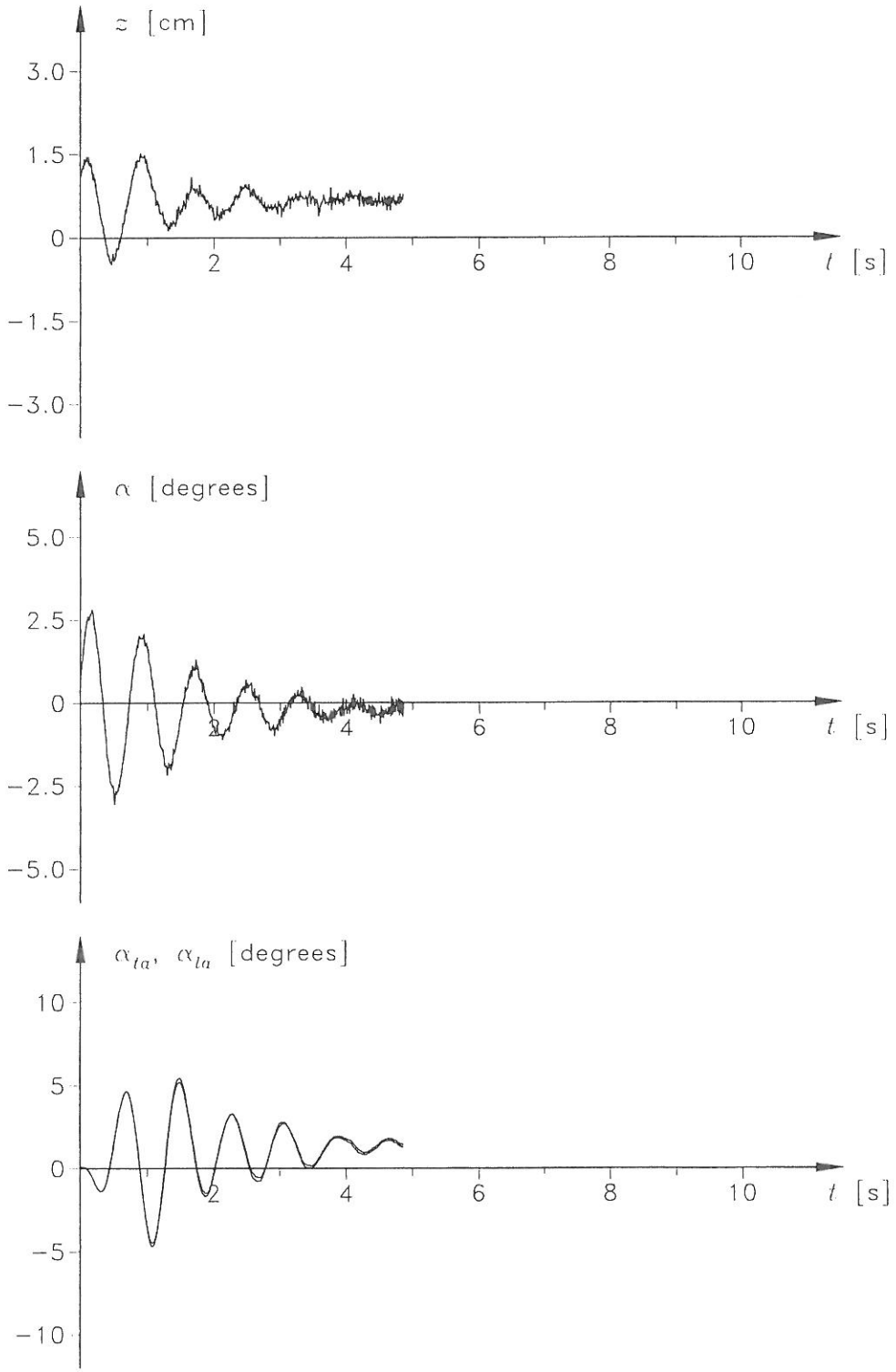

Figure F.16: Vertical motion, torsional motion and flap positions for experiment -0606000.018.

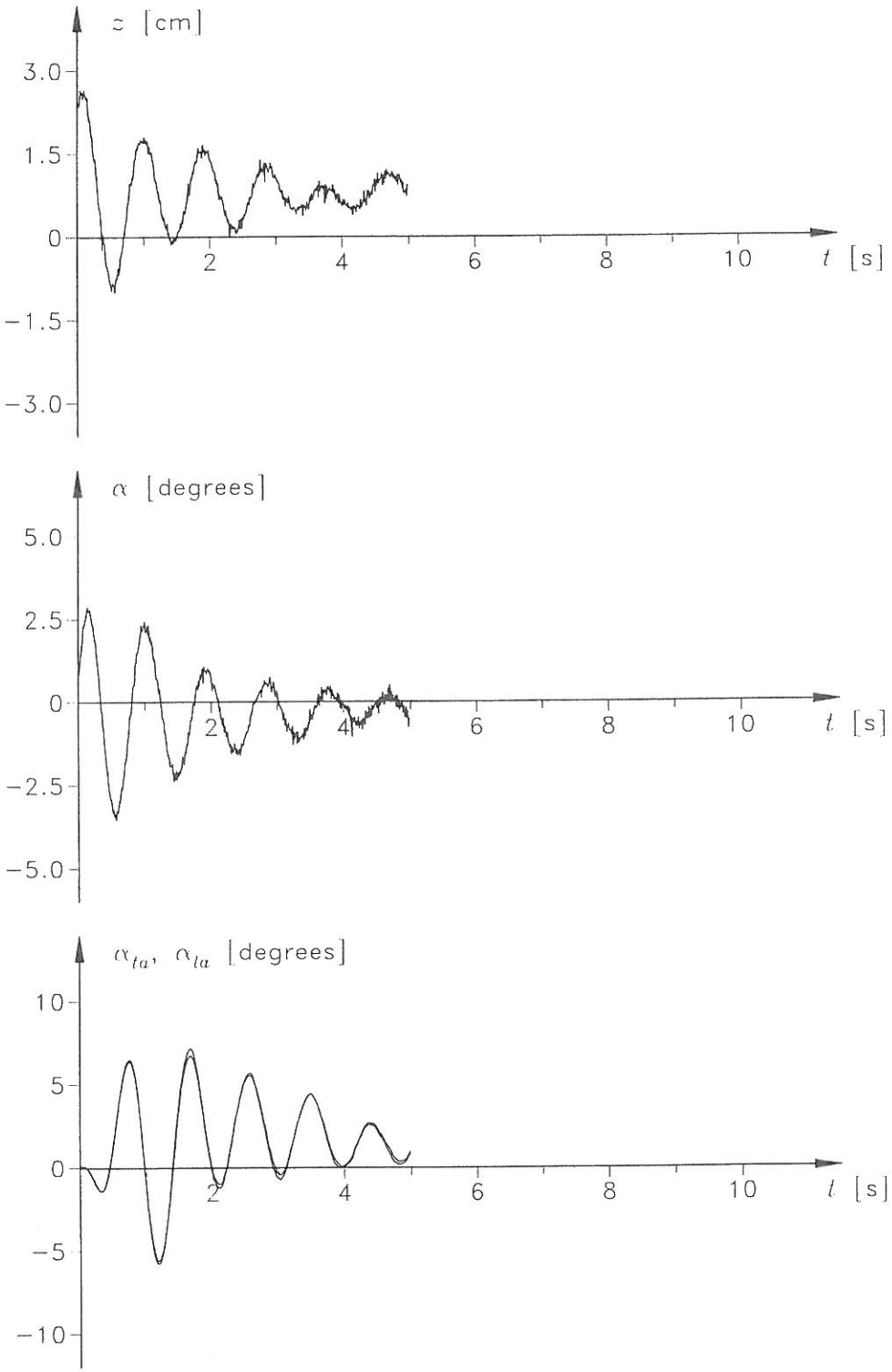

Figure F.17: Vertical motion, torsional motion and flap positions for experiment -0606000.023.

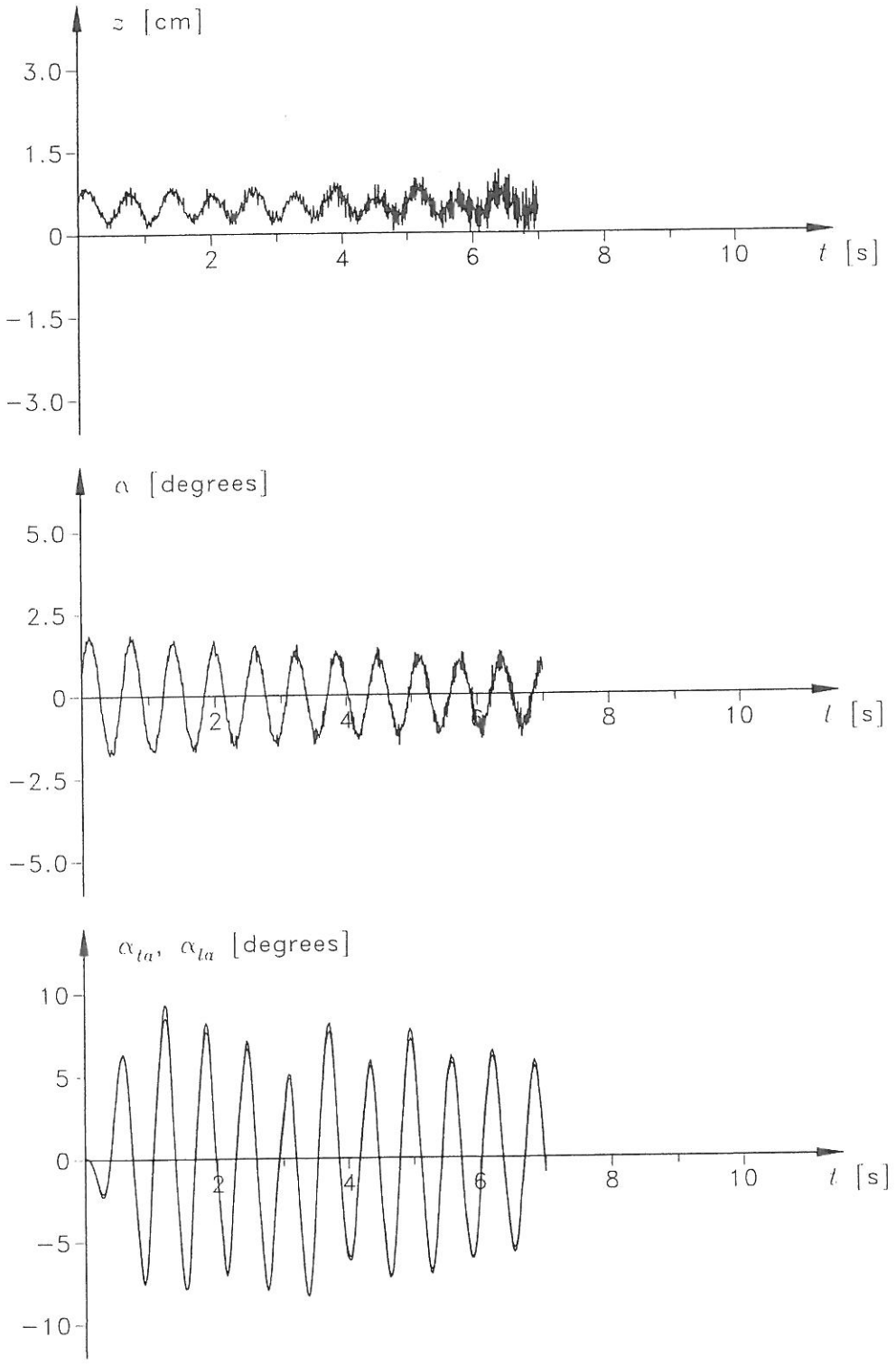

Figure F.18: Vertical motion, torsional motion and flap positions for experiment -2020000.000.

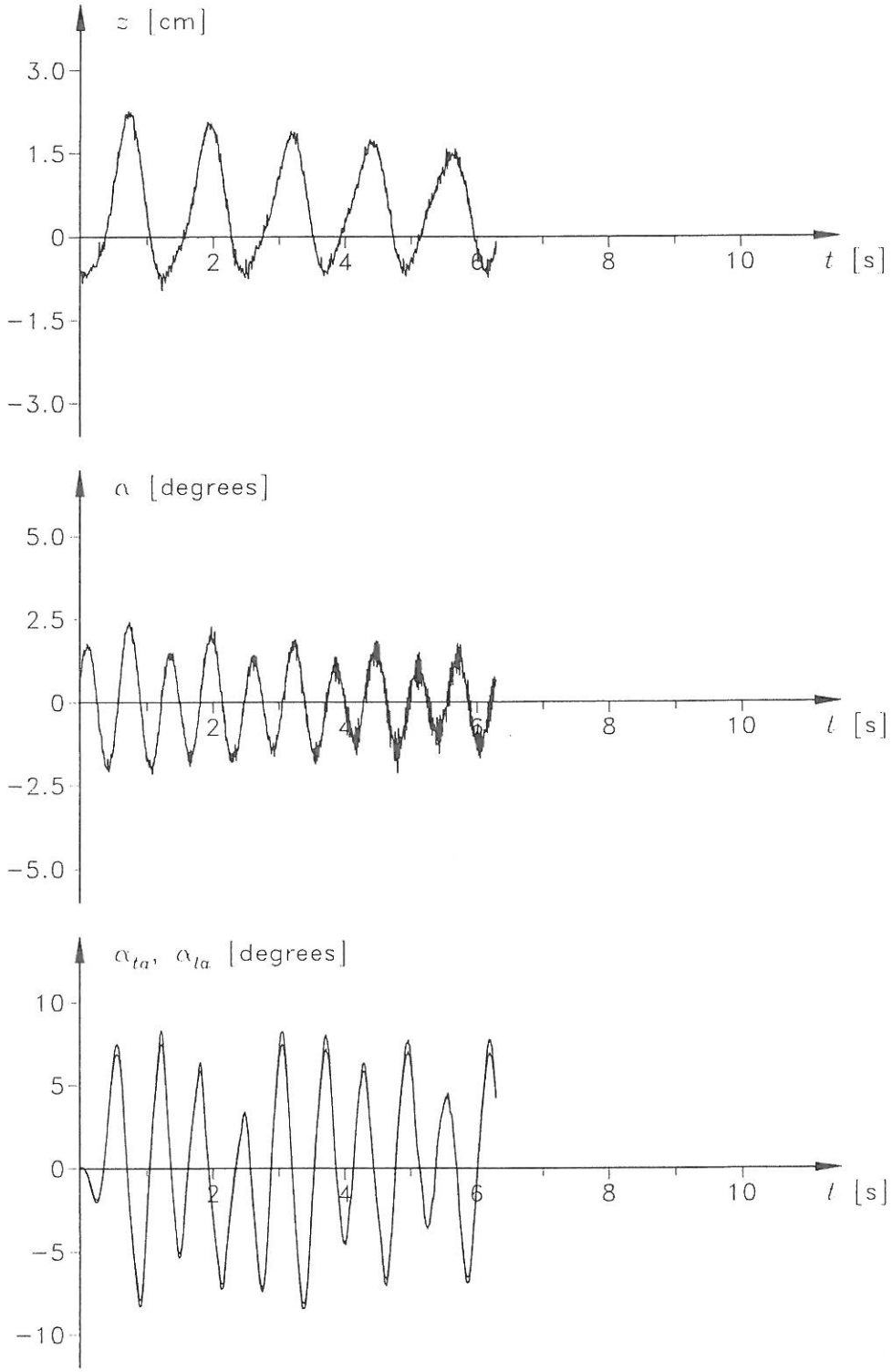

Figure F.19: Vertical motion, torsional motion and flap positions for experiment -2020000.005.

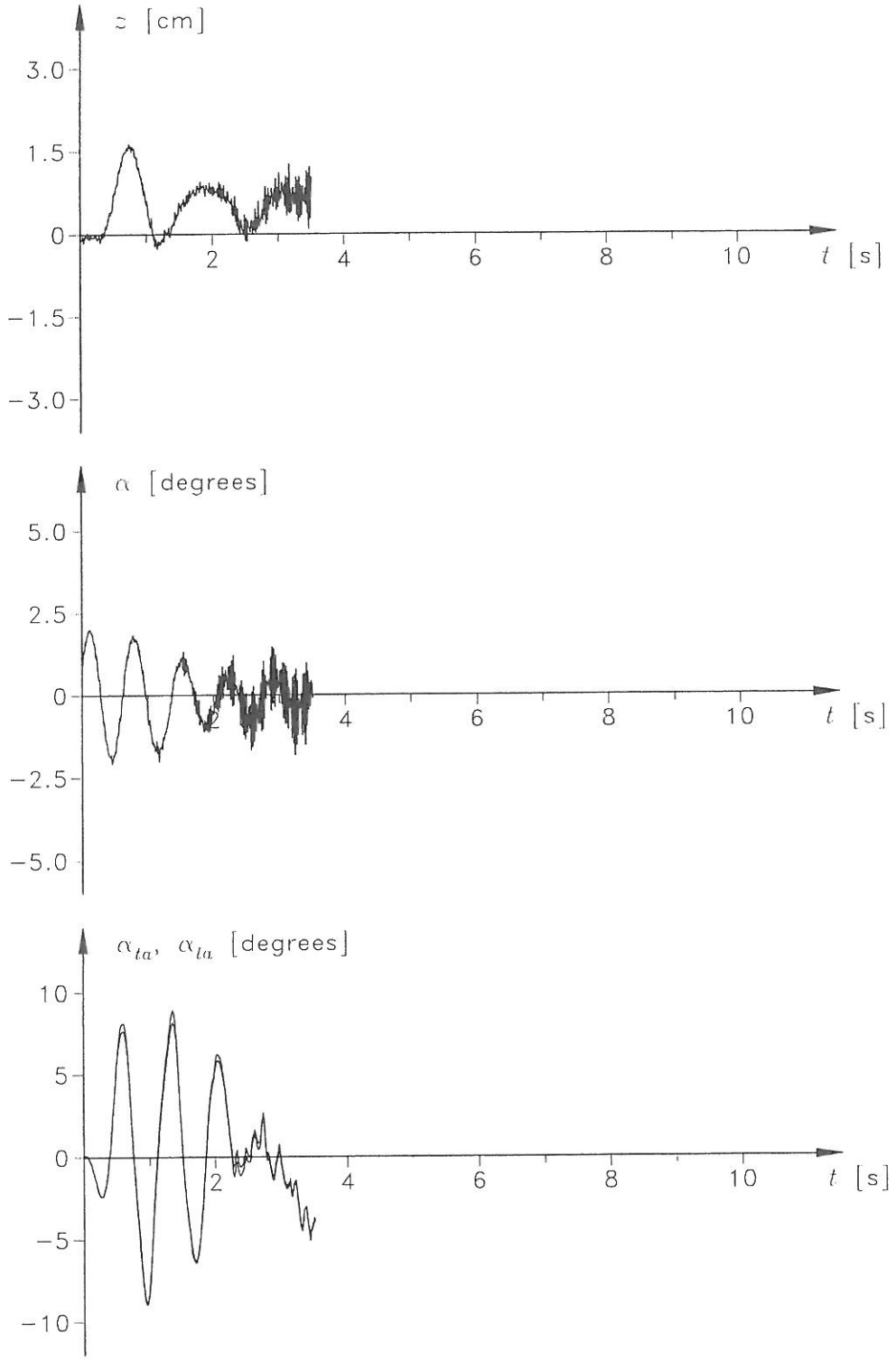

Figure F.20: Vertical motion, torsional motion and flap positions for experiment -2020000.008.

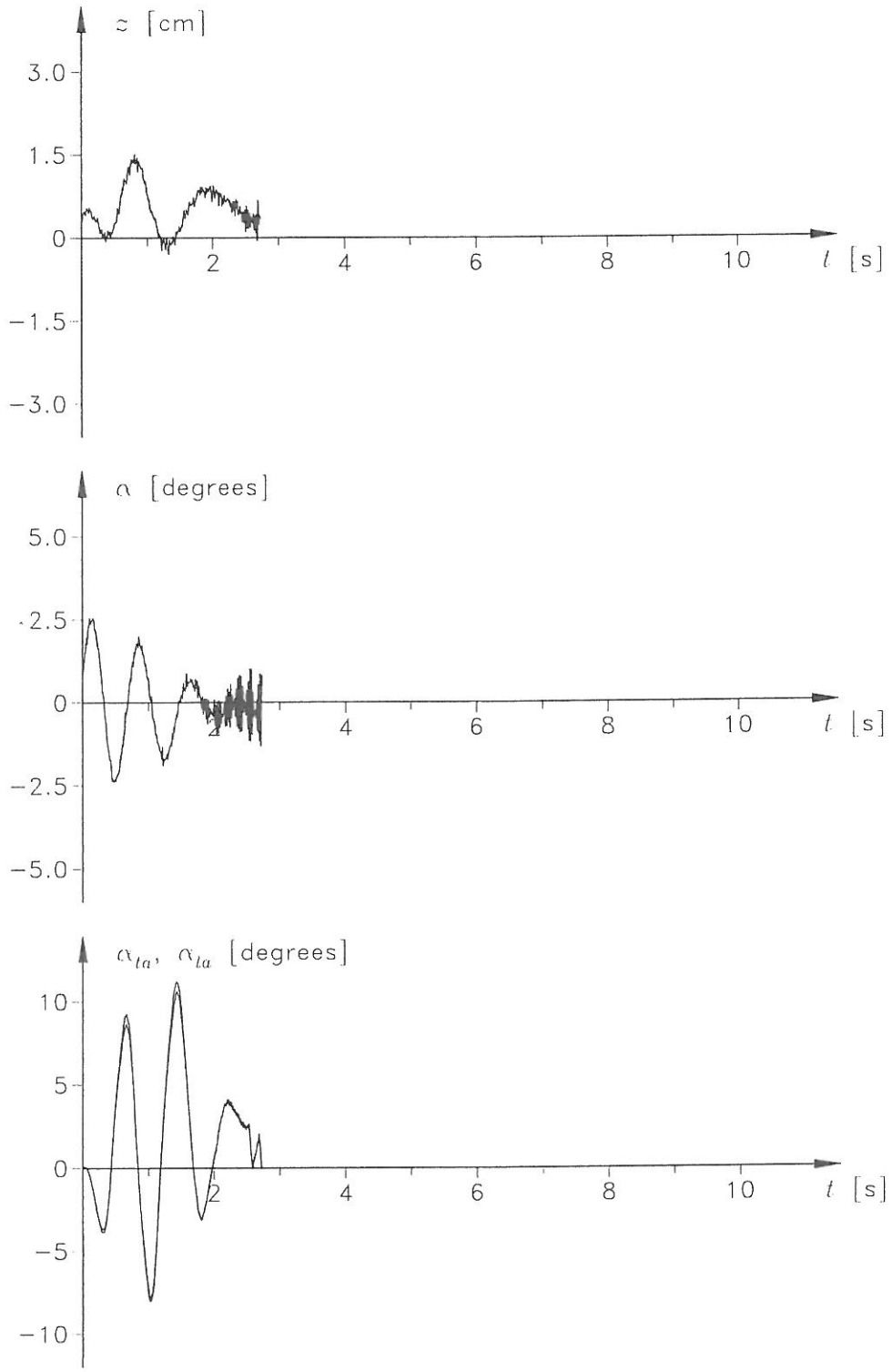

Figure F.21: Vertical motion, torsional motion and flap positions for experiment -2020000.013.

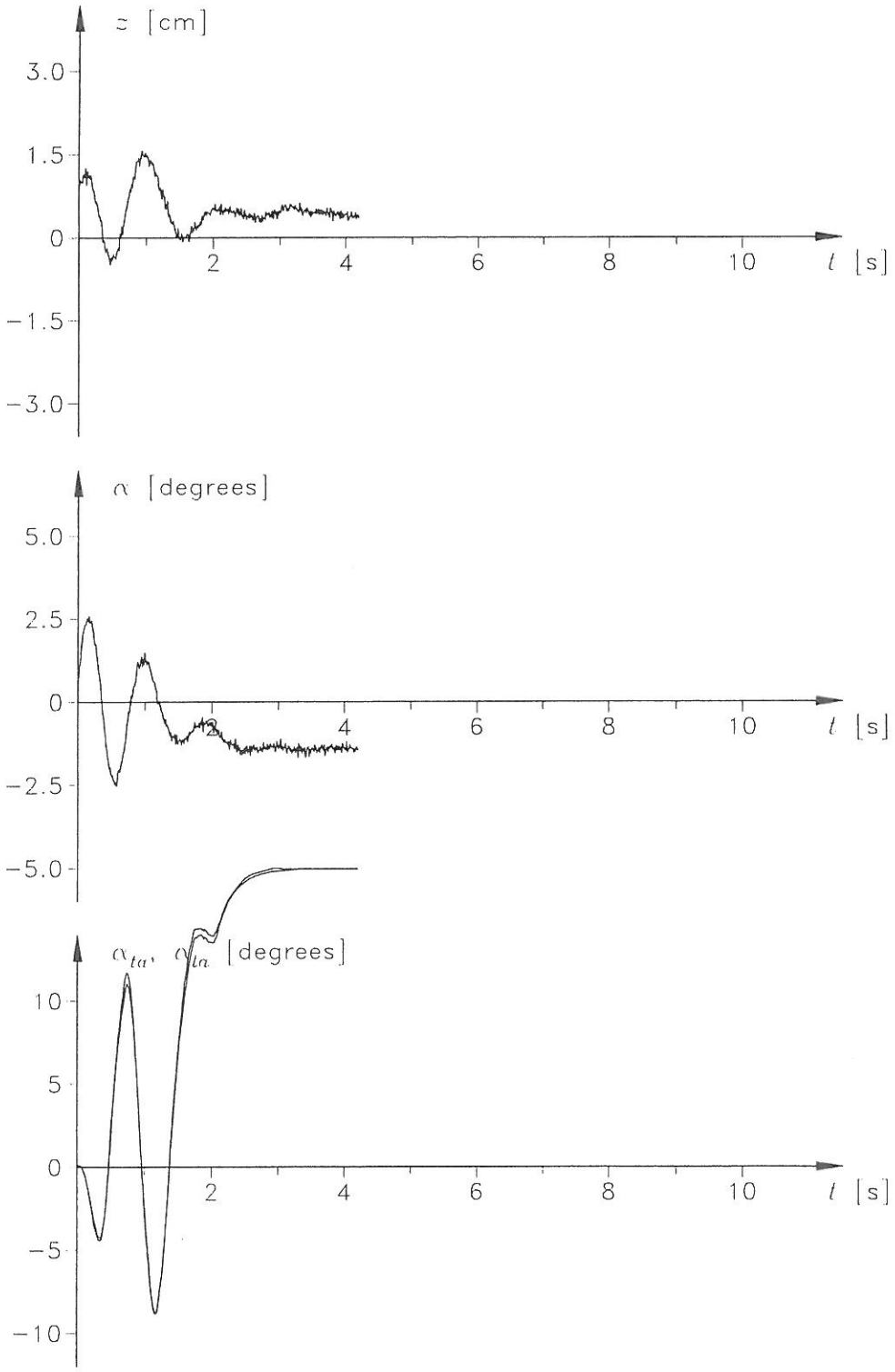

Figure F.22: Vertical motion, torsional motion and flap positions for experiment -2020000.018.

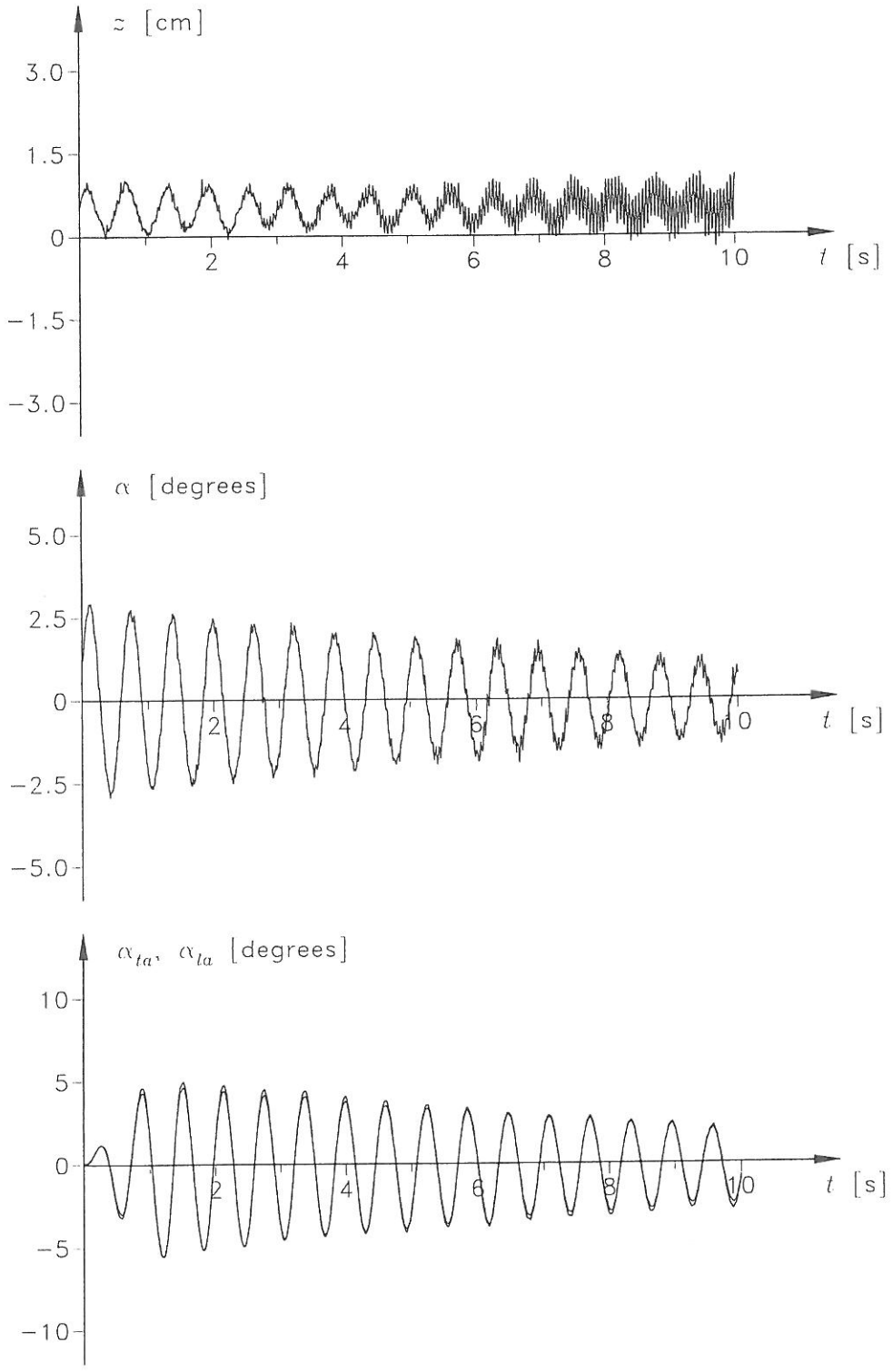

Figure F.23: Vertical motion, torsional motion and flap positions for experiment 06-06000.001.

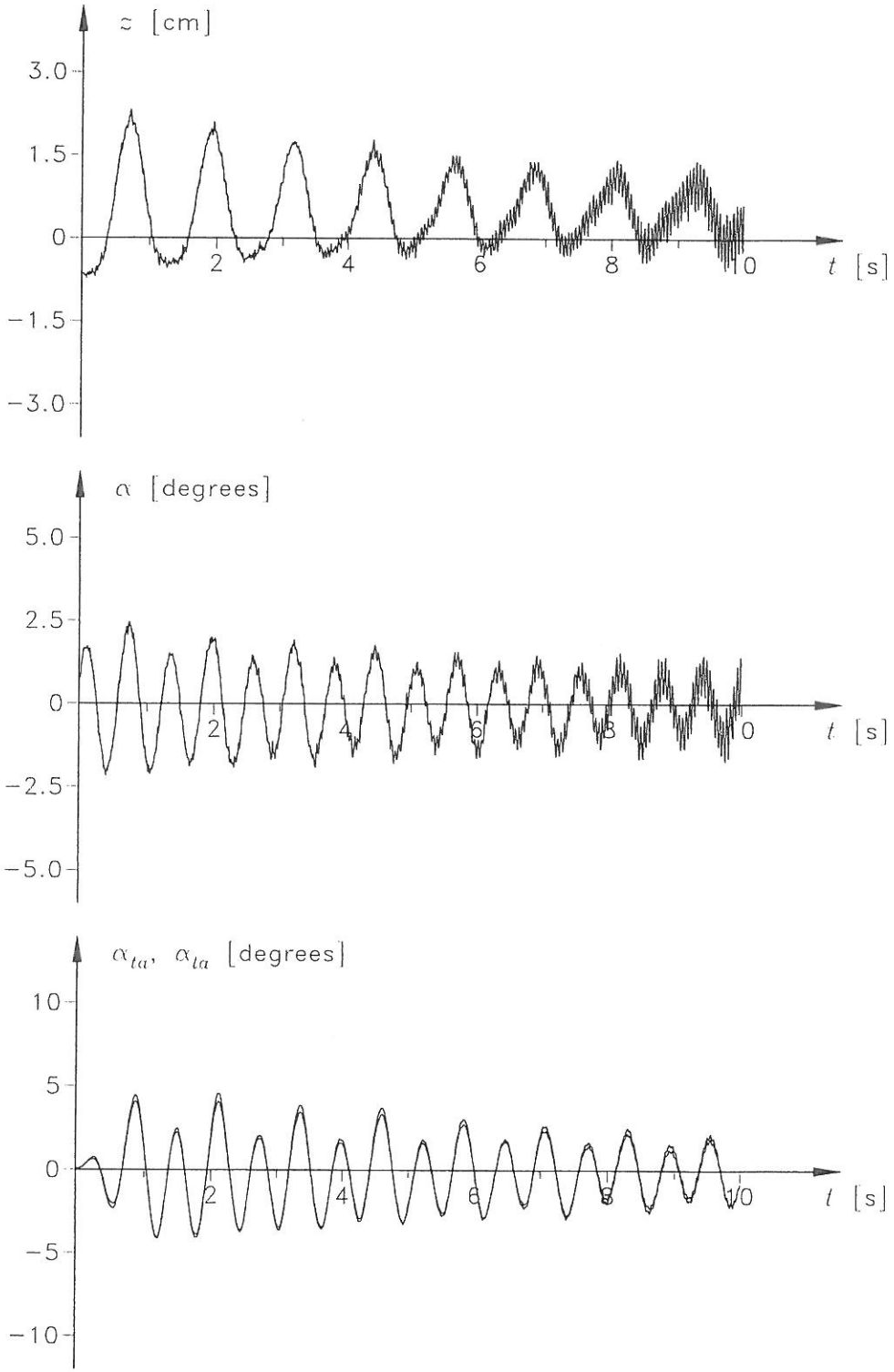

Figure F.24: Vertical motion, torsional motion and flap positions for experiment 06-06000.006.

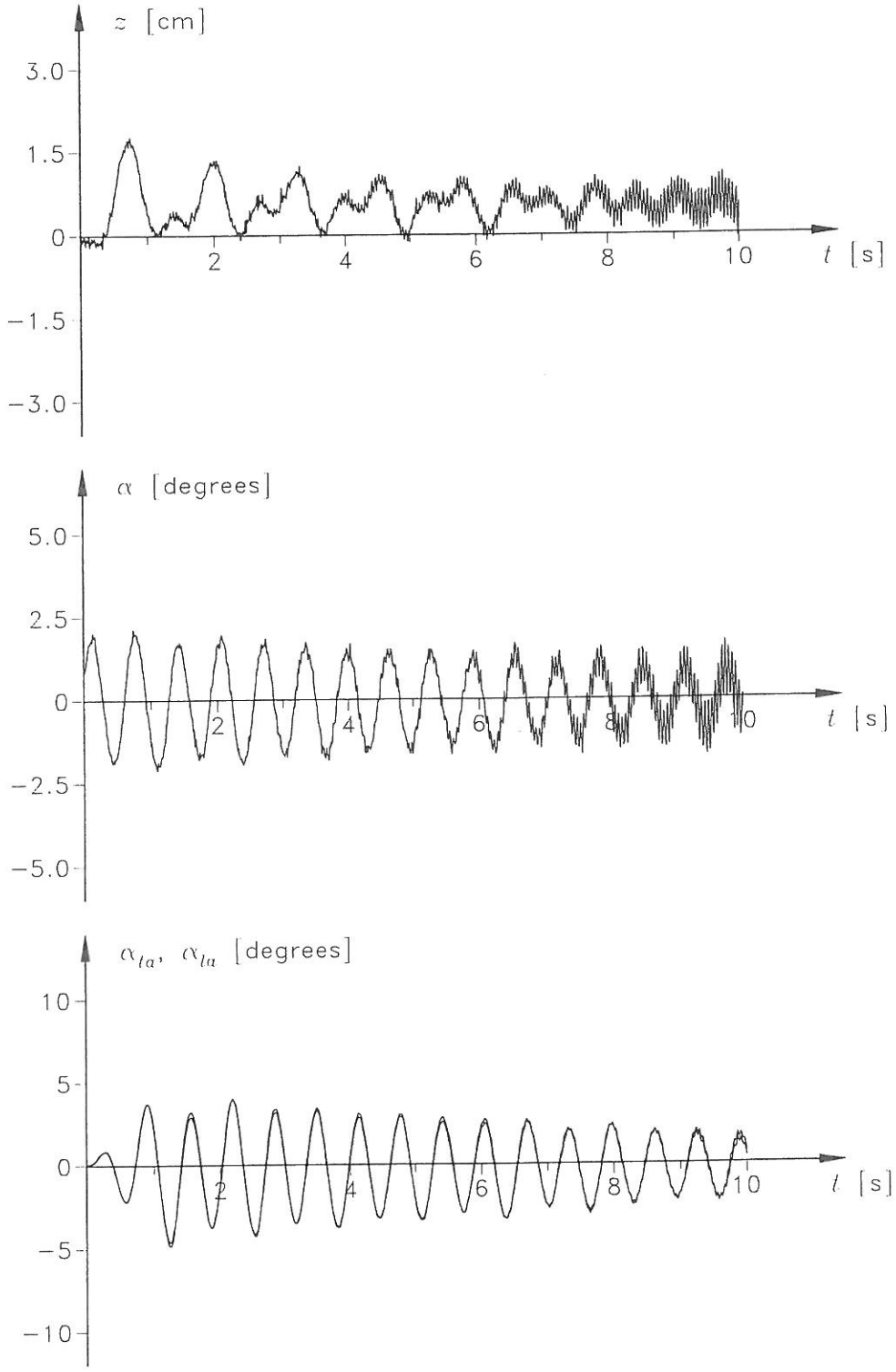

Figure F.25: Vertical motion, torsional motion and flap positions for experiment 06-06000.008.

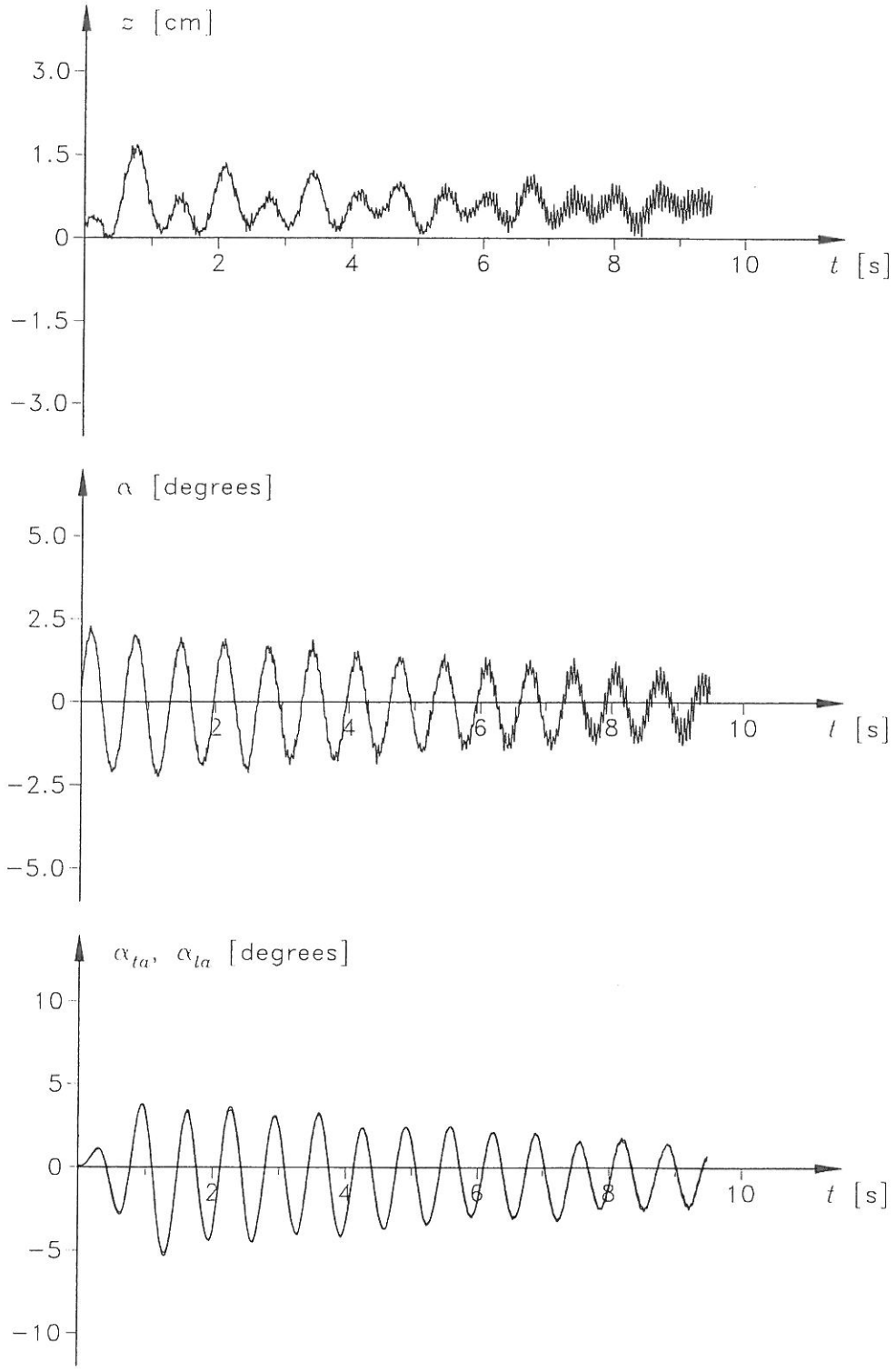

Figure F.26: Vertical motion, torsional motion and flap positions for experiment 06-06000.013.

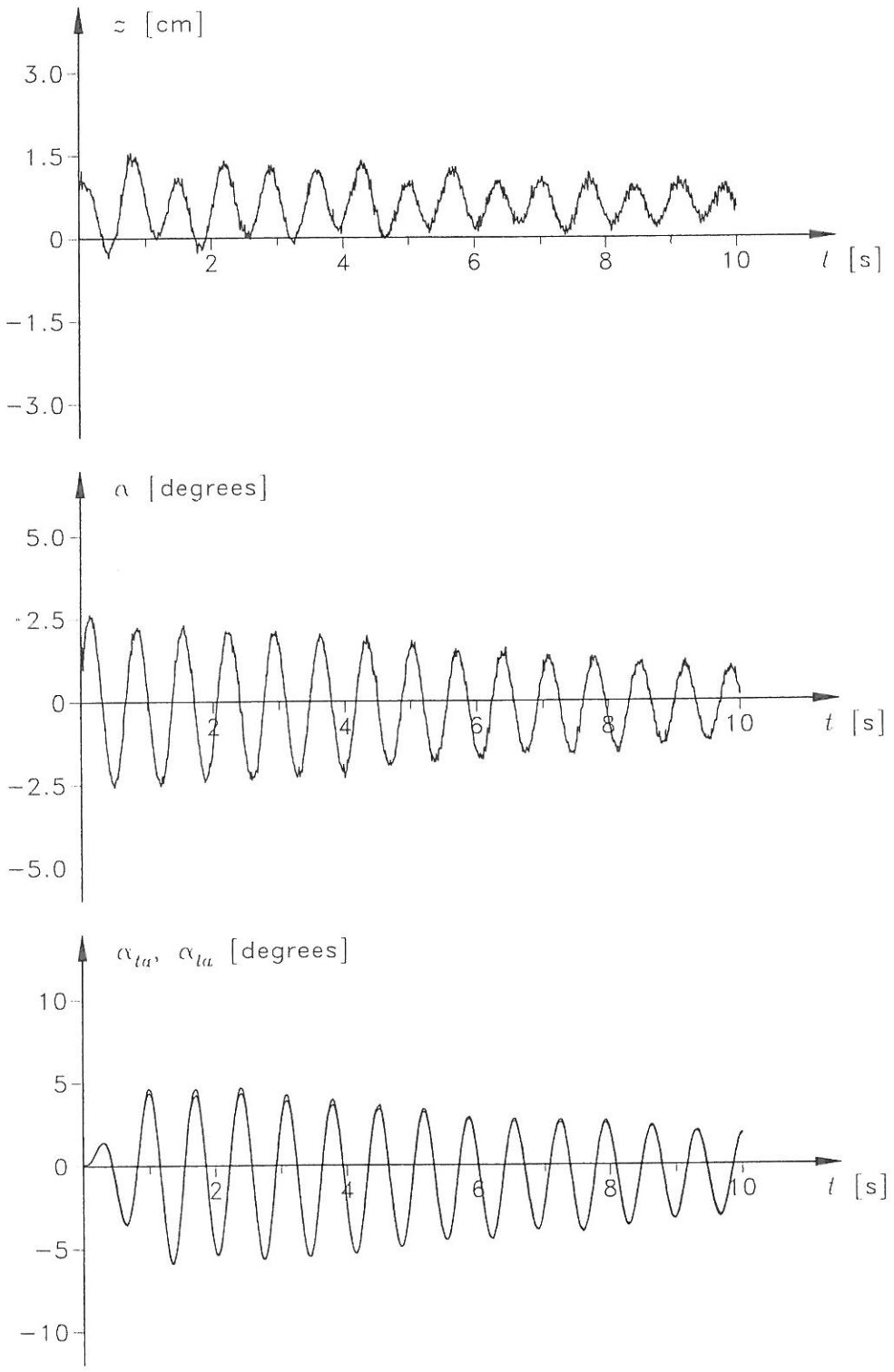

Figure F.27: Vertical motion, torsional motion and flap positions for experiment 06-06000.017.

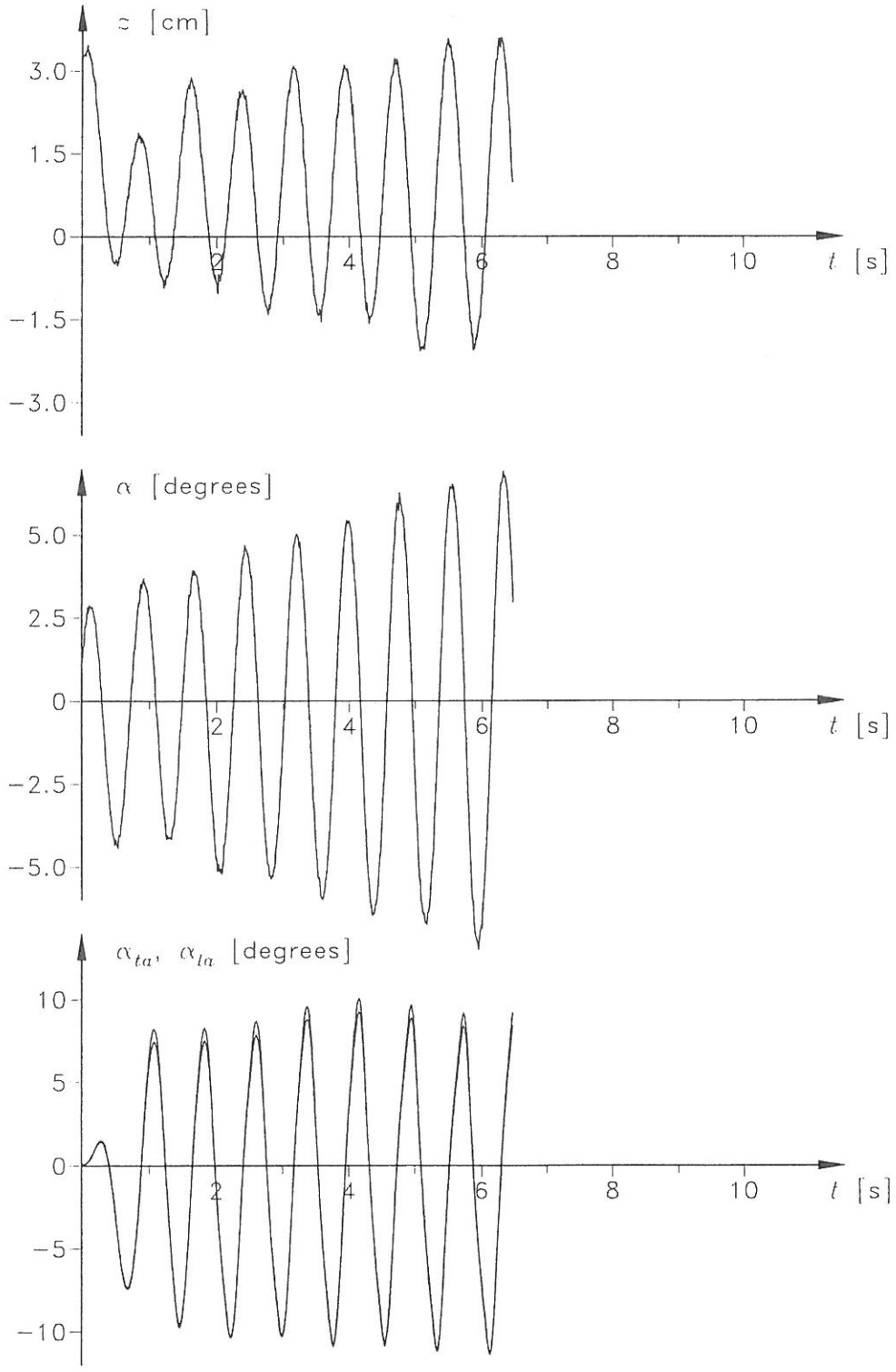

Figure F.28: Vertical motion, torsional motion and flap positions for experiment 06-06000.022.

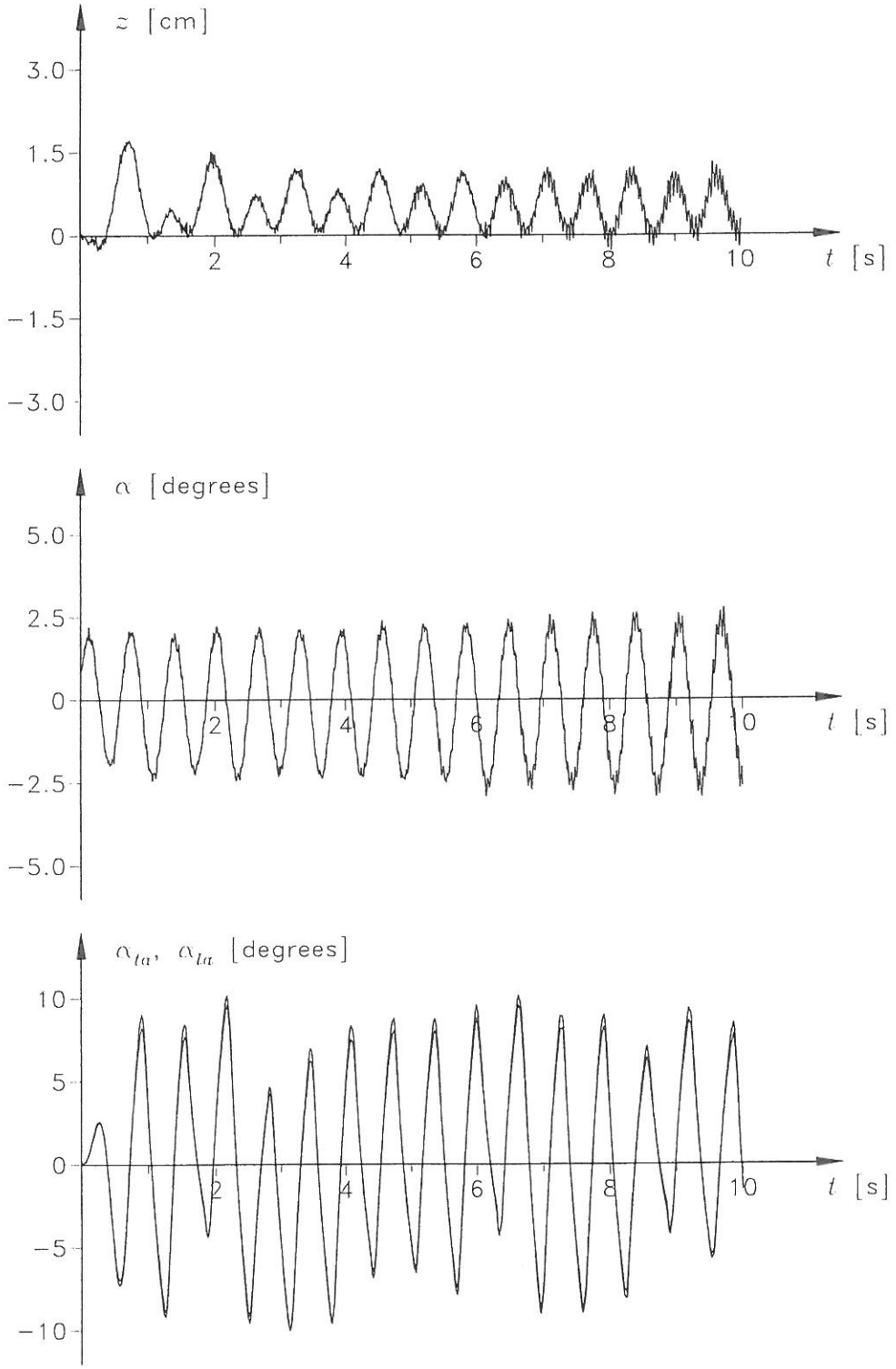

Figure F.29: Vertical motion, torsional motion and flap positions for experiment 20-20000.000.

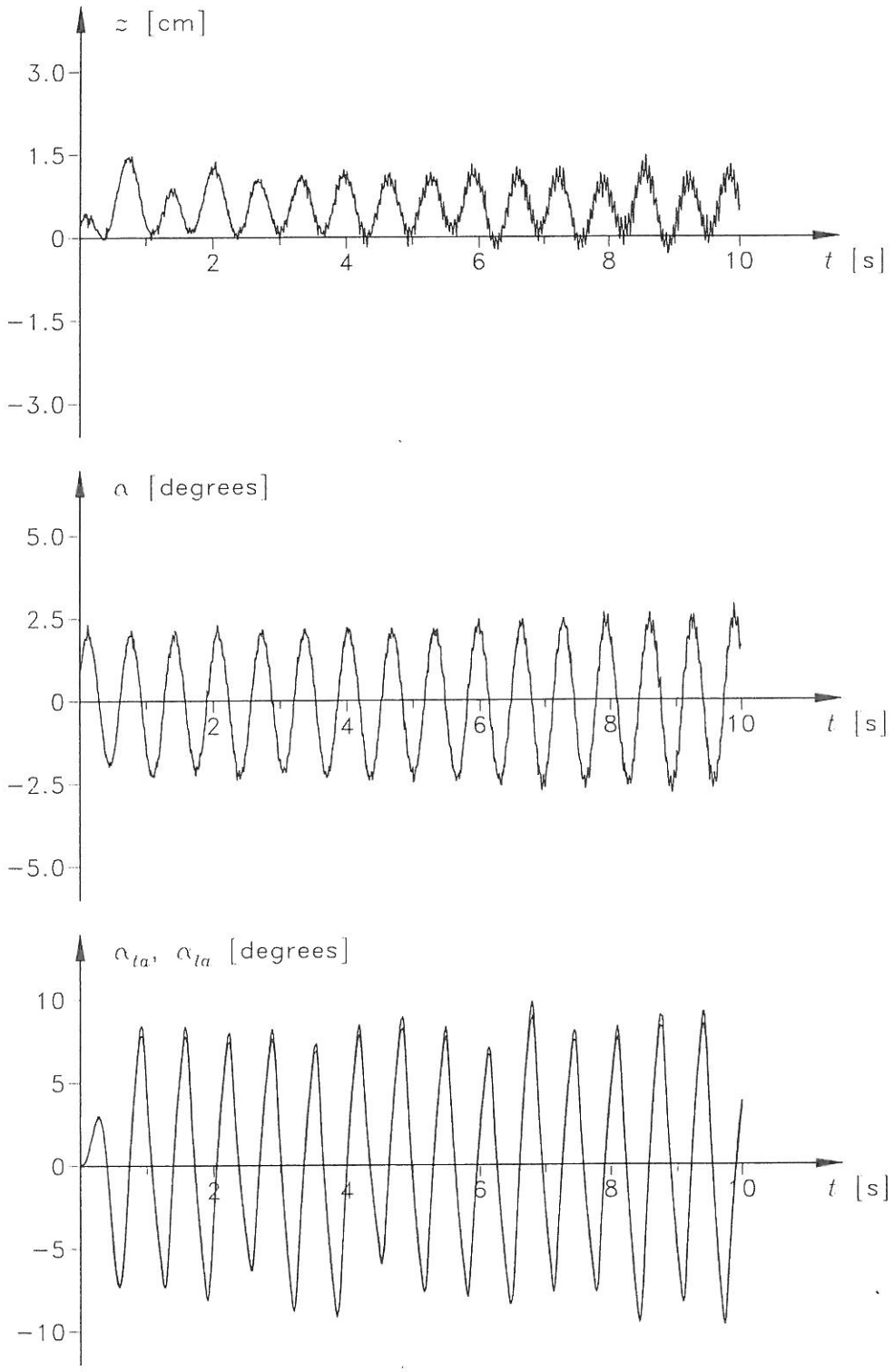

Figure F.30: Vertical motion, torsional motion and flap positions for experiment 20-20000.005.

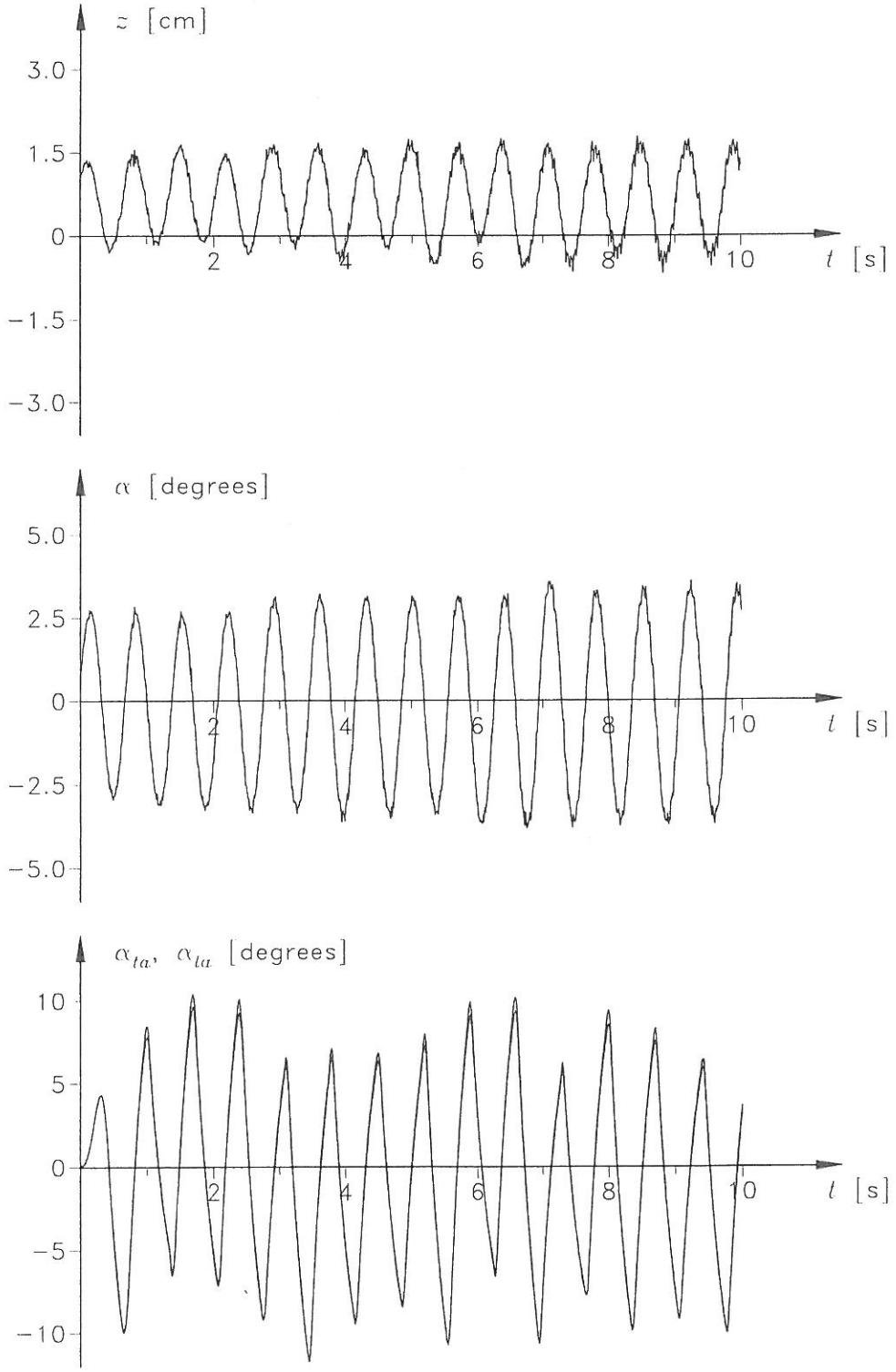

Figure F.31: Vertical motion, torsional motion and flap positions for experiment 20-20000.010.

Appendix G

Results of Experiments

G.1 Introduction

This appendix describes estimation of parameters for the model and flap configuration based on the results of the wind tunnel experiments. The positions measured during the experiments are rather noisy, all positions are therefore filtered by a software filter as described in appendix G.2.

The following parameters are estimated for the model and flap configuration:

- The circular frequencies for the vertical and torsional motion and the damping ratio for the torsional motion, see appendix G.3.
- The actual amplitude amplification factors and the phase angles between the angular motion of the model and the actual positions of the flaps, see appendix G.4.

G.2 Software Filter

A second order filter is used to filter the noisy position measurements after the experiments. A noisy measurement $u(k)$ at the time step k is filtered by

$$u_f(k) = 2pu_f(k-1) - p^2u_f(k-2) + (1-p)^2u(k) \tag{G.1}$$

where $u_f(k)$ is the filtered value at the time step k and p is the pole. If $p = 0$, the filtered values are equal to the measured noisy values, and if $p = 1$, the filtered values are not dependent on the measured values. Therefore, a large value of p will make smooth filtered values but the amplitude reduction and time delay compared to the measured values will be large.

In the following a pole of 0.5 is selected. When this pole is used, the output from the second order filter is very close to the mean value over the last five measured values. The delay of the filter is thereby close to 24 ms, and the amplitude reduction is rather small, see figure G.1. Estimation of the frequencies, damping and factors between the angular motion of the model and the actual positions of the flaps is not dependent on the time

delay and reduction of the filter, they are therefore not estimated.

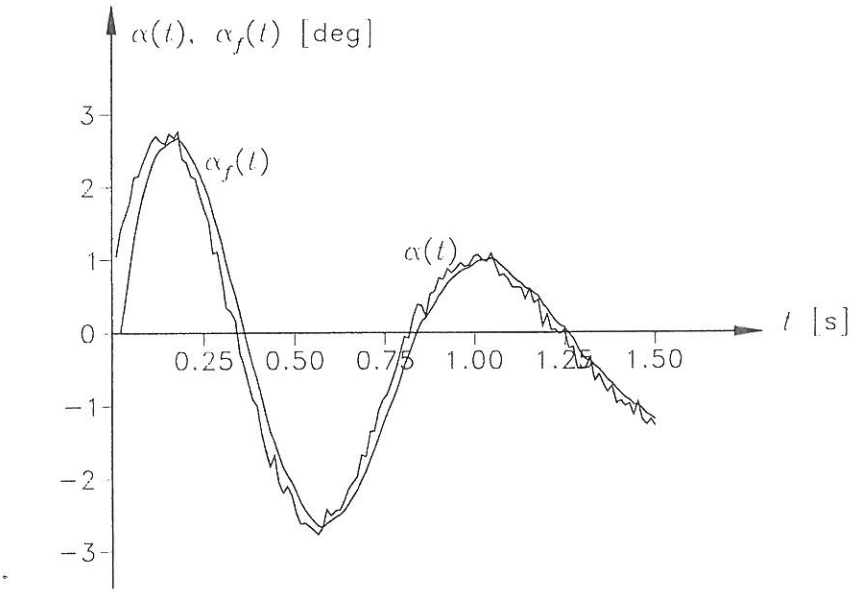

Figure G.1: Example of torsional motion $\alpha(t)$ and filtered torsional motion $\alpha_f(t)$ for flap configuration 2 and with wind speed 6.1 m/s.

G.3 Frequency and Damping

The circular frequencies ω_z and ω_α for the vertical and torsional motion, respectively, are estimated by counting a number of cycles for the filtered time series $z_f(t)$ and $\alpha_f(t)$. The damping ratio ζ_α is estimated for the filtered torsional motion $\alpha_f(t)$ by Hilbert transformation. The zero upcrossings of the motion are used to estimate the frequencies.

As described by Littler [25], the frequency will increase and the damping will decrease as the amplitude of the response reduces. Therefore, the selected decay will be limited to an excact number of cycles with rather large amplitudes. For the wind tunnel experiments the part of the time series before one second is eliminated because the flaps are started slowly during the first second.

The following procedure is used to estimate the parameters:

1. Filtering of data.
   (a) The time series $z(t)$ and $\alpha(t)$ are filtered through a second order filter with pole 0.5.
2. Justification of data.
   (a) The zero points of the time series are justified so the mean of each of the filtered motions z_f and α_f is zero.

3. At the start of the time series the data before the first upcrossing after one second are eliminated. The part of the decay to be analysed is selected independently for each time series.
   (a) At the start of the time series the data before the first upcrossing are eliminated.
   (b) The number of cycles n_c to include in the analysis is selected by visual inspection of the graph.
4. Estimation of frequency for both time series.
   (a) The period T is estimated by
   $$T = \frac{t_{n_c}}{n_c} \tag{G.2}$$
   where t_{n_c} is the time for n_c cycles.
   (b) The circular frequency ω is then estimated
   $$\omega = \frac{2\pi}{T} \tag{G.3}$$
5. For the torsional motion the damping ratio is estimated by Hilbert transformation.
   (a) Fourier transformation analysis of the filtered time series
   $$\alpha_{FT}(t) = \mathrm{FFT}(\alpha_f(t)) \tag{G.4}$$
   (b) The first half of the Fourier components is multiplied by $-i$ and the last half of the Fourier components is multiplied by i
   $$\left.\begin{array}{ll} \alpha_{FT,m}(j) = -i \cdot \alpha_{FT}(j), & j = 1, \ldots, 1/2 n_d \\ \alpha_{FT,m}(j) = i \cdot \alpha_{FT}(j), & j = 1/2 n_d + 1, \ldots, n_d \end{array}\right\} \tag{G.5}$$
   where n_d is the number of data.
   (c) Inverse Fourier transformation of the modified Fourier components
   $$\alpha_m = \mathrm{IFFT}(\alpha_{FT,m}) \tag{G.6}$$
   (d) The envelope curve A_e with the theoretical expression $A_\alpha e^{-\zeta_\alpha \omega_\alpha t}$ of the motion is found by
   $$A_e(j) = \sqrt{\alpha(j)^2 + \mathrm{Re}(\alpha_m(j)^2)}, \quad j = 1, \ldots, n_d \tag{G.7}$$
   (e) The damping ratio is estimated as the slope of the logarithm of the envelope curve for the selected part of the decay divided by minus the estimated circular frequency
   $$\zeta_\alpha = \frac{\mathrm{slope}(A_e)}{-\omega_\alpha} \tag{G.8}$$

The estimated parameters ω_z, ω_α and ζ_α are shown in tables G.1 and G.2 for no regulation of the flaps, in table G.3 for flap configuration 1, in table G.4 for flap configuration 2, in table G.5 for flap configuration 3 and in table G.6 for flap configuration 4.

The following notation is used in the tables:

- File name: the name of the file with stored data from an experiment.
- U: wind speed in $^{m}/_{s}$.
- ω_z: circular bending frequency in $^{rad}/_{s}$ estimated by using n_z cycles.
- ω_α: circular torsional frequency in $^{rad}/_{s}$ estimated by using n_α cycles.
- ζ_α: damping ratio (between the actual value and the critical value of the torsional damping constant) estimated by using n_ζ cycles corresponding to the Δt interval in seconds.

File name	U [$^{m}/_{s}$]	ω_z [$^{rad}/_{s}$] (n_z)	ω_α [$^{rad}/_{s}$] (n_α)	ζ_α (n_ζ; Δt)
00000000.000	0.0	5.25 (20)	—	—
00000000.001	0.0	5.25 (20)	—	—
00000000.002	0.0	5.24 (20)	—	—
00000000.003	0.0	5.23 (20)	—	—
00000000.004	0.0	5.23 (20)	—	—
Mean values	0.0	5.24	—	—
00000000.007	0.0	—	10.14 (20)	0.0049 (20; 1.0–13.4 s)
00000000.008	0.0	—	10.16 (20)	0.0048 (20; 1.0–13.4 s)
00000000.009	0.0	—	10.15 (20)	0.0051 (20; 1.0–13.4 s)
00000000.010	0.0	—	10.16 (20)	0.0047 (20; 1.0–13.4 s)
Mean values	0.0	—	10.15	0.0049
00000000.017	0.0	5.28 (20)	10.15 (20)	0.0056 (20; 1.0–13.4 s)
00000000.018	0.0	5.24 (20)	10.13 (20)	0.0059 (20; 1.0–13.4 s)
00000000.019	0.0	5.23 (20)	10.13 (20)	0.0057 (20; 1.0–13.4 s)
00000000.020	0.0	5.24 (20)	10.13 (20)	0.0060 (20; 1.0–13.4 s)
Mean values	0.0	5.25	10.14	0.0058
00000000.022	2.5	—	9.51 (15)	0.0177 (15; 1.0–10.9 s)
00000000.023	2.5	—	9.52 (15)	0.0189 (15; 1.0–10.9 s)
00000000.024	2.5	—	9.52 (15)	0.0164 (15; 1.0–10.9 s)
00000000.025	2.5	—	9.55 (15)	0.0190 (15; 1.0–10.8 s)
00000000.026	2.5	—	9.54 (15)	0.0195 (15; 1.0–10.9 s)
Mean values	2.5	—	9.53	0.0183
00000000.027	4.0	—	9.16 (12)	0.0222 (12; 1.0–9.2 s)
00000000.028	4.0	—	9.13 (12)	0.0216 (12; 1.0–9.3 s)
00000000.029	4.0	—	9.15 (12)	0.0222 (12; 1.0–9.2 s)
00000000.030	4.0	—	9.15 (12)	0.0218 (12; 1.0–9.2 s)
00000000.031	4.0	—	9.17 (12)	0.0212 (12; 1.0–9.2 s)
00000000.032	4.0	—	9.16 (12)	0.0216 (12; 1.0–9.2 s)
Mean values	4.0	—	9.15	0.0218

Table G.1: Estimated circular frequencies and damping for no regulation of the flaps. To be continued in table G.2.

File name	U [m/s]	ω_z [rad/s] (n_z)	ω_α [rad/s] (n_α)	ζ_α (n_ζ; Δt)
00000000.033	5.9	—	8.57 (10)	0.0274 (10; 1.0–8.3 s)
00000000.034	5.9	—	8.63 (10)	0.0240 (10; 1.0–8.3 s)
00000000.035	5.9	—	8.65 (10)	0.0260 (10; 1.0–8.3 s)
00000000.036	5.9	—	8.70 (10)	0.0256 (10; 1.0–8.2 s)
00000000.037	5.9	—	8.73 (9)	0.0265 (9; 1.0–7.5 s)
Mean values	5.9	—	8.66	0.0259
00000000.038	7.1	7.74 (9)	7.63 (9)	0.0192 (9; 1.0–8.4 s)
00000000.039	7.1	7.78 (9)	7.63 (9)	0.0157 (9; 1.0–8.4 s)
00000000.040	7.1	7.73 (9)	7.61 (9)	0.0232 (9; 1.0–8.4 s)
00000000.041	7.1	7.74 (9)	7.56 (9)	0.0182 (9; 1.0–8.4 s)
00000000.042	7.1	7.79 (9)	7.60 (9)	0.0188 (9; 1.0–8.4 s)
Mean values	7.1	7.76	7.61	0.0190
00000000.048	7.5	7.57 (7)	7.39 (7)	0.0148 (7; 1.0–6.9 s)
00000000.049	7.5	7.50 (7)	7.40 (7)	0.0235 (7; 1.0–6.9 s)
00000000.051	7.5	7.57 (7)	7.43 (7)	0.0234 (7; 1.0–6.9 s)
00000000.052	7.5	7.51 (7)	7.46 (7)	0.0192 (7; 1.0–6.9 s)
Mean values	7.5	7.54	7.42	0.0202
00000000.053	7.8	7.31 (15)	7.23 (15)	0.0041 (15; 1.0–14.0 s)
00000000.055	7.8	7.35 (15)	7.25 (15)	0.0027 (15; 1.0–14.0 s)
00000000.056	7.8	7.29 (15)	7.23 (15)	0.0050 (15; 1.0–14.0 s)
00000000.057	7.8	7.31 (15)	7.23 (15)	0.0016 (15; 1.0–14.0 s)
00000000.058	7.8	7.27 (15)	7.20 (15)	0.0047 (15; 1.0–14.1 s)
00000000.059	7.8	7.30 (15)	7.23 (15)	0.0046 (15; 1.0–14.0 s)
Mean values	7.8	7.31	7.23	0.0038
00000000.060	7.9	7.24 (12)	7.17 (12)	0.0068 (12; 1.0–11.5 s)
00000000.061	7.9	7.25 (12)	7.15 (12)	0.0013 (12; 1.0–11.5 s)
00000000.062	7.9	7.22 (12)	7.16 (12)	0.0055 (12; 1.0–11.5 s)
Mean values	7.9	7.24	7.16	0.0045
00000000.069	8.2	7.08 (20)	7.08 (20)	0.0027 (20; 1.0–18.7 s)
00000000.070	8.2	7.12 (20)	7.09 (20)	0.0016 (20; 1.0–18.7 s)
Mean values	8.2	7.10	7.09	0.0022

Table G.2: Estimated circular frequencies and damping for no regulation of the flaps. Continued from table G.1.

File name	U [m/s]	ω_z [rad/s] (n_z)	ω_α [rad/s] (n_α)	ζ_α (n_ζ; Δt)
-0606000.000	0.0	—	10.08 (20)	0.0080 (20; 1.0–13.5 s)
-0606000.001	0.0	—	10.08 (20)	0.0077 (20; 1.0–13.5 s)
-0606000.002	0.0	—	10.14 (20)	0.0072 (20; 1.0–13.4 s)
-0606000.004	0.0	—	10.10 (20)	0.0076 (20; 1.0–13.4 s)
Mean values	0.0	—	10.10	0.0076
-0606000.005	0.0	5.25 (8)	10.09 (8)	0.0052 (8; 1.0–6.0 s)
-0606000.006	0.0	5.23 (8)	10.09 (8)	0.0059 (8; 1.0–6.0 s)
Mean values	0.0	5.24	10.09	0.0056
-0606000.007	2.5	5.20 (5)	9.32 (5)	0.0343 (5; 1.0–4.4 s)
-0606000.008	2.5	5.20 (5)	9.35 (5)	0.0355 (5; 1.0–4.4 s)
-0606000.009	2.5	5.17 (5)	9.35 (5)	0.0343 (5; 1.0–4.4 s)
-0606000.010	2.5	5.25 (4)	9.32 (5)	0.0381 (5; 1.0–4.4 s)
-0606000.011	2.5	5.24 (4)	9.32 (5)	0.0345 (5; 1.0–4.4 s)
Mean values	2.5	5.21	9.33	0.0353
-0606000.013	4.0	—	8.90 (5)	0.0630 (5; 1.0–4.5 s)
-0606000.014	4.0	—	8.73 (5)	0.0640 (5; 1.0–4.6 s)
-0606000.015	4.0	—	8.76 (5)	0.0571 (5; 1.0–4.6 s)
-0606000.016	4.0	—	8.73 (5)	0.0532 (5; 1.0–4.6 s)
-0606000.017	4.0	—	8.70 (5)	0.0552 (5; 1.0–4.6 s)
Mean values	4.0	—	8.76	0.0585
-0606000.018	5.9	—	7.89 (3)	0.0878 (3; 1.0–3.4 s)
-0606000.019	5.9	—	7.74 (3)	0.0937 (3; 1.0–3.4 s)
-0606000.020	5.9	—	7.97 (3)	0.0980 (3; 1.0–3.4 s)
-0606000.021	5.9	—	7.97 (3)	0.0997 (3; 1.0–3.4 s)
-0606000.022	5.9	—	7.89 (3)	0.1023 (3; 1.0–3.4 s)
Mean values	5.9	—	7.89	0.0963
-0606000.023	7.1	7.59 (2)	6.80 (3)	0.0684 (3; 1.0–3.8 s)
-0606000.024	7.1	7.59 (2)	6.77 (3)	0.0811 (3; 1.0–3.8 s)
-0606000.025	7.1	7.43 (2)	6.74 (3)	0.0915 (3; 1.0–3.8 s)
-0606000.026	7.1	7.70 (2)	6.71 (2)	0.0934 (2; 1.0–2.9 s)
Mean values	7.1	7.58	6.76	0.0836

Table G.3: Estimated circular frequencies and damping for flap configuration 1.

File name	U [m/s]	ω_z [rad/s] (n_z)	ω_α [rad/s] (n_α)	ζ_α (n_ζ; Δt)
-2020000.000	0.0	—	10.14 (8)	0.0101 (8; 1.0– 6.0 s)
-2020000.001	0.0	—	10.07 (7)	0.0107 (7; 1.0– 5.4 s)
-2020000.002	0.0	—	10.18 (7)	0.0104 (7; 1.0– 5.3 s)
-2020000.003	0.0	—	10.07 (15)	0.0104 (15; 1.0–10.3 s)
-2020000.004	0.0	—	10.12 (12)	0.0114 (12; 1.0– 8.4 s)
Mean values	0.0	—	10.12	0.0106
-2020000.005	0.0	5.25 (4)	10.12 (8)	0.0097 (8; 1.0–6.0 s)
-2020000.006	0.0	5.25 (4)	10.12 (8)	0.0099 (8; 1.0–6.0 s)
Mean values	0.0	5.25	10.12	0.0098
-2020000.008	2.8	—	8.73 (2)	0.1073 (2; 1.0–2.4 s)
-2020000.009	2.8	—	8.65 (2)	0.1011 (2; 1.0–2.4 s)
-2020000.010	2.8	—	8.58 (2)	0.1444 (2; 1.0–2.5 s)
-2020000.011	2.8	—	8.45 (2)	0.1195 (2; 1.0–2.5 s)
-2020000.012	2.8	—	8.58 (2)	0.1320 (2; 1.0–2.5 s)
Mean values	2.8	—	8.60	0.1209
-2020000.013	4.1	—	7.93 (1)	0.2089 (1; 1.0–1.8 s)
-2020000.014	4.1	—	8.06 (1)	0.2012 (1; 1.0–1.8 s)
-2020000.015	4.1	—	7.81 (1)	0.2211 (1; 1.0–1.8 s)
-2020000.016	4.1	—	7.81 (1)	0.1652 (1; 1.0–1.8 s)
-2020000.017	4.1	—	7.81 (1)	0.1961 (1; 1.0–1.8 s)
Mean values	4.1	—	7.88	0.1985
-2020000.018	6.1	—	*7.0* *	0.4209 (0.9; 1.0–1.8 s)
-2020000.019	6.1	—	*7.0* *	0.4458 (0.8; 1.0–1.7 s)
Mean values	6.1	—	*7.0* *	0.4334

*Table G.4: Estimated circular frequencies and damping for flap configuration 2. * For the wind speed 6.1 m/s the motion is damped very fast. The torsional circular frequency for this wind speed is therefore predicted based on the estimated values for other wind speeds and flap configurations.*

File name	U [m/s]	ω_z [rad/s] (n_z)	ω_α [rad/s] (n_α)	ζ_α (n_ζ; Δt)
06-06000.001	0.0	—	10.12 (15)	0.0100 (15; 1.0–10.3 s)
06-06000.002	0.0	—	10.15 (15)	0.0098 (15; 1.0–10.3 s)
06-06000.003	0.0	—	10.09 (8)	0.0085 (8; 1.0– 6.0 s)
06-06000.004	0.0	—	10.12 (8)	0.0078 (8; 1.0– 6.0 s)
06-06000.005	0.0	—	10.12 (8)	0.0085 (8; 1.0– 6.0 s)
Mean values	0.0	—	10.12	0.0089
06-06000.006	0.0	5.16 (4)	10.12 (8)	0.0079 (8; 1.0–6.0 s)
06-06000.007	0.0	5.16 (4)	10.14 (8)	0.0071 (8; 1.0–6.0 s)
Mean values	0.0	5.16	10.13	0.0075
06-06000.008	2.5	—	9.79 (8)	0.0080 (8; 1.0–6.0 s)
06-06000.009	2.5	—	9.78 (15)	0.0112 (15; 1.0–10.6 s)
06-06000.010	2.5	—	9.79 (15)	0.0114 (15; 1.0–10.6 s)
06-06000.011	2.5	—	9.74 (8)	0.0087 (8; 1.0–6.2 s)
06-06000.012	2.5	—	9.79 (8)	0.0097 (8; 1.0–6.1 s)
Mean values	2.5	—	9.78	0.0098
06-06000.013	4.0	—	9.50 (8)	0.0115 (8; 1.0– 6.3 s)
06-06000.014	4.0	—	9.52 (15)	0.0104 (15; 1.0–10.9 s)
06-06000.015	4.0	—	9.54 (10)	0.0144 (10; 1.0– 7.6 s)
06-06000.016	4.0	—	9.50 (10)	0.0129 (10; 1.0– 7.6 s)
Mean values	4.0	—	9.52	0.0123
06-06000.017	5.9	9.13 (12)	9.07 (12)	0.0101 (12; 1.0–9.3 s)
06-06000.018	5.9	9.08 (12)	9.07 (12)	0.0099 (12; 1.0–9.3 s)
06-06000.019	5.9	9.07 (12)	8.98 (12)	0.0041 (12; 1.0–9.4 s)
06-06000.020	5.9	9.08 (12)	9.03 (12)	0.0013 (12; 1.0–9.3 s)
06-06000.021	5.9	9.15 (12)	9.01 (12)	0.0032 (12; 1.0–9.4 s)
Mean values	5.9	9.10	9.03	0.0057
06-06000.022	7.1	8.38 (6)	8.16 (6)	-0.0150 (6; 1.0–5.6 s)
06-06000.023	7.1	8.49 (6)	8.22 (6)	-0.0199 (6; 1.0–5.6 s)
Mean values	7.1	8.44	8.19	-0.0175

Table G.5: Estimated circular frequencies and damping for flap configuration 3.

File name	U [m/s]	ω_z [rad/s] (n_z)	ω_α [rad/s] (n_α)	ζ_α (n_ζ; Δt)
20-20000.000	2.8	—	9.84 (15)	-0.0024 (15; 1.0–10.6 s)
20-20000.001	2.8	—	9.83 (12)	-0.0016 (12; 1.0– 8.7 s)
20-20000.002	2.8	—	9.83 (15)	-0.0009 (15; 1.0–10.6 s)
20-20000.003	2.8	—	9.88 (15)	-0.0015 (15; 1.0–10.5 s)
20-20000.004	2.8	—	9.82 (15)	-0.0020 (15; 1.0–10.6 s)
Mean values	2.8	—	9.84	-0.0017
20-20000.005	4.2	9.59 (15)	9.64 (15)	-0.0023 (15; 1.0–10.8 s)
20-20000.006	4.2	9.57 (15)	9.64 (15)	-0.0011 (15; 1.0–10.8 s)
20-20000.007	4.2	9.54 (15)	9.61 (15)	-0.0006 (15; 1.0–10.8 s)
20-20000.008	4.2	9.57 (15)	9.61 (15)	-0.0008 (15; 1.0–10.8 s)
20-20000.009	4.2	9.58 (15)	9.59 (15)	-0.0007 (15; 1.0–10.8 s)
Mean values	4.2	9.57	9.62	-0.0011
20-20000.010	6.1	9.12 (12)	9.00 (12)	-0.0029 (12; 1.0–9.4 s)
20-20000.011	6.1	9.09 (12)	8.99 (12)	-0.0018 (12; 1.0–9.4 s)
20-20000.012	6.1	9.05 (12)	8.92 (12)	0.0001 (12; 1.0–9.4 s)
20-20000.013	6.1	9.03 (12)	8.91 (12)	-0.0005 (12; 1.0–9.5 s)
20-20000.014	6.1	9.05 (12)	8.91 (12)	-0.0017 (12; 1.0–9.5 s)
Mean values	6.1	9.07	8.95	-0.0014

Table G.6: Estimated circular frequencies and damping for flap configuration 4.

G.4 Amplification and Phase

The amplifications and phase angles between the filtered torsional motion and the filtered actual positions of the flaps are found for flap configurations 1–3 by minimizing an error defined as the sum of the squared differences between the torsional motion and flap position.

The following procedure is used to estimate the parameters:

1. Filtering of data. The time series $\alpha(t)$, $\alpha_{ta}(t)$ and $\alpha_{la}(t)$ are filtered through a second order filter with pole 0.5.

2. Estimation of the phase angles by minimization of the errors E_{φ_t} and E_{φ_l} defined by

$$\min_{\Delta t} E_{\varphi_t} = \sum (\alpha_f(t) - \alpha_{ta,f}(t+\Delta t))^2 \tag{G.9}$$

$$\min_{\Delta t} E_{\varphi_l} = \sum (\alpha_f(t) - \alpha_{la,f}(t+\Delta t))^2 \tag{G.10}$$

   where the sum is from the time 0.996 s to 3.996 s with the time step 0.012 s. Δt is the time delay that is estimated with the accuracy 0.012 s.

3. Estimation of the amplifications by minimization of the errors E_t and E_l defined by

$$\min_{a} E_t = \sum (a\alpha_f(t) - \alpha_{ta,f}(t+\Delta t_t))^2 \tag{G.11}$$

$$\min_{a} E_l = \sum (a\alpha_f(t) - \alpha_{la,f}(t+\Delta t_l))^2 \tag{G.12}$$

   where a is the amplification and Δt_t and Δt_l are the optimal time delays for the trailing and leading flap, respectively. The sum is from the time 0.996 s to 3.996 s with the time step 0.012 s. The optimal amplifications a_{ta} and a_{la} are estimated with the accuracy 0.01.

The estimated parameters Δt_t, Δt_l, a_{ta} and a_{la} are shown in table G.7 for flap configuration 1, in table G.8 for flap configuration 2 and in table G.9 for flap configuration 3. Only data from free torsional motion are used to estimate the parameters, i.e. when the wind speed is zero. Experiments without wind are not performed for flap configuration 4.

The following notation is used in the tables:

- File name: the name of the file with stored data from an experiment.
- Δt_t: estimated time delay for trailing flap in milliseconds.
- Δt_l: estimated time delay for leading flap in milliseconds.
- a_{ta}: estimated amplification factor for trailing flap.

File name	Δt_t [ms]	Δt_l [ms]	a_{ta}	a_{la}
-0606000.000	444	444	1.90	1.99
-0606000.001	444	444	1.91	1.98
-0606000.002	444	444	1.94	1.98
-0606000.004	444	444	1.90	1.95
Mean values	444	444	1.91	1.98

Table G.7: Estimated time delay and amplification factor for flap configuration 1.

File name	Δt_t [ms]	Δt_l [ms]	a_{ta}	a_{la}
-2020000.000	456	456	4.56	4.75
-2020000.001	444	444	3.81	4.02
-2020000.002	456	456	2.80	2.94
-2020000.003	456	456	2.70	2.83
-2020000.004	456	456	3.22	3.40
Mean values	454	454	3.42	3.59

Table G.8: Estimated time delay and amplification factor for flap configuration 2.

- a_{la}: estimated amplification factor for leading flap.

In table G.8 the amplification factors deviate much. For the results stored in files -2020000.002 and -2020000.003 the mean values of the positions of the flaps are oscillating, i.e. the flaps are not oscillating around the defined zero point.

File name	Δt_t [ms]	Δt_l [ms]	a_{ta}	a_{la}
06-06000.001	144	144	1.98	2.03
06-06000.002	144	144	2.02	2.04
06-06000.003	144	144	1.99	2.04
06-06000.004	144	144	1.97	2.03
06-06000.005	144	144	1.96	2.03
Mean values	144	144	1.98	2.03

Table G.9: Estimated time delay and amplification factor for flap configuration 3.

In tables G.10–G.12 the actual phase angle φ and the phase angle factor f for each time series are calculated based on the estimated time delays Δt. This delay is always the same for the flaps, the calculated factors are therefore valid for both the trailing and the leading flap. Note that the factors are equal, because the angles of both flaps are positive downwards. The following equations are used:

$$\varphi = \omega'_\alpha \Delta t \tag{G.13}$$

where ω'_α is the damped circular eigenfrequency for the time series.

$$f = \varphi \frac{6}{\pi} \tag{G.14}$$

File name	Δt [s]	φ [rad]	f
-0606000.000	0.444	4.48	8.55
-0606000.001	0.444	4.48	8.55
-0606000.002	0.444	4.50	8.60
-0606000.004	0.444	4.48	8.56
Mean values	0.444	4.49	8.56

Table G.10: Estimated time delay, phase angle and phase angle factor for flap configuration 1.

File name	Δt [s]	φ [rad]	f
-2020000.000	0.456	4.62	8.83
-2020000.001	0.444	4.47	8.54
-2020000.002	0.456	4.64	8.87
-2020000.003	0.456	4.59	8.77
-2020000.004	0.456	4.61	8.81
Mean values	0.454	4.59	8.76

Table G.11: Estimated time delay, phase angle and phase angle factor for flap configuration 2.

File name	Δt [s]	φ [rad]	f
06-06000.001	0.144	1.46	2.78
06-06000.002	0.144	1.46	2.79
06-06000.003	0.144	1.45	2.77
06-06000.004	0.144	1.46	2.78
06-06000.005	0.144	1.46	2.78
Mean values	0.144	1.46	2.78

Table G.12: Estimated time delay, phase angle and phase angle factor for flap configuration 3.

G.5 Divergence and Flutter Wind Velocity

The divergence wind velocity is given by (see Frandsen [10])

$$U_D = \frac{1}{b}\sqrt{\frac{k_\alpha}{\pi\rho}} \tag{G.15}$$

where b is the half width of the model, k_α is the stiffnes in torsion per unit length and ρ is the density of air.

The flutter wind velocity is estimated by Selberg's formula, see Larsen & Gimsing [23]

$$U_F = f_\alpha B 3.72 \sqrt{\frac{\sqrt{Im}}{\rho B^3}\left[1 - \left(\frac{f_z}{f_\alpha}\right)^2\right]} \tag{G.16}$$

where f_z and f_α are the eigenfrequency for bending and torsion, respectively, B is the width of the model (with long flaps), I is the mass moment of inertia per unit length and m is the mass per unit length.

The stiffness in torsion is

$$k_\alpha = a^2 k_z \tag{G.17}$$

where a is the distance between the axis of rotation and the springs.

The eigenfrequencies can be written

$$f_z = \frac{\omega_z}{2\pi} = \frac{1}{2\pi}\sqrt{\frac{k_z}{m}} \tag{G.18}$$

$$f_\alpha = \frac{\omega_\alpha}{2\pi} = \frac{a}{2\pi}\sqrt{\frac{k_z}{I}} \tag{G.19}$$

Equations (G.18) and (G.19) can be combined into

$$\left(\frac{f_z}{f_\alpha}\right)^2 = \frac{I}{a^2 m} \tag{G.20}$$

By using the above equations and $b = B/2$ the divergence and flutter wind velocity can be derived

$$U_D = \frac{2a}{B}\sqrt{\frac{k_z}{\pi\rho}} \tag{G.21}$$

$$U_F = \frac{a}{2\pi}\sqrt{\frac{k_z}{I}} B 3.72 \sqrt{\frac{\sqrt{Im}}{\rho B^3}\left[1 - \frac{I}{a^2 m}\right]} \tag{G.22}$$

The fixed parameters are the width of the model and the density of air, i.e.

$$B = 1.5 \cdot 0.625 = 0.938 \text{ m} \tag{G.23}$$

$$\rho = 1.2 \text{ kg/m}^3 \tag{G.24}$$

Inserting these parameters in equations (G.21) and (G.22) yields

$$U_D = 1.098 a \sqrt{k_z} \tag{G.25}$$

$$U_F = 0.558\sqrt{k_z}\sqrt{\sqrt{\frac{m}{I}}\left[a^2 - \frac{I}{m}\right]} \tag{G.26}$$

Changing the bending stiffness k_z, therefore, cannot separate the divergence and flutter velocities.

In the following it is assumed the the total spring stiffness (for four springs) is

$$k_z = \omega_z^2 m \tag{G.27}$$

where ω_z is the estimated circular frequency for bending.

For the wind tunnel experiments the following parameters are estimated and calculated

$$\omega_z = 5.2 \text{ rad/s} \tag{G.28}$$

$$\omega_\alpha = 10.1 \text{ rad/s} \tag{G.29}$$

$$m = \frac{26.553}{1.48} = 17.94 \text{ kg/m} \tag{G.30}$$

$$k_z = \omega_z^2 m = 5.2^2 \cdot 17.94 = 485 \text{ N/m}^2 \tag{G.31}$$

$$a = \frac{0.704}{2} = 0.352 \text{ m} \tag{G.32}$$

$$I = \frac{k_\alpha}{\omega_\alpha^2} = \frac{a^2 k_z}{\omega_\alpha^2} = \frac{0.352^2 \cdot 485}{10.1^2} = 0.589 \text{ kg m}^2/\text{m} \tag{G.33}$$

$$U_D = 1.098 \cdot 0.352 \cdot \sqrt{485} = 8.5 \text{ m/s} \tag{G.34}$$

$$U_F = 0.558\sqrt{485}\sqrt{\sqrt{\frac{17.94}{0.589}}\left[0.352^2 - \frac{0.589}{17.94}\right]} = 8.7 \text{ m/s} \tag{G.35}$$

Two parameters of the model can be used to separate divergence and flutter, namely by regulating both the mass moment of inertia I and the distance a between the axis of rotation and the springs.

The mass moment of inertia is increased by moving the four loads on the horizontal arm of the suspension system. By moving the loads from their positions 75 mm from the axis of rotation to 475 mm from this axis the mass moment of inertia is increased by

$$\Delta I = 0.5 \cdot 4(475 - 75)^2 \cdot 10^{-6} = 0.320 \text{ kg m}^2 \tag{G.36}$$

Thereby the total mass moment of inertia is

$$I + \Delta I = 0.589 \cdot 1.48 + 0.320 = 1.192 \text{ kg m}^2 = 0.805 \text{ kg m}^2/\text{m} \tag{G.37}$$

and the flutter wind velocity is

$$U_F = 0.558\sqrt{k_z}\sqrt{\sqrt{\frac{17.94}{0.805}}\left[a^2 - \frac{0.805}{17.94}\right]} = 1.212\sqrt{a^2 - 0.045}\sqrt{k_z} \tag{G.38}$$

a [m]	U_F [m/s]	U_D [m/s]	U_D/U_F
0.20	—	$0.220\sqrt{k_z}$	—
0.25	$0.161\sqrt{k_z}$	$0.275\sqrt{k_z}$	1.71
0.30	$0.258\sqrt{k_z}$	$0.329\sqrt{k_z}$	1.28
0.31	$0.274\sqrt{k_z}$	$0.340\sqrt{k_z}$	1.24
0.32	$0.291\sqrt{k_z}$	$0.351\sqrt{k_z}$	1.21
0.33	$0.307\sqrt{k_z}$	$0.362\sqrt{k_z}$	1.18
0.34	$0.322\sqrt{k_z}$	$0.373\sqrt{k_z}$	1.16
0.35	$0.338\sqrt{k_z}$	$0.384\sqrt{k_z}$	1.14
0.40	$0.411\sqrt{k_z}$	$0.439\sqrt{k_z}$	1.09
0.45	$0.481\sqrt{k_z}$	$0.494\sqrt{k_z}$	1.03

Table G.13: Flutter and divergence wind velocities for different distances between the axis of rotation and the springs.

The flutter and divergence wind velocities and the ratio between these are shown in table G.13 for different values of a.

The following values are selected:

$$a = 0.32 \text{ m} \tag{G.39}$$

$$U_F = 10 \text{ m/s} \tag{G.40}$$

Thereby the total stiffness of four new springs is

$$U_F = 0.291\sqrt{k_z} = 10 \text{ m/s} \quad \Rightarrow \quad k_z = 1180 \text{ N/m}^2 = 1748 \text{ N/m} \tag{G.41}$$

which corresponds to 437 N/m per spring. The new springs are ordered to have the stiffness 440 N/m, i.e. the total stiffness is

$$k_z = 4 \cdot 440 = 1760 \text{ N/m} = 1189 \text{ N/m}^2 \tag{G.42}$$

The new eigenfrequencies are

$$\omega_z = \sqrt{\frac{k_z}{m}} = \sqrt{\frac{1189}{17.94}} = 8.14 \text{ rad/s} \quad \Rightarrow \quad f_z = 1.30 \text{ Hz} \tag{G.43}$$

$$\omega_\alpha = \sqrt{\frac{a^2 k_z}{I}} = \sqrt{0.32^2 \frac{1189}{0.805}} = 12.3 \text{ rad/s} \quad \Rightarrow \quad f_\alpha = 1.96 \text{ Hz} \tag{G.44}$$

G.6 Flap Positioning

The equation of the torsional motion $\alpha(t)$ of free vibration of the bridge section model is given by

$$\left.\begin{aligned} &\ddot{\alpha}(t) + 2\zeta_\alpha \omega_\alpha \dot{\alpha}(t) + \omega_\alpha^2 \alpha(t) = 0, \quad t > 0 \\ &\alpha(0) = \alpha_0, \quad \dot{\alpha}(0) = \dot{\alpha}_0 \end{aligned}\right\} \tag{G.45}$$

All parameters with index α refer to the torsional motion $\alpha(t)$. The damping ratio ζ_α is the ratio between the actual value and the critical value of the torsional damping constant. The circular eigenfrequency for free vibration in torsion is denoted ω_α.

The solution to equation (G.45) is dependent on the magnitude of the damping ratio. For an underdamped system the solution is

$$\alpha(t) = e^{-\zeta_\alpha \omega_\alpha t}\left[\alpha_0 \cos(\omega'_\alpha t) + \frac{\dot{\alpha}_0 + \zeta_\alpha \omega_\alpha \alpha_0}{\omega'_\alpha}\sin(\omega'_\alpha t)\right], \quad t \geq 0, \quad \zeta_\alpha \in [0,1[\tag{G.46}$$

where the circular eigenfrequency for the damped system is given by

$$\omega'_\alpha = \omega_\alpha \sqrt{1-\zeta_\alpha^2} \tag{G.47}$$

Equation (G.46) can be rewritten

$$\alpha(t) = A_\alpha e^{-\zeta_\alpha \omega_\alpha t}\cos(\omega'_\alpha t - \varphi_\alpha), \quad t \geq 0, \quad \zeta_\alpha \in [0,1[\tag{G.48}$$

where

$$\left.\begin{aligned} A_\alpha \cos(\varphi_\alpha) &= \alpha_0 \\ A_\alpha \sin(\varphi_\alpha) &= \frac{\dot{\alpha}_0 + \zeta_\alpha \omega_\alpha \alpha_0}{\omega'_\alpha} \end{aligned}\right\} \tag{G.49}$$

A_α is the start amplitude (the amplitude of the envelope curve at the time $t = 0$) and φ_α is the phase angle.

As $e^{i\omega t} = \cos(\omega t) + i\sin(\omega t)$, equation (G.48) can be rewritten

$$\alpha(t) = A_\alpha e^{-\zeta_\alpha \omega_\alpha t}\mathrm{Re}\left(e^{i(\omega'_\alpha t - \varphi_\alpha)}\right) \tag{G.50}$$

The positioning of the flap is delayed by the phase angle φ_Δ compared to the desired position. The desired motion of the trailing flap with amplitude amplification factor a_t and phase angle φ_t is

$$\begin{aligned} \alpha_t(t) &= a_t A_\alpha e^{-\zeta_\alpha \omega_\alpha t}\mathrm{Re}\left(e^{i(\omega'_\alpha t - \varphi_\alpha - \varphi_\Delta - \varphi_t)}\right) \\ &= a_t A_\alpha e^{-\zeta_\alpha \omega_\alpha t}\mathrm{Re}\left(e^{i(\omega'_\alpha t - \varphi_\alpha)} e^{i(-\varphi_\Delta - \varphi_t)}\right) \\ &= a_t A_\alpha e^{-\zeta_\alpha \omega_\alpha t}\{\cos(\omega'_\alpha t - \varphi_\alpha)\cos(-\varphi_\Delta - \varphi_t) - \\ &\quad \sin(\omega'_\alpha t - \varphi_\alpha)\sin(-\varphi_\Delta - \varphi_t)\} \\ &= a_t \alpha(t)\{\cos(-\varphi_\Delta - \varphi_t) - \tan(\omega'_\alpha t - \varphi_\alpha)\sin(-\varphi_\Delta - \varphi_t)\} \end{aligned} \tag{G.51}$$

The time is set to zero at the first zero upcrossing of the torsional motion; thereby $\alpha_0 = 0$ and $\dot{\alpha}_0 > 0$ which implies that $\varphi_\alpha = \pi/2$.

The final regulation formulas are

$$\left.\begin{aligned} \alpha_t(t) &= a_t \alpha(t)\{\cos(-\varphi_\Delta - \varphi_t) - \tan(\omega'_\alpha t - \pi/2)\sin(-\varphi_\Delta - \varphi_t)\} \\ \alpha_l(t) &= -a_l \alpha(t)\{\cos(-\varphi_\Delta - \varphi_l) - \tan(\omega'_\alpha t - \pi/2)\sin(-\varphi_\Delta - \varphi_l)\} \end{aligned}\right\} \tag{G.52}$$

The flaps are started slowly by multiplying the desired position by a factor t/T_0 when $t < T_0$. The time for slow start is set to $T_0 = 1$ s.

G.7 Numerical Problems with Control Algorithm

As described in section 6.5 there are numerical problems when the control algorithm described by equation (G.52) is used.

Some of the problems are due to the fact that the desired flap angles for most phase angles must have a certain value when the model is horizontal, i.e. when $\alpha(t) = 0$ for e.g. $t = 0$. In the following L'Hôpital's Rule, see e.g. [38], is used to show that, theoretically, there should not be any problems.

In the following only the trailing flap is examined. Equation (G.52) can be rewritten:

$$\alpha_t(t) = a_t\alpha(t)\left\{\frac{\cos(\omega'_\alpha t - \pi/2)\cos(-\varphi) - \sin(\omega'_\alpha t - \pi/2)\sin(-\varphi)}{\cos(\omega'_\alpha t - \pi/2)}\right\} \tag{G.53}$$

where $\varphi = \varphi_\Delta + \varphi_t$. In this equation both the numerator $N(t)$ and the denominator $D(t)$ become zero when $t = 0$. The limit of $\alpha_t(0)$ is

$$\lim_{t\to 0}\alpha_t(t) = \frac{N'(0)}{D'(0)} = \frac{a_t\alpha'(0)\sin(-\varphi)}{\omega'_\alpha} \tag{G.54}$$

i.e. the desired flap position has a final non-zero value when $\alpha = 0$.

STRUCTURAL RELIABILITY THEORY SERIES

PAPER NO. 173: P. H. Kirkegaard, S. R. K. Nielsen, I. Enevoldsen: *Dynamic Vehicle Impact for Safety Assessment of Bridges.* ISSN 1395-7953 R9810.

PAPER NO. 175: C. Frier, J.D. Sørensen: *Stochastic Properties of Plasticity Based Constitutive Law for Concrete.* ISSN 1395-7953 R9727.

PAPER NO. 176: R. Iwankiewicz, S.R.K. Nielsen: *Analytical vs Simulation Solution Techniques for Pulse Problems in Non-Linear Stochastic Dynamics.* ISSN 1395-7953 R9760.

PAPER NO. 177: P. Thoft-Christensen: *Review of Industrial Applications of Structural Reliability Theory.* ISSN 1395-7953 R9750.

PAPER NO. 178: P. Thoft-Christensen, C. R. Middleton: *Reliability Assessment of Concrete Bridges.* ISSN 1395-7953 R9755.

PAPER NO. 179: C. R. Middleton, P. Thoft-Christensen: *Assessment of the Reliability of Concrete Bridges.* ISSN 1395-7953 R9756.

PAPER NO. 180: P. Thoft-Christensen: *Reliability Based Optimization of Fire Protection.* ISSN 1395-7953 R9757.

PAPER NO. 181: P. Thoft-Christensen: *On Industrial Application of Structural Reliability Theory.* ISSN 1395-7953 R9822.

PAPER NO. 182: Tom Lassen: *Experimental Investigation and Stochastic Modelling of the Fatigue Behaviour of Welded Steel Joints.* Ph.D. Thesis. ISSN 1395-7953 R9761.

PAPER NO. 183: P. Thoft-Christensen: *Assessment of the Reliability Profiles for Concrete Bridges.* ISSN 1395-7953 R9823.

PAPER NO. 184: H. I. Hansen, P. Thoft-Christensen: *Active Control of Long Bridges using Flaps.* ISSN 1395-7953 R9838.

PAPER NO. 185: H. I. Hansen, P. Thoft-Christensen: *Wind Tunnel Experiments with Active Control of Bridge Section Model.* ISSN 1395-7953 R9839.

PAPER NO. 186: H. I. Hansen: *Active Vibration Control of Long Suspension Bridges.* Ph.D. Thesis. ISSN 1395-7953 R9840.

Active Vib

ISSN 1395-7953 R9840

Dept. of Building Technology and Structural Engineering
Aalborg University
Sohngaardsholmsvej 57, DK-9000 Aalborg, Denmark
Phone: +45 9635 8080 Fax: +45 9814 8243
www.civil.auc.dk/i6